# Nucleosynthetic zinc isotope variations in meteorites

by

Rayssa Martins Pimentel

Department of Earth Sciences and Engineering

Imperial College London

Thesis submitted for the degree of Doctor of Philosophy

October 2023

## Statement of Originality

I declare that the contents of this thesis consist of my own work as performed under the supervision of Professor Mark Rehkämper. Any contributions from other individuals are duly credited, and all other works are appropriately referenced.

Rayssa Martins Pimentel

## Copyright Declaration

The copyright of this thesis rests with the author. Unless otherwise indicated, its contents are licensed under a Creative Commons Attribution – Non-Commercial 4.0 International Licence (CC BY-NC). Under this licence, you may copy and redistribute the material in any medium or format. You may also create and distribute modified versions of the work. This is on the condition that: you credit the author and do not use it, or any derivative works, for a commercial purpose.

When reusing or sharing this work, ensure you make the licence terms clear to others by naming the licence and linking to the licence text. Where a work has been adapted, you should indicate that the work has been changed and describe those changes.

Please seek permission from the copyright holder for uses of this work that are not included in this licence or permitted under UK Copyright Law.

## Acknowledgements

I would like to thank my supervisor, Mark Rehkämper, for the effort he put into getting me to Imperial; for always providing valuable insights and support (especially when things didn't work as planned); for his generosity with his time and resources; and, most of all, for teaching me how best to convey scientific ideas. I'd also like to thank Sven Kuthning for his work in the method development and collecting the initial data, Barry Coles and Katharina Kreissig for helping me through the many technical challenges posed by this project, and Tina van de Flierdt for being my mentor and supporter, and for always having great advice.

I also thank Alessandro Bragagni for performing the leaching procedure, initial ion exchange chromatography, and elemental analyses for Chapter 4, as well as Elin Morton for completing the procedure and performing the Zn isotope analyses for the Allende and Kainsaz leachates. I also thank Elin for reprocessing some of the data for other low concentration samples; for taking turns staying late on the mass spectrometer on our week-long sessions; for the cumulative hours of standing by while I do HF; and for all our collaborations.

I thank Saskia Goes for greatly improving the code for the Monte Carlo simulations, Frank Wombacher for helpful comments, and Mario Fischer-Gödde and two anonymous reviewers for providing feedback that considerably enriched earlier versions of Chapter 2. I'm also grateful for the President's PhD Scholarship for allowing international students like me to have this opportunity. Finally, I would like to thank my family and friends for always believing in me, and for the endless support and personal sacrifice without which this work would not have been possible.

*"Do not undertake a scientific career in quest of fame or money. There are easier and better ways to reach them. Undertake it only if nothing else will satisfy you; for nothing else is probably what you will receive. Your reward will be the widening of the horizon as you climb. And if you achieve that reward, you will ask no other."*

Cecilia Payne-Gaposchkin, 1996

## Abstract

Nucleosynthetic isotope anomalies have been extensively used as tracers to identify Earth's building blocks among other Solar System materials. However, while such anomalies have been well characterized for refractory elements, studies attempting to identify anomalies of volatile elements – many of which are essential for life – have found them to be undetectable with available precision levels, or of ambiguous origin, leaving the sources of terrestrial volatiles unconstrained. The present study focuses on characterizing the mass-independent isotope compositions of the moderately volatile element Zn in meteorites with the purpose of identifying anomalies, establishing their origin, and using them to constrain the sources of Earth's Zn.

The mass-independent Zn isotope compositions of twenty-seven meteorites were determined and found to be compatible with the predicted isotopic yields of two types of supernovae. Other mechanisms that can induce isotope fractionation were considered but reasonably discarded, making a nucleosynthetic origin the most likely explanation for the anomalies. The results were used in a series of mass balance mixing models intended to determine which of the available Solar System materials could have contributed to Earth's Zn budget. The models suggest that carbonaceous materials, which formed at much greater heliocentric distances than Earth, supplied nearly half of its Zn, with the remaining fraction originating from more locally sourced non-carbonaceous materials.

Further constraints provided by meteorite and terrestrial elemental, nucleosynthetic and mass-dependent isotope compositions of elements other than Zn were employed in additional models that attempted to constrain not only the mass, but also the volatile contributions of Earth's precursor materials. The results suggest that Earth accreted mainly (~60% of its mass) from highly volatile depleted differentiated non-carbonaceous bodies, with most of its volatile content being supplied by undifferentiated planetesimals. The addition of primitive material may therefore be necessary to establish the volatile content of terrestrial planets.

# Table of contents

**List of Figures** ..... **11**

**List of Tables** ..... **13**

**Chapter 1 – Introduction** ..... **16**
1.1 Background ..... 17
1.1.1. Volatile Depletion ..... 17
1.1.2. Nucleosynthetic isotope anomalies ..... 19
1.2 Aims and approach ..... 20
1.2.1. Origin of the anomalies ..... 20
1.2.2. Expand the characterization to other Solar System materials ..... 21
1.2.3. Origin of Earth's volatiles ..... 21
1.2.4. Heterogeneous distribution of anomalous Zn ..... 22
1.3 References ..... 24

**Chapter 2 – Nucleosynthetic zinc isotope anomalies in meteorites** ..... **28**
2.1 Introduction ..... 29
2.2 Samples ..... 30
2.3 Methods ..... 32
2.3.1 Sample preparation ..... 32
2.3.1.1. Laboratory and reagents ..... 32
2.3.1.2. Initial sample treatment and digestion ..... 32
2.3.1.3. Anion exchange separation of Zn ..... 32
2.3.2 Mass Spectrometry ..... 34
2.3.2.1. Zn isotope measurements ..... 34
2.3.2.2. Data reduction and presentation ..... 37
2.3.2.3. Quality control of Zn isotope data ..... 39
2.4 Results ..... 40
2.5 Discussion ..... 46
2.5.1 Origin of the anomalies ..... 46
2.5.1.1. Mass-dependent isotope fractionation ..... 46
2.5.1.2. Nuclear Field Shift Effect ..... 47
2.5.1.3. Nucleosynthetic Anomalies ..... 52
2.5.2. Origin of Earth's Zn ..... 57
2.5.2.1. Zn mass balance ..... 57
2.5.2.2. CC mass contribution ..... 60
2.5.2.3. Estimates from refractory element nucleosynthetic anomalies ..... 61
2.6 Conclusions ..... 64
2.7 References ..... 65

**Chapter 3 – Primitive asteroids as a major source of terrestrial volatiles** ..... **70**
3.1 Introduction ..... 71
3.2 Samples ..... 73
3.3 Methods ..... 75
3.3.1. Sample preparation ..... 75
3.3.2. Isotope measurements ..... 75
3.4 Results ..... 78
3.5 Discussion ..... 87
3.5.1 Origin of Earth's Zn ..... 87

3.5.2. The search for Earth's accreting material ..... 89
3.5.3. Unsampled material ..... 100
3.5.4. Mode of accretion and volatile depletion ..... 101
3.5.5. Implications for the formation of habitable planets ..... 108
3.6 Conclusions ..... 109
3.7 References ..... 111

**Chapter 4 – The origin of nucleosynthetic zinc isotope heterogeneity in the Solar System ..... 116**
4.1 Introduction ..... 117
4.2 Methods ..... 118
4.2.1 Sample preparation and leaching procedure ..... 118
4.2.2 Ion exchange chromatography ..... 122
4.2.3 Mass spectrometry ..... 123
4.3 Results ..... 125
4.4 Discussion ..... 130
4.4.1 Carrier phases of isotopically anomalous Zn ..... 130
4.4.2 Thermal processing ..... 135
4.4.3 Incomplete homogenization ..... 140
4.5 Conclusions ..... 144

**Summary and Outlook ..... 150**

**Appendix ..... 155**

# List of Figures

**Figure 1.1.** Abundances of main elements and Zn normalized to Al and to CI chondrites……19

**Figure 1.2.** Theoretical Zn isotope yields of different stellar sources, assuming variable physical parameters, compared to Solar System Zn isotope abundances……23

**Figure 2.1.** Mass-independent Zn isotope compositions of BSE rocks……41

**Figure 2.2.** Zn isotope anomalies for each meteorite group and the BSE, in $\varepsilon^{i}$Zn notation…42

**Figure 2.3.** Mass-dependent Zn isotope data ($\delta^{66}$Zn) and mass-independent Zn isotope compositions ($\varepsilon^{64}$Zn) for chondrites……47

**Figure 2.4.** Mass-independent Zn isotope data in $\varepsilon^{i}$Zn notation for the OCs……50

**Figure 2.5.** Predicted mass-independent Zn isotope fractionation induced by NFSE compared to measured meteorite and BSE compositions……51

**Figure 2.6.** Three isotope plots of mass-independent Zn results in ε notation……...53

**Figure 2.7.** Correlation between nucleosynthetic isotope anomalies of Zn and other Fe-peak elements……55

**Figure 2.8.** Inferred CC contribution to the bulk Earth Zn inventory from Monte Carlo simulations……...58

**Figure 2.9.** Estimates for the mass fractions of accreted CC material ($x_{cc}$)……...63

**Figure 3.1.** Mean Zn isotope compositions for the meteorite groups and the BSE, in $\varepsilon^{i}$Zn notation……83

**Figure 3.2.** Measured Zn isotope compositions in comparison to predicted nucleosynthetic isotope anomalies……84

**Figure 3.3.** Measured $^{64}$Zn isotope anomalies versus isotope anomalies of other Fe-peak elements……85

**Figure 3.4.** Measured $^{70}$Zn isotope anomalies versus isotope anomalies of other Fe-peak elements……86

**Figure 3.5.** Results from simulations to determine which combinations of CC and NC meteorites successfully produce an Earth-like nucleosynthetic Zn isotope composition……88

**Figure 3.6.** Mixing models that attempt to reproduce the isotope and elemental compositions of the bulk Earth……97

**Figure 3.7.** Nucleosynthetic isotope compositions of inner Solar System bodies over time.....105

**Figure 4.1.** Schematic diagram of leaching procedure……...……119

**Figure 4.2.** Photograph showing residues of the different leaching steps for the four meteorite samples……...120

**Figure 4.3.** Mass-independent Zn isotope compositions in $\varepsilon^{i}$Zn notation……...127

**Figure 4.4.** $\varepsilon^{64}$Zn results and Zn fraction (%)…….129

**Figure 4.5.** Results of model calculations that simulate mixing between two endmembers with nucleosynthetic Ti isotope compositions akin to CAIs and CI chondrites……...132

**Figure 4.6.** Variable nucleosynthetic Zn isotope compositions and bulk Zn content of chondritic meteorites……..138

**Figure 4.7.** Plots showing correlated variations between different nucleosynthetic isotope anomalies……144

**Figure A2.1.** Modelled trendlines for predicted nucleosynthetic Zn isotope anomalies…….156

# List of Tables

**Table 2.1.** Names, digested masses, identifiers and sources of the meteorites and BSE rocks analysed in this study……32

**Table 2.2.** Ion exchange column chemistry for Stage 1 of the Zn separation from meteorite and rock samples……34

**Table 2.3.** Ion exchange column chemistry for Stages 2 and 3 of the Zn separation from meteorite and rock samples……...35

**Table 2.4.** Operating conditions of the Nu Plasma MC-ICP-MS and the Nu Instruments DSN 100 desolvating sample introduction system……36

**Table 2.5.** Collector configurations that were used for the Zn isotope measurements ……37

**Table 2.6.** Mass-independent Zn isotope data for meteorites and BSE samples……..…43

**Table 2.7.** Estimates for the fraction of Zn derived from CC material, $x_{CC}^{Zn}$, from mass balance models…….…….60

**Table 2.8.** Estimates for the mass fraction of CC material accreted by the Earth, $x_{CC}$, from mass balance models…….……61

**Table 3.1.** Names, digested masses, identifiers and sources of the meteorites and BSE rock analysed in this study……74

**Table 3.2.** Collector configurations that were used for the Zn isotope measurements……...77

**Table 3.3.** Mass-independent Zn isotope data (in εZn notation) for the meteorites and BSE samples……79

**Table 3.4.** Compiled isotope data used in the modelling……...92

**Table 3.5.** Compiled concentration data for the elements and meteorite classes considered in the modelling……94

**Table 3.6.** Summary of results from the Monte Carlo simulations……97

**Table 4.1.** Names, digested masses, and sources of the meteorite samples……...…...120

**Table 4.2.** Summary of leaching procedure……121

**Table 4.3a.** Stage I of ion exchange chromatography……122

**Table 4.3b.** Stage II of ion exchange chromatography……..…..……122

**Table 4.4.** Collector configurations that were used for the Zn isotope measurements…….124

**Table 4.5.** Mass-independent Zn isotope data (in $\varepsilon^{i}$Zn notation) and Zn mass fractions (%) of the seven leaching steps for the four meteorite samples…….128

**Table 4.6.** Estimated and measured bulk compositions of meteorites…….129

**Table A2.1.** Ti and Cr isotope data utilized in Figure 2.7……157

**Table A2.2.** Mean $\varepsilon^{64}$Zn, $\varepsilon^{70}$Zn, and $\varepsilon^{66/67}Zn_{64/67}$ values of endmembers used in the mass balance calculations and their respective p-values…….……158

**Table A2.3.** Zn concentration data (in μg $g^{-1}$) for CCs, ECs, OCs and Earth reservoirs compiled from the literature and adopted in this study……159

**Table A4.1.** Zn and Al relative abundances for different meteorite groups adopted in this study.....160

**Table A4.2.** Compiled data of nucleosynthetic isotope compositions of different meteorite groups……161

# Chapter 1

# Introduction

## 1.1 Background

### 1.1.1. Volatile Depletion

From a cosmochemical perspective, volatiles are defined as elements or compounds that condensed from the solar nebula at temperatures below those of Mg, Si, and Fe (~1300K, (Lodders, 2003). Many of these elements are essential for life, including the six most abundant elements in living organisms (H, C, N, O, P, and S), as well as trace elements that are required for vital functions (F, Na, Cl, K, Mn, Cu, Zn, Se, and I). Therefore, establishing how Earth acquired its volatiles is essential for our understanding of the formation of habitable planets.

Some of these volatiles, and particularly the elements that are produced in the Big Bang and in the first stages of stellar nucleosynthesis (H, C, N, O, S), are especially abundant in the universe. Nonetheless, Earth is depleted in volatiles relative to the average composition of the Solar System (Allègre et al., 2001), as defined by the Sun and CI chondrites – a group of primitive meteorites (Lodders, 2003). Various extents of volatile depletion are also observed across meteorite groups (Braukmüller et al., 2019, Wasson and Kallemeyn, 1988, Wang and Lipschutz, 2007, Wang and Lipschutz, 2005, Jurewicz et al., 1991, Boynton et al., 1976, Laul et al., 1972), as well as on other planets and the Moon (O'Neill, 1991, Taylor, 2013, Peplowski et al., 2011). The extent of depletion also varies between elements, and this is influenced primarily by condensation temperature but also by chemical affinity (Braukmüller et al., 2019).

These elemental fractionations can be caused both by nebular processes that take place prior to planetary accretion and by secondary processes within planets and asteroids. Mechanisms that have been proposed to account for the observed depletions of different volatile elements include evaporative loss either prior to (Anders, 1968) or as a consequence of accretion (Ringwood, 1966), incomplete condensation from the solar nebula (Wasson and Chou, 1974), mixing between a volatile-rich and a volatile-poor component (Larimer and Anders, 1967), thermal metamorphism (Dodd, 1969), metal-silicate fractionation in the case of siderophile volatile elements (McDonough and Sun, 1995), and collisional erosion for some lithophile elements (O'Neill and Palme, 2008).

Due to its strong gravitational pull, Earth is unlikely to have preferentially lost substantial amounts of volatiles after it reached a threshold size (Newcombe et al., 2023), which is corroborated by the mass-dependent isotope compositions of moderately volatile elements in the bulk silicate Earth (BSE; Sossi et al., 2018, Tian et al., 2021). Hence, our volatile inventory mainly reflects the volatile content of Earth's precursor materials, most of which were non-carbonaceous (NC) bodies (Lodders, 2000, Warren, 2011, Dauphas, 2017, Burkhardt

et al., 2021). Meteorites derived from NC planetesimals, which, like Earth, also formed in the inner Solar System, have volatile contents that vary substantially, ranging from extreme depleted to very volatile-rich (Fig. 1.1; Kallemeyn and Wasson, 1986, Kallemeyn et al., 1989). In contrast, carbonaceous chondrites (CCs), which are thought to have accreted beyond the orbit of Jupiter, are typically volatile-rich (Fig. 1.1; Braukmüller et al., 2018, Wasson and Kallemeyn, 1988). CCs also showcase volatile element abundance patterns that are similar to the BSE, potentially implying a genetic relationship between them (Braukmüller et al., 2019).

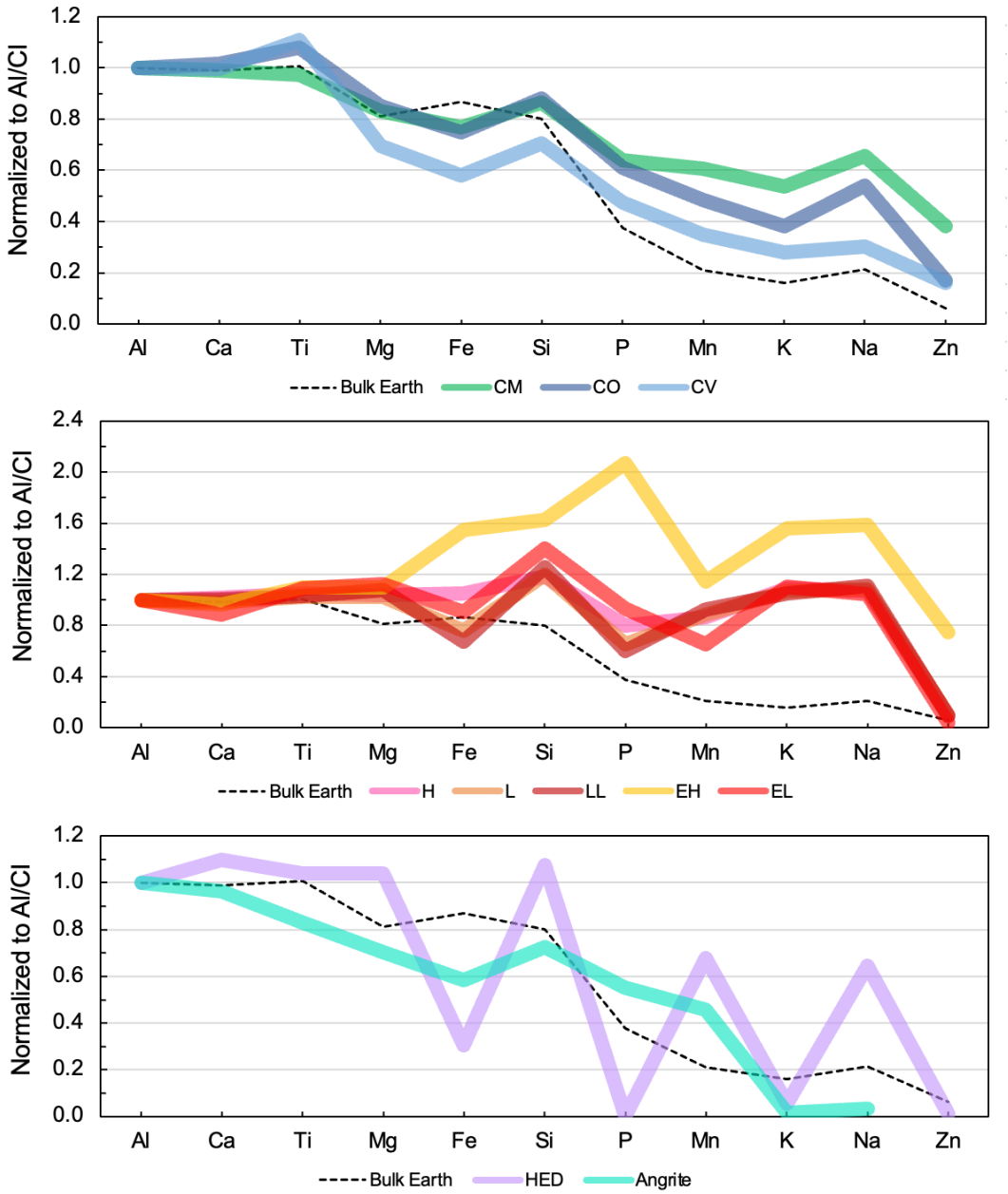



**Figure 2.1 Abundances of main elements and Zn normalized to Al and to CI chondrites.** Concentration data compiled for the bulk Earth, CCs (CM, CO, CV), NC chondrites (H, L, LL, EH, EL), and bulk NC achondrite parent bodies (HED, Angrite) is available in Table 3.5. Elements are listed in order of decreasing 50% condensation temperatures at nebular conditions (Lodders, 2003).

However, mixing between the CC and NC reservoirs was restricted by the growth of Jupiter, which took place within the first 4 Ma of Solar System formation (Kruijer et al., 2017). Subsequent influx of material from the outer Solar System was limited, and probably linked to gas giant migration events (Bottke et al., 2012, Walsh et al., 2012). This includes, for example, the addition of the late veneer during a period of heavy bombardment between 400-600 Ma into Solar System history, which resulted in the accretion of ~0.5% of Earth's mass (Walker et al., 2015), potentially comprising mainly CC materials (Fischer-Gödde et al., 2020). Importantly, habitable zones in planetary systems are currently defined by the range of distances from a star at which liquid water can exist at a planet's surface. This does not, however, take into account volatile depletion of the planetary material and the likelihood of materials present within that zone to harbor sufficient volatiles. Hence, determining whether volatiles from readily available, closely sourced materials suffice to establish Earth's volatile budget or whether this requires addition of more unusual, remotely formed materials may have important consequences for evaluating the potential of planetary habitability.

### 1.1.2. Nucleosynthetic isotope anomalies

Much effort has been devoted to finding Earth's building blocks among meteorites. This has been achieved primarily by exploring nucleosynthetic isotope anomalies of bulk meteorite samples. These small variations in isotope composition between Solar System materials reflect variable incorporation of presolar dust grains derived from specific stellar sources. Carbonaceous chondrites inherited a larger proportion of dust from explosive nucleosynthesis, which resulted in enrichments of neutron-rich and r-process isotopes for several elements, including Ca, Ti, Cr, Ni, Sr, Zr, Mo, and Ru (Trinquier et al., 2009, Dauphas et al., 2014, Qin et al., 2010, Regelous et al., 2008, Burkhardt et al., 2021, Fischer-Gödde et al., 2020, Yokoyama et al., 2015, Akram et al., 2015). In contrast, NC materials are depleted in the same isotopes. These signatures are not modified by secondary processes within parent bodies, such that they can be used to establish genetic links between different materials.

Such isotopic studies concluded that Earth formed primarily from NC-material, with a more limited contribution from CCs (Warren, 2011, Dauphas, 2017, Budde et al., 2019, Burkhardt et al., 2021). However, since these anomalies were initially only found for more refractory elements, which have abundances that are largely invariable across the Solar System, these results provide only limited constrains on the origin of Earth's volatiles. Furthermore, evidence for nucleosynthetic isotope anomalies of volatile elements in bulk meteorites was

scarce. In particular, early research on Cd, Te, and Zn isotopes failed to unambiguously demonstrate the presence of anomalies of nucleosynthetic origin (Fehr et al., 2005, Toth et al., 2020, Moynier et al., 2009). More recently, two Zn isotope studies revealed complementary $^{66}$Zn and $^{68}$Zn anomalies between CC and NC meteorites (Steller et al., 2022, Savage et al., 2022). Nonetheless, the lack of resolvable differences between meteorites and terrestrial samples for other Zn isotopes makes it difficult to infer whether these results are indeed of nucleosynthetic origin or potentially caused by mass-independent isotope fractionations. In contrast, a study by Kuthning (2020) was able to successfully resolve isotopic effects for all Zn isotopes, with results that displayed complementary anomalies for CC and NC meteorites. Yet, this study failed to identify potential stellar sources for the anomalous Zn, leaving its nucleosynthetic origin uncertain.

## 1.2 Aims and approach

The present study aimed to continue the research started by Kuthning (2020), focusing on four main goals, which can be summarized as follows: (1) to identify a potential source for the Zn isotope anomalies and determine whether they are of nucleosynthetic origin; (2) to expand the dataset of Kuthning (2020) to include achondritic meteorites, as well as additional chondrite groups; (3) to use these results to constrain the origin of Earth's Zn and the mass of CC material that was accreted; and (4) to investigate the cause of the heterogeneous distribution of anomalous Zn in the Solar System.

### 1.2.1. Origin of the anomalies

In principle, the Zn isotope anomalies can be caused by mass-independent isotope fractionation or by variable addition of presolar material from a specific stellar source. To test which processes may be responsible for the observed Zn isotope variations, theoretical models of relevant mechanisms were explored, and the modelling results were compared to the analytical data. Mass-independent isotope fractionation induced by nuclear field shift effects has been proposed to account for observed isotope anomalies for Te (Fujii et al., 2006), and, more recently, for Mo and Sn (Budde et al., 2023, Bragagni et al., 2023). Hence, theoretical models of nuclear field shift effects on Zn isotopes were performed, but they were incompatible with the observed Zn anomalies. Furthermore, Kuthning (2020) presented models of variable addition of low-mass AGB star-derived material, which did not produce isotope compositions that were consistent with the measured results for meteorites. Therefore, the present study

considered other nucleosynthetic sources (Fig. 1.2), such as Type Ia supernovae (SNIa; Woosley, 1997) and Type II supernovae (SNII; Woosley and Weaver, 1995), including the Electron Capture Core Collapse Supernovae subtype (ECSN; Wanajo et al., 2013). Unlike AGB-stars, these nucleosynthetic sources have been linked to observed isotope anomalies of other Fe-peak elements, such as Ca, Ti, and Cr (Dauphas et al., 2014, Qin et al., 2011). Hence, the expected correlations between the isotope anomalies of these elements and the Zn anomalies were also modelled. Since at least two plausible matches were found, and nuclear field shift effect can be reasonably eliminated, a nucleosynthetic origin for the Zn isotope anomalies is likely.

### 1.2.2. Expand the characterization to other Solar System materials

The Zn isotope study of Kuthning (2020) includes results of four CC groups, two OC groups, and two IAB complex iron meteorites. The work of Savage et al. (2023) is limited to chondrites, while Steller et al. (2023) also analysed one achondrite and three iron meteorite groups. While this is enough to characterize the complementarity between CC and NC meteorites, these groups alone do not provide a comprehensive picture of the potential Zn isotope variability that may be present within each reservoir. Hence, this study aimed to expand on the results of Kuthning (2020) by characterizing chondrites from additional groups, as well as achondrites. This not only aids with establishing an origin for the isotope anomalies, but most importantly, it provides a more complete representation of what kinds of materials were available during Earth's accretion, and which may have served as building blocks.

### 1.2.3. Origin of Earth's volatiles

With a nucleosynthetic origin established and a more comprehensive data set available, the origin of Earth's Zn can be constrained. This was done by performing extensive mass balance mixing modelling, utilizing different isotope ratios and combinations of meteorites. Together with constraints from Zn concentrations established by other studies, the amount of CC material accreted by Earth was also estimated. Further constraints were derived from other isotope systems, as well as elemental abundances, aiming to identify precursor materials that can account not only for Zn isotope composition and abundance, but for multiple elemental and isotopic characteristics. The results of these models, as well as estimates performed by other studies, are carefully considered, and potential implications for other volatile elements, and for the formation of habitable planets are also discussed.

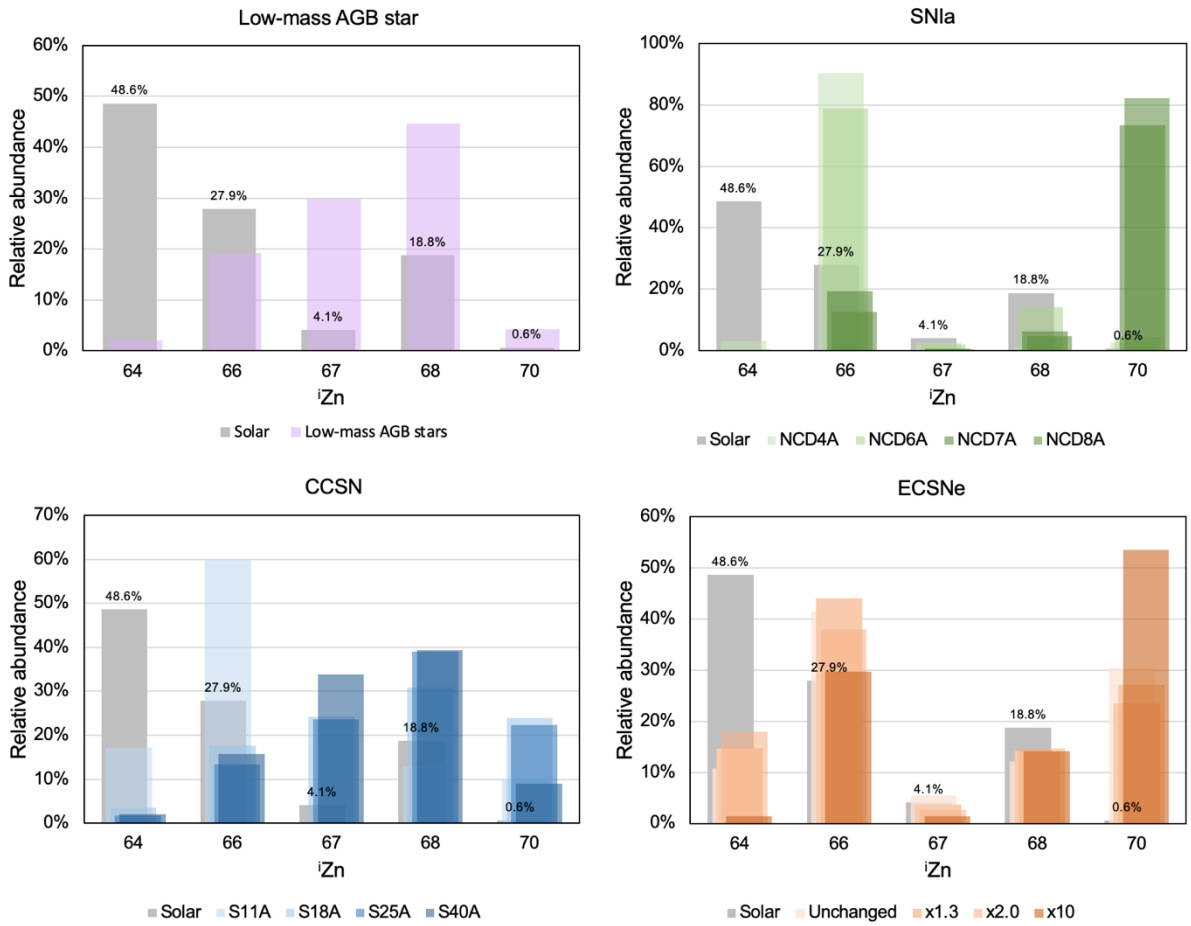



**Figure 1.2. Theoretical Zn isotope yields of different stellar sources, assuming variable physical parameters, compared to Solar System Zn isotope abundances.** Shown are predicted yields for low mass AGB stars (Bisterzo et al., 2011), SNIa (Woosley, 1997), SNII (Woosley and Weaver, 1995), and ECSN (Wanajo et al., 2013).

### 1.2.4. Heterogeneous distribution of anomalous Zn

The cause of the heterogeneous distribution of presolar dust through the Solar System is debated. The main hypotheses include thermal processing and preferential loss of certain carriers of anomalies within the inner Solar System (Trinquier et al., 2009), or temporal and spatial variations in the composition of the molecular cloud as the protoplanetary disk formed (Nanne et al., 2019). Thermal processing has been proposed to explain variable distribution of anomalies of several refractory elements, including Ti, Cr, Sr, Zr, and Pd (Trinquier et al., 2009, Ek et al., 2020, Yokoyama et al., 2015, Akram et al., 2015). The same mechanism has also been hypothesized to induce volatile depletion (Trinquier et al., 2009). However, this scenario has never been discussed considering anomalies of volatile element anomalies. To test this premise, this study includes a series of leaching experiments on CCs in an attempt to identify the carrier phase of the Zn anomalies. Finding which mineral phases host the anomalies, and establishing

if they are likely to be preferentially destroyed provides constraints on the feasibility of the thermal processing scenario.

## 1.3 References


AKRAM, W., SCHÖNBÄCHLER, M., BISTERZO, S. & GALLINO, R. 2015. Zirconium isotope evidence for the heterogeneous distribution of s-process materials in the Solar System. *Geochimica et Cosmochimica Acta,* 165**,** 484-500.

ALLÈGRE, C., MANHÈS, G. & LEWIN, É. 2001. Chemical composition of the Earth and the volatility control on planetary genetics. *Earth and Planetary Science Letters,* 185**,** 49-69.

ANDERS, E. 1968. Chemical processes in the early Solar System, as inferred from meteorites. *Accounts of Chemical Research,* 1**,** 289-298.

BISTERZO, S., GALLINO, R., STRANIERO, O., CRISTALLO, S. & KAPPELER, F. 2011. The s-process in low-metallicity stars - II. Interpretation of high-resolution spectroscopic observations with asymptotic giant branch models. *Monthly Notices of the Royal Astronomical Society,* 418**,** 284-319.

BOTTKE, W. F., VOKROUHLICKÝ, D., MINTON, D., NESVORNÝ, D., MORBIDELLI, A., BRASSER, R., SIMONSON, B. & LEVISON, H. F. 2012. An Archaean heavy bombardment from a destabilized extension of the asteroid belt. *Nature,* 485**,** 78-81.

BOYNTON, W. V., STARZYK, P. M. & SCHMITT, R. A. 1976. Chemical evidence for the genesis of the ureilites, the achondrite Chassigny and the nakhlites. *Geochimica et Cosmochimica Acta,* 40**,** 1439-1447.

BRAGAGNI, A., WOMBACHER, F., KIRCHENBAUR, M., BRAUKMÜLLER, N. & MÜNKER, C. 2023. Mass-independent Sn isotope fractionation and radiogenic $^{115}$Sn in chondrites and terrestrial rocks. *Geochimica et Cosmochimica Acta,* 344**,** 40-58.

BRAUKMÜLLER, N., WOMBACHER, F., FUNK, C. & MUNKER, C. 2019. Earth's volatile element depletion pattern inherited from a carbonaceous chondrite-like source. *Nature Geoscience,* 12**,** 564-568.

BRAUKMÜLLER, N., WOMBACHER, F., HEZEL, D. C., ESCOUBE, R. & MUNKER, C. 2018. The chemical composition of carbonaceous chondrites: Implications for volatile element depletion, complementarity and alteration. *Geochimica et Cosmochimica Acta,* 239**,** 17-48.

BUDDE, G., BURKHARDT, C. & KLEINE, T. 2019. Molybdenum isotopic evidence for the late accretion of outer Solar System material to Earth. *Nature Astronomy,* 3**,** 736-741.

BUDDE, G., TISSOT, F. L. H., KLEINE, T. & MARQUEZ, R. T. 2023. Spurious molybdenum isotope anomalies resulting from non-exponential mass fractionation. *Geochemistry***,** 126007.

BURKHARDT, C., SPITZER, F., MORBIDELLI, A., BUDDE, G., RENDER, J. H., KRUIJER, T. S. & KLEINE, T. 2021. Terrestrial planet formation from lost inner Solar System material. *Science Advances,* 7**,** eabj7601.

DAUPHAS, N. 2017. The isotopic nature of the Earth's accreting material through time. *Nature,* 541**,** 521-524.

DAUPHAS, N., CHEN, J. H., ZHANG, J., PAPANASTASSIOU, D. A., DAVIS, A. M. & TRAVAGLIO, C. 2014. Calcium-48 isotopic anomalies in bulk chondrites and achondrites: Evidence for a uniform isotopic reservoir in the inner protoplanetary disk. *Earth and Planetary Science Letters,* 407**,** 96-108.

DODD, R. T. 1969. Metamorphism of the ordinary chondrites: a review. *Geochimica et Cosmochimica Acta,* 33**,** 161-203.

EK, M., HUNT, A. C., LUGARO, M. & SCHONBACHLER, M. 2020. The origin of s-process isotope heterogeneity in the solar protoplanetary disk. *Nature Astronomy,* 4**,** 273-281.

FEHR, M. A., REHKAMPER, M., HALLIDAY, A. N., WIECHERT, U., HATTENDORF, B., GUNTHER, D., ONO, S., EIGENBRODE, J. L. & RUMBLE, D. 2005. Tellurium isotopic composition of the early Solar System - A search for effects resulting from stellar nucleosynthesis, Sn-126 decay, and mass-independent fractionation. *Geochimica et Cosmochimica Acta,* 69**,** 5099-5112.

FISCHER-GÖDDE, M., ELFERS, B. M., MUNKER, C., SZILAS, K., MAIER, W. D., MESSLING, N., MORISHITA, T., VAN KRANENDONK, M. & SMITHIES, H. 2020. Ruthenium isotope vestige of Earth's pre-late-veneer mantle preserved in Archaean rocks. *Nature,* 579**,** 240-244.

FUJII, T., MOYNIER, F. & ALBARÈDE, F. 2006. Nuclear field vs. nucleosynthetic effetcs as cause of isotopic anomalies in the early Solar System. *Earth and Planetary Science Letters,* 247**,** 1-9.
JUREWICZ, A. J., MITTLEFEHLDT, D. W. & JONES, J. H. 1991. Partial Melting of the Aliende (CV3) Meteorite: Implications for Origins of Basaltic Meteorites. *Science,* 252**,** 695-8.
KALLEMEYN, G. W., RUBIN, A. E., WANG, D. & WASSON, J. T. 1989. Ordinary chondrites: Bulk compositions, classification, lithophile-element fractionations and composition-petrographic type relationships. *Geochimica et Cosmochimica Acta,* 53**,** 2747-2767.
KALLEMEYN, G. W. & WASSON, J. T. 1986. Composition of enstatite (EH3, EH4,5) and EL6) chondrites: Implications regarding their formation. *Geochimica et Cosmochimica Acta,* 50**,** 2153-2164.
KRUIJER, T. S., BURKHARDT, C., BUDDE, G. & KLEINE, T. 2017. Age of Jupiter inferred from the distinct genetics and formation times of meteorites. *Proceedings of the National Academy of Sciences,* 114**,** 6712-6716.
KUTHNING, S. 2021. Investigation of mass-independent isotope effects of Zn and Cd in meteorites. PhD Thesis, Imperial College London.
LARIMER, J. W. & ANDERS, E. 1967. Chemical fractionations in meteorites – II. Abundance patterns and their interpretation. *Geochimica et Cosmochimica Acta,* 31**,** 1239-1270.
LAUL, J. C., KEAYS, R. R., GANAPATHY, R., ANDERS, E. & MORGAN, J. W. 1972. Chemical fractionations in meteorites–V. Volatile and siderophile elements in achondrites and ocean ridge basalts. *Geochimica et Cosmochimica Acta,* 36**,** 329-345.
LODDERS, K. 2000. An Oxygen Isotope Mixing Model for the Accretion and Composition of Rocky Planets. *Space Science Reviews,* 92**,** 341-354.
LODDERS, K. 2003. Solar System abundances and condensation temperatures of the elements. *The Astrophysical Journal,* 591**,** 1220-1247.
MCDONOUGH, W. F. & SUN, S.-S. 1995. The composition of the Earth. *Chemical Geology,* 120**,** 223-253.
MOYNIER, F., DAUPHAS, N. & PODOSEK, F. A. 2009. A search for $^{70}$Zn anomalies in meteorites. *The Astrophysical Journal,* 700**,** L92-L95.
NANNE, J. A. M., NIMMO, F., CUZZI, J. N. & KLEINE, T. 2019. Origin of the non-carbonaceous–carbonaceous meteorite dichotomy. *Earth and Planetary Science Letters,* 511**,** 44-54.
NEWCOMBE, M. E., NIELSEN, S. G., PETERSON, L. D., WANG, J., ALEXANDER, C. M. O. D., SARAFIAN, A. R., SHIMIZU, K., NITTLER, L. R. & IRVING, A. J. 2023. Degassing of early-formed planetesimals restricted water delivery to Earth. *Nature,* 615**,** 854-857.
O'NEILL, H. S. C. 1991. The origin of the Moon and the early history of the Earth – A chemical model. Part 2: The Earth. *Geochimica et Cosmochimica Acta,* 55**,** 1159-1172.
O'NEILL, H. S. C. & PALME, H. 2008. Collisional erosion and the non-chondritic composition of the terrestrial planets. *Philosophical Transactions of the Royal Society A,* 366**,** 4205-4238.
PEPLOWSKI, P. N., EVANS, L. G., HAUCK, S. A., MCCOY, T. J., BOYNTON, W. V., GILLIS-DAVIS, J. J., EBEL, D. S., GOLDSTEN, J. O., HAMARA, D. K., LAWRENCE, D. J., MCNUTT, R. L., NITTLER, L. R., SOLOMON, S. C., RHODES, E. A., SPRAGUE, A. L., STARR, R. D. & STOCKSTILL-CAHILL, K. R. 2011. Radioactive Elements on Mercury's Surface from MESSENGER: Implications for the Planet's Formation and Evolution. *Science,* 333**,** 1850-1852.
QIN, L., CARLSON, R. W. & ALEXANDER, C. M. O. D. 2011. Correlated nucleosynthetic isotopic variability in Cr, Sr, Ba, Sm, Nd and Hf in Murchison and QUE 97008. *Geochimica et Cosmochimica Acta,* 75**,** 7806-7828.
QIN, L. P., ALEXANDER, C. M. O., CARLSON, R. W., HORAN, M. F. & YOKOYAMA, T. 2010. Contributors to chromium isotope variation of meteorites. *Geochimica et Cosmochimica Acta,* 74**,** 1122-1145.
REGELOUS, M., ELLIOTT, T. & COATH, C. D. 2008. Nickel isotope heterogeneity in the early Solar System. *Earth and Planetary Science Letters,* 272**,** 330-338.
RINGWOOD, A. E. 1966. Chemical evolution of the terrestrial planets. *Geochimica et Cosmochimica Acta,* 30**,** 41-104.

SAVAGE, P. S., MOYNIER, F. & BOYET, M. 2022. Zinc isotope anomalies in primitive meteorites identify the outer Solar System as an important source of Earth's volatile inventory. *Icarus,* 386**,** 115172.
SOSSI, P. A., NEBEL, O., O'NEILL, H. S. C. & MOYNIER, F. 2018. Zinc isotope composition of the Earth and its behaviour during planetary accretion. *Chemical Geology,* 477**,** 73-84.
STELLER, T., BURKHARDT, C., YANG, C. & KLEINE, T. 2022. Nucleosynthetic zinc isotope anomalies reveal a dual origin of terrestrial volatiles. *Icarus,* 386**,** 115171.
TAYLOR, G. J. 2013. The bulk composition of Mars. *Geochemistry,* 73**,** 401-420.
TIAN, Z., MAGNA, T., DAY, J. M. D., MEZGER, K., SCHERER, E. E., LODDERS, K., HIN, R. C., KOEFOED, P., BLOOM, H. & WANG, K. 2021. Potassium isotope composition of Mars reveals a mechanism of planetary volatile retention. *Proceedings of the National Academy of Sciences,* 118**,** e2101155118.
TOTH, E. R., FEHR, M. A., FRIEBEL, M. & SCHÖNBÄCHLER, M. 2020. Cadmium isotopes in chondrites and acid leachates: Nucleosynthetic homogeneity and a monitor for thermal neutron capture effects. *Geochimica et Cosmochimica Acta,* 274**,** 286-301.
TRINQUIER, A., ELLIOTT, T., ULFBECK, D., COATH, C., KROT, A. N. & BIZZARRO, M. 2009. Origin of nucleosynthetic isotope heterogeneity in the solar protoplanetary disk. *Science,* 324**,** 374-376.
WALKER, R. J., BERMINGHAM, K., LIU, J., PUCHTEL, I. S., TOUBOUL, M. & WORSHAM, E. A. 2015. In search of late-stage planetary building blocks. *Chemical Geology,* 411**,** 125-142.
WALSH, K. J., MORBIDELLI, A., RAYMOND, S. N., O'BRIEN, D. P. & MANDELL, A. M. 2012. Populating the asteroid belt from two parent source regions due to the migration of giant planets - "The Grand Tack". *Meteoritics & Planetary Science,* 47**,** 1941-1947.
WANAJO, S., JANKA, H.-T. & MÜLLER, B. 2013. Electron-capure supernovae as origin of $^{48}$Ca. *The Astrophysycal Journal Letters,* 767**,** L26.
WANG, M.-S. & LIPSCHUTZ, M. E. 2005. Thermal Metamorphism of Primitive MeteoritesXII. The Enstatite Chondrites Revisited. *Environmental Chemistry,* 2**,** 215-226.
WANG, M.-S. & LIPSCHUTZ, M. E. 2007. Trace elements in primitive meteorites—VII Antarctic unequilibrated ordinary chondrites. *Geochimica et Cosmochimica Acta,* 71**,** 1062-1073.
WARREN, P. H. 2011. Stable-isotopic anomalies and the accretionary assemblage of the Earth and Mars: A subordinate role for carbonaceous chondrites. *Earth and Planetary Science Letters,* 311**,** 93-100.
WASSON, J. T. & CHOU, C.-L. 1974. Fractionation of moderately volatile elements in ordinary chondrites. *Meteoritics,* 9**,** 69-84.
WASSON, J. T. & KALLEMEYN, G. W. 1988. Compositions of chondrites. *Philosophical Transactions of the Royal Society A,* 325**,** 535-544.
WOOSLEY, S. E. 1997. Neutron-rich nucleosynthesis in carbon deflagration supernovae. *The Astrophysycal Journal,* 476**,** 801-810.
WOOSLEY, S. E. & WEAVER, T. A. 1995. The evolution and explosion of massive Stars II: Explosive hydrodynamics and nucleosynthesis. *The Astrophysical Journal Supplement Series,* 181-235.
YOKOYAMA, T., FUKAMI, Y., OKUI, W., ITO, N. & YAMAZAKI, H. 2015. Nucleosynthetic strontium isotope anomalies in carbonaceous chondrites. *Earth and Planetary Science Letters,* 416**,** 46-55.

# Chapter 2

# Nucleosynthetic zinc isotope anomalies in meteorites

## 2.1 Introduction

The Solar System formed from an initially hot protoplanetary disk. As the disk cooled, refractory metals and metal oxides - which have high condensation temperatures - formed the first material to condense into solid dust grains, followed by Fe metal and Mg silicates (Lodders, 2003). The relative abundances of these refractory elements in all Solar System bodies are similar to the Sun and Ivuna-type carbonaceous chondrite (CI) meteorites, which are thought to be representative of the Solar System as a whole (Wasson and Kallemeyn, 1988). Volatile elements, which have condensation temperatures below those of Mg, Si and Fe, condensed later, and all other groups of meteorites are depleted in volatiles compared to CIs, to various extents (Wasson and Kallemeyn, 1988, Wang and Lipschutz, 2007, Braukmüller et al., 2019, Wang and Lipschutz, 2005). This depletion was inherited by the terrestrial planets, having been established for Earth, the Moon, Mars and Mercury (Allègre et al., 2001, O'Neill, 1991, Taylor, 2013, Peplowski et al., 2011). However, it is unclear how these bodies obtained their volatile elements.

The origins of Earth's building blocks can be constrained using nucleosynthetic isotope anomalies measured between bulk meteorites and the bulk silicate Earth (BSE). These small isotopic variations are produced by heterogeneous distribution of isotopically distinct material during formation of the Solar System. This material is inherited from presolar processes, such as nucleosynthesis in stars or supernovae. Nucleosynthetic anomalies that have been characterized to date reveal an isotopic dichotomy between carbonaceous and non-carbonaceous (NC) meteorites (Warren, 2011). The carbonaceous group consists primarily of carbonaceous chondrite (CC) meteorites and the NC group of enstatite chondrite (EC) and ordinary chondrite (OC) meteorites. CCs have higher abundances than NCs of neutron-rich isotopes of the Fe-peak elements Ca, Ti, Cr, Ni and lower abundances of the slow neutron capture (s-process) nuclides of Zr, Mo, Ru, and Pd (Warren, 2011, Dauphas et al., 2014, Budde et al., 2019a, Fischer-Gödde et al., 2015, Akram et al., 2015, Ek et al., 2020). This dichotomy has been suggested to reflect spatial separation of two isotopic reservoirs, with NC material in the inner Solar System, and CC material on orbits outside that of Jupiter (Kruijer et al., 2017).

The isotopic signature of the BSE indicates that Earth accreted primarily from NC material with a small but non-negligible contribution of CC material (Warren, 2011, Budde et al., 2019, Dauphas, 2017, Schiller et al., 2018, Fitoussi et al., 2016). However, previously reported nucleosynthetic isotope anomalies were for refractory metals, which have nearly uniform elemental abundance ratios throughout the Solar System. In contrast, ratios of volatile

to refractory elements are variable in generally volatile-rich CCs and volatile-poor OCs, and even more so in ECs, with the latter presenting both severe volatile depletions and high volatile abundances that could potentially account for much of Earth's volatile inventory (Lodders, 1998, Piani et al., 2020). As a variably depleted moderately volatile element that is potentially produced in some of the same nucleosynthetic sites that are thought to have induced Ca and Ti anomalies (Woosley, 1997, Wanajo et al., 2013), Zn is a prime candidate to use as a tracer of volatile distribution in the early Solar System.

## 2.2 Samples

The present study included ten meteorites, with all relevant information, including meteorite sources, summarized in Table 2.1. The analyses encompassed (i) three carbonaceous chondrites (CC), including two CV3s and one CO3 (ii) two EHs (EC); and (iii) five OCs of groups H, L and LL. Two rocks of the bulk silicate Earth (BSE) were analysed for quality control (Table 2.1). The BSE rocks encompass the United States Geological Survey (USGS) geological reference material BHVO-2, a Hawaiian basalt, as well as a glacial sediment from the west coast of Greenland (P6Bt; Crocket, 2009). These meteorites and the BSE rocks were either used up completely by destructive analysis during the course of the study or remaining sample aliquots are stored at the Department of Earth Science & Engineering, Imperial College London.

**Table 2.1. Names, digested masses, identifiers and sources of the meteorites and BSE rocks analysed in this study.**

| Samples | Type | Mass (g) | Identifier | Source |
|---|---|---|---|---|
| *Meteorites* | | | | |
| Allende | CV3 | 2.255 to 2.480 | | Natural History Museum London |
| LAR 12002 | CV3 | 0.253* | LAR 12002.43 | US Antarctic Meteorite Program |
| MIL 090025 | CO3 | 0.251* | MIL 090025.12 | US Antarctic Meteorite Program |
| NWA 13299 | EH3 | 0.456 | | Private collector |
| Indarch | EH4 | 1.302 | M4 1403, #22 | Field Museum Chicago |
| Forest Vale | H4 | 0.62 | USNM 4852 | Smithsonian National Museum of Natural History |
| Saratov | L4 | 0.83 | BM.1997 | Natural History Museum London |
| Homestead | L5 | 1.03 | BM.1962,157 | Natural History Museum London |
| Bishunpur | LL3.1 | 0.213* | BM.80339 | Natural History Museum London |
| Soko Banja | LL4 | 1.47 | BM.51857 | Natural History Museum London |
| *BSE rocks* | | | | |
| BHVO-2 | Hawaiian basalt | | | US Geological Survey |
| P6Bt | Glacial till (W Greenland) | | | Crocket (2009) |

* Digested powder aliquots are from much larger (>2 g) homogenized powder samples.

## 2.3 Methods

### 2.3.1 Sample preparation

#### 2.3.1.1. Laboratory and reagents

Digestion and further preparation of the samples and the subsequent Zn isotopic measurements were carried out in the Mass Spectrometry and Isotope Geochemistry (MAGIC) Laboratories at the Department of Earth Science & Engineering of Imperial College London. All sample preparation was conducted in ISO Class 6 clean rooms, using ISO Class 4 laminar flow benches for critical steps. The water used was of ≥18.2 MΩ cm quality from a Millipore purification system. All acids were purified from reagent grade stock acids by sub-boiling distillation in either quartz glass (15.3 M $HNO_3$, 6 M HCl) or Teflon (28 M HF, 12 M HCl, 8.5 M HBr) stills.

#### 2.3.1.2. Initial sample treatment and digestion

Powder aliquots of the chondritic meteorites with masses of about 0.2 g to 2.5 g (Table 2.1) were obtained by crushing sample chips with an agate mortar and pestle. When present, fusion crusts were removed before crushing with a rotary tool and SiC grinding bits. For most meteorites, more than about 0.5 g of powder were digested to ensure sample homogeneity; for a few samples smaller powder aliquots from larger masses of homogenized powder were digested (Table 2.1). The chondritic meteorites and BSE rocks were digested in Savillex Teflon beakers in a 2 + 1 mixture of 28 M HF + 15.3 M $HNO_3$ at 120˚ C for at least two days on a hotplate. Following this, the samples were dried, refluxed in 6 M HCl for at least another two days and dried again.

#### 2.3.1.3. Anion exchange separation of Zn

After digestion, the dried samples were re-dissolved in an appropriate volume of 3 M HCl by refluxing for ≥12 hr. Prior to the anion exchange chemistry, the sample solutions were cooled and centrifuged to remove any solid residues. The three-stage anion exchange chromatography procedure was modified from published methods (Bridgestock et al., 2014, Moore et al., 2017, Wombacher et al., 2003, Palk et al., 2018) and from Kuthning (2020), as described in Tables 2.2 and 2.3. The first stage employed 100-200 mesh Bio-Rad AG-1X8 anion exchange resin, either in

quartz glass columns with 2 ml resin beds or Teflon shrink-fit columns with 250 µl resin beds (Table 2.2). In both cases, the same acids were used for resin cleaning and equilibration as well sample loading and elution but with volumes scaled to the resin bed size (Wombacher et al., 2003, Palk et al., 2018).

The Zn fractions from the first separation stage were dried and re-dissolved in 1 ml 1 M HCl for loading onto the columns of the second separation stage (Table 2.3). This second stage utilized Teflon shrink-fit columns with 250 µl of 100-200 mesh Bio-Rad AG-MP1 anion exchange resin, with a resin cleaning and elution procedure largely following published methods (Bridgestock et al., 2014, Moore et al., 2017) and described in detail in Table 2.3. The Zn fractions from the second-stage separation were dried, dried again with a few drops of 15.3 M $HNO_3$ and taken up in 1 ml 1 M HCl for the final stage of the Zn separation. This third stage was a duplicate of the second-stage column chemistry with 250 µl of 100-200 mesh Bio-Rad AG-MP1 anion exchange resin (Table 2.3). The Zn fractions from the stage 3 columns were dried, dried again after refluxing with 15.3 M $HNO_3$ and stored for the Zn isotope measurements.

**Table 2.2. Ion exchange column chemistry for Stage 1 of the Zn separation from meteorite and rock samples.** The separation used either large quartz glass columns with 2 ml resin beds (of 6 mm diameter) and a reservoir volume (RV) of 50 ml or small Teflon columns with 250 µl resin beds, with a bed height and diameter of about 25 mm and 3.5 mm, respectively.

| Reagent | Quartz Columns Volume (ml) | Teflon Columns Volume (µl) | Effect |
|---|---|---|---|
| AG 1X8 100-200 mesh resin | 2 | 250 | Add resin slurry in 0.1 M HCl |
| 2 M $HNO_3$ | 15 | 2 x RV | Clean resin |
| $H_2O$ | 2 | 1000 | Clean resin |
| 6 M HCl | 26 | 1 x RV | Convert resin to $Cl^-$ form |
| 0.5 M HCl | 12 | | Resin conditioning |
| 3 M HCl | 6 | 600 | Resin equilibration |
| Sample in 3 M HCl | 10 | 1000-2000 | Sample loading; elution of Mg, Al, S, Ti, V, Cr, Fe, Ge, Ba |
| 3 M HCl | 2 | 200 | Elution incl. Mg, Al, S, Ti, V, Cr, Fe, Ge, Ba |
| 0.5 M HCl | 30 | 3000 | Elution incl. Mg, Al, S, Ti, V, Cr, Fe, Ge, Ba |
| 1 M HCl | 10 | 1000 | Matrix elution (e.g., Mo) |
| 2 M HCl | 12 | 1000 | Matrix elution |
| 6 M HCl | 16 | 1500 | Matrix elution (e.g., Ag) |
| 0.1 M HBr + 0.5 M $HNO_3$ | 20 | 3000 | Elution of Zn |

**Table 2.3. Ion exchange column chemistry for Stages 2 and 3 of the Zn separation from meteorite and rock samples.** The separation was carried out in Teflon shrink-fit columns with a reservoir volume (RV) of 2 ml and a resin volume of about 250 µl, with a bed height and diameter of about 25 mm and 3.5 mm, respectively.

| Reagent | Volume (µl) | Effect |
|---|---|---|
| AG MP1 100-200 mesh resin | 250 | Add resin slurry in 0.1 M HCl |
| 0.1 M $HNO_3$ | 2 x RV | Clean resin |
| $H_2O$ | 1000 | Clean resin |
| 6 M HCl | 3000 | Convert resin to $Cl^-$ form |
| 1 M HCl | 2000 | Resin equilibration |
| Sample in 1 M HCl | 1000 | Sample loading |
| 1 M HCl | 8000 | Matrix elution |
| 0.01 M HCl | 7000 | Elution of Zn |

| Reagent | Volume (µl) | Effect |
|---|---|---|
| AG MP1 100-200 mesh resin | 250 | Add resin slurry in 0.1 M HCl |
| 0.1 M HNO3 | 2 x RV | Clean resin |
| H2O | 1000 | Clean resin |
| 6 M HCl | 3000 | Convert resin to Cl- form |
| 1 M HCl | 2000 | Resin equilibration |
| Sample in 1 M HCl | 1000 | Sample loading |
| 1 M HCl | 8000 | Matrix elution |
| 0.01 M HCl | 7000 | Elution of Zn |

### 2.3.2 Mass Spectrometry

#### 2.3.2.1. Zn isotope measurements

All isotope analyses were carried out with a Nu Instruments Nu Plasma II multiple collector inductively coupled plasma mass spectrometer (MC-ICP-MS). A Nu Instruments DSN 100 desolvation system fitted with glass cross flow nebulizers with solution flow rates of about 120 µl $min^{-1}$ were employed for sample introduction in conjunction with a CETAC ASX-112FR autosampler. Normal operating conditions are summarized in Table 2.4.

The Zn isotope analyses were carried out using two Faraday cup configurations, termed M64 and M70, because the mass dispersion of the Nu Plasma II instrument did not permit simultaneous monitoring of all five Zn isotopes and the required interference monitors (Table 2.5). The M64 configuration covers the isotopes $^{64}Zn$, $^{66}Zn$, $^{67}Zn$ and $^{68}Zn$ as well as the $^{62}Ni$ monitor

to correct for interferences from $^{64}$Ni. The M70 configuration covers $^{66}$Zn, $^{67}$Zn, $^{68}$Zn, $^{70}$Zn and also monitors $^{72}$Ge to correct for interferences from $^{70}$Ge (Table 2.5). All ion beams were monitored using Faraday cups fitted with $10^{11}$ Ω resistors, with each run encompassing 3 blocks with 20 data acquisition cycles of 8 s each. Each run was started by a peak centering routine whilst each block commenced with a 60 s measurement of the electronic baselines of the Faraday collectors whilst the ion beam was deflected in the electrostatic analyser.

For the measurements, samples and Zn reference materials were introduced as solutions in 0.1 M $HNO_3$ and this acid was also used for intermittent washing of the sample introduction system. The Zn isotope analyses with the M64 and M70 collector configurations were carried out at different Zn concentrations, as the fractional abundance of $^{70}$Zn is much lower than that of $^{64}$Zn, at about 0.6% versus 49.2% (Table 2.5). Measurements using the M64 and M70 configurations therefore utilized Zn concentrations of about 150 to 300 ng ml$^{-1}$ and 250 to 400 ng ml$^{-1}$, respectively, depending on the instrumental sensitivity, which was normally 230 to 420 V (μg ml$^{-1}$)$^{-1}$ for Zn.

All Zn isotope analyses were carried out with the sample–standard bracketing technique, whereby sample runs were symmetrically bracketed by two or four runs of a 'matching' solution of the London Zn isotope reference material. As the concentrations of the sample stock solutions were known, it was possible to prepare the sample run solutions with concentrations, which matched those of the bracketing London Zn isotope standards to within 10% to 15%.

**Table 2.4. Operating conditions of the Nu Plasma MC-ICP-MS and the Nu Instruments DSN 100 desolvating sample introduction system.**

| **Nu Plasma II MC-ICP-MS** | |
|---|---|
| RF Power | 1300 W |
| Acceleration potential | 6000 V |
| Ar coolant gas flow | 13 l min$^{-1}$ |
| Ar auxiliary gas flow | 1 l min$^{-1}$ |
| Expansion chamber vacuum | ~0.75 mbar |
| Analyser vacuum | ~2 x $10^{-9}$ mbar |
| Faraday cup resistors | $10^{11}$ Ω |
| Sensitivity for Zn | 230 – 420 V (μg ml$^{-1}$)$^{-1}$ |

| **Nu Instrument DSN-100 desolvating nebulizer system** | |
|---|---|
| Spray chamber temperature | 110°C |
| Desolvator temperature | 160°C |
| Argon sweep gas | ~3.4 to 5 l $min^{-1}$ |
| Nebuliser pressure | ~60 psi |
| Sample uptake rate | ~120 µl $min^{-1}$ |

**Table 2.5. Collector configurations that were used for the Zn isotope measurements, abundances of the isotopes of Zn as well as spectral interferences from isobars, $Ba^{2+}$ and the most relevant molecular ions.**

| Faraday collector | L4 | L2 | Ax | H1 | H2 | H4 | H6 | H7 | H8 |
|---|---|---|---|---|---|---|---|---|---|
| **Collector configuration M64** | $^{62}Ni$ | $^{64}Zn$ | | | $^{66}Zn$ | $^{67}Zn$ | $^{68}Zn$ | $^{137}Ba^{2+}$ | |
| Isotope abundance Zn | | 49.2% | | | 27.7% | 4.0% | 18.5% | | |
| Isotope abundance Ni | 3.6% | 0.1% | | | | | | | |
| Isotope abundance $Ba^{2+}$ ions | | | | | 0.1% | 2.4% | 7.9% | 11.2% | |
| **Collector configuration M70** | $^{66}Zn$ | $^{67}Zn$ | $^{68}Zn$ | $^{137}Ba^{2+}$ | | $^{70}Zn$ | | | $^{72}Ge$ |
| Isotope abundance Zn | 27.7% | 4.0% | 18.5% | | | 0.6% | | | |
| Isotope abundance Ge | | | | | | 20.5% | | | 27.5% |
| Isotope abundance $Ba^{2+}$ ions | 0.1% | 2.4% | 7.9% | 11.2% | | | | | |

| **Mass number** | **62** | **64** | **66** | **67** | **68** | **68.5** | **70** | **72** |
|---|---|---|---|---|---|---|---|---|
| Collector configuration M64 | L4 | Ax | H2 | H4 | H6 | H7 | | |
| Collector configuration M70 | | | L4 | L2 | Ax | H1 | H4 | H8 |
| $Zn^+$ ions | | 49.2% | 27.7% | 4.0% | 18.5% | | 0.6% | |
| $Ni^+$ ions | 3.6% | 0.9% | | | | | | |
| $Ge^+$ ions | | | | | | | 20.5% | 27.5% |
| $Ba^{2+}$ ions | | | 0.1% | 2.4% | 7.9% | 11.2% | | |
| MgAr | | 80.0% | 11.0% | | | | | |
| AlAr | | | | 100% | | | | |
| SiAr | | | | | 92.2% | | 3.1% | |
| SAr | | | | | | | | 95.0% |
| TiO | 8.2% | 73.7% | 5.2% | | | | | |
| VO | | | 0.2% | 99.8% | | | | |
| CrO | | | 4.3% | | 83.8% | | 2.4% | |
| FeO | | | | | | | 5.8% | 91.8% |

### 2.3.2.2. Data reduction and presentation

The raw measured isotope ratios were corrected (during the measurements) for instrumental mass bias by internal normalization using the exponential law (Wombacher and Rehkämper, 2003). Several different normalization schemes were originally trialled. Of these, normalization to $^{66}Zn/^{67}Zn$, with $^{66}Zn/^{67}Zn = 6.883939$ (Berglund and Wieser, 2011) best resolves the Zn isotope anomalies and was therefore adopted in most of our analyses. Data for this normalization scheme were collected with both the M64 and the M70 cup configurations and the combined results are shown in Figs. 2.1, and 2.2, and listed in Table 2.6, which also include data

from Kuthning (2020). Additional results, obtained via internal normalization to $^{64}Zn/^{67}Zn = 12.170590$ (Berglund and Wieser, 2011) using only the M64 collector configuration, demonstrate the consistency of the data (Figs. 2.1, 2.2, Table 2.6).

Further results obtained with the M64 configuration are presented for internal normalization to $^{64}Zn/^{68}Zn = 2.665308$ (Berglund and Wieser, 2011). This normalization avoids $^{67}Zn$, which is particularly susceptible to nuclear field shift effects, and allows a comparison with the previously published Zn isotope data (Moynier et al., 2009a). The data collected in this manner are less suitable for resolving the expected and observed Zn isotope anomalies, so are not discussed in the main text. They are, however, discussed in a section below to evaluate whether the observed anomalies are a consequence of nuclear field shift effects.

The corrections for isobaric overlap of $^{64}Ni$ with $^{64}Zn$ and $^{70}Ge$ with $^{70}Zn$ were also carried out as part of the data reduction. They incorporate a correction for instrumental mass bias and employed ratios of $^{64}Ni/^{62}Ni = 0.254671$ and $^{70}Ge/^{72}Ge = 0.74933$ (Berglund and Wieser, 2011). As the $^{64}Zn/^{67}Zn$ normalization features $^{64}Zn$, which is corrected for the presence of isobaric $^{64}Ni$, an iterative procedure that optimizes both the mass bias and spectral interference corrections was employed for data reduction.

The Zn isotope data are reported using the ε notation, to denote deviations of the measured isotope ratio for a sample (sam) from the value determined for the London Zn reference standard (std) in parts per $10^4$:

$$\varepsilon^{i/j}Zn_{k/j} = \left(\frac{(\,^{i}Zn/\,^{j}Zn)_{sam}}{(\,^{i}Zn/\,^{j}Zn)_{std}} - 1\right) x\ 10^4 \qquad \text{(Eq. 2.1)}$$

where i/j is the isotope ratio of interest and k/j the normalization ratio. As data obtained via the $^{66}Zn/^{67}Zn$ normalization scheme is most frequently quoted in the manuscript, a simplified $\varepsilon^{i}Zn$ notation is adopted in this case. The full $\varepsilon^{i/j}Zn_{k/j}$ notation, however, is used to denote Zn isotope data normalized to $^{64}Zn/^{67}Zn$ and $^{64}Zn/^{68}Zn$. In practice, the εZn values of samples were ubiquitously calculated relative to the mean isotopic results that were obtained for about 20 to 40 runs of the London Zn standard during the same measurement session.

For individual meteorites and meteorite groups with only a single sample (CI, CO chondrites), the mean and 2sd (two standard deviations) were determined from the results of n individual runs; the respective 2se uncertainties were calculated as 2sd/√n, using the n individual

sample runs. For other meteorite groups, the mean and 2sd values were determined from the mean values of x distinct meteorites in the group; the 2se errors were calculated as 2sd/√x for x distinct meteorites.

#### 2.3.2.3. Quality control of Zn isotope data

Zinc background levels (blanks) were highly variable (between about 30 and 300 ng) during the course of the study, mainly depending on the volume of digestion acids used (as dictated by sample size) and the methods employed for digestion and Zn separation. In all cases, however, the total Zn blanks were less than 1% of the Zn present in the samples, so no corrections were applied.

Isobaric interferences from Ni during runs of samples ($Ni/Zn \approx 7.1 \times 10^{-7}$ to $5.5 \times 10^{-5}$) and London Zn standards ($Ni/Zn \approx 7.4 \times 10^{-7}$ to $2.5 \times 10^{-5}$) were consistently at similar levels and amounted to maximum interference corrections of $^{64}Ni/^{64}Zn \approx 2 \times 10^{-6}$. For Ge, the interference levels were slightly higher but also almost identical for analyses of samples ($Ge/Zn \approx 9.4 \times 10^{-6}$ to $5.8 \times 10^{-5}$) and London Zn solutions ($Ge/Zn \approx 9.6 \times 10^{-6}$ to $5.8 \times 10^{-5}$), with a typical (median) $Ge/Zn \approx 2.2 \times 10^{-5}$ for both. The median and maximum Ge interference levels are equivalent to interference corrections, as quantified by $^{70}Ge/^{70}Zn$, of about $7 \times 10^{-4}$ and $1.9 \times 10^{-3}$, respectively. As the εZn values of samples are determined relative to London Zn results obtained in the same measurement session and runs of doped solutions with larger interference levels of $Ni/Zn = 1 \times 10^{-4}$ and $Ge/Zn = 3 \times 10^{-4}$ did not produce any resolvable analytical biases, we regard the applied Ni and Ge interference corrections as robust.

Comprehensive mass scans that were routinely carried out on the Zn fractions of meteorite samples and in-run monitoring at mass numbers 62 ($^{62}Ni$, $^{46}Ti^{16}O$) and 72 ($^{72}Ge$, $^{56}Fe^{16}O$) demonstrate that other spectral interferences on Zn isotopes, from $Ba^{2+}$ and molecular ions (e.g., $MgAr^+$, $AlAr^+$, $SiAr^+$, $TiO^+$, $CrO^+$, $FeO^+$) were at unproblematic levels. Interferences from $Ba^{2+}$ ions could, in principle, be measured during the runs (e.g., by monitoring $^{137}Ba^{2+}$ at mass number 68.5) and corrected as part of the data reduction. However, $Ba^{2+}$ monitors at mass numbers 67.5 and 68.5 yielded $Ba^{2+}$ levels equivalent to $^{137}Ba^{2+}/^{137}Ba \approx 0.3$ for London Zn solutions, in accord with the $Ba^{2+}/Ba^+$ ratios of about 0.05 to 0.2 typically expected for Ba ionization in the plasma of quadrupole ICP-MS instruments (Pupyshev and Semenova, 2001). In contrast, the meteorite

samples gave unexpectedly high ratios of $^{137}Ba^{2+}/^{137}Ba \approx 1.5$. As analyses of both sample and London Zn solutions ubiquitously showed similar Ba/Zn ratios of $1\text{-}2 \times 10^{-5}$, we expect actual $Ba^{2+}$ interference levels on $^{66}Zn$, $^{67}Zn$ and $^{68}Zn$ to be negligible at $\leq 1.5 \times 10^{-6}$. Given that samples and London Zn solutions had almost identical Ba/Zn ratios, no corrections for $Ba^{2+}$ interferences were applied.

The two different BSE rocks (Table 2.1) were analysed multiple times, and together two other previously analysed samples (Kuthning, 2020) define a mean εZn value for the BSE that is identical to the expected result of εZn = 0 within 2se error, regardless of the internal normalization scheme that was used (Fig. 2.1, Table 2.6). Due to their compositions (with relatively high Ba, Al, Si, Ti and low Zn abundances), the BSE samples should suffer from larger spectral interferences from $Ba^{2+}$ and many relevant molecular ions (Table 2.5) than the meteorites.

## 2.4 Results

The results are shown on Table 2.6, which also includes results from Kuthning (2020). All meteorites show small but resolvable deviations from the BSE (Fig. 2.2). The CCs have an excess of neutron-rich $^{70}Zn$, a smaller excess for $\varepsilon^{68}Zn$ and a depletion in $\varepsilon^{64}Zn$. The NC meteorites have complementary patterns, with negative anomalies for $\varepsilon^{70}Zn$ and $\varepsilon^{68}Zn$, but positive deviations for $\varepsilon^{64}Zn$. Similar results are obtained if other isotope ratios are employed for internal normalization (e.g., $^{64}Zn/^{67}Zn$; Fig. 2.2). Measurements of BSE standards show no substantial deviations from $\varepsilon^{i}Zn = 0$ (BSE in Fig. 2.1, 2.2).

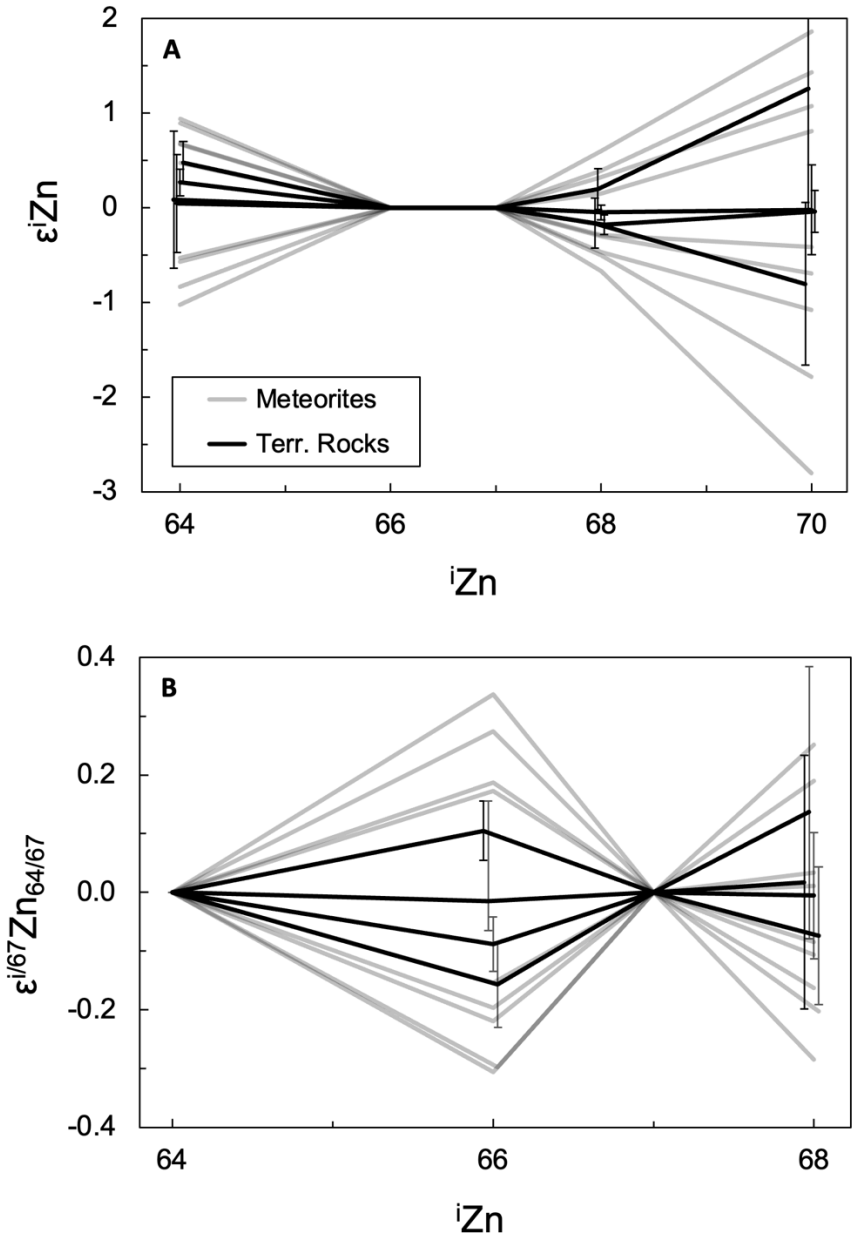



**Figure 2.1. Mass-independent Zn isotope compositions of BSE rocks.** Shown are the mean (A) $\varepsilon^{i}Zn$ and (B) $\varepsilon^{i/67}Zn_{64/67}$ data for four BSE rocks (black); error bars indicate ±2se. These five samples were repeatedly analysed for quality control. Unlike the meteorites (plotted in light grey for comparison), the BSE rocks show either no or only barely resolvable deviations from εZn = 0, with an overall BSE mean that is identical to εZn = 0 within ±2se uncertainty (all data shown in Table 2.6).

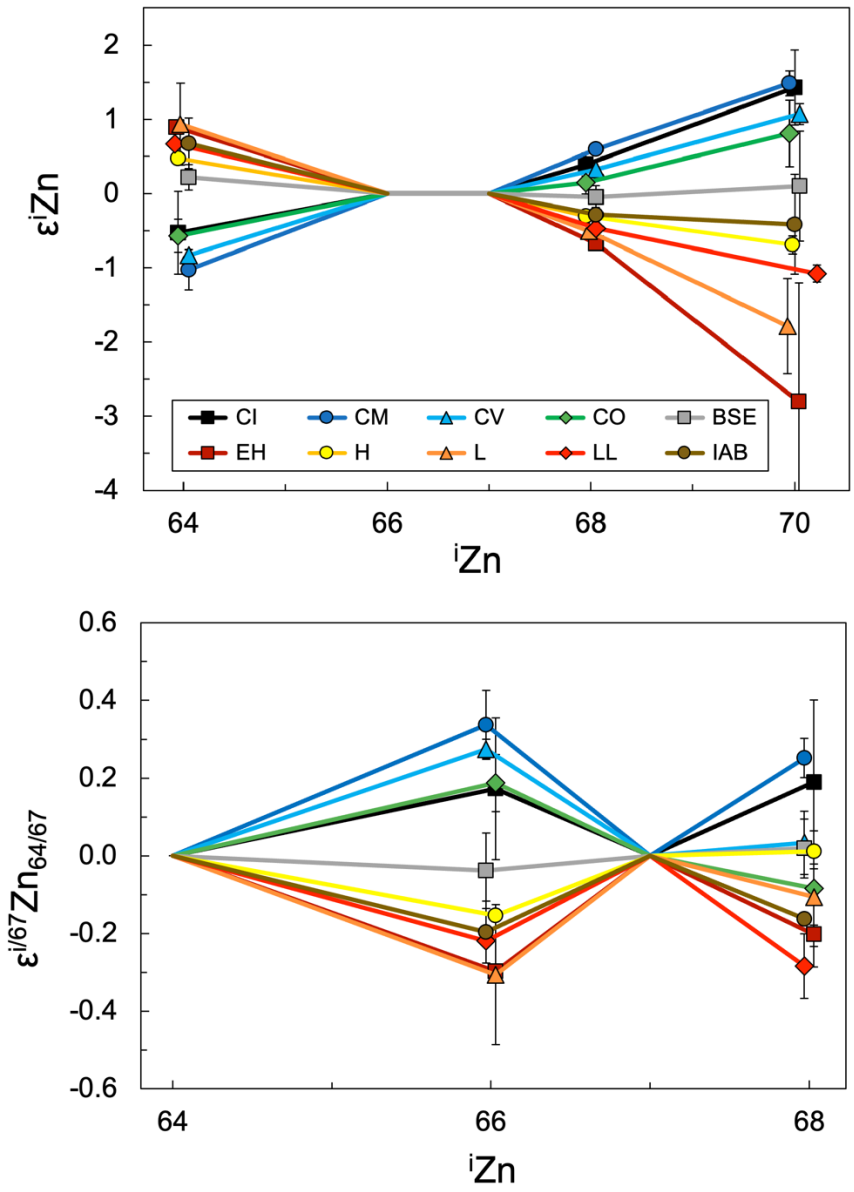



**Figure 2.2. Zn isotope anomalies for each meteorite group and the BSE, in $\varepsilon^{i}$Zn notation. (A)** Carbonaceous chondrites (CI, CM, CV, CO chondrites) and non-carbonaceous group meteorites (ECs, including two EHs (high iron), OCs, including H (high iron), L (low iron), and LL (low iron, low metal) chondrites, and IAB complex irons) have complimentary patterns with CCs enriched in $^{68}$Zn and $^{70}$Zn and depleted in $^{64}$Zn (relative to the BSE with $\varepsilon^{i}$Zn = 0). NCs have the opposite pattern, with depletions in $^{68}$Zn and $^{70}$Zn and enrichments in $^{64}$Zn. There is no data for $\varepsilon^{66}$Zn and $\varepsilon^{67}$Zn since these isotopes are used for internal normalization. The meteorite and BSE data are listed in Table 2.6; error bars indicate ±2se. **(B)** Same as (A), but for data obtained using $^{64}$Zn/$^{67}$Zn for mass bias normalization.

**Table 2.6. Mass-independent Zn isotope data (in εZn notation) for meteorites and BSE samples.** m: number of sample digest aliquots processed separately through column chemistry. n is the total number of individual analytical runs for a given meteorite, for one or several powder/digest solution aliquots. x is the number of distinct meteorite/BSE samples in a group. *From Kuthning (2020). **Mean of multiple sample digest aliquots, including results from Kuthning (2020) and from this study.

| | | Data normalised to $^{66}Zn/^{67}Zn$ | | | | | | | | | | | |
|---|---|---|---|---|---|---|---|---|---|---|---|---|---|
| **Sample** | | **$\varepsilon^{64/67}Zn$** | **2se** | **2sd** | **m/n** | **$\varepsilon^{68/67}Zn$** | **2se** | **2sd** | **m/n** | **$\varepsilon^{70/67}Zn$** | **2se** | **2sd** | **m/n** |
| Orgueil* | CI1 | -0.53 | 0.56 | 1.11 | 1/4 | 0.39 | 0.15 | 0.38 | 1/6 | 1.43 | 0.50 | 0.87 | 1/3 |
| Jbilet Winselwan* | CM2 | -1.22 | 0.15 | 0.41 | 1/7 | 0.65 | 0.06 | 0.24 | 1/16 | 2.12 | 0.25 | 0.74 | 1/9 |
| Murchison* | CM2 | -0.83 | 0.99 | 1.98 | 1/4 | 0.55 | 0.26 | 0.47 | 1/7 | 1.61 | 0.83 | 1.43 | 1/3 |
| Allende** | CV3 | -0.91 | 0.21 | 1.52 | 8/51 | 0.36 | 0.15 | 1.33 | 8/82 | 0.91 | 0.60 | 3.33 | 8/31 |
| LAR 12002 | CV3 | -0.85 | 0.28 | 0.83 | 1/9 | 0.33 | 0.19 | 0.71 | 1/14 | 1.19 | 0.21 | 0.46 | 1/5 |
| NWA 4502* | CV3 | -0.74 | 0.23 | 0.90 | 2/16 | 0.28 | 0.08 | 0.43 | 2/28 | 1.12 | 0.25 | 0.85 | 2/12 |
| MIL 090025 | CO3 | -0.57 | 0.22 | 0.67 | 1/9 | 0.15 | 0.16 | 0.61 | 1/15 | 0.81 | 0.45 | 1.10 | 1/6 |
| *CC mean (x=7)* | | -0.81 | 0.16 | 0.43 | 15/100 | 0.39 | 0.12 | 0.31 | 15/168 | 1.20 | 0.20 | 0.53 | 15/68 |
| NWA 13299 | EH3 | 0.85 | 0.34 | 1.06 | 1/10 | -0.64 | 0.36 | 1.75 | 1/23 | -3.93 | 1.68 | 6.07 | 1/13 |
| Indarch | EH4 | 0.93 | 0.29 | 0.88 | 1/9 | -0.70 | 0.16 | 0.61 | 1/15 | -1.67 | 0.67 | 1.63 | 1/6 |
| *EC mean (x=2)* | | 0.89 | 0.06 | 0.08 | 2/19 | -0.67 | 0.05 | 0.07 | 2/38 | -2.80 | 1.60 | 2.26 | 2/19 |
| Brownfield (1937)* | H3.7 | 0.50 | 0.37 | 0.90 | 1/6 | -0.36 | 0.13 | 0.46 | 1/12 | -0.78 | 0.38 | 0.92 | 1/6 |
| Forest Vale | H4 | 0.44 | 0.13 | 0.49 | 1/14 | -0.24 | 0.16 | 0.80 | 1/24 | -0.61 | 0.45 | 1.43 | 1/10 |
| Saratov | L4 | 0.63 | 0.11 | 0.39 | 1/14 | -0.41 | 0.21 | 0.96 | 1/21 | -1.89 | 0.72 | 1.91 | 1/7 |
| Tennasilm* | L4 | 1.61 | 0.61 | 1.05 | 1/3 | -0.57 | 0.17 | 0.42 | 1/6 | -1.06 | 0.77 | 1.33 | 1/3 |
| Homestead | L5 | 0.57 | 0.27 | 0.72 | 1/7 | -0.54 | 0.26 | 0.98 | 1/14 | -2.41 | 0.81 | 2.14 | 1/7 |
| Bishunpur | LL3 | 0.68 | 0.26 | 0.79 | 1/9 | -0.41 | 0.13 | 0.50 | 1/15 | -1.00 | 0.48 | 1.17 | 1/6 |
| Soko Banja | LL4 | 0.66 | 0.30 | 1.02 | 2/12 | -0.53 | 0.12 | 0.61 | 2/27 | -1.16 | 0.48 | 1.84 | 2/15 |
| *OC mean (x=7)* | | 0.73 | 0.28 | 0.74 | 8/77 | -0.44 | 0.08 | 0.21 | 8/119 | -1.27 | 0.45 | 1.19 | 8/54 |
| *NCC mean (x=9)* | | 0.76 | 0.22 | 0.67 | 10/96 | -0.49 | 0.09 | 0.27 | 10/157 | -1.61 | 0.66 | 1.97 | 10/73 |
| Canyon Diablo* | IAB complex | 0.92 | 0.36 | 1.13 | 1/10 | -0.36 | 0.15 | 0.63 | 1/18 | -0.89 | 0.27 | 0.77 | 1/8 |
| Toluca* | IAB complex | 0.44 | 0.007 | 0.01 | 1/2 | -0.21 | 0.13 | 0.25 | 1/4 | 0.06 | 0.06 | 0.08 | 1/2 |
| *NC mean (x=11)* | | 0.75 | 0.19 | 0.64 | 12/96 | -0.45 | 0.09 | 0.30 | 12/179 | -1.39 | 0.62 | 2.04 | 12/83 |
| BHVO-2 | basalt | 0.48 | 0.22 | 1.17 | 4/28 | -0.18 | 0.10 | 0.65 | 4/39 | -0.04 | 0.22 | 0.92 | 4/17 |
| BTHO* | basalt | 0.08 | 0.72 | 1.62 | 6/35 | -0.16 | 0.26 | 0.59 | 6/62 | -0.80 | 0.86 | 2.10 | 6/27 |
| D-174* | gabbro | 0.05 | 0.52 | 1.27 | 6/10 | 0.20 | 0.22 | 0.53 | 6/27 | 1.26 | 1.30 | 3.17 | 6/17 |
| P6Bt | glacial till | 0.27 | 0.14 | 0.69 | 3/16 | -0.05 | 0.08 | 0.47 | 3/24 | -0.02 | 0.47 | 1.64 | 3/8 |
| *BSE mean (x=4)* | | 0.22 | 0.17 | 0.34 | 19/89 | -0.05 | 0.15 | 0.30 | 19/152 | 0.10 | 0.74 | 1.48 | 19/63 |

Continued on next page.

**Table 2.6. Continued.**

| | | Data normalised to $^{64}Zn/^{67}Zn$ | | | | | | | |
|---|---|---|---|---|---|---|---|---|---|
| **Sample** | | **$\varepsilon^{66/67}Zn$** | **2se** | **2sd** | **m/n** | **$\varepsilon^{68/67}Zn$** | **2se** | **2sd** | **m/n** |
| Orgueil* | CI1 | 0.17 | 0.18 | 0.37 | 1/4 | 0.19 | 0.21 | 0.42 | 1/4 |
| Jbilet Winselwan* | CM2 | 0.40 | 0.05 | 0.14 | 1/7 | 0.22 | 0.13 | 0.33 | 1/7 |
| Murchison* | CM2 | 0.28 | 0.33 | 0.65 | 1/4 | 0.29 | 0.07 | 0.13 | 1/4 |
| Allende** | CV3 | 0.30 | 0.07 | 0.50 | 8/51 | 0.13 | 0.11 | 0.82 | 8/51 |
| LAR 12002 | CV3 | 0.28 | 0.09 | 0.28 | 1/9 | -0.04 | 0.23 | 0.68 | 1/9 |
| NWA 4502* | CV3 | 0.24 | 0.07 | 0.30 | 2/16 | 0.01 | 0.09 | 0.37 | 2/16 |
| MIL 090025 | CO3 | 0.19 | 0.07 | 0.22 | 1/9 | -0.08 | 0.15 | 0.45 | 1/9 |
| *CC mean (x=7)* | | 0.27 | 0.05 | 0.14 | 15/100 | 0.10 | 0.10 | 0.26 | 15/100 |
| NWA 13299 | EH3 | -0.29 | 0.10 | 0.32 | 1/10 | -0.14 | 0.23 | 0.71 | 1/10 |
| Indarch | EH4 | -0.31 | 0.10 | 0.29 | 1/9 | -0.26 | 0.14 | 0.41 | 1/9 |
| *EC mean (x=2)* | | -0.30 | 0.01 | 0.02 | 2/19 | -0.20 | 0.08 | 0.12 | 2/19 |
| Brownfield (1937)* | H3.7 | -0.16 | 0.12 | 0.30 | 1/6 | 0.01 | 0.15 | 0.37 | 1/6 |
| Forest Vale | H4 | -0.14 | 0.04 | 0.16 | 1/14 | 0.01 | 0.17 | 0.64 | 1/14 |
| Saratov | L4 | -0.21 | 0.03 | 0.13 | 1/14 | -0.02 | 0.23 | 0.87 | 1/14 |
| Tennasilm* | L4 | -0.53 | 0.20 | 0.34 | 1/3 | -0.14 | 0.12 | 0.21 | 1/3 |
| Homestead | L5 | -0.19 | 0.09 | 0.24 | 1/7 | -0.16 | 0.22 | 0.57 | 1/7 |
| Bishunpur | LL3 | -0.22 | 0.09 | 0.26 | 1/9 | -0.23 | 0.16 | 0.47 | 1/9 |
| Soko Banja | LL4 | -0.22 | 0.10 | 0.34 | 2/12 | -0.34 | 0.23 | 0.79 | 2/12 |
| *OC mean (x=7)* | | -0.24 | 0.09 | 0.24 | 8/65 | -0.12 | 0.09 | 0.25 | 8/65 |
| *NCC mean (x=9)* | | -0.25 | 0.07 | 0.22 | 10/84 | -0.14 | 0.08 | 0.23 | 10/84 |
| Canyon Diablo* | IAB complex | -0.29 | 0.10 | 0.50 | 1/10 | -0.14 | 0.23 | 0.34 | 1/10 |
| Toluca* | IAB complex | -0.10 | 0.16 | 0.00 | 1/2 | -0.16 | 0.21 | 0.04 | 1/2 |
| *NC mean (x=11)* | | -0.24 | 0.06 | 0.21 | 12/96 | -0.15 | 0.06 | 0.21 | 12/96 |
| BHVO-2 | basalt | -0.16 | 0.07 | 0.39 | 4/28 | -0.07 | 0.12 | 0.62 | 4/28 |
| BTHO* | basalt | 0.11 | 0.05 | 0.10 | 6/35 | 0.02 | 0.22 | 0.43 | 6/35 |
| D-174* | gabbro | -0.02 | 0.17 | 0.42 | 6/10 | 0.14 | 0.25 | 0.61 | 6/10 |
| P6Bt | glacial till | -0.09 | 0.05 | 0.23 | 3/16 | -0.01 | 0.11 | 0.53 | 3/16 |
| *BSE mean (x=4)* | | -0.04 | 0.10 | 0.19 | 19/89 | 0.02 | 0.08 | 0.15 | 19/89 |

Continued on next page.

**Table 2.6. Continued.**

| | | Data normalised to $^{64}Zn/^{68}Zn$ | | | | | | | |
|---|---|---|---|---|---|---|---|---|---|
| **Sample** | | **$\varepsilon^{66/68}Zn$** | **2se** | **2sd** | **m/n** | **$\varepsilon^{67/68}Zn$** | **2se** | **2sd** | **m/n** |
| Orgueil* | CI1 | 0.09 | 0.28 | 0.56 | 1/4 | -0.14 | 0.16 | 0.31 | 1/4 |
| Jbilet Winselwan* | CM2 | 0.22 | 0.10 | 0.25 | 1/7 | -0.16 | 0.10 | 0.27 | 1/7 |
| Murchison* | CM2 | 0.15 | 0.40 | 0.79 | 1/4 | -0.22 | 0.05 | 0.10 | 1/4 |
| Allende** | CV3 | 0.23 | 0.05 | 0.36 | 8/51 | -0.07 | 0.09 | 0.62 | 8/51 |
| LAR 12002 | CV3 | 0.31 | 0.15 | 0.46 | 1/9 | 0.03 | 0.17 | 0.51 | 1/9 |
| NWA 4502* | CV3 | 0.26 | 0.09 | 0.38 | 2/16 | 0.00 | 0.07 | 0.28 | 2/16 |
| MIL 090025 | CO3 | 0.23 | 0.09 | 0.26 | 1/9 | 0.06 | 0.11 | 0.34 | 1/9 |
| *CC mean (x=7)* | | 0.21 | 0.05 | 0.14 | 15/100 | -0.07 | 0.07 | 0.20 | 15/100 |
| NWA 13299 | EH3 | -0.23 | 0.10 | 0.31 | 1/10 | 0.11 | 0.17 | 0.54 | 1/10 |
| Indarch | EH4 | -0.16 | 0.11 | 0.33 | 1/9 | 0.20 | 0.10 | 0.31 | 1/9 |
| *EC mean (x=2)* | | -0.19 | 0.05 | 0.07 | 2/19 | 0.15 | 0.06 | 0.09 | 2/19 |
| Brownfield (1937)* | H3.7 | -0.19 | 0.15 | 0.37 | 1/6 | -0.01 | 0.11 | 0.28 | 1/6 |
| Forest Vale | H4 | -0.16 | 0.07 | 0.27 | 1/14 | -0.01 | 0.13 | 0.49 | 1/14 |
| Saratov | L4 | -0.21 | 0.13 | 0.49 | 1/14 | 0.01 | 0.18 | 0.66 | 1/14 |
| Tennasilm* | L4 | -0.37 | 0.23 | 0.40 | 1/3 | 0.11 | 0.09 | 0.16 | 1/3 |
| Homestead | L5 | -0.08 | 0.13 | 0.35 | 1/7 | 0.12 | 0.16 | 0.43 | 1/7 |
| Bishunpur | LL3 | -0.08 | 0.11 | 0.32 | 1/9 | 0.17 | 0.12 | 0.36 | 1/9 |
| Soko Banja | LL4 | -0.06 | 0.16 | 0.55 | 2/12 | 0.26 | 0.17 | 0.60 | 2/12 |
| *OC mean (x=7)* | | -0.17 | 0.07 | 0.20 | 8/65 | 0.09 | 0.07 | 0.19 | 8/65 |
| *NCC mean (x=9)* | | -0.17 | 0.06 | 0.18 | 10/84 | 0.11 | 0.06 | 0.18 | 10/84 |
| Canyon Diablo* | IAB complex | -0.20 | 0.08 | 0.24 | 1/10 | 0.13 | 0.07 | 0.23 | 1/10 |
| Toluca* | IAB complex | -0.04 | 0.00 | 0.00 | 1/2 | 0.13 | 0.02 | 0.03 | 1/2 |
| *NC mean (x=11)* | | -0.16 | 0.05 | 0.18 | 12/96 | 0.11 | 0.05 | 0.16 | 12/96 |
| BHVO-2 | basalt | -0.12 | 0.11 | 0.56 | 4/28 | 0.06 | 0.09 | 0.47 | 4/28 |
| BTHO* | basalt | -0.01 | 0.15 | 0.36 | 6/35 | 0.01 | 0.15 | 0.30 | 6/35 |
| D-174* | gabbro | -0.08 | 0.08 | 0.18 | 6/10 | -0.10 | 0.19 | 0.46 | 6/10 |
| P6Bt | glacial till | -0.08 | 0.09 | 0.02 | 3/16 | 0.00 | 0.08 | 0.08 | 3/16 |
| *BSE mean (x=4)* | | -0.07 | 0.04 | 0.08 | 19/89 | -0.01 | 0.06 | 0.11 | 19/89 |

## 2.5 Discussion

### 2.5.1 Origin of the anomalies

#### 2.5.1.1. Mass-dependent isotope fractionation

In principle, it is possible that the results reflect mass-dependent Zn isotope fractionation. These effects should, however, have been corrected for by the use of internal normalization (Section 2.3.2.2). In line with this, the identical values within uncertainty for $\varepsilon^{66/67}Zn_{64/67}$ and $\varepsilon^{68/67}Zn_{64/67}$ for most meteorites imply that the results do not fall on the mass-dependent fractionation line (Fig. 2.2, Table 2.6). This hypothesis can be further tested by comparing the presented results with independently measured mass-dependent Zn isotope variations in meteorites. Coupled εZn-$\delta^{66}$Zn results are available for seven meteorites (Orgueil CI1; Murchison, Jbilet Winselwan, CM2; Allende CV3; Brownfield (1937) H3.7; Bishunpur LL3.1; Indarch EH4) that were analysed here for εZn and previously for $\delta^{66}$Zn (Fig. 2.3; Luck et al., 2005, Moynier et al., 2011, Creech and Moynier, 2019). Mass-dependent results are quantified using $\delta^{66}$Zn values, which denote the difference of the $^{66}Zn/^{64}Zn$ isotope ratio of a sample from the JMC Lyon Zn isotope reference material in parts per 1000 (‰).

If the εZn results reflected mass-dependent fractionation, they would be expected to correlate with $\delta^{66}$Zn. However, the available data offer no evidence of such a relationship (Fig. 2.3). For example, the $\delta^{66}$Zn values of CI, CM, CO and CV chondrites are distinct but no such differences are apparent for $\varepsilon^{64}$Zn (Fig. 2.3). In addition, both ECs and OCs have highly variable $\delta^{66}$Zn values, which record alteration of the original composition by subsequent parent body processes, while εZn results are consistent within group. The heavy Zn isotope compositions of many OCs and some ECs are most likely due to Zn mobilization and loss by thermal or shock metamorphism, with associated isotope fractionation (Moynier et al., 2017, Luck et al., 2005). Whilst the low $\delta^{66}$Zn values of other OCs might record parent body compositions, as they cannot be the consequence of evaporative Zn loss, it is more likely that they reflect recondensation of mobilized Zn with associated isotope fractionation, as has been found for Cd isotopes (Wombacher et al., 2003). However, it is clear the εZn values were not affected by the same processes that produced the $\delta^{66}$Zn variations observed in these meteorites.

Furthermore, the available mass-dependent Zn isotope data for chondrites provide only limited constraints on the carbonaceous versus non-carbonaceous origin of Earth's Zn inventory. CCs, ECs and OCs display overlapping $\delta^{66}$Zn values, but the data for the latter two meteorite groups are more variable (Fig. 2.3). This reflects that ECs and OCs are more impacted

by secondary alteration within the parent asteroids, such that the bulk $\delta^{66}Zn$ values of the meteorite parent bodies are uncertain (Moynier et al., 2017, Luck et al., 2005). The $\delta^{66}Zn$ value estimated for the BSE overlaps with results published for CV and CO carbonaceous as well ordinary and enstatite chondrites (Fig. 2.3; Pringle et al., 2017, Luck et al., 2005, Moynier et al., 2011, Barrat et al., 2012, Sossi et al., 2018, Huang et al., 2018, Creech and Moynier, 2019). This provides no constraints on the source of Earth's Zn inventory as it could be derived to 100% from any of these meteorite groups or any mixture between them.

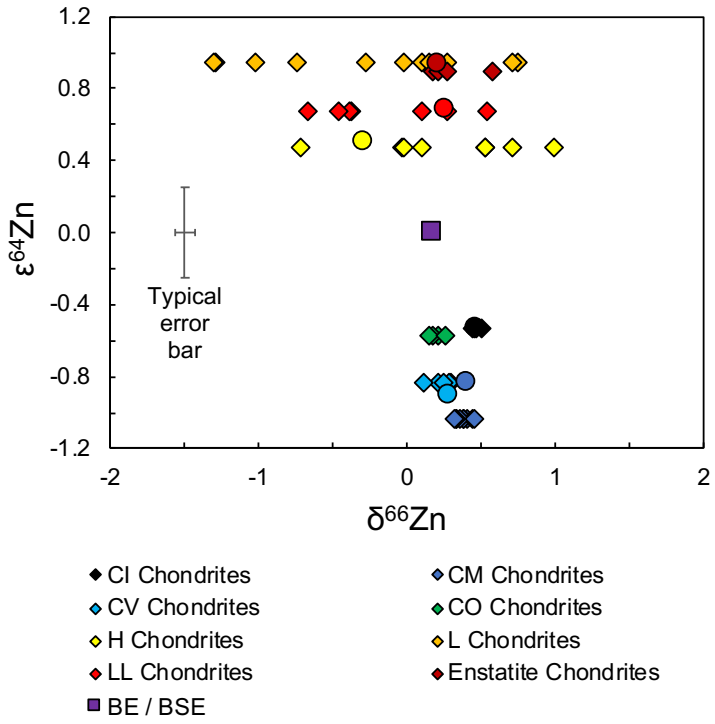



**Figure 2.3. Mass-dependent Zn isotope data ($\delta^{66}Zn$) and mass-independent Zn isotope compositions ($\varepsilon^{64}Zn$) for chondrites.** Circles are data for 7 meteorites that were analysed both in this study or in Kuthning (2020) and previously for $\delta^{66}Zn$ (Orgueil CI1; Murchison, Jbilet Winselwan, CM2; Allende CV3; Brownfield (1937) H3.7; Bishunpur LL3.1; Indarch EH4). For the meteorites shown as diamonds, the published $\delta^{66}Zn$ results were combined with the mean $\varepsilon^{64}Zn$ value of the respective meteorite group. The composition of the BE and BSE is $\delta^{66}Zn = 0.20‰$ (Pickard et al., 2022) and $\varepsilon^{64}Zn = 0$. The 'typical error bar' denotes uncertainties of $\delta^{66}Zn = \pm 0.08‰$ (2sd) and $\varepsilon^{64}Zn = \pm 0.25$ (2se). The $\delta^{66}Zn$ data for meteorites are from (Pringle et al., 2017, Luck et al., 2005, Moynier et al., 2011, Barrat et al., 2012, Mahan et al., 2018, Sossi et al., 2018, Creech and Moynier, 2019).

### 2.5.1.2. Nuclear Field Shift Effect

Alternatively, the εZn values could reflect mass-independent isotope fractionations from nuclear field shift effects (NFSEs). Such fractionations can be generated by the same processes and in the same settings that produce mass-dependent isotope effects (Fujii et al., 2006a), but rather than being dictated by mass, NFSEs scale with the nuclear charge radii of

the nuclei. Mass-independent isotope fractionations are more evident for elements with high atomic masses (e.g., U, Tl, Hg) and are thought to become smaller with decreasing atomic mass (Dauphas and Schauble, 2016). As such, they have not been detected in natural samples for elements with atomic numbers Z < 80 (Hg). However, it was previously proposed that NFSEs may be responsible for Mo, Ru, and Te isotope anomalies in bulk meteorites (Fujii et al., 2006b, Moynier et al., 2009b). We therefore evaluated whether the Zn isotope signatures we measured in this study are possibly a consequence of NFSEs. In principle, the investigated samples could have acquired mass-independent isotope fractionations from NFSEs in one of two settings. First, they could be an indigenous fingerprint of the meteorites that records Solar System processes. Second, the isotope fractionation could have occurred in the laboratory during processing of the meteorites. Both possibilities are discussed below.

#### 2.5.1.2.1. Laboratory-induced NFSEs

The presented results indicate systematic and complimentary mass-independent Zn isotope effects for CCs versus NC meteorites, with an intermediate signature for Earth's Zn (Fig. 2.2). Such systematic and consistent isotope effects are unlikely to be generated by an analytical procedure, which would be expected to induce random analytical artefacts. If mass-independent isotope fractionation was to occur in the laboratory, the most likely origin would be the Zn separation by the column chemistry procedure (Tables 2.2, 2.3). This is because mass-dependent isotope fractionation of Zn and other metals can occur during column chromatography if the yields are incomplete; mass-independent isotope fractionation has been observed for Zn during such procedures (Fujii et al., 2001). For most of our samples, the Zn yields during sample preparation (including column chemistry) were >80%. For a few samples, however, the yields were as low as 20%. No samples have a correlation between Zn yields and εZn values. For example, the aliquot of sediment sample P6Bt with the lowest Zn yield (of 42%) had $\varepsilon^{64}Zn = 0.13 \pm 0.46$ (2se, n = 4), consistent with the London Zn standard. Furthermore, the Allende aliquot with the lowest Zn yield (of 21%) produced a mean $\varepsilon^{64}Zn$ value (of $-1.47 \pm 0.42$; 2se, n = 4) that is consistent with the overall Allende mean of $\varepsilon^{64}Zn = -0.91 \pm 0.21$ (2se, n = 51) that includes data for aliquots with yields exceeding 90%. This lack of correlation between Zn yields and the mass-independent Zn isotope results leads us to conclude that the observed anomalies are unlikely to be an artefact of Zn loss and associated isotope fractionation during sample preparation.

#### 2.5.1.2.2. Natural NFSEs

In principle, the systematic Zn isotope anomalies of CC versus NC meteorites might originate from processes that induced mass-independent Zn isotope fractionations from NFSEs in the protoplanetary disk. However, if the complementary mass-independent Zn isotope compositions of the outer and inner Solar System reservoirs were generated by NFSEs, such a dichotomy would also be expected for their mass-dependent Zn isotope compositions. Whilst the $\delta^{66}$Zn values of many enstatite and ordinary chondrites are not complementary to those of CCs (Fig. 2.3), this does not provide conclusive evidence for the absence of large-scale isotope fractionation in the protoplanetary disk. Rather, it most likely reflects that the former meteorites were altered by secondary processes involving thermal mobilization of Zn on the parent bodies. In particular, both ECs and OCs display highly variable $\delta^{66}$Zn values, which are thought to reflect different extents of evaporative Zn loss and associated mass-dependent isotope fractionation during thermal and shock metamorphism (Moynier et al., 2017, Luck et al., 2005).

If NFSEs were important for Zn, such parent body processes would have also impacted the mass-independent Zn isotope compositions of the meteorites. However, our data show no resolvable differences in εZn values between ordinary chondrites that were subjected to different extents of thermal metamorphism, as recorded by petrographic grades of between 3.1 and 5 (Fig. 2.4, Table 2.6). The data include results for two meteorites that differ substantially in their mass-dependent Zn isotope composition with $\delta^{66}$Zn values of $-0.30 \pm 0.05$‰ (Brownfield (1937) H3.7) and $0.25 \pm 0.05$‰ (Bishunpur LL3.1; Luck et al., 2005). Furthermore, ANOVA tests conducted for the OCs show no statistically significant differences in the Zn isotope compositions of these meteorites (with $p > 0.15$, Table A2.2). It is therefore unlikely that the observed εZn anomalies are a consequence of mass-independent Zn isotope fractionation that occurred during thermal processing of Solar System matter in the protoplanetary disk.

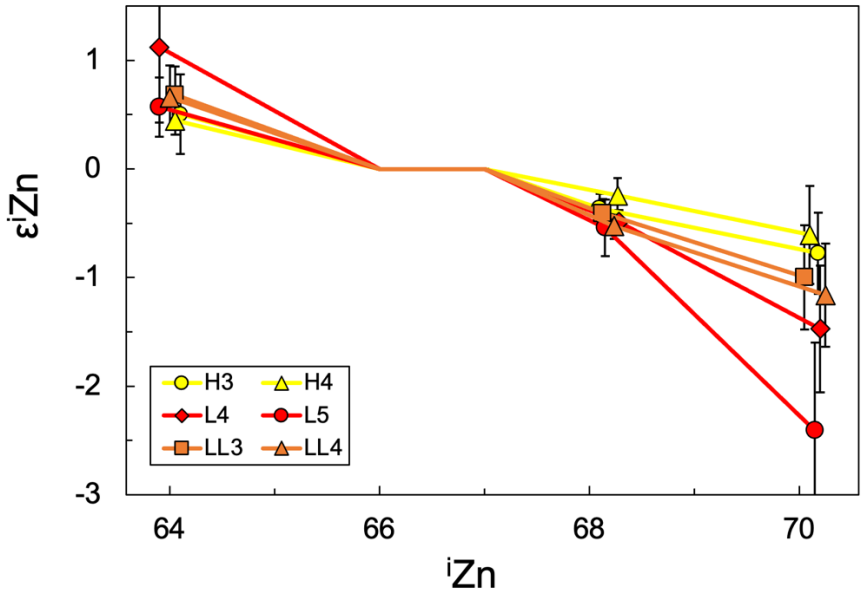



**Figure 2.4. Mass-independent Zn isotope data in $\varepsilon^{i}$Zn notation for the OCs.** Shown are $\varepsilon^{i}$Zn data for H, L, and LL ordinary chondrites, which are further subdivided according to their petrographic grades. No analytically resolvable differences are observed for the meteorites of each group, regardless of their petrographic grade. Mass-dependent Zn isotope data are available for two of the meteorites shown here and these have $\delta^{66}$Zn values of –0.30 ± 0.05‰ (Brownfield (1937) H3.7) and 0.25 ± 0.05‰ (Bishunpur LL3.1; Luck et al., 2005). The $\varepsilon^{i}$Zn data are listed in Table 2.6; error bars indicate ±2se.

Finally, if the observed εZn anomalies are a consequence of NFSEs, they should follow predictions from models of NFSE-based mass-independent isotope fractionation. The mass-independent Zn isotope fractionation that results from NFSEs is given by (Fujii et al., 2006a):

$$\varepsilon^{i/y}Zn_{x/y} = \left(\delta\langle r^2\rangle_{m_y,m_i} - \frac{m_x(m_i-m_y)}{m_i(m_x-m_y)}\delta\langle r^2\rangle_{m_y,m_x}\right)\cdot\alpha \qquad \text{(Eq. 2.6)}$$

where the εZn value is obtained for isotope ratio (i/y), internally normalized to ratio (x/y) to correct for instrumental mass discrimination, $m_i$ corresponds to the atomic mass of nuclei i, $\delta(r^2)_{my,mi}$ is the difference in mean-squared nuclear charge radii of the nuclei y and i, and α is a temperature-dependent and scalable parameter. We used nuclear charge radii data of (Angeli and Marinova, 2013) to determine εZn values obtained with internal normalization to $^{66}$Zn/$^{67}$Zn and $^{64}$Zn/$^{68}$Zn, and checked with alternative nuclear charge radii (Xie et al., 2019) for Zn isotope data measured with the $^{64}$Zn/$^{68}$Zn normalization scheme (Fig. 2.5, Table 2.6).

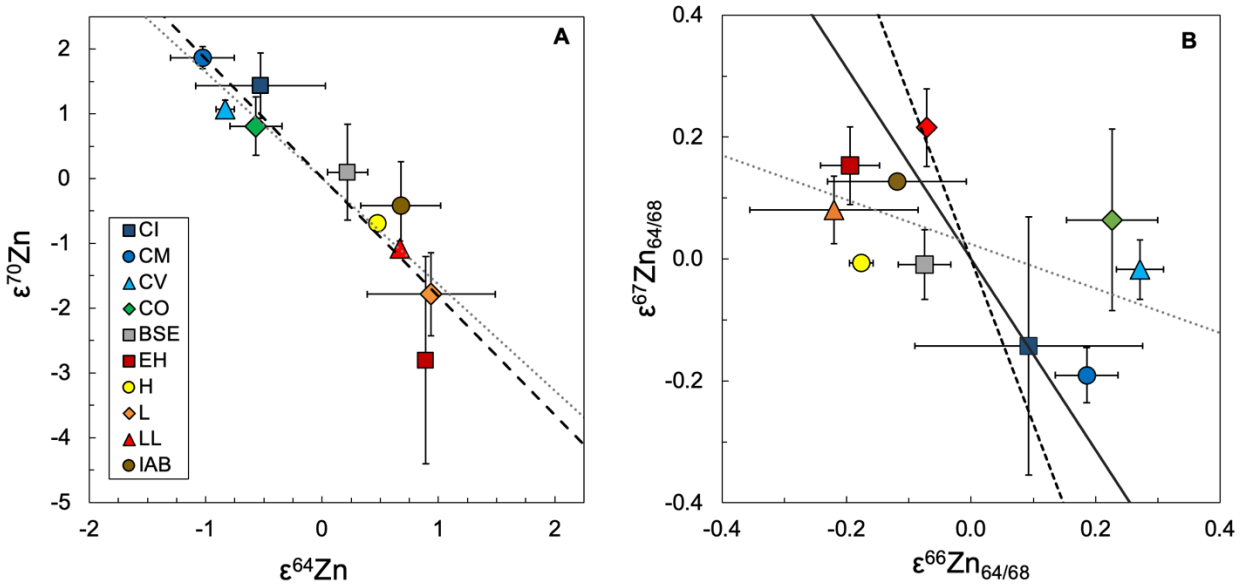



**Figure 2.5. Predicted mass-independent Zn isotope fractionation induced by NFSE compared to measured meteorite and BSE compositions.** (A) $\varepsilon^{70}Zn$ as a function of $\varepsilon^{64}Zn$ for meteorite groups and the BSE. Data points indicate meteorite groups and BSE standards. Trend predicted by a NFSE model (black dashed line) using nuclear charge radii data from Angeli and Marinova (2013) and a best-fit trendline for the samples (dotted black line) are shown for comparison. (B) Same as (A) but for εZn data obtained using $^{64}Zn/^{68}Zn$ for mass bias normalization and showing the trends for two NFSE models, which used the nuclear charge radii data of (Angeli and Marinova, 2013) and (Xie et al., 2019), as dashed and solid black lines, respectively. All modelled trends are compatible with the Zn isotope data determined using the $^{66}Zn/^{67}Zn$ normalization scheme (panel A). However, most of the measured meteorite data obtained using $^{64}Zn/^{68}Zn$ for internal normalization are not in accord with the steep trends predicted by the NFSE models, as the meteorites define a best-fit correlation (dashed line) with a more moderate slope (panel B). The data are from Table 2.6; error bars indicate ±2se.

When Zn isotope data normalized to $^{66}Zn/^{67}Zn$ are evaluated, the modelled NFSE trend matches our measurements (Fig. 2.5). However, the trends predicted by the NFSE are expected to be similar to nucleosynthetic yields because the nuclear configuration (which impacts nuclear volume and charge radius) is also linked to properties such as nuclear binding energy, which are relevant in nucleosynthetic processes (Dauphas and Schauble, 2016). As NFSEs tend to generate the most prominent anomalies for nuclides with odd atomic mass numbers, results obtained using the $^{64}Zn/^{68}Zn$ normalization were also examined. In this case, the $\varepsilon^{66/68}Zn_{64/68}$ and $\varepsilon^{67/68}Zn_{64/68}$ values of the meteorites show small but still resolvable anomalies. The anomalies are, however, are not compatible with the two NFSE trends, which predict larger $\varepsilon^{67/68}Zn_{64/68}$ anomalies for a given value of $\varepsilon^{66/68}Zn_{64/68}$, regardless of which set of nuclear charge radii data are used (Fig. 2.5). This further suggests that the Zn isotope anomalies observed for meteorites are unlikely to be caused by NFSEs.

### 2.5.1.3. Nucleosynthetic Anomalies

To assess whether the observed Zn isotope anomalies are of nucleosynthetic origin they must link to a feasible stellar source that produces the minor neutron-rich $^{70}$Zn isotope (0.6%), and $^{68}$Zn and $^{66}$Zn, without overproducing abundant $^{64}$Zn (49.2%). All five stable Zn nuclides are produced by the weak s-process in the He-burning shells of massive stars and by alpha-rich freezeout at quasi-equilibrium conditions in supernovae explosions, with only minor contributions from the main s-process in low mass AGB stars (Clayton, 2003). The $^{70}$Zn yields of both the main and the weak s-process are too low to produce the $^{70}$Zn enrichments observed for CCs (Bisterzo et al., 2011, Pignatari et al., 2010). Type II supernovae (SNII) have high production rates of $^{64}$Zn, such that the observed $\varepsilon^{64}$Zn anomalies could be explained by an excess of SNII-derived presolar matter in the non-carbonaceous meteorites (Woosley and Weaver, 1995). This is, however, the opposite of what is seen for other Fe-peak element isotope anomalies, such as Ca or Ti, which are thought to result from a depletion of anomalous presolar matter in non-carbonaceous meteorites. Furthermore, the $^{68}$Zn yields of SNII are highly sensitive to the mass of the star, such that both an excess or a deficit of this isotope can be produced relative to an excess of $^{70}$Zn.

In contrast, both SNIa and ECSN produce appreciable amounts of $^{66}$Zn, $^{68}$Zn and $^{70}$Zn, with low yields of $^{64}$Zn (Woosley, 1997, Wanajo et al., 2013). Previous research suggests that anomalies of the neutron-rich isotopes of other Fe-peak elements derive either from SNIa or ECSN (Dauphas et al., 2014, Woosley, 1997, Qin et al., 2010, Wanajo et al., 2013). Hence, to assess whether the observed mass-independent Zn isotope anomalies might reflect contributions of Zn produced in SNIa (Woosley, 1997) or ECSN (Wanajo et al., 2013), mass balance modelling was carried out. In the models, hypothetical materials with the isotopic composition of each nucleosynthetic source were mixed with baseline material that was assigned the BSE Zn isotope composition, which defined $\varepsilon$Zn = 0 in analyses of the London Zn isotope reference material (Berglund and Wieser, 2011).

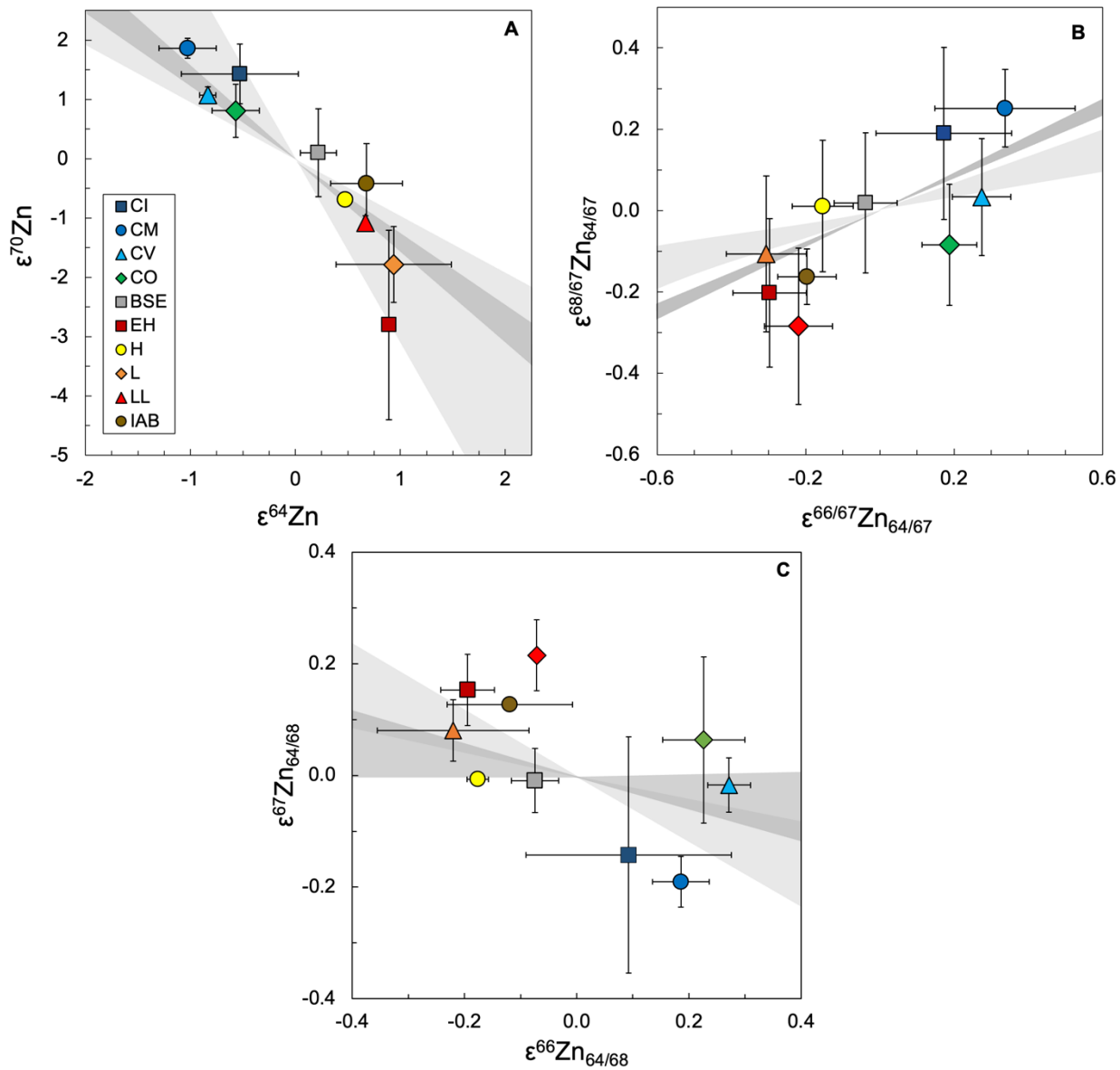



**Figure 2.6. Three isotope plots of mass-independent Zn results in ε notation. (A)** $\varepsilon^{70}Zn$ as a function of $\varepsilon^{64}Zn$ for meteorite groups and the BSE. Data points indicate meteorite groups and BSE standards. Shaded areas indicate predictions from models of Zn nucleosynthesis in Type Ia supernovae (Woosley, 1997) in light grey, and electron capture supernovae (Wanajo et al., 2013) in dark grey. The meteorite and BSE data are listed in Table 2.6; error bars indicate ±2se. **(B)** Same as panel (A), but for data obtained using $^{64}Zn/^{67}Zn$ for mass bias normalization. **(C)** Same as panel (A), but for data obtained using $^{64}Zn/^{68}Zn$ for mass bias normalization.

For the ECSN model, the isotope abundances were taken from (Wanajo et al., 2013; their figure 5) whilst the abundances employed in the SNIa model are from (Woosley, 1997; their table 4A). The dilution factor employed was $1\times10^{-6}$, chosen to produce anomalies within the range of observed values ($\varepsilon Zn < 5$). The calculated isotope compositions were converted to εZn notation using Eq. 1. For both the ECSN and the SNIa model, the previous publications (Woosley, 1997, Wanajo et al., 2013) provide multiple isotope abundance estimates, which

correspond to different assigned values for the ignition density. Thus, four trendlines were produced for the ECSN model, corresponding to the unchanged model, as well as the models in which the densities were multiplied by factors of ×1.3, ×2 and ×10 (Fig. A2.1). Likewise, four trendlines were calculated for the SNIa model, namely NCD4A, NCD6A, NCD7A, and NCD8A (Fig. A2.1). When isotope abundances were not given, they were assumed to be zero. The shaded areas in Figures 2.6 and 2.7 correspond to the areas delimited by the trendlines with the lowest and highest gradients, which thus encompass the remaining two trendlines.

Both the models for ECSN and for SNIa are fully compatible with the compositions of the meteorites for the $^{66}Zn/^{67}Zn$ and $^{64}Zn/^{67}Zn$ normalization schemes (Fig. 2.6). Furthermore, unlike the NFSEs models (Section 2.5.1.2), the nucleosynthetic models are also in line with the results obtained using the $^{64}Zn/^{68}Zn$ normalization. As such, while neither of these sources can be preferred over the other, they are both capable of producing the observed anomalies, which corroborates with a nucleosynthetic origin.

Since these sources have also been linked to nucleosynthetic anomalies of other elements, including Ca, Ti, and Cr (Dauphas et al., 2014, Qin et al., 2010), the same nucleosynthetic models that were employed for Zn were also used to generate hypothetical nucleosynthetic $^{50}Ti$ and $^{54}Cr$ isotope anomalies (Fig. 2.7). Subsequently, the slope of the expected correlations in plots of $\varepsilon^{70}Zn$ vs. $\varepsilon^{50}Ti$ and $\varepsilon^{70}Zn$ vs $\varepsilon^{54}Cr$ were determined from (Dauphas et al., 2014):

$$\varepsilon^{i/y}Zn_{x/y} = \frac{\rho_{Zn}^{i/y} - \rho_{Zn}^{x/y}\,\mu_{Zn}^{i/y}/\mu_{Zn}^{x/y}}{\rho_{E}^{j/b} - \rho_{E}^{a/b}\,\mu_{E}^{j/b}/\mu_{E}^{a/b}}\; c\,{}^{y}{}_{b}Zn_{E}\; \varepsilon^{j/b}E_{a/b}, \qquad \text{(Eq. 2.2)}$$

with

$$\rho_{E}^{p/q} = ({}^{p}E/{}^{q}E)_{star}/({}^{p}E/{}^{q}E)_{Sun} - 1 \qquad \text{(Eq. 2.3)}$$

where $({}^{p}E/{}^{q}E)$ denotes isotope ratios of the elements (E) Ti or Cr and Zn (when E = Zn) for either the modelled stellar source (star) or the Solar System (Sun);

$$\mu_{E}^{p/q} = \ln(m_{{}^{p}E}/m_{{}^{q}E}) \qquad \text{(Eq. 2.4)}$$

where $(m_{{}^{p}E}/m_{{}^{q}E})$ denote ratios of the exact atomic masses of Ti or Cr and Zn (when E = Zn);

$$c\,{}^{y}{}_{b}Zn_{E} = ({}^{y}Zn/{}^{b}E)_{star}/({}^{y}Zn/{}^{b}E)_{Sun} \qquad \text{(Eq. 2.5)}$$

where ( $^{y}$Zn/ $^{b}$E) is the ratio of a Zn to a Ti or Cr isotope for either the modelled stellar source (star) or the Solar System (Sun). The average Ti and Cr isotope anomalies observed for each meteorite group were calculated based on the available literature, as summarized in Table A2.1 (Qin et al., 2010, Trinquier et al., 2009, Zhang et al., 2012).

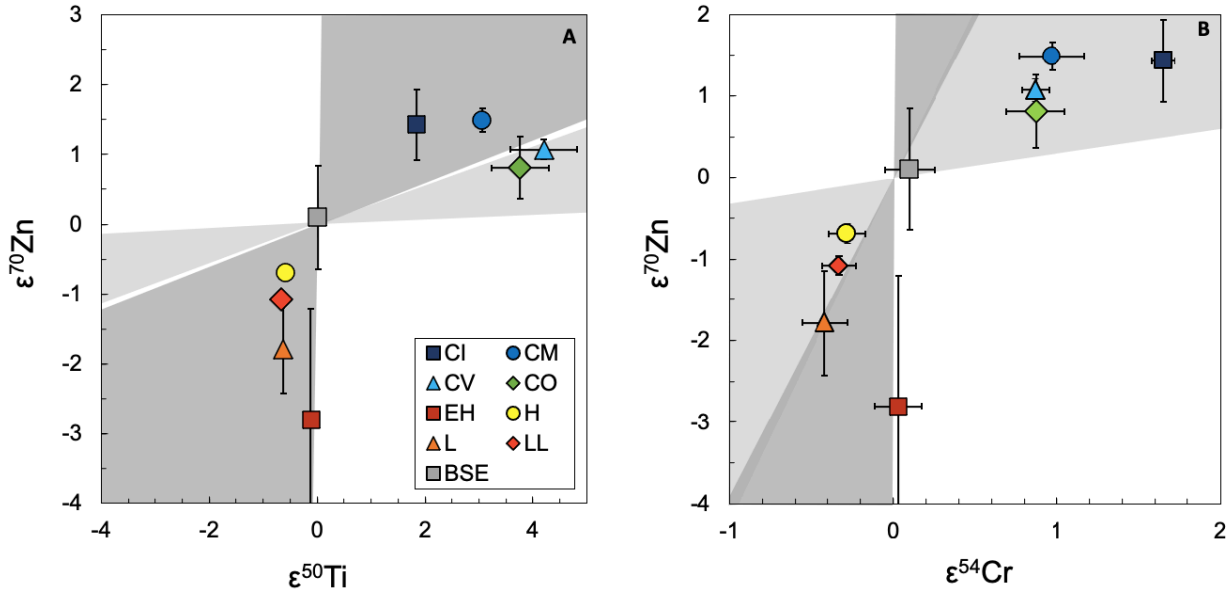



**Figure 2.7. Correlation between nucleosynthetic isotope anomalies of Zn and other Fe-peak elements.** (A) $\varepsilon^{70}$Zn versus $\varepsilon^{50}$Ti and (B) $\varepsilon^{70}$Zn versus $\varepsilon^{54}$Cr (Table A2.1) for CCs (CI, CM, CV, CO), ECs (EH) and OCs (H, L, LL); the BSE data give the mean result for the four BSE rocks. Predicted correlation between the anomalies for SNIa (light grey area) and ECSN (dark grey area) are also shown. Previous work has shown a dichotomy in the $\varepsilon^{50}$Ti and $\varepsilon^{54}$Cr data of carbonaceous versus non-carbonaceous meteorites (Qin et al., 2010, Trinquier et al., 2009). Whilst there is no clear correlation, the $\varepsilon^{70}$Zn data are in accord with this dichotomy. The combined results are also consistent with the modelled nucleosynthetic isotope anomalies, except for EHs which show no resolvable anomalies relative to the BSE for refractory elements, unlike for Zn. The $\varepsilon^{70}$Zn data for the meteorites and BSE rocks are from Table 2.6; the error bars show ±2se. The $\varepsilon^{50}$Ti and $\varepsilon^{54}$Cr data (and data sources) are in Table A2.1; error bars indicate ±2se.

Comparing $\varepsilon^{70}$Zn to anomalies in $^{50}$Ti and $^{54}$Cr (Fig. 2.7, Table A2.1) confirms the dichotomy in compositions between CC and NC meteorites. However, most of our meteorite data do not follow the isotopic trends predicted by combining nucleosynthetic production models of the different elements. It is nevertheless plausible for the $\varepsilon^{70}$Zn and $^{48}$Ca, $^{50}$Ti, $^{54}$Cr enrichments to be produced in the same nucleosynthesis sites, because the differing trends could be produced by the different physical and chemical properties of the elements. For example, moderately volatile Zn has a much lower 50% condensation temperature ($T_{C50}$ = 726 K) than Ca, Ti and Cr ($T_{C50}$ ≈ 1290 to 1570 K; Wood et al., 2019), so condensation

of isotopically distinct Zn from SNIa and/or ECSN into presolar dust grains was likely less efficient than for the more refractory elements (Ek et al., 2020, Marhas and Sharda, 2018). Zinc also has more affinity for sulphide than Ca, Ti and Cr (Christy, 2018) so isotopically anomalous Zn could have been concentrated into distinct mineral phases, which may have been lost during subsequent thermal processing (Trinquier et al., 2009). While the presolar carrier phases of the Zn anomalies are unknown, in CCs, Zn is predominantly hosted in the fine-grained meteorite matrix, with Zn elemental abundances that exceed those in chondrules (quenched silicate spherules) by factors of 3 to 6 (Bland et al., 2005, Pringle et al., 2017, Hellmann et al., 2020). Additionally, leaching studies have shown that Zn in chondrites is primarily (>80%) hosted in sulphides and silicates (Pringle et al., 2017, Luck et al., 2005).

Whilst the nucleosynthetic isotope anomalies of more refractory metals display significant isotopic diversity within the CC and NC reservoirs (Burkhardt et al., 2021), the Zn isotope data are much less variable. The mean Zn isotope compositions of all CC groups we measured overlap within their uncertainties. We hence performed analysis of variance (ANOVA) tests and found the groups are statistically indistinguishable (Table A2.2). Likewise, the $\varepsilon^{64}$Zn values of the ECs, OCs and IABs all overlap within error (Fig. 2.2, Table 2.6), with ANOVA tests indicating the groups are statistically indistinguishable.

### 2.5.2. Origin of Earth's Zn

#### 2.5.2.1. Zn mass balance

The complementary Zn isotope anomalies of CCs and NC meteorites indicate a mixed source for Zn in the BSE. The contributions of each reservoir to Earth's Zn inventory can be estimated by mass balance:

$$\varepsilon^{64}Zn_{BE} = x_{CC}^{Zn} \cdot \varepsilon^{64}Zn_{CC} + x_{NCC}^{Zn} \cdot \varepsilon^{64}Zn_{NCC} \quad \text{(Eq. 2.10)}$$

where $x^{Zn}$ is the Zn fraction derived from each reservoir, and $x_{CC}^{Zn} + x_{NCC}^{Zn} \equiv 1$. Because Zn did not partition strongly into metal during Earth's core formation (Table A2.3), the nucleosynthetic Zn isotope composition of the BSE was built up throughout Earth's accretion history (Mahan et al., 2018). It is therefore assumed that the BSE and bulk Earth (BE) have identical Zn isotope compositions, which is constrained by the composition of the London Zn terrestrial standard ($\varepsilon^{64}Zn = 0$) and by the uncertainty corresponding to the long-term reproducibility of four BSE rocks (±0.17, Table 2.6). Chondrites are often assumed to be the building blocks of planets, because they (mostly) preserve their original elemental and isotopic compositions and can account for most of the Solar System's isotopic diversity (Dauphas, 2017, Lodders, 2000). The overall mean values of CCs ($\varepsilon^{64}Zn = -0.81 \pm 0.16$, n=7, where n is the number of meteorites) and ECs and OCs (non-carbonaceous chondrites, NCCs; $\varepsilon^{64}Zn = 0.76 \pm 0.22$, n=9) are therefore taken as representative of the CC and NC material accreted by Earth (Table 2.6).

Assuming these parameters, a Monte Carlo simulation with 10,000 trials was performed, in which the $\varepsilon^{64}Zn$ compositions of the CC and NCC endmembers were allowed to vary within ±2se of their respective mean values, and the fractions of Zn from each source ranged between 0 and 1. Only the results that yielded BE-like compositions were taken as successful. The results of this model suggest that, to reproduce the BE Zn isotope composition, 48±15% (2sd) of Earth's Zn was derived from the CC reservoir, and the remainder from NCCs (Fig. 2.8). In other words, CCs and NCCs contributed about equally to Earth's Zn.

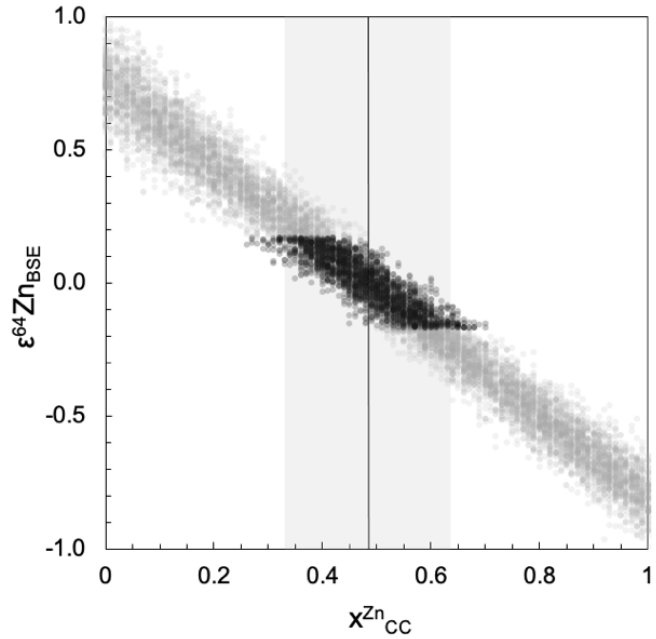



**Figure 2.8. Inferred CC contribution to the bulk Earth Zn inventory from Monte Carlo simulations.** The diagram plots the $\varepsilon^{64}Zn_{BE}$ values versus the Zn fractions derived from the CC reservoir ($x_{CC}^{Zn}$) as obtained from 10,000 mass balance simulations. Shown in black are trials that recovered the BE Zn isotope composition of $\varepsilon^{64}Zn_{BE} = 0.00 \pm 0.17$. The vertical line and grey shaded region represent the mean and 2sd of all successful trials ($x_{CC}^{Zn} = 0.48 \pm 0.15$).

To test whether the outcome of the modelling is affected by the selection of meteorites or by the isotope ratio used in the calculations, seventeen additional models were performed, employing different meteorite endmembers and one of three isotope ratios ($^{64}Zn$, $\varepsilon^{70}Zn$ and $\varepsilon^{66/67}Zn_{64/67}$). Three CC and four NC endmembers including between one and five meteorite groups were tested, and their compositions were defined as the mean of their groups (Table A2.2).

The mixing between these endmembers was modelled using the same approach described above, but now for 1,000 trials each. The endmember compositions were assigned by randomly generating numbers within ±2se of their means (Table A2.2). Similarly, a random number between 0 and 1 was attributed to $x_{CC}^{Zn}$, and $x_{NC}^{Zn} = (1 - x_{CC}^{Zn})$. Again, Earth's composition is defined by the London Zn reference material ($\varepsilon^{i}Zn_{BE} = 0$) and the uncertainty that is associated with the long-term reproducibility of the procedure, as characterized by analyses the four BSE samples (±0.17, ±0.74, and ±0.10 for $\varepsilon^{64}Zn$, $\varepsilon^{70}Zn$ and $\varepsilon^{66/67}Zn_{64/67}$, respectively; Table 2.6). Only simulations that produced an $\varepsilon^{i}Zn_{BE}$ within these intervals (uncertainties) were considered successful.

The average $x_{CC}^{Zn}$ values obtained from all simulations are identical within uncertainty (Table 2.7), with an overall mean of $x_{CC}^{Zn} \approx 0.52$. Although providing lower precision, the models that employed $\varepsilon^{70}Zn$ or $\varepsilon^{66/67}Zn_{64/67}$ corroborate the results of models that employ the preferred isotope ratio, $\varepsilon^{64}Zn$. The results also demonstrate that the selection of meteorite groups has negligible impact on the outcome of the modelling. Additional modelling was carried out for the most extreme scenarios, such as one that employs only CM and H chondrites, which represent the least and most Earth-like groups within the CC and NC reservoirs, respectively. The fraction of CC-derived Zn that is needed to reproduce Earth's Zn isotope composition in this case are $0.31 \pm 0.15$, $0.33 \pm 0.37$, and $0.31 \pm 0.24$ for $\varepsilon^{64}Zn$, $\varepsilon^{70}Zn$ and $\varepsilon^{66/67}Zn_{64/67}$, respectively, which still overlap, within the uncertainties, with the preferred estimate of $0.48 \pm 0.15$. Similarly, if the most and least Earth-like CC and NC groups are used (CO and EH chondrites), the modelling yields $x_{CC}^{Zn}$ values of $0.61 \pm 0.17$, $0.72 \pm 0.34$, and $0.61 \pm 0.24$ using $\varepsilon^{64}Zn$, $\varepsilon^{70}Zn$ and $\varepsilon^{66/67}Zn_{64/67}$, respectively. Again, these results are compatible with the preferred $x_{CC}^{Zn}$ estimate. Altogether, the models indicate that, to reproduce the Earth's Zn isotope composition, considerable Zn contributions from both the carbonaceous and the NC reservoir are required.

Furthermore, ANOVA tests were carried out to compare the Zn isotope compositions of individual meteorites within a given endmember (or 'meteorite grouping'; Table A2.2). These analyses showed no significant isotopic differences within the different groupings, with p-values that exceed the critical value for all three isotope ratios, even when all available CCs and NCs are included (Table A2.2). In contrast, ANOVA tests comparing CCs with the NC meteorites (EC-OC-IAB) return p-values of $3\times10^{-4}$, $4\times10^{-4}$, and $2\times10^{-21}$ for $\varepsilon^{64}Zn$, $\varepsilon^{70}Zn$ and $\varepsilon^{66/67}Zn_{64/67}$, respectively. The ANOVA analyses therefore show that the Zn isotope compositions of meteorites within the same CC or NC grouping are statistically indistinguishable, whilst typical CC and NC isotope compositions are statistically distinct from one another.

The limited variance in Zn isotope compositions within each reservoir contrasts with the diversity that is observed for other isotope systems. In particular, ECs and OCs have distinct nucleosynthetic Ti, Cr, Zr, Mo, and Ru isotope compositions (Burkhardt et al., 2021), whilst the Mo and Ru isotope compositions of IAB complex irons are different from ECs and OCs (Burkhardt et al., 2021). The same is true for CCs, which display large isotopic differences for some refractory element isotope systems (i.e., $\varepsilon^{94}Mo_{CI} = 0.79 \pm 0.41$ and $\varepsilon^{94}Mo_{CM} =$

4.82 ± 0.20; Burkhardt et al., 2021). This could arise from a more homogeneous distribution of anomalous Zn within each reservoir than in the material that is responsible for the isotope anomalies of more refractory elements.

**Table 2.7. Estimates for the fraction of Zn derived from CC material, $x_{CC}^{Zn}$, from mass balance models.** Results are from Monte Carlo simulations that employ different combinations of CC and NC endmembers and one of three selected isotope ratios. All results are indistinguishable within uncertainties, suggesting that the selection of endmembers or isotope ratio does not substantially impact the outcome of the models.

| | $\varepsilon^{64}Zn$ | | $\varepsilon^{70}Zn$ | | $\varepsilon^{66/67}Zn_{64/67}$ | |
|---|---|---|---|---|---|---|
| **Endmembers** | $x^{Zn}_{CC}$ | 2sd | $x^{Zn}_{CC}$ | 2sd | $x^{Zn}_{CC}$ | 2sd |
| CI-CM-CO-CV + EC-OC-IAB | 0.48 | 0.15 | 0.57 | 0.33 | 0.49 | 0.25 |
| CI-CM-CO-CV + EC-OC | 0.48 | 0.15 | 0.53 | 0.35 | 0.48 | 0.25 |
| CI-CM + OC | 0.46 | 0.18 | 0.45 | 0.33 | 0.45 | 0.28 |
| CI-CM + EC | 0.52 | 0.14 | 0.63 | 0.29 | 0.53 | 0.23 |
| CO-CV + OC | 0.53 | 0.12 | 0.55 | 0.40 | 0.48 | 0.28 |
| CO-CV + EC | 0.48 | 0.18 | 0.69 | $^{+0.31}_{-0.33}$ | 0.56 | 0.22 |

### 2.5.2.2. CC mass contribution

Next, a similar approach was used to estimate the mass fraction of CC material accreted by the Earth ($x_{CC}$). In this case, two equations were employed:

$$\varepsilon^{i}Zn_{BE} = \frac{x_{CC} \cdot [Zn]_{CC} \cdot \varepsilon^{i}Zn_{CC} + x_{NC} \cdot [Zn]_{NC} \cdot \varepsilon^{i}Zn_{NC}}{x_{CC} \cdot [Zn]_{CC} + x_{NC} \cdot [Zn]_{NC}} \quad \text{(Eq. 2.8)}$$

and

$$[Zn]_{BE} = x_{CC} \cdot [Zn]_{CC} + x_{NC} \cdot [Zn]_{NC} \quad \text{(Eq. 2.9)}$$

The modelling then employed the same endmember meteorite group combinations and isotope ratios as were used in conjunction with Eq. 2.7 above (Table A2.2). The Zn concentration of the CC endmember was randomly assigned between 115 μg $g^{-1}$ and 320 μg $g^{-1}$, which correspond to the average compiled Zn abundances of the CO-CV and CI groups, respectively (Table A2.3; the CM group has an intermediate Zn concentration). Although the Zn elemental abundance of the BSE is well defined (54 ± 2 μg $g^{-1}$, Table A2.3), $[Zn]_{BE}$ is less well constrained at 40 to 70 μg $g^{-1}$, because the extent of Zn partitioning into Earth's core is uncertain (Table A2.3). Hence, the same procedure was adopted for $[Zn]_{BE}$, which was allowed to range from 40 μg $g^{-1}$ to 70 μg $g^{-1}$. The Zn elemental abundances of ECs and OCs span a

much wider range (7.5 to 519 μg $g^{-1}$, Table A2.3), so we treat $[Zn]_{NCC}$ as a free parameter. As above, only simulations that reproduced the BE Zn isotope composition (within uncertainty) were considered. The resulting $x_{CC}$ averages are all identical within uncertainty (Table 2.8), with an overall mean of $x_{CC} \approx 0.14$ for all eighteen simulations.

In summary, the results of all eighteen models are consistent, regardless of which Zn isotope ratio is employed or which meteorite groups are used as endmembers. This was further verified by an ANOVA test, which compared the $x_{CC}^{Zn}$ and $x_{CC}$ results obtained for the six different endmember combinations (Tables 2.7, 2.8). This test yielded p-values of 0.25 and 0.34 for $x_{CC}^{Zn}$ and $x_{CC}$, respectively, which both exceed the critical value of $p_{crit} = 0.05$, indicating no evidence for statistically significant differences.

**Table 2.8. Estimates for the mass fraction of CC material accreted by the Earth, $x_{CC}$, from mass balance models.** Same as Table 2.7, but for the total mass fraction of CC material accreted by Earth, rather than the Zn mass fraction.

| | $\varepsilon^{64}Zn$ | | $\varepsilon^{70}Zn$ | | $\varepsilon^{66/67}Zn_{64/67}$ | |
|---|---|---|---|---|---|---|
| **Endmembers** | $x_{CC}$ | 2sd | $x_{CC}$ | 2sd | $x_{CC}$ | 2sd |
| CI-CM-CO-CV + EC-OC-IAB | 0.13 | 0.10 | 0.15 | 0.14 | 0.14 | 0.16 |
| CI-CM-CO-CV + EC-OC | 0.13 | 0.10 | 0.14 | 0.14 | 0.13 | 0.12 |
| CI-CM + OC | 0.13 | 0.10 | 0.13 | 0.13 | 0.13 | 0.12 |
| CI-CM + EC | 0.14 | 0.11 | 0.18 | 0.15 | 0.15 | 0.12 |
| CO-CV + OC | 0.15 | 0.11 | 0.15 | 0.16 | 0.16 | 0.19 |
| CO-CV + EC | 0.13 | 0.10 | 0.19 | 0.16 | 0.13 | 0.13 |

For the preferred model (CI-CM-CO-CV + EC-OC, $\varepsilon^{64}Zn$), we find that 13±10% (2sd) of Earth's mass is derived from CC material (Fig. 2.9). At the lower end of this range (at $x_{CC} \approx$ 3-5%) Earth must have incorporated CI-like material, while larger $x_{CC}$ mass fractions require that more volatile depleted CCs were accreted (Fig. 2.9). The successful simulations were also used to estimate the Zn concentration of the NC endmember, which yields a mean of 33 ± 15 μg $g^{-1}$ for our preferred model, and identical results within uncertainty for all other models.

### 2.5.2.3. Estimates from refractory element nucleosynthetic anomalies

The Zn based results for the CC mass contribution can be compared to previous studies that applied refractory element and O isotope compositions to evaluate the origin of Earth's accreted material (Fig. 2.9). A CC mass fraction of 42% CI material has been proposed (Schiller

et al., 2018), based on differences in $\varepsilon^{48}Ca$ between the BSE and other inner Solar System bodies. For such a high CC fraction to be consistent with our Zn results, the BE Zn elemental abundance would need to be ~280 μg $g^{-1}$ to produce $\varepsilon Zn_{BE} \approx 0$, which by far exceeds most estimates for the BE Zn abundance (40-70 μg $g^{-1}$, Table A2.3). In contrast, another study (Dauphas, 2017) inferred a much smaller CC contribution of 5% CO-CV material, based on an inversion of refractory element and O isotope compositions. In that case, the Zn contribution from the CO-CV component is too small to be compatible with the Zn isotope mass balance, requiring the BE to have only ~12 μg $g^{-1}$ Zn, which is implausibly low.

Studies based on O isotope compositions proposed that Earth accreted from a mix of ECs and OCs with addition of 4% CI plus 5% CV material (Lodders, 2000), or 10% CM-like material (Albarède, 2009); which are near the maximum probability value for the preferred Zn model (~11%, Fig, 2.9). Another proposal is that Earth formed primarily from NC material, composed of OCs and angrites (NC achondritic meteorites), with addition of 3-21% CI and 8-11% CV material (Fitoussi et al., 2016). Whilst this estimate is largely in accord with the Zn isotope mass balance (Fig. 2.9), and the current sample set does not indicate any significant variability within the NC reservoir, the lack of Zn isotope data for angrite meteorites precludes any firm conclusions about the suitability of this scenario.

It is difficult to explain the BSE Mo isotope composition using combinations of meteoritic materials (Burkhardt et al., 2021). One possibility is an additional NC component that has not been identified in measured meteorites, which would need to be enriched in both s-process isotopes and neutron-rich nuclei of Fe-peak elements; if such a reservoir exists, it implies the accretion of ~4% CC material (Burkhardt et al., 2021). This scenario can be reconciled with our Zn isotope data if Earth accreted CI-like matter, but it conflicts with O isotope constraints (Albarède et al., 2013, Lodders, 2000). If the unidentified component is instead carbonaceous (Budde et al., 2019), the mass balance would allow for a larger CC contribution that is more consistent with our Zn isotope data. In the latter scenario, 30-60% of the BSE Mo budget would be derived from the carbonaceous reservoir (Budde et al., 2019). This can be reconciled with our Zn isotope constraints because Mo is more siderophile than Zn, so the BSE Mo isotope composition reflects only the final 10-20% of accretion, implying a minimum Mo-based $x_{CC}$ of 3-12%. Therefore, a ~10% CC contribution composed of CMs or a mixture of CI, CM and CO-CV chondrites can be reconciled with refractory element nucleosynthetic isotope anomalies (Budde et al., 2019, Fitoussi et al., 2016), O isotope constraints (Albarède et al., 2013, Lodders, 2000) and the present results (Fig. 2.9).

Notably, the Zn mass balance calculations assume that the CC material and Earth did not experience Zn loss before or during accretion, and based on this the results suggest that the NC material was, on average, depleted in Zn relative to CCs. While some NC meteorites have high Zn elemental abundances (>300 µg $g^{-1}$; Table A2.3), an accretion scenario with a volatile-rich NC component and volatile-depleted CC material can only be accommodated in the Zn mass balance if $x_{CC}$ is large. However, that is difficult to reconcile with refractory element isotope compositions, which largely suggest a small contribution from CCs. Substantial loss of Zn from accreting planets or the accreting material would introduce mass-dependent isotope fractionation, leaving residual bodies enriched in heavy isotopes of volatile elements, as measured for Zn and K in lunar rocks (Sossi et al., 2018, Tian et al., 2021). A similar signature is not observed for the BSE, indicating that Earth's volatile depletion arose from processes in the protoplanetary disk rather than subsequent evaporation during accretion (Sossi et al., 2018, Tian et al., 2021).

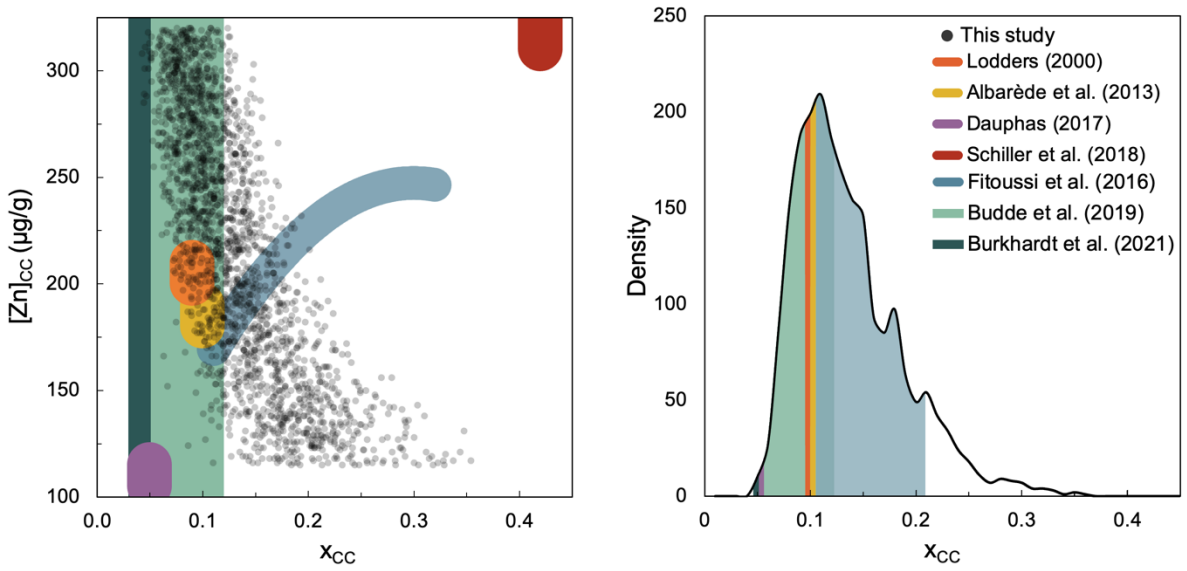



**Figure 2.9. Estimates for the mass fractions of accreted CC material ($x_{cc}$).** (A) Estimates are plotted against corresponding Zn elemental abundances. Black dots show results from our Monte Carlo simulations and colored regions indicate $x_{CC}$ estimates from previous studies in orange Lodders (2000), yellow (Albarède et al., 2013), light blue (Fitoussi et al., 2016), purple (Dauphas, 2017), red (Schiller et al., 2018), light green (Budde et al., 2019), and dark green (Burkhardt et al., 2021). (B) Probability density curve (black) for the estimated $x_{CC}$ from our Monte Carlo simulations. Estimates from previous studies are also shown in the same colors as in panel (A). Our simulations have the highest density at $x_{CC} \approx 11\%$, equivalent to mean $[Zn]_{CC}$ concentrations of about 150-320 µg $g^{-1}$. Considering additional constraints from literature studies that derived similar $x_{CC}$ estimates (Budde et al., 2019b, Fitoussi et al., 2016, Albarède et al., 2013, Lodders, 2000), the mean $[Zn]_{CC}$ elemental abundance is limited to about 170-220 µg $g^{-1}$, compatible with CM chondrites (Table A2.3).

If the volatile elements in the BSE are representative of the accreting material, our results also constrain the mean Zn abundance of the NC material added to Earth. If about half of Earth's Zn, with $[Zn]_{BE}$ = 40 to 70 μg $g^{-1}$, was provided by NC bodies with a combined mass of 77% to 97% of Earth, this implies a Zn abundance of 18 to 48 μg g-1 in the NC material. That is consistent with measured ranges for ECs (7.5 to 519 μg $g^{-1}$) and OCs (14 to 158 μg $g^{-1}$; Table A2.3). Elements with condensation temperatures similar to Zn (500 K< $T_{C50}$ <750 K) are depleted by the same factor in CCs, with a similar trend also observed for the BSE (Braukmüller et al., 2019). Because our Zn isotope data indicate that about half of Earth's Zn inventory was derived from the addition of ~11% carbonaceous material, it is likely that this material also made substantial contributions to Earth's budgets of other moderately and highly volatile elements.

## 2.6 Conclusions

Meteorites from a range of groups are characterized by mass-independent Zn isotope compositions that are distinct from the BSE. CC and NC meteorites display complementary compositions, with CCs being depleted in $^{64}Zn$ and enriched in $^{68}Zn$ and $^{70}Zn$, and NCs showing opposing patterns. These features are difficult to reconcile with either mass-dependent or mass-independent fractionation. They are, however, fully compatible with theoretical nucleosynthetic isotope anomalies produced by ECSN or SNIa, suggesting that the results reflect a nucleosynthetic origin.

These results can, hence, be used to constrain the origin of Earth's Zn inventory by modelling mixes between different meteorite groups. Extensive modelling employing different isotope ratios and meteorite combinations yielded consistent results, with Earth's mass-independent Zn isotope composition being successfully reproduced by mixing nearly equal amounts of Zn derived from the CC and NC reservoirs. When combined with Zn concentrations, these results can also constrain the mass of CC material that must be added to an NC-like proto-Earth to reproduce its estimated Zn content. These models produced a preferred value of 13±10% (2sd) of Earth's mass being derived from CCs, with maximum probability at ~11%, which can be reconciled with independent estimates derived from oxygen and refractory element nucleosynthetic isotope compositions.

## 2.7 References


AKRAM, W., SCHÖNBÄCHLER, M., BISTERZO, S. & GALLINO, R. 2015. Zirconium isotope evidence for the heterogeneous distribution of s-process materials in the Solar System. *Geochimica et Cosmochimica Acta,* 165**,** 484-500.

ALBARÈDE, F. 2009. Volatile accretion history of the terrestrial planets and dynamic implications. *Nature,* 461**,** 1227-1233.

ALBARÈDE, F., BALLHAUS, C., BLICHERT-TOFT, J., LEE, C.-T., MARTY, B., MOYNIER, F. & YIN, Q.-Z. 2013. Asteroidal impacts and the origin of terrestrial and lunar volatiles. *Icarus,* 222**,** 44–52.

ALLÈGRE, C., MANHÈS, G. & LEWIN, É. 2001. Chemical composition of the Earth and the volatility control on planetary genetics. *Earth and Planetary Science Letters,* 185**,** 49-69.

ANDERS, E. & GREVESSE, N. 1989. Abundances of the elements: Meteoritic and solar. *Geochimica et Cosmochimica Acta,* 53**,** 197-214.

ANGELI, I. & MARINOVA, K. P. 2013. Table of experimental nuclear ground state charge radii: An update. *Atomic Data and Nuclear Data Tables,* 99**,** 69-95.

BARRAT, J. A., ZANDA, B., MOYNIER, F., BOLLINGER, C., LIORZOU, C. & BAYON, G. 2012. Geochemistry of CI chondrites: major and trace elements, and Cu and Zn isotopes. *Geochimica et Cosmochimica Acta,* 83**,** 79-92.

BERGLUND, M. & WIESER, M. E. 2011. Isotopic compositions of the elements 2009 (IUPAC Technical Report). *Pure and Applied Chemistry,* 83**,** 397-410.

BISTERZO, S., GALLINO, R., STRANIERO, O., CRISTALLO, S. & KAPPELER, F. 2011. The s-process in low-metallicity stars - II. Interpretation of high-resolution spectroscopic observations with asymptotic giant branch models. *Monthly Notices of the Royal Astronomical Society,* 418**,** 284-319.

BLAND, P. A., ALARD, O., BENEDIX, G. K., KEARSLEY, A. T., MENZIES, O. N., WATT, L. E. & ROGERS, N. W. 2005. Volatile fractionation in the early Solar System and chondrule/matrix complementarity. *Proceedings of the National Academy of Sciences,* 102**,** 13755-13760.

BRAUKMÜLLER, N., WOMBACHER, F., HEZEL, D. C., ESCOUBE, R., MUNKER, C. 2018. The chemical composition of carbonaceous chondrites: Implications for volatile element depletion, complementarity and alteration. *Geochimica et Cosmochimica Acta,* 239, 17-48.

BRAUKMÜLLER, N., WOMBACHER, F., FUNK, C. & MUNKER, C. 2019. Earth's volatile element depletion pattern inherited from a carbonaceous chondrite-like source. *Nature Geoscience,* 12**,** 564-568.

BRIDGESTOCK, L. J., WILLIAMS, H., REHKÄMPER, M., LARNER, F., GISCARD, M. D., HAMMOND, S., ANDREASEN, R., COLES, B., BENEDIX, G. K., WOOD, B. J., THEIS, K. J., SCHÖNBÄCHLER, M. & SMITH, C. 2014. Unlocking the zinc isotope systematics of iron meteorites. *Earth and Planetary Sciences Letters,* 400**,** 153–164.

BUDDE, G., BURKHARDT, C. & KLEINE, T. 2019. Molybdenum isotopic evidence for the late accretion of outer Solar System material to Earth. *Nature Astronomy,* 3**,** 736-741.

BURKHARDT, C., SPITZER, F., MORBIDELLI, A., BUDDE, G., RENDER, J. H., KRUIJER, T. S. & KLEINE, T. 2021. Terrestrial planet formation from lost inner Solar System material. *Science Advances,* 7**,** eabj7601.

CHRISTY, A. G. 2018. Quantifying lithophilicity, chalcophilicity and siderophilicity. *European Journal of Mineralogy***,** 193–204.

CLAYTON, D. 2003. Handbook of Isotopes in the Cosmos, Cambridge: Cambridge University Press.

CREECH, J. B. & MOYNIER, F. 2019. Tin and zinc stable isotope characterisation of chondrites and implications for early Solar System evolution. *Chemical Geology,* 511**,** 81-90.

CROCKET, K. 2009. *Pb and Nd isotope constraints on continental weathering and ocean circulation in the North Atlantic during the last glacial/interglacial cycle.* PhD Thesis, University of Bristol.

DAUPHAS, N. 2017. The isotopic nature of the Earth's accreting material through time. *Nature,* 541**,** 521-524.

DAUPHAS, N., CHEN, J. H., ZHANG, J., PAPANASTASSIOU, D. A., DAVIS, A. M. & TRAVAGLIO, C. 2014. Calcium-48 isotopic anomalies in bulk chondrites and achondrites: Evidence for a uniform isotopic reservoir in the inner protoplanetary disk. *Earth and Planetary Sciences Letters,* 407**,** 96-108.

DAUPHAS, N. & SCHAUBLE, E. A. 2016. Mass Fractionation Laws, Mass-Independent Effects, and Isotopic Anomalies. *Annual Review of Earth and Planetary Sciences,* 44**,** 709-783.

EK, M., HUNT, A. C., LUGARO, M. & SCHONBACHLER, M. 2020. The origin of s-process isotope heterogeneity in the solar protoplanetary disk. *Nature Astronomy,* 4**,** 273-281.

FISCHER-GÖDDE, M., BURKHARDT, C., KRUIJER, T. S. & KLEINE, T. 2015. Ru isotope heterogeneity in the solar protoplanetary disk. *Geochimica et Cosmochimica Acta,* 168**,** 151-171.

FITOUSSI, C., BOURDON, B. & WANG, X. Y. 2016. The building blocks of Earth and Mars: A close genetic link. *Earth and Planetary Science Letters,* 434**,** 151-160.

FUJII, T., HIRATA, T., SHIBAHARA, Y. & NISHIZAWA, K. 2001. Mass-dependent and mass-independent isotope effects of zinc in chemical exchange reactions using liquid chromatography with a cryptand stationary phase. *Physical Chemistry Chemical Physics,* 3**,** 3125-3129.

FUJII, T., MOYNIER, F. & ALBARÈDE, F. 2006a. Nuclear field vs. nucleosynthetic effetcs as cause of isotopic anomalies in the early Solar System. *Earth and Planetary Sciences Letters,* 247**,** 1-9.

FUJII, T., MOYNIER, F., TELOUK, P. & ALBAREDE, F. 2006b. Mass-Independent Isotope Fractionation of Molybdenum and Ruthenium and the Origin of Isotopic Anomalies in Murchison. *The Astrophysical Journal,* 647**,** 1506-1516.

HELLMANN, J. L., HOPP, T., BURKHARDT, C. & KLEINE, T. 2020. Origin of volatile element depletion among carbonaceous chondrites. *Earth and Planetary Science Letters,* 549**,** 116508.

HUANG, J., CHEN, S., ZHANG, X.-C. & HUANG, F. 2018. Effects of Melt Percolation on Zn Isotope Heterogeneity in the Mantle: Constraints From Peridotite Massifs in Ivrea-Verbano Zone, Italian Alps. *Journal of Geophysical Research: Solid Earth,* 123**,** 2706-2722.

KALLEMEYN, G. W. & WASSON, J. T. 1986. Composition of enstatite (EH3, EH4,5) and EL6) chondrites: Implications regarding their formation. *Geochimica et Cosmochimica Acta,* 50**,** 2153-2164.

KUTHNING, S. 2021. Investigation of mass-independent isotope effects of Zn and Cd in meteorites. PhD Thesis, Imperial College London

KONG, P., MORI, T. & EBIHARA, M. 1997. Compositional continuity of enstatite chondrites and implications for heterogeneous accretion of the enstatite chondrite parent body. *Geochimica et Cosmochimica Acta,* 61**,** 4895-4914.

KRUIJER, T. S., BURKHARDT, C., BUDDE, G. & KLEINE, T. 2017. Age of Jupiter inferred from the distinct genetics and formation times of meteorites. *Proceedings of the National Academy of Sciences,* 114**,** 6712-6716.

LAUL, J. C., KEAYS, R. R., GANAPATHY, R., ANDERS, E. & MORGAN, J. W. 1972. Chemical fractionations in meteorites–V. Volatile and siderophile elements in achondrites and ocean ridge basalts. *Geochimica et Cosmochimica Acta,* 36**,** 329-345.

LODDERS, K. 1998. The planetary scientist's companion*.* New York, Oxford University Press.

LODDERS, K. 2000. An Oxygen Isotope Mixing Model for the Accretion and Composition of Rocky Planets. *Space Science Reviews,* 92**,** 341-354.

LODDERS, K. 2003. Solar System abundances and condensation temperatures of the elements. *The Astrophysycal Journal,* 591**,** 1220-1247.

LUCK, J.-M., BEN OTHMAN, D. & ALBARÈDE, F. 2005. Zn and Cu isotopic variations in chondrites and iron meteorites: Early solar nebula reservoirs and parent-body processes. *Geochimica et Cosmochimica Acta,* 69**,** 5351-5363.

MAHAN, B., SIEBERT, J., BLANCHARD, I., BORENSZTAJN, S., BADRO, J. & MOYNIER, F. 2018. Constraining compositional proxies for Earth's accretion and core formation through high pressure and high temperature Zn and S metal-silicate partitioning. *Geochimica Et Cosmochimica Acta,* 235**,** 21-40.

MARHAS, K. K. & SHARDA, P. 2018. Transition Elements in Supernova Presolar Grains: Condensation versus Implantation. *The Astrophysical Journal*.

MCDONOUGH, W. F. & SUN, S.-S. 1995. The composition of the Earth. *Chemical Geology,* 120**,** 223-253.

MCDONOUGH, W. F. Compositional Model for the Earth's Core in Treatise in Geochemistry Vol. 3. 2nd Edition. Oxford: Elsevier.

MOORE, R. E. T., LARNER, F., COLES, B. J. & REHKÄMPER, M. 2017. High precision zinc stable isotope measurement of certified biological reference materials using the double spike technique and multiple collector-ICP-MS. *Analytical and Bioanalytical Chemistry,* 409**,** 2941–295.

MOYNIER, F., DAUPHAS, N. & PODOSEK, F. A. 2009a. A search for $^{70}$Zn anomalies in meteorites. *The Astrophysycal Journal,* 700**,** L92-L95.

MOYNIER, F., FUJII, T. & ALBARÈDE, F. 2009b. Nuclear field shift effect as a possible cause of Te isotopic anomalies in the early Solar System-An alternative explanation of Fehr et al. (2006 and 2009). *Meteoritics & Planetary Science,* 44**,** 1735-1742.

MOYNIER, F., PANIELLO, R. C., GOUNELLE, M., ALBARÈDE, F., BECK, P., PODOSEK, F. & ZANDA, B. 2011. Nature of volatile depletion and genetic relationships in enstatite chondrites and aubrites inferred from Zn isotopes. *Geochimica et Cosmochimica Acta,* 75**,** 297-307.

MOYNIER, F., VANCE, D., FUJII, T. & SAVAGE, P. 2017. The Isotope Geochemistry of Zinc and Copper. *Reviews in Mineralogy and Geochemistry***,** 543-600.

O'NEILL, H. S. C. 1991. The origin of the Moon and the early history of the Earth – A chemical model. Part 2: The Earth. *Geochimica Et Cosmochimica Acta,* 55**,** 1159-1172.

PALK, C., ANDREASEN, R., REHKÄMPER, M., STUNT, A., KREISSIG, K., COLES, B., SCHÖNBÄCHLER, M. & SMITH, C. 2018. Variable Tl, Pb, and Cd concentrations and isotope compositions of enstatite and ordinary chondrites—Evidence for volatile element mobilization and decay of extinct 205Pb. *Meteoritics & Planetary Science,* 53**,** 167-186.

PALME, H., O'Neill, S. C. 2014. *Cosmochemical Estimates of Mantle Composition* in *Treatise on Geochemistry Vol.3,* 2nd Edition. Oxford: Elsvier.

PANIELLO, R. C. 2013. Volitization of Extraterrestrial Materials as Determined by Zinc Isotopic Analysis. PhD Thesis, Washington University in Saint Louis.

PEPLOWSKI, P. N., EVANS, L. G., HAUCK, S. A., 2ND, MCCOY, T. J., BOYNTON, W. V., GILLIS-DAVIS, J. J., EBEL, D. S., GOLDSTEN, J. O., HAMARA, D. K., LAWRENCE, D. J., MCNUTT, R. L., JR., NITTLER, L. R., SOLOMON, S. C., RHODES, E. A., SPRAGUE, A. L., STARR, R. D. & STOCKSTILL-CAHILL, K. R. 2011. Radioactive elements on Mercury's surface from MESSENGER: implications for the planet's formation and evolution. *Science,* 333**,** 1850-2.

PIANI, L., MARROCCHI, Y., RIGAUDIER, T., VACHER, L. G., THOMASSIN, D. & MARTY, B. 2020. Earth's water may have been inherited from material similar to enstatite chondrite meteorites. *Science,* 369**,** 1110-1113.

PICKARD, H., PALK, E., SCHÖNBÄCHLER, M., MOORE, R. E. T., COLES, B. J., KREISSIG, K., NILSSON-KERR, K., HAMMOND, S. J., TAKAZAWA, E., HÉMOND, C., TROPPER, P., BARFOD, D. N. & REHKÄMPER, M. 2022. The cadmium and zinc isotope compositions of the silicate Earth – Implications for terrestrial volatile accretion. *Geochimica et Cosmochimica Acta,* 338**,** 165-180.

PIGNATARI, M., GALLINO, R., HEIL, M., WIESCHER, M., KAPPELER, F., HERWIG, F. & BISTERZO, S. 2010. The weak s-process in massive stars and its dependence on the neutron capture cross sections. *The Astrophysical Journal,* 710**,** 1557-1577.

PRINGLE, E. A., MOYNIER, F., BECK, P., PANIELLO, R. & HEZEL, D. C. 2017. The origin of volatile element depletion in early Solar System material: Clues from Zn isotopes in chondrules. *Earth and Planetary Science Letters,* 468**,** 62-71.

PUPYSHEV, A. A. & SEMENOVA, E. V. 2001. Formation of doubly charged atomic ions in the inductively coupled plasma. *Spectrochimica Acta Part B: Atomic Spectroscopy,* 56**,** 2397-2418.

QIN, L. P., ALEXANDER, C. M. O., CARLSON, R. W., HORAN, M. F. & YOKOYAMA, T. 2010. Contributors to chromium isotope variation of meteorites. *Geochimica et Cosmochimica Acta,* 74**,** 1122-1145.

SCHILLER, M., BIZZARRO, M. & FERNANDES, V. A. 2018. Isotopic evolution of the protoplanetary disk and the building blocks of Earth and the Moon. *Nature,* 555**,** 507-510.
SOSSI, P. A., NEBEL, O., O'NEILL, H. S. C. & MOYNIER, F. 2018. Zinc isotope composition of the Earth and its behaviour during planetary accretion. *Chemical Geology,* 477**,** 73-84.
TAYLOR, G. J. 2013. The bulk composition of Mars. *Geochemistry,* 73**,** 401-420.
TIAN, Z., MAGNA, T., DAY, J. M. D., MEZGER, K., SCHERER, E. E., LODDERS, K., HIN, R. C., KOEFOED, P., BLOOM, H. & WANG, K. 2021. Potassium isotope composition of Mars reveals a mechanism of planetary volatile retention. *Proceedings of the National Academy of Sciences,* 118**,** e2101155118.
TRINQUIER, A., ELLIOTT, T., ULFBECK, D., COATH, C., KROT, A. N. & BIZZARRO, M. 2009. Origin of nucleosynthetic isotope heterogeneity in the solar protoplanetary disk. *Science,* 324**,** 374-376.
WANAJO, S., JANKA, H.-T. & MÜLLER, B. 2013. Electron-capure supernovae as origin of $^{48}$Ca. *The Astrophycal Journal Letters,* 767**,** L26.
WANG, M.-S. & LIPSCHUTZ, M. E. 2005. Thermal Metamorphism of Primitive Meteorites-XII. The Enstatite Chondrites Revisited. *Environmental Chemistry,* 2**,** 215-226.
WANG, M.-S. & LIPSCHUTZ, M. E. 2007. Trace elements in primitive meteorites—VII Antarctic unequilibrated ordinary chondrites. *Geochimica et Cosmochimica Acta,* 71**,** 1062-1073.
WANG, H. S., LINEWEAVER, C. H., IRELAND, T. R. 2018. The elemental abundances (with uncertainties) of the most Earth-like planet. *Icarus,* 299, 460-474.
WARREN, P. H. 2011. Stable-isotopic anomalies and the accretionary assemblage of the Earth and Mars: A subordinate role for carbonaceous chondrites. *Earth and Planetary Science Letters,* 311**,** 93-100.
WASSON, J. T. & KALLEMEYN, G. W. 1988. Compositions of Chondrites. *Philosophical Transactions of the Royal Society A,* 325**,** 535-544.
WOMBACHER, F. & REHKÄMPER, M. 2003. Investigation of the mass discrimination of multiple collector ICP-MS using neodymium isotopes and the generalised power law. *Journal of Analytical Atomic Spectrometry,* 18**,** 1371-1375.
WOMBACHER, F., REHKÄMPER, M., MEZGER, K. & MÜNKER, C. 2003. Stable isotope compositions of cadmium in geological materials and meteorites determined by multiple collector-ICPMS. *Geochimica et Cosmochimica Acta,* 67**,** 4639-4654.
WOOD, B. J., SMYTHE, D. J. & HARRISON, T. 2019. The condensation temperatures of the elements: A reappraisal. *American Mineralogist,* 104**,** 844-856.
WOOSLEY, S. E. 1997. Neutron-rich nucleosynthesis in carbon deflagration supernovae. *The Astrophysical Journal,* 476**,** 801-810.
WOOSLEY, S. E. & WEAVER, T. A. 1995. The evolution and explosion of massive Stars II: Explosive hydrodynamics and nucleosynthesis. *The Astrophysical Journal Supplement Series,* 181-235.
XIE, L., YANG, X. F., WRAITH, C., BABCOCK, C., BIEROŃ, J., BILLOWES, J., BISSELL, M. L., BLAUM, K., CHEAL, B., FILIPPIN, L., FLANAGAN, K. T., GARCIA RUIZ, R. F., GINS, W., GAIGALAS, G., GODEFROID, M., GORGES, C., GROB, L. K., HEYLEN, H., JÖNSSON, P., KAUFMANN, S., KOWALSKA, M., KRÄMER, J., MALBRUNOT-ETTENAUER, S., NEUGART, R., NEYENS, G., NÖRTERSHÄUSER, W., OTSUKA, T., PAPUGA, J., SÁNCHEZ, R., TSUNODA, Y. & YORDANOV, D. T. 2019. Nuclear charge radii of 62−80Zn and their dependence on cross-shell proton excitations. *Physics Letters B,* 797**,** 134805.
ZHANG, J., DAUPHAS, N., DAVIS, A. M., LEYA, I. & FEDKIN, A. 2012. The proto-Earth as a significant source of lunar material. *Nature Geoscience,* 5**,** 251-255.

# Chapter 3

# Primitive asteroids as a major source of terrestrial volatiles

## 3.1 Introduction

Despite an expanding search in the Solar System and other parts of the universe, life remains undetected outside of our planet. With the advancement of observational technology and a seemingly infinite pool of potentially habitable exoplanets, determining specific processes that led to the habitable conditions on Earth becomes increasingly more important. Yet, both the nature of Earth's accreting materials and the manner in which they coalesced are still debated.

A common approach to address these questions is to use nucleosynthetic isotope anomalies to identify Earth's building blocks among diverse Solar System materials. These small but detectable differences in isotope compositions result from the heterogeneous distribution of isotopically distinct grains through the cloud of gas and dust from which all Solar System materials formed. An important advantage of this approach is that the anomalies are not altered by secondary isotope fractionation induced by physical or chemical processes. This makes them a reliable signature, which can be used to establish genetic links between different materials.

Most meteorite groups in our inventory have been extensively characterized, revealing a clear dichotomy in the distribution of material in the Solar System. Carbonaceous meteorites, which are thought to originate from beyond the orbit of Jupiter, are generally enriched in the neutron-rich isotopes of Fe-peak elements such as Ca, Ti, Cr, Ni, and Zn (Dauphas et al., 2014, Trinquier et al., 2009, Trinquier et al., 2007, Render et al., 2018, Savage et al., 2022, Steller et al., 2022, Chapter 2) and depleted in the s-process isotopes of heavier elements such as Sr, Zr, Mo, Ru and Nd (Akram et al., 2015, Moynier et al., 2012, Burkhardt et al., 2016, Dauphas et al., 2002, Fischer-Gödde and Kleine, 2017). In contrast, the inner Solar System, which is sampled by non-carbonaceous (NC) meteorites, is characterized by a depletion in the same neutron-rich isotopes and an enrichment in s-process isotopes. Variations are also found within each reservoir to a lesser extent. This diversity among Solar System materials has been exploited by multiple studies that attempted to reproduce Earth's nucleosynthetic isotope composition by modelling mixtures between different meteorite groups. Some of these studies have shown that it is possible to reproduce Earth's composition by mixing only chondritic meteorites, which are derived from primitive, undifferentiated planetesimals (Lodders, 2000, Dauphas, 2017; Chapter 2). In addition to carbonaceous chondrites (CC), the other two main components in these models are typically ordinary and enstatite chondrites (OC and EC, respectively), which are the two most common types of non-carbonaceous chondrites (NCC).

Enstatite chondrites are typically inferred to account for most of Earth's mass, since their nucleosynthetic isotope composition is often indistinguishable from Earth's.

A scenario where Earth accreted primarily from chondrites is, however, not without caveats. Chondrites have mass-dependent Si and Mg isotope compositions that are incompatible with estimates for the bulk silicate Earth (BSE; Fitoussi and Bourdon, 2012, Hin et al., 2017, Pringle et al., 2014). Furthermore, some of the BSE's elemental ratios, such as Mg/Si, suggest a much more limited contribution from ECs (Fitoussi and Bourdon, 2012). In turn, these mass-dependent isotope compositions are readily explained by Earth having accreted large amounts of differentiated material which went through substantial volatile loss, such as the parent bodies of some achondritic meteorites (Hin et al., 2017).

Volatile elements, which condense at relatively low temperatures of <1100 K, are fundamental for the emergence of life, and the six most abundant elements in living organisms are highly to moderately volatile. Nonetheless, these elements are variably depleted in all Solar System materials relative to the Sun and CI chondrites, a group of primitive meteorites whose composition is identical to the solar photosphere. Different extents of volatile depletion are observed in the terrestrial planets and the Moon (McDonough, 2014, Taylor, 2013, Peplowski et al., 2011, O'Neill, 1991). Furthermore, while NCCs and achondrites range from very depleted to enriched in volatiles (Wasson and Kallemeyn, 1988, Kallemeyn et al., 1989, Kallemeyn and Wasson, 1986, Wasson et al., 1976, O'Neill and Palme, 2008), CCs are typically volatile-rich (Braukmüller et al., 2019).

For years, the notion that objects formed beyond the snow line are enriched in volatiles compared to the terrestrial planets led to theories about their potential role in establishing Earth's volatile budget (Marty, 2012, Albarède et al., 2013, Morbidelli et al., 2000). This hypothesis was substantiated when the dichotomy between inner and outer Solar System was shown to extend to nucleosynthetic isotope anomalies of two moderately volatile elements, Zn and K (Chapter 2, Savage et al., 2022, Steller et al., 2022, Nie et al., 2023). These studies revealed that both reservoirs provided substantial contributions to Earth's K and Zn inventories. However, meteorites from differentiated bodies, whose volatile contents can vary extensively, are still largely uncharacterized for isotope anomalies of volatile elements.

## 3.2 Samples

The present study focused primarily on characterizing the mass-independent Zn isotope compositions of meteorites derived from differentiated planetesimals, including both the silicate and metal fractions, as sampled by achondrites and iron meteorites, respectively, but new CCs and NCCs were also included. In detail, the study encompassed (i) eight achondrites, including three ureilites, one howardites, two eucrites, one acapulcoite and one aubrite; (ii) two IAB complex iron meteorites (iii) three carbonaceous chondrites (CC); (iv) six enstatite chondrites (EC); and (v) one R chondrite. Altogether, 20 meteorites were analysed, with all relevant information, including meteorite sources, summarized in Table 3.1. Multiple aliquots of the United States Geological Survey (USGS) geological reference material BCR-2 were analysed for quality control (Table 3.1).

These meteorites and terrestrial rocks were either used up completely by destructive analysis during the course of the study (Orgueil, Murchison, NWA 13299, MIL 07028, MAC 88136, Djoua, Nantan, Toluca) or remaining sample aliquots (Winchcombe, Indarch, PCA 91238, LAR 06025, NWA 11880, NWA 11754, NWA 11757, NWA 11890, NWA 11395, NWA 12265, NWA 8287, BCR-2) are stored at the Department of Earth Science & Engineering, Imperial College London.

**Table 3.1. Names, digested masses, identifiers and sources of the meteorites and BSE rock analysed in this study.**

| Samples | Type | Total mass (g) | Used mass (g) | Status | Identifier | Source |
|---|---|---|---|---|---|---|
| *Meteorites* | | | | | | |
| Orgueil | CI1 | 0.36 | 0.158 | Fully destroyed | BM.36104 | Natural History Museum London |
| Murchison | CM2 | 1.26 | 0.612 | Fully destroyed | ME 2644, #26.55 | Field Museum Chicago |
| Winchcombe | CM2 | 1.9398 | 0.250 | Stored | Bag 10.2 Stone 1 | Natural History Museum London |
| NWA 13299 | EH3 | 0.456 | 0.456 | Fully destroyed | | Private collector |
| Indarch | EH4 | 1.37 | 1.302 | Stored | M4 1403, #22 | Field Museum Chicago |
| MIL 07028 | EH3 | 7.65 | 0.12 | Fully destroyed | MIL 07028,33 | US Antarctic Meteorite Program [$] |
| PCA 91238 | EH3 | 0.853 | 0.370 | Stored | PCA 91238,29 | US Antarctic Meteorite Program [$] |
| LAR 06252 | EH3 | 7.31 | 0.253 | Stored | LAR 06252,45 | US Antarctic Meteorite Program [$] |
| MAC 88136 | EL3 | 0.54 | 0.140 | Stored | MAC 88136,119 | US Antarctic Meteorite Program [$] |
| NWA 11880 | R3.5-4 | 1.24 | 0.308 | Stored | | Private collector |
| NWA 11754 | Ureilite | 1.630 | 0.250 | Stored | | Private collector |
| NWA 11757 | Ureilite | 4.28 | 2.000 | Stored | | Private collector |
| NWA 11890 | Ureilite | 1.35 | 0.400 | Stored | | Private collector |
| NWA 11395 | Howardite | 11.55 | 2.45 | Stored | | Private collector |
| NWA 12265 | Eucrite | 18.2 | 3.5 | Stored | | Private collector |
| NWA 14443 | Eucrite | 2.74 | 2.74 | Fully destroyed | | Private collector |
| NWA 8287 | Acapulcoite | 0.54 | 0.165 | Stored | | Private collector |
| Djoua | Aubrite | 2.3 | 2.3 | Fully destroyed | | Private collector |
| Nantan | IAB | 7.6 | | Fully destroyed | | Private collector |
| Toluca [#] | IAB | 10.8 | | Fully destroyed | | Private collector |
| *BSE rock* | | | | | | |
| BCR-2 | Columbia River Basalt | | | Stored | | US Geological Survey |

Total mass corresponds to original mass of the sample, a fraction of which was crushed to powder (typically >1g) and a final powder aliquot was separated for this study. # Sample Toluca 2 is from (Bridgestock et al., 2014). $ US Antarctic meteorite samples are from the Antarctic Search for Meteorites (ANSMET) program funded by NSF and NASA; they are characterized and curated by the Dept. of Mineral Sciences of the Smithsonian Institution and the Astromaterials Curation Office at NASA Johnson Space Center.

## 3.3 Methods

### 3.3.1. Sample preparation

Digestion and preparation of the samples and the subsequent Zn isotopic measurements were carried out in the Mass Spectrometry and Isotope Geochemistry (MAGIC) Laboratories at the Department of Earth Science & Engineering of Imperial College London following the procedures outlined in Chapter 2. All sample preparation was conducted in ISO Class 6 clean rooms, using ISO Class 4 laminar flow benches for critical steps. The water used was of ≥ 18.2 MΩ cm quality from a Millipore purification system. All acids were purified from reagent grade stock acids by sub-boiling distillation in either quartz glass (15.3 M $HNO_3$, 6 M HCl) or Teflon (28 M HF, 12 M HCl, 8.5 M HBr) stills.

The original samples, weighing between 0.36 g and 18.2 g, were crushed in an agate mortar and pestle. Smaller fractions, ranging from 0.158 g to 2.74 g were subsequently aliquoted for this study, depending on the expected Zn content. They were digested in Savillex Teflon beakers as follows. First, they were refluxed in a 2 + 1 mixture of 28 M HF + 15.3 M $HNO_3$ at 120° C for at least two days on a hotplate, and then dried down and the process was repeated in 6 M HCl. Following digestion, the samples were purified using the three-stage anion exchange procedure described in Chapter 2. Some samples (Orgueil, Murchison, Toluca) were previously crushed, digested and treated (Chapter 2) and the results presented in this chapter reflect new isotope measurements.

### 3.3.2. Isotope measurements

The isotope analyses were conducted with a Nu Instruments Nu Plasma II multiple collector inductively coupled plasma mass spectrometer (MC-ICP-MS). A Nu Instruments DSN 100 desolvation system fitted with glass cross flow nebulizers with solution flow rates of about 120 µl $min^{-1}$ were employed for sample introduction in conjunction with a CETAC ASX-112FR autosampler. The analyses were carried out using two different Faraday cup configurations: The M64 configuration covers the isotopes $^{64}Zn$, $^{66}Zn$, $^{67}Zn$, $^{68}Zn$, and $^{62}Ni$, while the M70 configuration covers $^{66}Zn$, $^{67}Zn$, $^{68}Zn$, $^{70}Zn$, and $^{72}Ge$ (Table 3.2). All ion beams were monitored using Faraday cups fitted with $10^{11}$ Ω resistors, with each run encompassing 3 blocks with 20 data acquisition cycles of 8 s each. Each run was started by a peak centering routine whilst each block commenced with a 60 s measurement of the electronic baselines of the Faraday collectors whilst the ion beam was deflected in the electrostatic analyzer.

Monitoring of $^{73}$Ge on the H10 Faraday cup during M70 block measurements (Table 3.2) revealed that Ge was consistently below the detection level. As such, no Ge corrections are needed, and the ion beam collected in Faraday cup H8 of the M64 block analyses can be attributed exclusively to $^{70}$Zn. Hence, provided that the H8 beam was sufficiently high (typically >0.4V) and stable, $\varepsilon^{70}$Zn values collected in M64 block measurements are reported for the samples NWA 11395, NWA 12265, NWA 14443, and Djoua.

The solutions were introduced in 0.1 M $HNO_3$, typically containing 400-500 ng $g^{-1}$ of Zn, with instrumental sensitivity ranging between 150 and 200 V/(µg $ml^{-1}$). All analyses were carried out with the sample–standard bracketing technique, in which sample runs were symmetrically bracketed by runs of the London Zn isotope reference material. Samples concentrations typically matched the standard concentrations within 10 to 15%.

The Zn results are reported using the ε notation, which denotes deviations of the measured isotope ratio for a sample (sam) from the value determined for the London Zn reference standard (std) in parts per $10^4$:

$$\varepsilon^{\mathrm{i/j}}Zn_{\mathrm{k/j}} = \left(\frac{(\,^{\mathrm{i}}Zn/\,^{\mathrm{j}}Zn)_{\mathrm{sam}}}{(\,^{\mathrm{i}}Zn/\,^{\mathrm{j}}Zn)_{\mathrm{std}}} - 1\right) x\ 10^4 \qquad \text{(Eq. 3.1)}$$

where i/j is the isotope ratio of interest and k/j the normalization ratio. As data obtained via the $^{66}$Zn/$^{67}$Zn normalization scheme is most frequently quoted in the manuscript, a simplified $\varepsilon^{\mathrm{i}}$Zn notation is adopted in this case. The full $\varepsilon^{\mathrm{i/j}}Zn_{\mathrm{k/j}}$ notation, however, is used to denote Zn isotope data normalized to $^{64}$Zn/$^{67}$Zn and $^{64}$Zn/$^{68}$Zn. The εZn values were calculated relative to the mean isotopic ratios of about 20 to 40 runs of the London Zn standard during the same measurement session.

**Table 3.2. Collector configurations that were used for the Zn isotope measurements, abundances of the isotopes of Zn as well as spectral interferences from isobars, $Ba^{2+}$ and the most relevant molecular ions.**

| **Faraday collector** | **L4** | **L2** | **Ax** | **H1** | **H2** | **H4** | **H6** | **H7** | **H8** | **H10** |
|---|---|---|---|---|---|---|---|---|---|---|
| **Collector configuration M64** | $^{62}Ni$ | $^{64}Zn$ | | | $^{66}Zn$ | $^{67}Zn$ | $^{68}Zn$ | $^{137}Ba^{2+}$ | $^{70}Zn$ | |
| Isotope abundance Zn | | 49.2% | | | 27.7% | 4.0% | 18.5% | | 0.6% | |
| Isotope abundance Ni | 3.6% | 0.1% | | | | | | | | |
| Isotope abundance $Ba^{2+}$ ions | | | | | 0.1% | 2.4% | 7.9% | 11.2% | | |
| Isotope abundance Ge | | | | | | | | | 20.5% | |
| **Collector configuration M70** | $^{66}Zn$ | $^{67}Zn$ | $^{68}Zn$ | $^{137}Ba^{2+}$ | | $^{70}Zn$ | | | $^{72}Ge$ | $^{73}Ge$ |
| Isotope abundance Zn | 27.7% | 4.0% | 18.5% | | | 0.6% | | | | |
| Isotope abundance Ge | | | | | | 20.5% | | | 27.5% | 7.8% |
| Isotope abundance $Ba^{2+}$ ions | 0.1% | 2.4% | 7.9% | 11.2% | | | | | | |

## 3.4 Results

The meteorite results show resolvable deviations from the terrestrial standard for all samples analysed in this study (Table 3.3). In line with other isotope systems and with previous Zn isotope studies (Chapter 2, Steller et al., 2022, Savage et al., 2022), CCs have an excess of the neutron-rich isotopes $^{68}$Zn, $^{70}$Zn and a deficit in $^{64}$Zn and $^{67}$Zn, with the NC meteorites showing complementary patterns (Fig. 3.1). In turn, measurements of the terrestrial rock standard BCR-2 show no substantial deviations from $\varepsilon^{i}$Zn = 0 (BSE in Fig. 3.1).

The Zn isotope anomalies are likely produced in the same sites as the anomalies of other Fe-peak elements, namely $^{48}$Ca, $^{50}$Ti, $^{54}$Cr, and $^{62}$Ni. Thus, the results obtained here are compared to modelled nucleosynthetic isotope anomalies produced by Type Ia supernovae (SNIa, Wanajo et al., 2013) and electron capture core-collapse supernovae (ECSN, Woosley 1997), which have been previously linked to $^{48}$Ca anomalies (Dauphas et al., 2014). The models were produced following the procedures introduced in Chapter 2. The measured anomalies are generally compatible with both nucleosynthetic sources, regardless of the isotope ratio used for internal normalization (Fig. 3.2), supporting a nucleosynthetic origin for the anomalies.

The results are overall in agreement with isotope anomalies of the other Fe-peak elements (Fig. 3.3 and 3.4). However, the Zn isotope anomalies of CCs are often smaller than predicted by the models for a given anomaly of another element, especially Ca and Ti. This is not unexpected, as the latter elements have significantly higher condensation temperatures, such that incomplete condensation of Zn from the stellar source, subsequential thermal processing and/or different carrier phases could potentially decouple the anomalies. Notably, the Ca and Ti isotope anomalies generally appear to increase with the volume of Ca-Al-rich inclusions (CAIs), while the Zn isotope anomalies stay roughly the same (Figs. 3.3 and 3.4). CAIs are refractory components that are thought to be the first solids to have condensed in the Solar System, at significantly higher temperatures (>1500 K) than the 50% condensation temperature of 726 K for Zn (Lodders, 2003). Additionally, Cr and Ni are both more refractory and more siderophile than Zn, such that the isotope anomalies of these elements could be hosted in different phases with distributions that are decoupled prior to accretion of the CC parent bodies.

**Table 3.3. Mass-independent Zn isotope data (in εZn notation) for the meteorites and BSE samples.**

| | | Data normalised to $^{66}Zn/^{67}Zn$ | | | | | | | | | | | |
|---|---|---|---|---|---|---|---|---|---|---|---|---|---|
| **Sample** | | **$\varepsilon^{64/67}Zn$** | **2se** | **2sd** | **m/n** | **$\varepsilon^{68/67}Zn$** | **2se** | **2sd** | **m/n** | **$\varepsilon^{70/67}Zn$** | **2se** | **2sd** | **m/n** |
| Orgueil | CI1 | -0.93 | 0.20 | 0.62 | 1/10 | 0.54 | 0.08 | 0.32 | 1/17 | 0.93 | 0.33 | 0.88 | 1/7 |
| Murchison | CM2 | -1.32 | 0.34 | 0.76 | 1/5 | 0.53 | 0.09 | 0.34 | 1/13 | 1.12 | 0.49 | 1.38 | 1/8 |
| Winchcombe | CM2 | -0.92 | 0.21 | 0.52 | 1/8 | 0.57 | 0.09 | 0.37 | 1/15 | 1.24 | 0.22 | 0.59 | 1/7 |
| NWA 13299 | EH3 | 0.76 | 0.24 | 0.80 | 2/11 | -0.42 | 0.19 | 0.78 | 1/17 | -1.16 | 0.50 | 1.23 | 1/6 |
| MIL 07028 | EH3 | 0.61 | 0.24 | 0.59 | 1/6 | -0.18 | 0.14 | 0.45 | 1/10 | -1.20 | 0.44 | 0.88 | 1/4 |
| PCA 91238 | EH3 | 0.97 | 0.29 | 0.70 | 1/6 | -0.49 | 0.17 | 0.62 | 1/13 | -1.07 | 0.51 | 1.34 | 1/7 |
| LAR 06252 | EH3 | 0.96 | 0.26 | 0.64 | 1/6 | -0.49 | 0.08 | 0.27 | 1/12 | -1.32 | 0.24 | 0.48 | 1/6 |
| Indarch | EH4 | 0.93 | 0.29 | 0.88 | 1/9 | -0.70 | 0.16 | 0.61 | 1/15 | -1.67 | 0.67 | 1.63 | 1/6 |
| MAC 88136 | EL3 | 0.63 | 0.25 | 0.76 | 1/9 | -0.45 | 0.15 | 0.54 | 1/13 | -1.47 | 0.60 | 1.20 | 1/4 |
| NWA 11880 | R3.5-4 | 1.01 | 0.29 | 0.82 | 2/8 | -0.41 | 0.11 | 0.46 | 2/17 | -1.15 | 0.35 | 1.05 | 2/9 |
| NWA 11754 | Ureilite | 1.35 | 0.30 | 0.79 | 2/7 | -0.69 | 0.23 | 0.82 | 2/13 | -1.47 | 0.35 | 0.86 | 2/6 |
| NWA 11757 | Ureilite | 0.97 | 0.21 | 0.52 | 1/6 | -0.53 | 0.18 | 0.54 | 1/9 | -1.51 | 1.04 | 2.08 | 1/3 |
| NWA 11890 | Ureilite | 1.43 | 0.29 | 0.82 | 1/8 | -0.65 | 0.10 | 0.39 | 1/16 | -1.27 | 0.18 | 0.50 | 1/8 |
| NWA 11395 | Howardite | 1.87 | 0.86 | 1.49 | 1/3 | -1.31 | 0.33 | 0.58 | 1/3 | -3.33 | 0.85 | 1.48 | 1/3 |
| NWA 12265 | Eucrite | 1.13 | 0.84 | 1.89 | 1/5 | -0.41 | 0.29 | 0.65 | 1/5 | -1.64 | 0.86 | 1.93 | 1/5 |
| NWA 14443 | Eucrite | 1.18 | 0.33 | 0.87 | 1/7 | -0.58 | 0.18 | 0.48 | 1/7 | -1.68 | 0.87 | 1.94 | 1/5 |
| NWA 8287 | Acapulcoite | 1.03 | 0.27 | 0.85 | 1/10 | -0.67 | 0.14 | 0.59 | 1/17 | -1.58 | 0.13 | 0.34 | 1/7 |
| Djoua | Aubrite | 1.40 | 1.06 | 2.12 | 1/4 | -0.57 | 0.62 | 1.24 | 1/4 | -2.55 | 3.22 | 5.57 | 1/3 |
| Toluca | IAB complex | 0.69 | 0.42 | 0.72 | 1/3 | -0.36 | 0.16 | 0.42 | 1/7 | -0.67 | 0.74 | 1.48 | 1/4 |
| Nantan | IAB complex | 0.59 | 0.47 | 0.82 | 1/3 | -0.48 | 0.11 | 0.31 | 1/8 | -1.06 | 0.37 | 0.83 | 1/5 |
| BCR-2 | Earth | 0.02 | 0.11 | 0.72 | 2/46 | 0.01 | 0.04 | 0.44 | 2/114 | 0.03 | 0.10 | 0.93 | 2/68 |

Continued on next page.

**Table 3.3. Continued.**

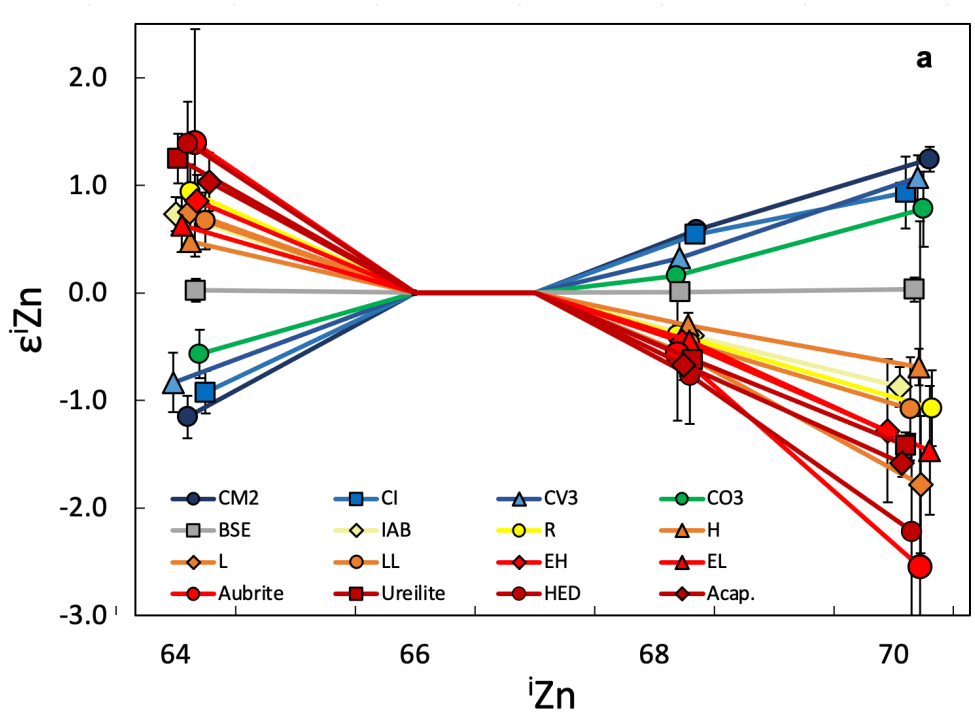
| | | Data normalised to $^{64}Zn/^{67}Zn$ | | | | | | | |
|---|---|---|---|---|---|---|---|---|---|
| **Sample** | | **$\varepsilon^{66/67}Zn$** | **2se** | **2sd** | **m/n** | **$\varepsilon^{68/67}Zn$** | **2se** | **2sd** | **m/n** |
| Orgueil | CI1 | 0.30 | 0.06 | 0.21 | 1/10 | 0.18 | 0.10 | 0.30 | 1/10 |
| Murchison | CM2 | 0.43 | 0.11 | 0.25 | 1/5 | 0.19 | 0.12 | 0.27 | 1/5 |
| Winchcombe | CM2 | 0.30 | 0.07 | 0.20 | 1/8 | 0.21 | 0.13 | 0.37 | 1/8 |
| NWA 13299 | EH3 | -0.26 | 0.07 | 0.23 | 2/11 | -0.18 | 0.22 | 0.72 | 2/11 |
| MIL 07028 | EH3 | -0.20 | 0.09 | 0.19 | 1/6 | 0.16 | 0.19 | 0.47 | 1/6 |
| PCA 91238 | EH3 | -0.32 | 0.09 | 0.23 | 1/6 | -0.32 | 0.26 | 0.65 | 1/6 |
| LAR 06252 | EH3 | -0.32 | 0.09 | 0.21 | 1/6 | -0.18 | 0.12 | 0.30 | 1/6 |
| Indarch | EH4 | -0.26 | 0.12 | 0.26 | 1/5 | -0.18 | 0.12 | 0.27 | 1/5 |
| MAC 88136 | EL3 | -0.21 | 0.08 | 0.25 | 1/9 | -0.09 | 0.14 | 0.42 | 1/9 |
| NWA 11880 | R3.5-4 | -0.33 | 0.09 | 0.27 | 2/8 | -0.23 | 0.17 | 0.49 | 2/8 |
| NWA 11754 | Ureilite | -0.44 | 0.10 | 0.26 | 1/7 | -0.29 | 0.28 | 0.73 | 1/7 |
| NWA 11757 | Ureilite | -0.32 | 0.07 | 0.17 | 1/6 | -0.17 | 0.22 | 0.54 | 1/6 |
| NWA 11890 | Ureilite | -0.47 | 0.10 | 0.27 | 1/8 | -0.35 | 0.07 | 0.21 | 1/8 |
| NWA 11395 | Howardite | -0.70 | 0.31 | 0.54 | 1/3 | -0.62 | 0.06 | 0.10 | 1/3 |
| NWA 12265 | Eucrite | -0.38 | 0.28 | 0.62 | 1/5 | -0.04 | 0.20 | 0.45 | 1/5 |
| NWA 14443 | Eucrite | -0.40 | 0.11 | 0.30 | 1/7 | -0.22 | 0.10 | 0.25 | 1/7 |
| NWA 8287 | Acapulcoite | -0.22 | 0.08 | 0.28 | 1/10 | -0.22 | 0.13 | 0.40 | 1/10 |
| Djoua | Aubrite | -0.47 | 0.35 | 0.71 | 1/4 | -0.10 | 0.35 | 0.70 | 1/4 |
| Nantan | IAB | -0.20 | 0.15 | 0.27 | 1/3 | -0.18 | 0.19 | 0.33 | 1/3 |
| Toluca | IAB | -0.23 | 0.14 | 0.24 | 1/3 | -0.23 | 0.10 | 0.18 | 1/3 |
| BCR-2 | Earth | -0.01 | 0.04 | 0.24 | 1/46 | -0.01 | 0.06 | 0.42 | 1/46 |

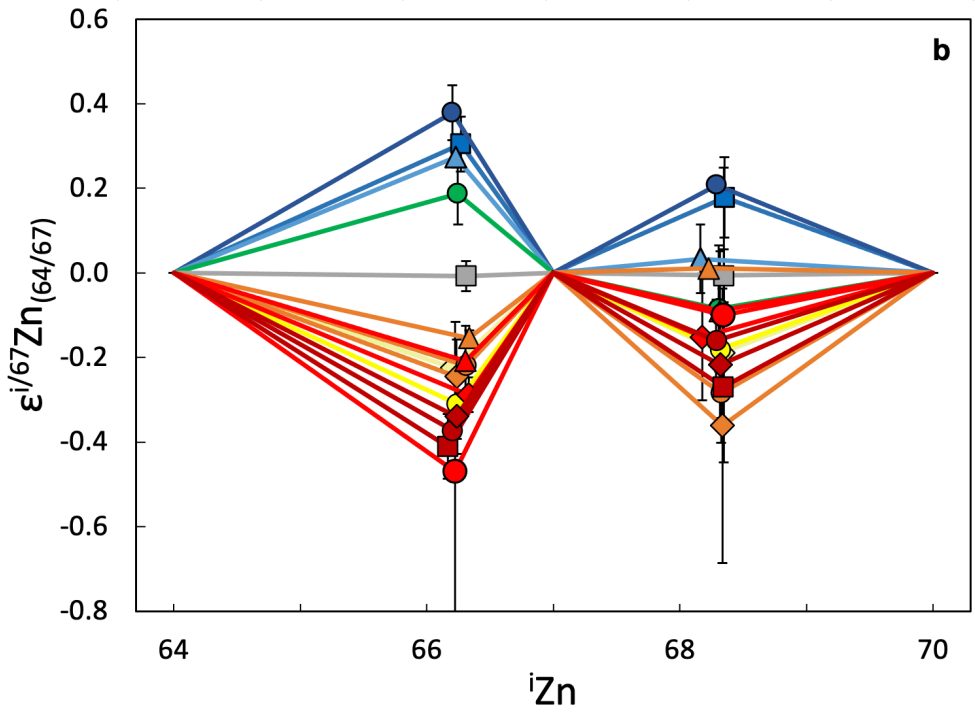
Continued on next page.

**Table 3.3. Continued.**

| | | Data normalised to $^{64}Zn/^{68}Zn$ | | | | | | | |
|---|---|---|---|---|---|---|---|---|---|
| **Sample** | | **$\varepsilon^{66/68}Zn$** | **2se** | **2sd** | **m/n** | **$\varepsilon^{67/68}Zn$** | **2se** | **2sd** | **m/n** |
| Orgueil | CI1 | 0.19 | 0.09 | 0.29 | 1/10 | -0.14 | 0.07 | 0.23 | 1/10 |
| Murchison | CM2 | 0.32 | 0.09 | 0.20 | 1/5 | -0.15 | 0.09 | 0.29 | 1/5 |
| Winchcombe | CM2 | 0.19 | 0.11 | 0.29 | 1/8 | -0.16 | 0.10 | 0.28 | 1/8 |
| NWA 13299 | EH3 | -0.16 | 0.08 | 0.26 | 2/11 | 0.14 | 0.17 | 0.55 | 2/11 |
| MIL 07028 | EH3 | -0.27 | 0.08 | 0.20 | 1/6 | -0.12 | 0.15 | 0.36 | 1/6 |
| PCA 91238 | EH3 | -0.17 | 0.12 | 0.28 | 1/6 | 0.24 | 0.20 | 0.49 | 1/6 |
| LAR 06252 | EH3 | -0.24 | 0.09 | 0.21 | 1/6 | 0.13 | 0.09 | 0.23 | 1/6 |
| Indarch | EH4 | -0.17 | 0.10 | 0.23 | 1/5 | 0.14 | 0.09 | 0.21 | 1/5 |
| MAC 88136 | EL3 | -0.16 | 0.07 | 0.22 | 1/9 | 0.07 | 0.11 | 0.32 | 1/9 |
| NWA 11880 | R3.5-4 | -0.23 | 0.07 | 0.19 | 2/8 | 0.17 | 0.13 | 0.37 | 2/8 |
| NWA 11754 | Ureilite | -0.30 | 0.08 | 0.22 | 1/7 | 0.22 | 0.21 | 0.55 | 1/7 |
| NWA 11757 | Ureilite | -0.28 | 0.13 | 0.32 | 1/6 | 0.13 | 0.41 | 0.17 | 1/6 |
| NWA 11890 | Ureilite | -0.32 | 0.05 | 0.15 | 1/8 | 0.26 | 0.05 | 0.16 | 1/8 |
| NWA 11395 | Howardite | -0.25 | 0.26 | 0.46 | 1/3 | 0.53 | 0.06 | 0.11 | 1/3 |
| NWA 12265 | Eucrite | -0.35 | 0.32 | 0.72 | 1/5 | 0.04 | 0.15 | 0.34 | 1/5 |
| NWA 14443 | Eucrite | -0.26 | 0.11 | 0.29 | 1/7 | 0.18 | 0.07 | 0.20 | 1/7 |
| NWA 8287 | Acapulcoite | -0.25 | 0.07 | 0.21 | 1/10 | 0.16 | 0.10 | 0.30 | 1/10 |
| Djoua | Aubrite | -0.39 | 0.27 | 0.54 | 1/4 | 0.08 | 0.27 | 0.55 | 1/4 |
| Nantan | IAB | -0.15 | 0.19 | 0.32 | 1/3 | 0.13 | 0.15 | 0.15 | 1/3 |
| Toluca | IAB | -0.10 | 0.09 | 0.16 | 1/3 | 0.17 | 0.08 | 0.14 | 1/3 |
| BCR-2 | Earth | 0.00 | 0.04 | 0.28 | 1/46 | 0.00 | 0.05 | 0.32 | 1/46 |

m: number of sample digest aliquots processed separately through column chemistry. n is the total number of individual analytical runs for a given meteorite, for one or several powder/digest solution aliquots. x is the number of distinct meteorite/BSE samples in a group.


a
2.0
1.0
0.0
-1.0
-2.0
-3.0
εiZn
CM2
CI
CV3
CO3
BSE
IAB
R
H
L
LL
EH
EL
Aubrite
Ureilite
HED
Acap.
64
66
68
70
iZn


b
0.6
0.4
0.2
0.0
-0.2
-0.4
-0.6
-0.8
εi/67Zn(64/67)
64
66
68
70
iZn

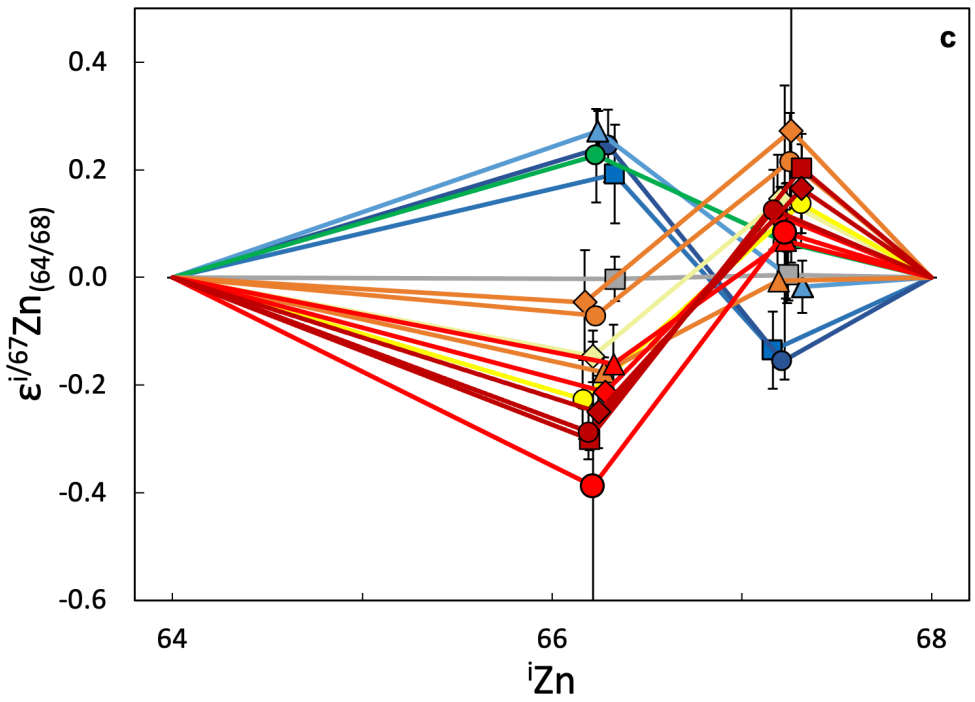



**Figure 3.1. Mean Zn isotope compositions for the meteorite groups and the BSE, in $\varepsilon^{i}$Zn notation.** The plotted results reflect compiled data from this Chapter and Chapter 2 for carbonaceous chondrites (CI, CM, CV, CO) and non-carbonaceous group meteorites (ECs, including five EHs, one EL, OCs, including H, L, and LL chondrites, IAB and IIICD complex irons, ureilites, HEDs, and acapulcoites. Panels show results obtained using different isotope ratios for internal normalization: (a) $^{66}$Zn/$^{67}$Zn; (b) $^{64}$Zn/$^{67}$Zn; and (c) $^{64}$Zn/$^{68}$Zn. The CC and NC groups have complimentary patterns with CCs enriched in $^{68}$Zn and $^{70}$Zn and depleted in $^{64}$Zn and $^{67}$Zn (relative to the BSE with $\varepsilon^{i}$Zn = 0). NCs have the opposite pattern, with depletions in $^{68}$Zn and $^{70}$Zn and enrichments in $^{64}$Zn and $^{67}$Zn. The terrestrial sample is indistinguishable from the Zn standard and intermediate between CCs and NCs. The meteorite and BSE data are listed in Table 3.3 and Table 2.6 (Chapter 2); Uncertainties for groups with a single sample correspond to ±2se of that sample (EL, aubrite, acapulcoite, CO, BSE); for groups with two samples (H, LL, R), uncertainties correspond to ±2sd; for groups with more than two samples, the uncertainties correspond to ±2se.

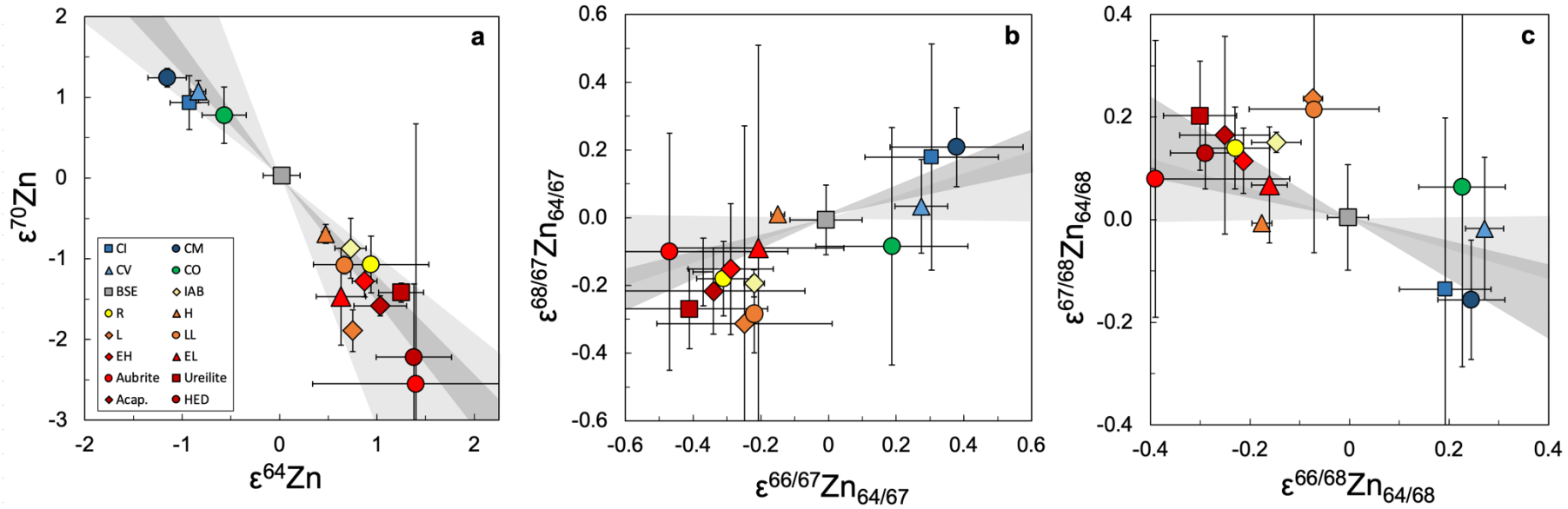



**Figure 3.2. Measured Zn isotope compositions in comparison to predicted nucleosynthetic isotope anomalies.** Group means encompass results from this study and from Chapter 2 and are shown for data obtained with internal normalization to (a) $^{66}Zn/^{67}Zn$, (b) $^{64}Zn/^{67}Zn$, and (c) $^{64}Zn/^{68}Zn$. Measured isotope compositions for meteorites are in agreement with modelled anomalies for Type Ia (SNIa, light grey) and electron capture core collapse (ECSN, dark grey) supernovae.

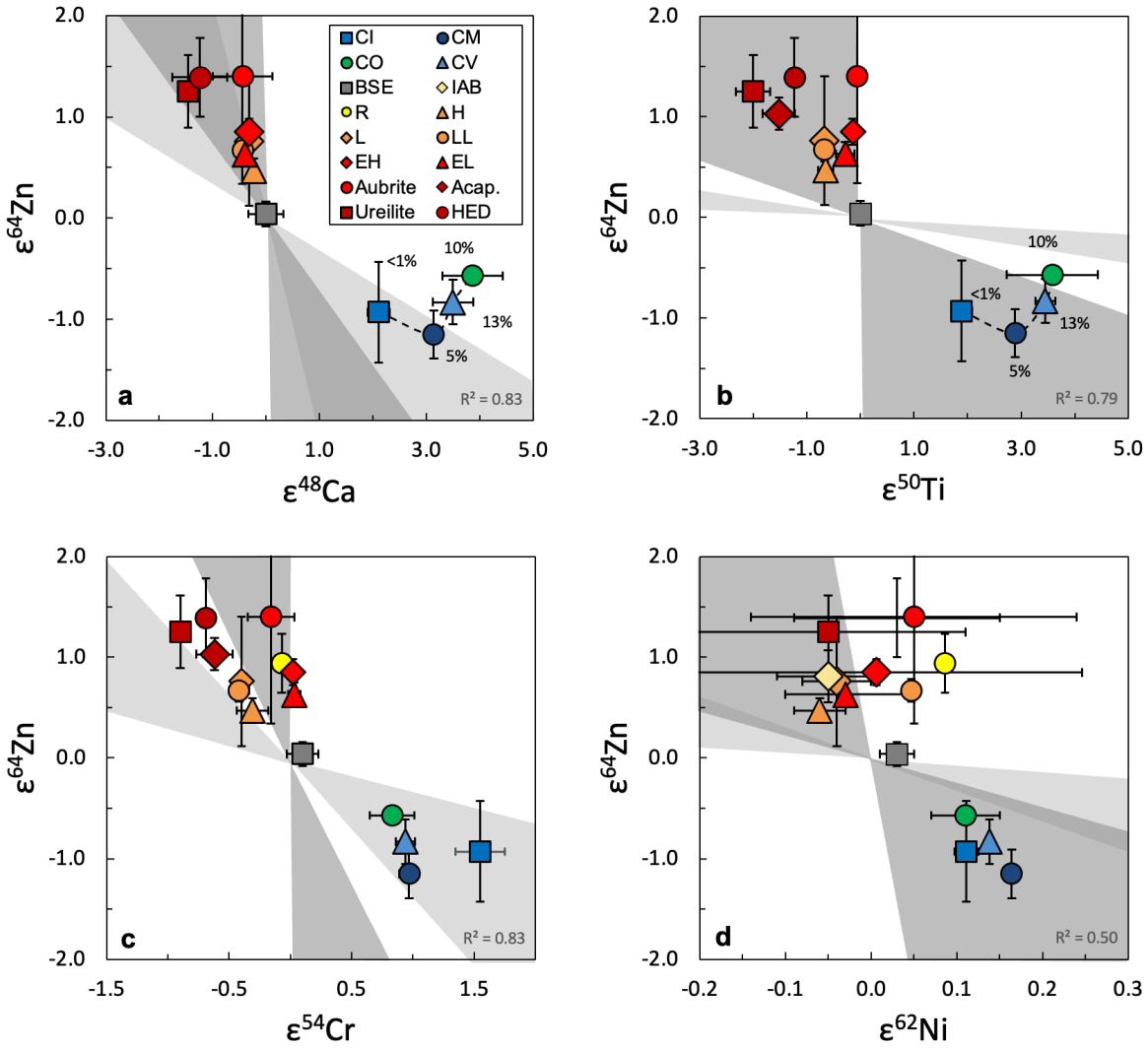



**Figure 3.3. Measured $^{64}$Zn isotope anomalies versus isotope anomalies of other Fe-peak elements.** The results are in agreement with predictions for anomalies of (a) $^{42}$Ca, (b) $^{50}$Ti, (c) $^{54}$Cr, and (d) $^{62}$Ni. The light grey and dark grey fields correspond to modelled anomalies for SNIa and ECSN sources, respectively. Panels (a) and (b) also show the estimated volume (%) of CAIs in CC meteorite classes. The Ca and Ti isotope anomalies roughly increase with the volume of CAIs, while the Zn isotope anomalies barely change, causing the trend to diverge from the modelled composition predicted for nucleosynthesis in SNIa and ECSN environments.

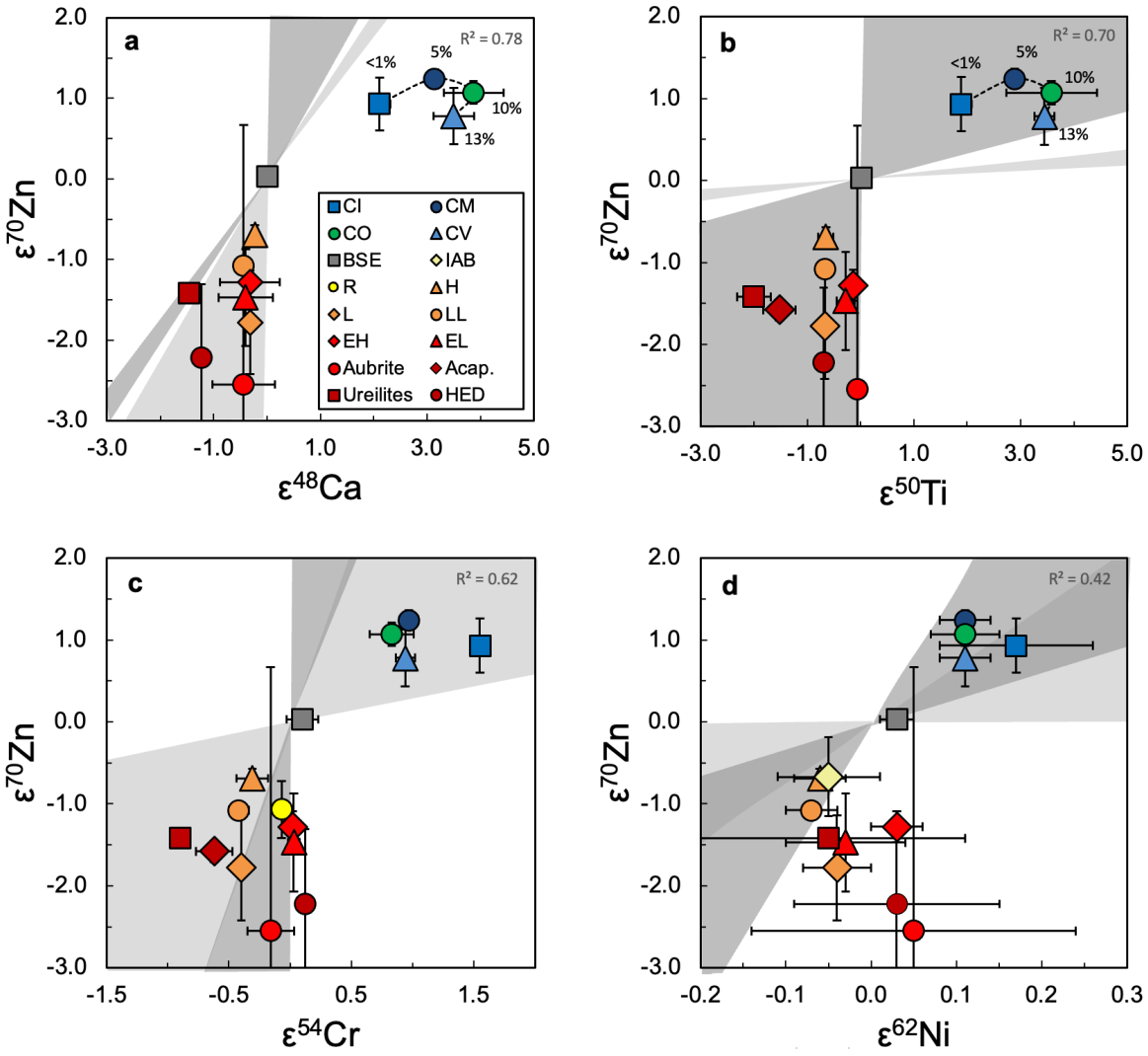



**Figure 3.4. Measured $^{70}$Zn isotope anomalies versus isotope anomalies of other Fe-peak elements.** The results are in agreement with predictions for anomalies of (a) $^{42}$Ca, (b) $^{50}$Ti, (c) $^{54}$Cr, and (d) $^{62}$Ni.

## 3.5 Discussion

### 3.5.1 Origin of Earth's Zn

While the mass fraction of carbonaceous material accreted by Earth has been estimated previously using nucleosynthetic isotope anomalies of refractory elements, these estimates do not constrain the CC contribution to Earth's Zn budget. This is because, unlike for refractory elements, the Zn concentrations of different Solar System materials vary substantially. In general, CCs are rich in Zn, with concentrations ranging from ~100 to almost 400 μg $g^{-1}$ (Braukmüller et al., 2019), but NCCs can have as little as a few μg $g^{-1}$ to over 300 μg $g^{-1}$ of Zn (Wasson and Kallemeyn, 1988, Lodders & Fegley, 1998). Furthermore, the Zn concentrations of achondrite parent bodies are unconstrained, with measurements of achondritic meteorites recording variable concentrations from less than 1 μg $g^{-1}$ to over 300 μg $g^{-1}$ (Paniello et al., 2012, Wasson et al., 1976). Furthermore, the bulk Earth (BE) Zn content is debated due to uncertainties about partitioning of Zn into the core (McDonough, 2005, Mahan et al., 2017), and the Zn concentrations of iron meteorite parent bodies are even more difficult to constrain.

Despite potentially contributing just 10% of Earth's mass or less (Dauphas, 2017, Lodders, 2000, Albarède, 2009, Morbidelli et al., 2000, Burkhardt et al., 2021), carbonaceous material was previously estimated to account for 30 to 50% of Earth's Zn (Chapter 2, Steller et al., 2022, Savage et al., 2022). To further improve these estimates, this study performed a Monte Carlo simulation of a multi-component mixing model between different meteorite groups, including previously uncharacterized chondrites (Rumuruti chondrites), and achondrites (HEDs, ureilites, aubrites, and acapulcoites). Furthermore, the model employs improved estimates for the compositions of previously characterized groups with new data for four ECs and one CM, as well as more precise results for a CI, a CM, an L and a IAB complex iron meteorite that had been previously analysed.

A 10,000-trial Monte Carlo simulation of a mixture between all meteorite classes characterized here and in Chapter 2 was performed employing the following equations:

$$\varepsilon^{64}Zn_{BE} = \sum_{i=1}^{n} p_i \times \varepsilon^{64}Zn_i \times f_i \quad \text{(Eq. 3.2)}$$

$$f_i = {}^{r_i}/_{\sum_{i=1}^{n}(p_i \times r_i)} \quad \text{(Eq. 3.3)}$$

where i corresponds to one of the sixteen different classes. A value of either 0 or 1 was randomly assigned to $p_i$ to determine whether each class would be included in a given trial. The mass fraction of each class, $f_i$, was attributed by randomly generating a number $r_i$ between

1 and 99, and then normalizing it to the sum of the $r_i$ values for all classes included in a trial. The $\varepsilon^{64}Zn$ ratio was preferred due to the abundance of $^{64}Zn$ isotope, which leads to better precision. The isotope compositions of each class were generated in a normal distribution, varying from the class mean within the respective uncertainty. Since Zn was, at most, only slightly siderophile during Earth's accretion, it is reasonable to assume that $\varepsilon^{64}Zn_{BE} = \varepsilon^{64}Zn_{BSE}$, which is characterized by the terrestrial sample BCR-2, with a mean of $\varepsilon^{64}Zn = 0.02 \pm 0.11$ (2se). The sums of the fractions of all CC and NC classes are taken to represent the Zn mass fraction derived from each reservoir, but only trials that yielded results within the terrestrial values were considered valid.

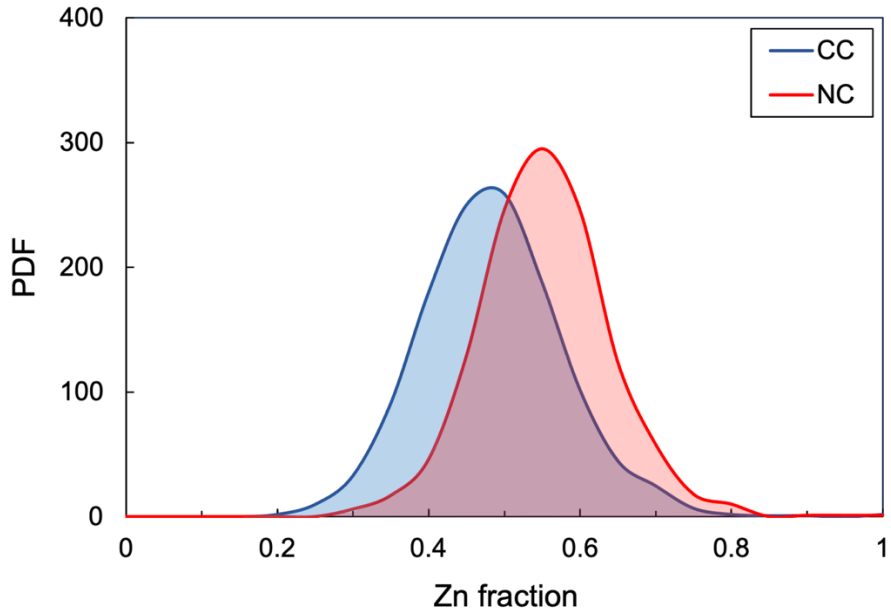



**Figure 3.5. Results from simulations to determine which combinations of CC and NC meteorites successfully produce an Earth-like nucleosynthetic Zn isotope composition.** The probability density functions (PDF) of the Zn mass fractions derived from CC and NC reservoirs, encompassing 1201 solutions, yield a mean $\varepsilon^{64}Zn = 0.03 \pm 0.12$ (2sd). The average mass fraction of Zn from CCs is 46 ± 19% (2sd), in line with estimates from Chapter 2. All meteorite groups characterized in this study and in Chapter 2 were used in the model (CI, CM, CO, CV, EH, EL, H, L, LL, R, IAB, HEDs, ureilites, aubrites, acapulcoites).

The 1201 valid solutions yielded a mean Zn mass fraction of 46 ± 19% (2sd) from CCs (Fig 3.5), in line with results from Chapter 2 (48 ± 15%, 2sd). No CC group appears to be favoured over the others, with all groups appearing in 70-80% of solutions contributing an average Zn mass fraction of ~17% each. Among NCCs, R chondrites appear less frequently (39% of solutions), while OCs and ECs feature in ~75-90% solutions. NC achondrites also appear in ~90% of solutions, while NC irons appear in ~60%. The mean Zn fractions from NCCs, NC achondrites and NC irons are 32 ± 14%, 19 ± 12%, and 13 ± 9%, respectively, with

an overall NC mean of 53 ± 9% (2sd). Notably, the lower end of the range determined for the CC Zn fraction (~30-50%) is compatible with estimates obtained in other recent Zn studies. Steller et al. (2022) obtained an estimated 36 ± 19% contribution from CCs employing CC and NC means, while results from Savage et al. (2022) yield a peak at 30% assuming CC and EC means for the two endmembers. Furthermore, while the probability density of the Monte Carlo simulations performed in this study peak at ~46% of Earth's Zn being derived from CCs, other factors must be considered in order to assess the likelihood of this outcome, such as the availability of the materials included in the models in the desired proportions during Earth's accretion, which is, at present, unconstrained. As such, a CC contribution of anywhere between ~30 and 65% of Earth's Zn inventory is therefore possible.

These results contrast with an estimate for K, which suggest a 20% contribution from CCs (Nie et al., 2023). A perfect correlation between different volatile elements is, however, not to be expected since they have distinct condensation temperatures, geochemical affinities, and nucleosynthetic origins. For instance, while both Zn and K are lithophile, Zn condenses at 726 K and is produced mainly through alpha-rich freezeout in supernovae, while K condenses at 1006 K and is produced in Type II supernovae (Lodders, 2003, Clayton, 2003). Nonetheless, it is likely that CCs also played an important role in supplying other volatiles to Earth. Since the volatile depletion patterns of CCs follow the sequence predicted by condensation from the solar nebula, the enrichment in Zn also extends to other moderately volatile elements – a pattern that is also observed for the BSE (Braukmüller et al., 2019). Furthermore, it is worth noting that addition of CMs would increase the estimated K contribution from CCs, as these meteorites have nucleosynthetic K isotope compositions that are indistinguishable from Earth (Nie et al., 2023).

### 3.5.2. The search for Earth's accreting material

The search for Earth's accreting material has led to multiple studies that used nucleosynthetic isotope anomalies as tracers to identify potential building blocks, often arriving at different mixing proportions of CC and NC material. Early work by Lodders (2000) was able to reproduce Earth's oxygen isotope composition by mixing 10% CI and CV material with 90% NCC material. Albarède et al. (2013) later showed this CC mix can also be replaced by a 9% addition of CMs. Still assuming chondritic nucleosynthetic isotope compositions but using a much more comprehensive approach, Dauphas (2017) was able to reproduce Earth's O, Ca, Ti, Cr, Ni, Mo, Ru, and Nd isotope compositions with 5% CO-CV, 25% OC, and 70% EC material.

Other studies included achondrites in their estimates, which can lead to very different results. Warren (2011) came to a 24/76 split between CCs and NCs using Cr, Ti and O isotopes. Fitoussi et al., (2016) favoured addition of 18-28% of a CI-CV mixture to NC material consisting of OCs and angrites. Schiller et al. (2018) inferred a 42% contribution from CI material to ureilite-like embryos based on Ca isotope anomalies, whilst Onyett et al. (2023) estimated a 26% CI contribution from nucleosynthetic Si isotope anomalies, with the remaining mass coming from NC achondrites. Inclusion of achondrites in such estimates often yields larger CC mass fractions. This reflects that many NC achondrites have more extreme depletions in the neutron-rich isotopes of the Fe-peak elements than chondrites. An exception to this is the estimate by Burkhardt et al., (2021), which is based primarily on s-process elements (Mo, Zr, Sr, Nd), but also includes Cr, and which arrived at a CC contribution of just 4%.

There are, however, additional factors that favour the incorporation of achondrites in Earth's building blocks. Multiple studies have shown that some achondrites have considerably heavier mass-dependent Si isotope compositions than chondrites, a feature that is also seen in the BSE (Fitoussi and Bourdon, 2012). Similarly, the mass-dependent Mg isotope compositions of achondrites and the BSE are heavier compared to results obtained for chondrites (Hin et al., 2017). It is hence difficult to reproduce the mass-dependent isotope fractionations observed for the BSE if only chondrites are assumed as precursor materials, even when extreme scenarios of Si sequestration into the core or a hidden Si reservoir in the lower mantle are considered (Fitoussi and Bourdon, 2012). Instead, these signatures most likely reflect accretion of differentiated planetesimals, which experienced substantial vapour loss from magma oceans during accretionary growth (Hin et al., 2017, Pringle et al., 2014).

Taking these factors into account, the models discussed in the following attempt to not only reproduce the Earth's nucleosynthetic isotope composition but also the concentrations of key major elements. The models are based on Monte Carlo simulations in which arbitrarily selected meteorite classes were mixed in randomly generated proportions. The isotope data included in the models are $\Delta^{17}O$, $\varepsilon^{48}Ca$, $\varepsilon^{50}Ti$, $\varepsilon^{54}Cr$, $\varepsilon^{62}Ni$, $\varepsilon^{64}Zn$, $\varepsilon^{96}Zr$, $\varepsilon^{84}Sr$, $\varepsilon^{145}Nd$, whilst the elemental data encompass the major elements Na, Mg, Si, P, Ca, K, Ti, Fe, and Mn, normalized to Al and to CI chondrites. Results were also calculated for $\delta^{30}Si$ and $\delta^{25}Mg$ as well as the Al-normalized O, Zn, Sr, Zr, and Nd concentrations but these data were not used as criteria for the selection of valid solutions. All concentration and isotope data used in the models can be found in Tables 3.4 and 3.5.

Due to the lack of data for some isotope systems ($\varepsilon^{96}$Zr, $\varepsilon^{84}$Sr, and $\varepsilon^{145}$Nd), and of bulk parent body major element concentrations for some meteorite groups (R chondrites, acapulcoites, ureilites, aubrites, and IAB complex iron), only CCs, ECs, OCs, HED, and angrites were included in the models. Notably, some data is also missing for the parent bodies of angrites and HED meteorites. For instance, estimates for their bulk Zn concentrations are unavailable, as are Zr and Nd concentrations of the bulk angrite parent body, Nd abundance of the HED parent body, as well as the nucleosynthetic Zn isotope composition of angrites.

The Zn concentrations of the HED and angrite parent bodies were thus allowed to vary within the observed ranges of the respective meteorites, which correspond to 0.11 – 8.9 μg $g^{-1}$ and 5 – 12 μg $g^{-1}$ for HEDs and angrites, respectively (Table 3.5; Paniello et al., 2012; Warren & Kallemeyn, 1990; Warren and Kallemeyn, 1995). Notably, it is possible that the available samples are not representative of the bulk parent bodies, since they may have experienced further extents of volatile depletion, possibly due to magmatic processes or volatilization caused by impacts. However, the low Zn concentrations of diogenites (0.29 – 3.10 μg $g^{-1}$; Paniello et al., 2012), which sample deeper layers of the HED parent body, and the heavy Zn isotope compositions of unbrecciated eucrites imply that evaporation and Zn loss were not limited to impact-driven volatilization or to crustal samples (Paniello et al. 2012).

Furthermore, since Zn does not partition strongly into metal, the Zn concentrations of the bulk parent bodies are likely lower than the silicate fractions sampled by the meteorites. Hence, while the limited constraints preclude further estimates for the bulk Zn concentrations of the achondritic parent bodies, it seems unlikely that they would be substantially higher than measured values of achondritic meteorites. In turn, since Zr and Nd concentrations do not vary as substantially as Zn among different Solar System materials, the concentrations of these elements for the achondrite parent bodies were allowed to vary within the range of concentrations estimated for the BE.

Because angrites are rare (only 20 specimens) and have very low Zn contents, it was not possible to characterize the nucleosynthetic Zn isotope composition of this meteorite class for this study. However, the $\varepsilon^{64}$Zn value for angrites was estimated independently through bivariate regressions following the method of Wu and Yu (2018). Three regressions were performed based on the correlations between $\varepsilon^{64}$Zn and $\varepsilon^{48}$Ca, $\varepsilon^{50}$Ti, and $\varepsilon^{54}$Cr, which show good to excellent agreement (Fig. 3.3). The results of the three regressions ($\varepsilon^{64}$Zn = 0.82 ± 0.35, 0.88 ± 0.13, and 0.96 ± 0.20 for correlations with $\varepsilon^{48}$Ca, $\varepsilon^{50}$Ti, and $\varepsilon^{54}$Cr, respectively) were averaged, and the uncertainties of the slopes, the intercepts, and of the measured $\varepsilon^{48}$Ca,

$\varepsilon^{50}$Ti, and $\varepsilon^{54}$Cr values for angrites were propagated, resulting in an estimated $\varepsilon^{64}$Zn = 0.89 ± 0.42 for angrites.

With the exception of Cr and Ni, isotope anomalies of siderophile elements (Mo, Ru, Fe) were not included in the models because they only trace the final stages of accretion. Nickel is a major element and the nucleosynthetic Ni isotope anomalies determined so far for CC and NC meteorites are relatively small and often unresolvable (Table 3.4); Ni isotope compositions are therefore not expected to be a limiting factor for the models. Chromium can also behave as a lithophile element and has a relatively low metal-silicate partition coefficient ($D_{met\text{-}sil} \cong$ 2-3, Siebert et al., 2011) compared other siderophile elements for which anomalies have been found; in particular Mo and Ru have $D_{met\text{-}sil}$ values of about 90-150 and >10,000, respectively (Siebert et al., 2011; Mann et al., 2012). Chromium isotopes also show excellent agreement with the $\varepsilon^{64}$Zn anomalies characterized in this study ($R^2$ = 0.83, Fig. 3.3), suggesting that the models are expected to yield similar solutions for these isotope systems. As such, both the Ni and Cr isotope anomalies were included in the models and used as criteria for the selection of valid results.

The Monte Carlo simulations were designed according to the following equations:

$$R_{BE} = \frac{\sum_{i=1}^{n} p_i \times R_i \times [E]_i \times f_i}{\sum_{i=1}^{n} p_i \times [E]_i \times f_i} \quad \text{(Eq. 3.4)}$$

$$[E]_{BE} = \sum_{i=1}^{n} p_i \times [E]_i \times f_i \quad \text{(Eq. 3.5)}$$

where i corresponds to the different meteorite groups included in the model (Tables 3.4 and 3.5). A value of either 0 or 1 was randomly assigned to $p_i$ to define whether each class would be included in a given trial. The mass fraction of each class, $f_i$, was defined by randomly generating a number $r_i$ between 1 and 20 for CCs and 1 and 99 for NCs, and then normalizing it to the sum of the $r_i$ values for all classes included in each trial, according to equation 3.2. The CC mass fraction was purposefully assigned smaller values compared to NCs to optimize the number of valid solutions, as most previous studies suggest that the CC mass fraction is relatively limited (Chapter 2, Dauphas, 2017, Fitoussi et al., 2016, Lodders, 2000, Burkhardt et al., 2021). Notably, r values for NCs were also allowed within the CC range (1-20), such that large proportions (>50%) of CC material were still possible, but less likely. The isotope ratios $R_i$ were generated in a normal distribution, varying within uncertainties from their respective class means (Table 3.4). The concentrations of each element $[E]_i$ were randomly generated numbers between the lowest and highest measured results in the case of chondrites or estimated values for the different bulk achondrite parent bodies (Table 3.5).

**Table 3.4. Compiled isotope data used in the modelling.**

| **Group** | Reservoir | $\Delta^{17}O$ | 95% CI | $\varepsilon^{48}Ca$ | 95% CI | $\varepsilon^{50}Ti$ | 95% CI | $\varepsilon^{54}Cr$ | 95% CI | $\varepsilon^{62}Ni$ | 95% CI | $\varepsilon^{64}Zn$ | 2se/2sd* |
|---|---|---|---|---|---|---|---|---|---|---|---|---|---|
| CI | CC | 0.07 | 0.28 | 2.11 | 0.20 | 1.89 | 0.15 | 1.55 | 0.07 | 0.17 | 0.09 | -0.93 | 0.20 |
| CM | CC | -2.52 | 0.46 | 3.14 | 0.14 | 2.89 | 0.15 | 0.97 | 0.08 | 0.11 | 0.03 | -1.15 | 0.20 |
| CO | CC | -4.21 | 0.68 | 3.87 | 0.56 | 3.58 | 0.85 | 0.83 | 0.18 | 0.11 | 0.04 | -0.57 | 0.22 |
| CV | CC | -3.99 | 0.33 | 3.50 | 0.38 | 3.45 | 0.19 | 0.94 | 0.08 | 0.11 | 0.03 | -0.83 | 0.08 |
| H | NC | 0.67 | 0.10 | -0.23 | 0.03 | -0.65 | 0.14 | -0.31 | 0.13 | -0.06 | 0.03 | 0.47 | 0.06* |
| L | NC | 0.97 | 0.09 | -0.32 | 0.11 | -0.67 | 0.10 | -0.4 | 0.06 | -0.04 | 0.04 | 0.76 | 0.26 |
| LL | NC | 1.11 | 0.11 | -0.44 | 0.09 | -0.67 | 0.08 | -0.42 | 0.08 | -0.07 | 0.03 | 0.67 | 0.02* |
| *OC Mean* | | *0.92* | *0.05* | *-0.31* | *0.09* | *-0.66* | *0.06* | *-0.37* | *0.06* | *-0.06* | *0.02* | *0.63* | *0.13* |
| EH | NC | -0.09 | 0.12 | -0.32 | 0.56 | -0.14 | 0.07 | 0.02 | 0.05 | 0.03 | 0.03 | 0.87 | 0.13 |
| EL | NC | -0.04 | 0.08 | -0.40 | 0.51 | -0.28 | 0.17 | 0.03 | 0.05 | -0.03 | 0.07 | 0.63 | 0.25 |
| *EC Mean* | | *-0.06* | *0.03* | *-0.37* | *0.37* | *-0.20* | *0.08* | *0.03* | *0.03* | *0.00* | *0.03* | *0.75* | *0.07* |
| HED | NC | -0.24 | 0.06 | -1.24 | 0.29 | -1.23 | 0.05 | -0.69 | 0.08 | 0.03 | 0.12 | 1.39 | 0.39 |
| Angrites | NC | -0.08 | 0.06 | -1.06 | 0.33 | -1.18 | 0.08 | -0.43 | 0.06 | 0.01 | 0.05 | 0.89[a] | 0.42* |
| BSE | | -0.05 | 0.06 | 0.00 | 0.04 | 0.00 | 0.01 | 0.10 | 0.13 | 0.03 | 0.02 | 0.02 | 0.11 |
| UM1 | NC | -0.06 | 0.03 | -0.37 | 0.37 | -0.20 | 0.08 | 0.03 | 0.03 | 0.00 | 0.03 | 0.75 | 0.07 |
| UM2 | NC | 0.92 | 0.05 | -0.31 | 0.09 | -0.66 | 0.06 | -0.37 | 0.06 | -0.06 | 0.02 | 0.63 | 0.13 |

Continued on next page.

**Table 3.4. Continued.**

| **Group** | Reservoir | $\varepsilon^{96}$Zr | 95% CI | $\varepsilon^{84}$Sr | 95% CI | $\varepsilon^{145}$Nd | 95% CI / 2sd* | $\delta^{30}$Si | 2sd | $\delta^{25}$Mg | 2se |
|---|---|---|---|---|---|---|---|---|---|---|---|
| CI | CC | 0.34 | 0.54 | 0.40 | 0.10 | 0.02 | 0.02 | -0.52 | 0.02 | -0.100 | 0.007 |
| CM | CC | 0.70 | 0.67 | 0.40 | 0.09 | 0.06 | 0.03 | -0.53 | 0.02 | -0.145 | 0.010 |
| CO | CC | 0.94 | 0.20 | 0.41 | 0.21 | 0.06 | 0.02 | -0.46 | 0.07 | -0.158 | 0.010 |
| CV | CC | 0.96 | 0.37 | 0.63 | 0.10 | 0.04 | 0.04 | -0.48 | 0.12 | -0.139[b] | 0.011 |
| H | NC | 0.32 | 0.08 | -0.13 | 0.10 | 0.07 | 0.04 | -0.46 | 0.05 | -0.145 | 0.018 |
| L | NC | 0.40 | 0.40 | -0.11 | 0.10 | 0.04 | 0.06 | -0.48 | 0.01 | -0.147[c] | 0.004 |
| LL | NC | 0.34 | 0.25 | -0.43 | 0.10 | 0.01 | 0.03 | -0.40 | 0.06 | -0.150 | 0.003 |
| *OC Mean* | | *0.32* | *0.04* | *-0.17* | *0.15* | *0.05* | *0.03* | *-0.44* | *0.06* | *-0.147* | *0.003* |
| EH | NC | 0.04 | 0.24 | -0.21 | 0.12 | 0.03 | 0.04 | -0.77 | 0.08 | -0.133 | 0.007 |
| EL | NC | 0.20 | 0.40 | - | - | 0.03 | 0.02 | -0.59 | 0.09 | -0.134 | 0.003 |
| *EC Mean* | | *0.08* | *0.20* | *-0.21* | *0.12* | *0.03* | *0.02* | *-0.68* | *0.18* | *-0.134* | *0.001* |
| HED | NC | 0.37 | 0.12 | 0.01 | 0.10 | 0.06 | 0.02* | -0.43 | 0.11 | -0.111 | 0.016 |
| Angrites | NC | 0.51 | 0.10 | 0.00 | 0.10 | 0.07 | 0.02 | -0.33 | 0.12 | -0.079 | 0.010 |
| BSE | | 0.01 | 0.03 | -0.19 | 0.16 | -0.01 | 0.04* | -0.29 | 0.08 | -0.121 | 0.005 |
| UM1 | NC | 0.08 | 0.20 | -0.21 | 0.12 | 0.03 | 0.02 | -0.68 | 0.18 | -0.134 | 0.001 |
| UM2 | NC | 0.32 | 0.04 | -0.17 | 0.15 | 0.05 | 0.03 | -0.44 | 0.06 | -0.147 | 0.003 |

References: Burkhardt et al., 2017, Burkhardt et al., 2021, Frossard et al., 2021, Hin et al., 2017, Armytage et al., 2011, Pringle et al., 2013, Savage and Moynier, 2013, Pringle et al., 2014. A: Estimated by bivariant regression, see text for details. B: no data available so CC mean was used instead. C: no data available, so OC mean was used.

**Table 3.5. Compiled concentration data for the elements and meteorite classes considered in the modelling.**

| Class | Bulk Earth | CI | CM | CO | CV | H |
|---|---|---|---|---|---|---|
| References | [1-5, 15] | [6, 7] | [6, 7] | [6, 7] | [6, 7] | [6, 8] |
| Na (%) | 0.125 – 0.267 | 0.25 – 0.58 | 0.087 – 0.46 | 0.365 – 0.41 | 0.238 – 0.316 | 0.591 – 0.659 |
| Mg (%) | 13.9 – 15.4 | 9.5 – 10.5 | 11.5 – 12.4 | 10.8 – 13 | 12.5 – 14.5 | 13.8 – 14.4 |
| Al (%) | 1.41 – 1.63 | 0.80 – 0.86 | 1.1 – 1.24 | 1.11 – 1.43 | 1.42. -1.75 | 1.1 – 1.2 |
| Si (%) | 14.2 – 16.8 | 10.5 | 12.9 | 15.9 | 15.6 | 16.9 |
| P ($\mu g\ g^{-1}$) | 555 – 1920 | 845 – 1108 | 900 – 1108 | 1010 – 1060 | 990 – 1041 | 1080 |
| Ca (%) | 1.54 – 1.77 | 0.78 – 1.01 | 1.01 – 1.55 | 1.28 – 1.58 | 1.59 – 1.90 | 1.17 – 1.33 |
| K ($\mu g\ g^{-1}$) | 135 – 197 | 407 – 608 | 206 – 518 | 272 – 345 | 251 – 310 | 727 – 860 |
| Ti ($\mu g\ g^{-1}$) | 762 – 822 | 381 – 458 | 520 – 664 | 601 -656 | 753 – 980 | 600 |
| Fe (%) | 29.6 – 32.7 | 18.2 – 21.3 | 21 – 23.6 | 21.7 – 24.8 | 22.2 – 23.8 | 26.4 – 29.7 |
| Mn ($\mu g\ g^{-1}$) | 750 – 2594 | 1900 – 2061 | 1700 – 1920 | 1475 – 1650 | 1334 – 1465 | 2180 – 2430 |
| O (%) | 20.12 – 31.67 | 46 | 43.2 | 37 | 37 | 35.7 |
| Cr ($\mu g\ g^{-1}$) | 3300 – 4466 | 2575 – 3001 | 3033 – 3478 | 3111 – 3550 | 3253 – 3603 | 3460 – 3870 |
| Ni (%) | 1.69 – 1.85 | 1.07 – 1.26 | 1.2 – 1.42 | 1.2 – 1.4 | 1.29 – 1.42 | 1.55 – 1.77 |
| Zn ($\mu g\ g^{-1}$) | 40 – 74 | 312 – 391 | 182 – 214 | 100 – 119 | 112 – 127 | 41 – 55 |
| Zr ($\mu g\ g^{-1}$) | 6.32 – 7.1 | 3.87 – 5 | 4.48 – 10.1 | 4.92 – 12.7 | 5.85 – 15.3 | 10 |
| Sr ($\mu g\ g^{-1}$) | 13 – 14.7 | 3.8-4 | 8 | 7.8 | 8.3 | 6.3 |
| Nd ($\mu g\ g^{-1}$) | 0.761 – 0.869 | 0.457 | 0.631 | 0.772 | 0.99 | 0.628 |

Continued on next page.

**Table 3.5. Continued.**

| Class | L | LL | EH | EL | HED | Angrite | UM1/2 |
|---|---|---|---|---|---|---|---|
| References | [6, 8] | [6, 8] | [6, 9] | [6, 9] | [10 - 15] | [15 - 17] | [10 - 17] |
| Na (%) | 0.58 - 0.731 | 0.576 - 0.728 | 0.474 - 0.78 | 0.51 - 0.63 | 0.104 - 0.54 | 0.02 | 0.02 - 0.54 |
| Mg (%) | 14.1 - 15.2 | 14.7 - 15.5 | 9.6 11.9 | 13.3 - 14.6 | 15 - 18.4 | 12.0 | 12.0 - 18.4 |
| Al (%) | 1.17 - 1.26 | 1.16 - 1.31 | 0.74 - 0.87 | 1 - 1.14 | 1.2 - 1.9 | 1.43 | 1.2 - 1.43 |
| Si (%) | 18.5 | 18.9 | 16.7 | 18.6 | 20.9 - 21.5 | 13.1 | 13.1 - 21.5 |
| P ($\mu g\ g^{-1}$) | 950 | 850 | 2000 | 1170 | 1877 | 938 | 938 - 1877 |
| Ca (%) | 1.23 - 1.38 | 1.18 - 1.39 | 0.65 - 1 | 0.85 - 1.2 | 1.3 - 2.14 | 1.50 | 1.3 - 2.14 |
| K ($\mu g\ g^{-1}$) | 505 - 950 | 637 - 922 | 402 - 1240 | 600 - 845 | 30 - 54 | 12 | 12 - 54 |
| Ti ($\mu g\ g^{-1}$) | 630 | 620 | 450 | 580 | 347.4 - 830 | 599.0 | 347.4 - 830 |
| Fe (%) | 20.3 - 24.5 | 17.6 - 21.2 | 24.9 - 31.5 | 19.5 - 27 | 11.1 - 29.2 | 19.4 | 11.1 - 29.2 |
| Mn ($\mu g\ g^{-1}$) | 2410 - 2700 | 2490 - 2720 | 1820 - 2650 | 1120 - 2560 | 1394 - 4336 | 1549 | 1394 - 4336 |
| O (%) | 37.7 | 40 | 28 | 31 | 34.48 - 42.65 | 34.5 | 34.48 - 42.65 |
| Cr ($\mu g\ g^{-1}$) | 3630 - 3940 | 3630 - 4060 | 2820 - 3870 | 2460 - 3870 | 1916 - 4611 | 2737 | 1916 - 4611 |
| Ni (%) | 1.1 - 1.47 | 0.89 - 1.12 | 1.51 - 2.02 | 1.03 - 1.6 | 0.02 - 1.7 | 1 | 0.02 - 1.7 |
| Zn ($\mu g\ g^{-1}$) | 43.5 - 63 | 41 - 60.6 | 21 - 342 | 13 - 26 | 0.11 – 8.9[a] | 5 – 12[a] | 0.11 - 12 |
| Zr ($\mu g\ g^{-1}$) | 11.1 | 11.1 | 7.2 | 8.2 | 7.9 | 6.32 – 7.1[b] | 6.32 – 7.1[b] |
| Sr ($\mu g\ g^{-1}$) | 5.9 | 5.9 | 4.9 | 5.2 | 16.6 | 10 | 10 – 16.6 |
| Nd ($\mu g\ g^{-1}$) | 0.682 | 0.659 | 0.46 | 0.233 | 0.761 - 0.869[b] | 0.761 - 0.869[b] | 0.761 - 0.869[b] |

References: [1] McDonough (2014); [2] McDonough (1995); [3] Wang et al. (2018); [4] Kargel (1993); [5] Morgan (1980); [6] Wasson & Kallemeyn (1988); [7] Braükmuller et al. (2018); [8] Kallemeyn et al (1989); [9] Kallemeyn & Wasson (1986); [10] Dreibus et al. (1977); [11] Ashcroft et al. (2015); [12] Morgan et al. (1977); [13] Paniello et al. (2012), [14] Jurewics et al. (1991); [15] Liebske & Khan (2019); [16] Warren & Kallemeyn (1990); [17] Warren & Kallemeyn (1995); a: no estimates for bulk parent body were available, so both the HED and Angrite parent bodies were allowed to vary within measured values for meteorites; b: no estimates for bulk parent body available, allowed to vary within estimated BE range.

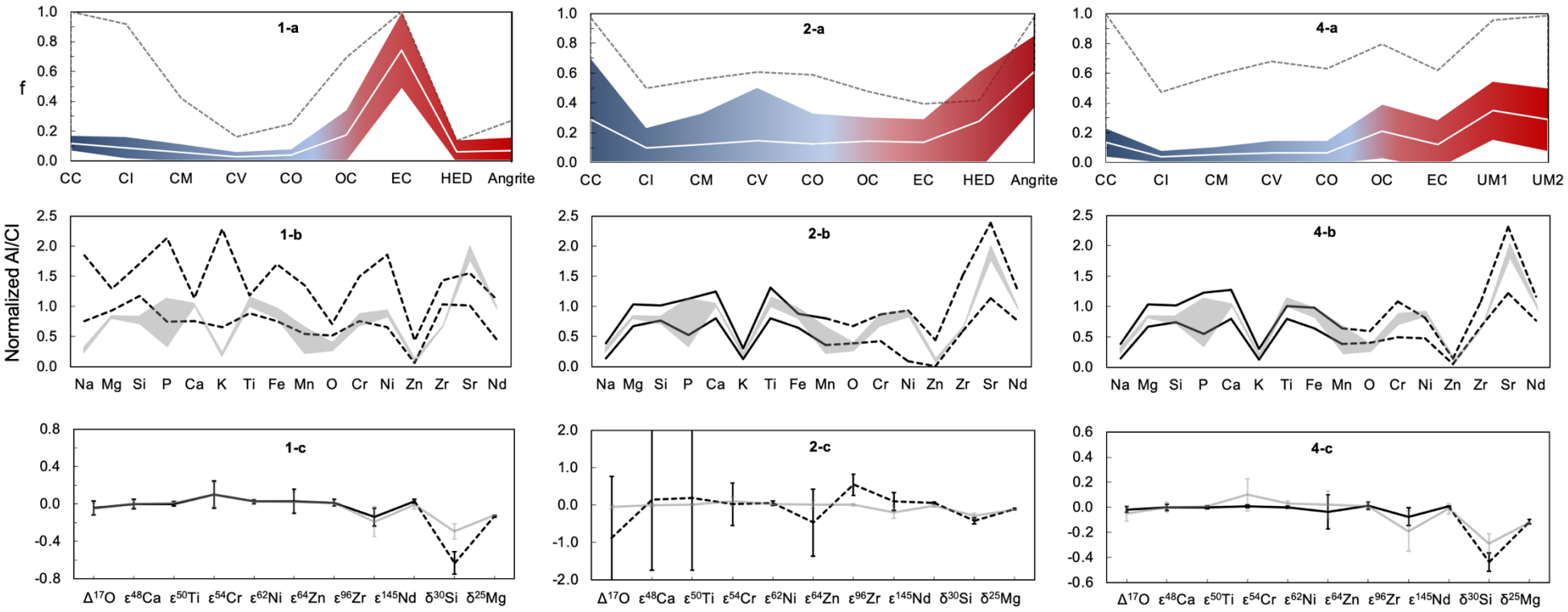



**Figure 3.6. Mixing models that attempt to reproduce the isotope and elemental compositions of the bulk Earth.** The numbers on the panels correspond to the Run number of the simulation (Table 3.6). a) mean mass fraction obtained for each meteorite group for all valid solutions (white line) and respective uncertainties (2sd, coloured fields). The dashed line illustrates the frequency in which each group appears in valid solutions, whereby f = 1 means that a given group appears in 100% of valid solutions. The CC fraction denotes the sum of all CC groups. b) Ratio of a given element to Al, normalized to CI chondrites. The lines represent the highest and lowest values obtained for all valid solutions, while the grey field shows estimates for the BE (Table 3.5). Elements shown with a solid line were used as criteria for the selection of valid results, while elements with dashed line were not. c) Mean isotope compositions for all valid solutions of each run, with error bars indicating twice the standard deviation from the mean. Ratios shown with a solid line were used as criteria for selection of valid results, while ratios with a dashed line were not. The grey line denotes literature data for the BSE (Table 3.4).

The results of the models are shown in Figure 3.6 and summarized in Table 3.6. The resulting mass fractions, isotope ratios and major element compositions correspond to the mean and twice the standard deviation of all valid trials. The first run (Run 1) encompassed $2 \times 10^9$ simulations and only the results that yielded terrestrial isotope compositions were considered valid (Fig. 3.6). This resulted in an average $f_{CC}$ mean of 12 ± 5% (2sd), with CIs appearing more frequently (in 92% of solutions) followed by CMs (42%), COs (25%), and lastly by CVs (16%). As expected, ECs are by far the most recurring group, appearing in 100% of solutions with a mass fraction of 74 ± 25%, while OCs appear in 70% of solutions with a fraction of 17 ± 17%. Angrites and HEDs feature in 27% and 14% of solutions, but their mass fractions are limited to just $6^{+7}_{-6}$ % and $7^{+9}_{-7}$ %, respectively. The CC mass fraction is compatible with estimates by some studies that employed chondrites as endmembers (Lodders, 2000, Albarède et al., 2013). As expected, however, this approach yields a much more volatile rich BE, with Na/Al, Mg/Al, Si/Al, and K/Al ratios that clearly exceed all current estimates. Furthermore, it also generates a BSE Si isotope composition that is significantly lighter than data-based estimates (Savage et al., 2010).

In Run 2, $10^5$ simulations were performed, but only the solutions that yielded elemental ratios within 20% of terrestrial values were selected. The general 20% window was allowed since concentration measurements and estimates aren't typically accompanied by uncertainties. Following these criteria, the results yield a much wider range of CC mass fractions of $29^{+41}_{-29}$ %, with all CC classes appearing in 50-60% of solutions with mean fractions ranging from $10^{+13}_{-10}$ % to $15^{+35}_{-15}$ % for CIs and CVs, respectively. ECs and OCs are still featured prominently, appearing in 39% and 48% of valid solutions, respectively. However, the mass fractions of these groups are much more limited in this scenario, with both averaging at $14^{+16}_{-14}$ each. Finally, HEDs and angrites appear in 42 and 98% of solutions, with mean mass fractions of $28^{+33}_{-28}$ % and 61 ± 24%, respectively.

Notably, even the elemental ratios that were not used as criteria for the selection of valid results are also reproduced in Run 2. This stands in contrast to Run 1, where the Sr/Al ratio was substantially lower than estimates for the BE, while O/Al and Zr/Al were marginally different. Run 2 also produced $\delta^{30}$Si and $\delta^{25}$Mg values that largely overlap with BSE estimates, with means of $\delta^{30}Si = -0.42 \pm 0.09$ and $\delta^{25}Mg = -0.11 \pm 0.02$ (2sd) for all valid solutions, even though the Si and Mg isotope data were not used as criteria for the selection of acceptable results. However, these mixing proportions lead to highly variable nucleosynthetic isotope

compositions, which are mostly incompatible with Earth, particularly for O, Zn, and Zr, which are, on average, more CC-like.

Finally, Run 3 with $10^8$ simulations, used both the nucleosynthetic isotope compositions and the elemental data as criteria for the selection of valid results. This run, however, yielded no valid solutions, which implies that a scenario in which Earth accreted only from known sampled materials is highly unlikely. Thus, it appears that a component that has achondrite-like volatile element depletions but NCC-like nucleosynthetic isotope compositions is required. A potential solution for this is if aubrites are considered as one of the main contributors to Earth's accretion. These achondritic meteorites have nucleosynthetic O, Ca, Ti, Cr, and Ni isotope compositions that are indistinguishable from Earth, and they are substantially more volatile-depleted than ECs, with Zn concentrations ranging from 0.5 to 2 μg $g^{-1}$ (Burkhardt et al., 2021; Wolf et al., 1983). However, the nucleosynthetic isotope compositions of s-process elements, and parent-body elemental concentrations for this meteorite group are unavailable, making it difficult to test this hypothesis. But it is worth noting that the $\delta^{30}$Si value of aubrites is indistinguishable from some chondrites, and clearly lighter than the BSE (Table 3.4).

**Table 3.6. Summary of results from the Monte Carlo simulations.**

| Run | 1 | 2 | 3 | 4 |
|---|---|---|---|---|
| Nucleosynthetic isotope composition | ✓ | | ✓ | ✓ |
| Major element ratios | | ✓ | ✓ | ✓ |
| Endmembers | CC, NCC, Achondrites | CC, NCC, Achondrites | CC, NCC, Achondrites | CC, NCC, UM |
| Trials | $10^9$ | $10^6$ | $10^8$ | $10^9$ |
| Solutions | 713 | 8011 | 0 | 1098 |
| CC (%, ± 2sd) | 12 ± 5 | $29^{+41}_{-29}$ | - | 14 ± 9 |
| NCC (%, ± 2sd) | 86 ± 11 | 19 ± 16 | - | 24 ± 13 |
| Achondrites/UM (%, ± 2sd) | $10^{+14}_{-10}$ | $73^{+27}_{-47}$ | - | 62 ± 13 |

Groups included in the models: CI, CM, CO, CV, EH, EL, H, L, LL, HEDs, angrites, unsampled material 1 and 2 (UM1 and UM2: HED/angrite-like elemental abundances and mass-dependent isotope compositions, but EC and OC-like nucleosynthetic isotope compositions for UM1 and UM2, respectively). Checkmarks indicate BE characteristics that are successfully reproduced in each run.

### 3.5.3. Unsampled material

The models suggest that Earth likely accreted unsampled, volatile-depleted material with an NCC-like nucleosynthetic isotope composition. Therefore, another simulation (Run 4) was performed which included two hypothetical unsampled materials, representing differentiated planetesimals. Since ECs and OCs accounted for ~90% of the mass in Run 1, which successfully reproduced nucleosynthetic isotope compositions, in Run 4 the unsampled materials are assumed to average out to OC and EC-like nucleosynthetic isotope compositions, with mean OC and EC values attributed to Unsampled Materials 1 and 2 (UM1 and UM2), respectively. In turn, achondrites correspond to most of the mass in Run 2 (73 ± 47%), such that their elemental abundances appear to be most compatible with the BE. Furthermore, the mass-dependent Si and Mg isotope compositions of achondrites are also heavier than those of chondrites, and largely overlap with BE estimates (Table 3.4). Hence, the elemental abundances and mass-dependent Si and Mg isotope compositions of both UM1 and UM2 were allowed to vary within estimates for the HED and angrite parent bodies.

For Run 4, both the nucleosynthetic isotope and the major element compositions were used as criteria for selection, in addition to the final BE Zn concentration, which is estimated to be between 40 and 70 $\mu g\ g^{-1}$ (McDonough, 2014, Mahan et al., 2018b, Wang et al., 2018). This yielded a 14 ± 9% CC contribution, with 24 ± 13% from NCCs, and the remaining 62 ± 13% coming from the unsampled materials, with 35 ± 20% from UM1 and 29 ± 21% from UM2. As expected, despite not being used as criteria, the remaining elemental data (O, Cr, Ni, Zn, Zr, Sr, Nd) are largely compatible with BE values. The resulting $\delta^{25}$Mg values are also typically consistent with BSE estimates, while the mean $\delta^{30}$Si is lighter, but still overlaps with estimates for the BSE. As such, both Earth's volatile element depletion and its nucleosynthetic isotope composition can be accounted for by accreting primarily from differentiated planetesimals with nucleosynthetic isotope compositions akin to OCs and ECs.

The need for some unsampled material in Earth's accretion was previously raised, because the nucleosynthetic Mo isotope composition of the BSE also requires the addition of material that is more s-process enriched than any known meteorites (Burkhardt et al., 2021). Therefore, it is possible that the unsampled material proposed in this study is also more enriched in s-process isotopes than the ECs or OCs compositions that currently define UM1 and UM2. This would satisfy the Mo isotope constraints, and likely change the proportions of CC vs NC materials. However, as Mo is moderately siderophile and only records the final stages of accretion, it is not necessary for all UM1 and UM2 material to be s-process enriched,

as this is not a requirement that follows from the s-process isotope anomalies of other elements that are considered in the models. Instead, it is conceivable that only the mass fraction of unsampled material that ultimately determined the BSE Mo isotope ratios had a more extreme s-process enrichment, and this may hence have had only a minor impact on the overall BE composition.

Based on its metal-silicate partition coefficient, Mo isotopes have been inferred to record the final ~10-20% of Earth's accretion (Dauphas, 2017). Mass balance estimates of Earth's accreting material that are based on Mo isotope data typically apply the same Mo concentration for all materials. This implies that the Mo isotope composition of the BSE is dominated by the Moon-forming impactor Theia, with a negligible contribution from previously accreted material, and a much more limited supply coming from the late veneer (Burkhardt et al., 2021, Budde et al., 2019). This may, however, not be the case. At the time of the giant impact, ~30-150 Ma after CAIs (Dauphas and Chaussidon, 2011), Theia would have completed its differentiation, such that most of its Mo would have segregated to the core. If Mo is assumed to have the same $D_{met\text{-}sil}$ value on Theia as in the BE (D=90-150, Siebert et al., 2011), Theia's silicate fraction would hold only ~1% of its Mo budget. Thus, for Theia's Mo contribution to be recorded by the BSE, its core and the BSE would have to at least partially equilibrate.

However, the extent of this equilibration is debated, with Hf-W based estimates ranging from as little as 4% to complete equilibration (Halliday, 2004, Kleine et al., 2009, Rudge et al., 2010, Touboul et al., 2015). As such, it is unclear how much of the BE's mass actually corresponds to this s-process enriched material recorded by the BSE's Mo composition. A complete equilibration scenario implies that ~5-10% of Earth's mass equates to this s-process enriched material. Alternatively, if equilibration was inefficient, the total mass of s-process enriched material could be more limited, such that this material may be diluted enough by the remaining accreting material that its compositional impact on s-process isotope anomalies of lithophile elements is negligible. However, the possibility that the unsampled material proposed here also had nucleosynthetic isotope compositions that were distinct from NCCs and possibly more s-process enriched cannot be discarded.

### 3.5.4. Mode of accretion and volatile depletion

Volatile depletion has been attributed to processes taking place both prior to or during accretion, such as incomplete condensation of chondrite components from the nebular gas

(Wasson and Chou, 1974), or evaporative loss from magma oceans during planetesimal differentiation (Ringwood, 1966). Since the models presented in this study constrain not only the origin (inner or outer Solar System) but also the extent of volatile depletion of Earth's precursor materials, they may also provide constraints for the cause of volatile depletion and the mode of accretion.

The formation of terrestrial planets has been traditionally ascribed to amalgamation of progressively larger objects, starting with pebbles, progressing to planetesimals, and finally entering an oligarchic growth phase, where planetary embryos grow by accreting planetesimals (Wetherill, 1994, Canup and Agnor, 2000). In contrast, more recently, it was proposed that planetary embryos grow mainly through accretion of pebbles, similarly to what is thought to account for the rapid growth of gas giants (Johansen et al., 2021, Levison et al., 2015). In other words, in the first case, proto-Earth accreted from many planetesimals, while with pebble accretion, the number of planetesimals and planetary embryos involved was more limited, and a more substantial mass fraction was delivered by pebbles. Hence, these two scenarios have different implications for the proportion of CC and NC materials accreted by Earth, and for its volatile depletion.

The pebble accretion hypothesis dictates that Earth would have incorporated large amounts of undifferentiated material (Johansen et al., 2021, Levison et al., 2015). Proponents of this hypothesis suggest that NC planetesimals grew by accreting CI-like matrix material whilst the solar nebula was still present (Schiller et al., 2018, Onyett et al., 2023). Initial estimates based on $\varepsilon^{48}$Ca anomalies indicate the addition of 42% CI pebbles to ureilite-like planetary embryos to reproduce Earth's composition. Hence, this scenario conflicts with the outcomes of this study, as Run 4 suggests that Earth accreted mainly from differentiated materials with NCC-like isotope compositions (~60%), with the remaining mass coming from a mix of CCs and NCCs. This divergence arises because the proposed mixing proportion between CIs and ureilites is not compatible with other isotope systems, particularly as a 90/10 split between CIs and ureilites is required to reproduce the BSE O isotope composition. Furthermore, the incorporation of such a large fraction of CI-material during terrestrial accretion would lead to an extremely volatile-rich Earth.

A more recent pebble accretion model based on mass-independent Si isotopes concluded that Earth formed by addition of 26 ± 9% CI pebbles to broadly NC achondrite-like embryos (Onyett et al., 2023). This more conservative estimate relaxes the constraints on other isotope systems, as some NC achondrites have much more Earth-like O isotope composition

than ureilites (e.g., angrites, aubrites, Table 3.4). However, in order to accommodate the Zn isotope mass balance, a 26% contribution from CIs would still require that this component lost most of its Zn content, while the NC achondrites had to retain substantial amounts of Zn. In detail, a Zn concentration of 40-70 μg $g^{-1}$ for the BE, a 26/74 mass split between the CC and NC components, and a 45% Zn contribution from CCs, yields a Zn concentration of ~70-120 μg $g^{-1}$ for the CC component, which is much lower than CI values of 312-390 μg $g^{-1}$ (Table 3.5). In addition, the mass balance indicates a Zn abundance of ~23-43 μg $g^{-1}$ for the NC component, which is higher than observations for angrites and HED meteorites (0.11-12 μg $g^{-1}$, Table 3.5), for example.

To account for some of these discrepancies, Onyett et al. (2023) proposed that thermal processing of the pebble material during its passage through the gas envelopes around planetary embryos could not only account for substantial volatile loss but also decouple nucleosynthetic isotope anomalies, due to the distinct volatilities and thermal stabilities of different elements and their carrier phases. Such thermal processing is, however, very poorly constrained for carrier phases other than SiC and for elements other than Mo. Further studies are therefore required to test whether this mechanism is compatible with the observed BE isotope and elemental abundances.

Importantly, the estimated 26 ± 9% CI contribution to Earth's accreting material can be improved by constraining the Si abundances of the endmembers. Onyett et al. (2023) assumed invariable Si concentrations for the accreting materials, contrary to the distinct measured and estimated values for CIs, NC achondrites and the BE (Table 3.5). Furthermore, if the temperatures in the envelopes are high enough to induce substantial loss of volatiles and even appreciable amounts of Mo (50% $T_C$ = 1590 K, Lodders, 2003), then it is reasonable to assume that non-negligible amounts of Si (50% $T_C$ = 1310 K) would also be lost from the CI component during envelope processing, which would impact the elemental mass balance of the accretion model. Notably, Si loss is also likely required to account for Earth's non-chondritic and heavy $\delta^{30}$Si value (Pringle et al., 2014, Hin et al., 2017).

Alternatively, if envelope processing cannot account for Earth's volatile depletion, there are other plausible mechanisms that could induce volatile depletion in the pebble material prior to its accretion. Other CC groups are variably depleted in volatiles compared to CIs, with some classes, such as CB, CH, and CR, showing appreciable extents of depletion (Pringle et al., 2017, Braukmüller et al., 2018). This is partially due to the depletion of volatiles in chondrules (Pringle et al., 2017, Mahan et al., 2018a), but also in the matrix of other CC groups

compared to CI dust (Alexander, 2005). As described above, the estimated Zn concentration for the CC component of the Onyett et al. (2023) accretion scenario is ~70-120 μg/g, which is consistent with the Zn abundances observed for CKs, COs, and CVs (Braukmüller et al., 2018).

Replacing CIs with other CC groups would, however, increase the proportion of CC material required to reproduce the BSE's nucleosynthetic Si isotope composition, as other CC groups have Si isotope compositions that more closely resemble the BSE than CIs ($\mu^{30}Si_{CC}$ = 10.4 ± 3.6 to 19.1 ± 3.2, $\mu^{30}Si_{CI}$ = 32.8 ± 2.0; Onyett et al., 2023). As a consequence, the ratio of accreted chondrites to achondrites would have to be higher than the 26/74 estimate of Onyett et al. (2023). Furthermore, the nucleosynthetic Si isotope compositions of most CCs and NCCs overlap within uncertainties, suggesting that they can generally be interchanged. Thus, if the CI component in the pebble accretion scenario is assumed to be a mixture of different CC and NCC materials, then this scenario may be compatible with the estimate of Run 4, which yielded a 38/62 ratio between chondrites and achondrites. Hence, for the purposes of reproducing the nucleosynthetic isotope composition of the BSE, it would become irrelevant whether the chondritic material was delivered in the form of pebbles (comprised of matrix, chondrules, and refractory inclusions of different origins), or as fully formed planetesimals.

Notably, all CC groups display similar $\delta^{30}$Si values, which are lighter than the BSE, and ECs are even lighter than CCs (Table 3.4). Their mass-dependent Si isotope compositions likely reflect equilibrium condensation of different chondrite components from a nebular gas (Martins et al., 2021), while the BSE and bulk achondrite parent-body compositions have been linked to evaporative loss (Pringle et al., 2014; Hin et al., 2017). Hence, replacing the CI component with other types of less volatile rich chondritic material does not eliminate the need for additional Si loss from at least some of the accreting material.

Onyett et al. (2023) also noted a shift in mass-independent Si isotope compositions between achondrites and chondrites that correlates with the model ages of the parent bodies. More specifically, the Si isotope anomalies increase in the order NC achondrites, NCCs, and CCs, which also corresponds to the order in which the respective parent bodies accreted. The authors suggest this reflects progressive admixing of CI-like dust, such that bodies formed in the inner Solar System become more CI-like over time. While this may on average be the case for the isotope anomalies of Si and some other elements, including $\varepsilon^{48}$Ca, NCCs can also be less CI-like than some NC achondrites for other isotope systems, such as $\varepsilon^{95}$Mo (Fig. 3.7, Table 3.4). This reflects that for s-process isotope anomalies, the Earth and ECs often display endmember compositions, with NC achondrites (except aubrites) showing intermediate isotope

signatures between ECs and CCs. Once again, this decoupling may be addressed by envelope processing, but further studies are required to determine if that is plausible.

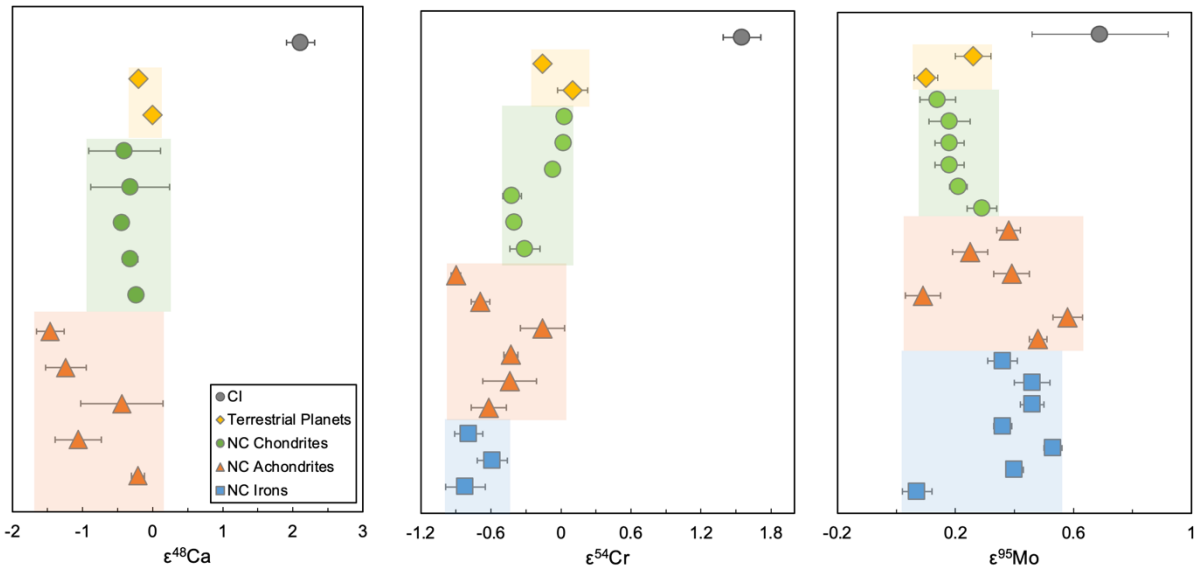



**Figure 3.7. Nucleosynthetic isotope compositions of inner Solar System bodies over time.** Shown are $\varepsilon^{48}$Ca, $\varepsilon^{54}$Cr, $\varepsilon^{95}$Mo values for CIs (grey circle), terrestrial planets (BSE, Mars; yellow diamonds), NC chondrites (green circles), NC achondrites (orange triangles), and NC iron (blue squares) meteorites. Ca, Cr, and Mo were selected to highlight both Fe-peak and s-process isotope variations for elements with lithophile and siderophile behaviour. Isotope data from Burkhardt et al. (2021).

While the proposed temporal shift towards more CI-like compositions may not be consistently observed for all nucleosynthetic isotope systems, NC achondrites and iron meteorites display considerably more variable isotope compositions than NCCs and the terrestrial planets (Fig. 3.7, Table 3.4). Iron meteorites are thought to be derived from planetesimals that formed in the first ~1.5 Ma after the condensation of CAIs, while achondrite parent bodies are generally considered to have formed between 2-5 Ma after CAIs (Dauphas and Chaussidon, 2011). These meteorites thus correspond to the first generation of planetesimals, and their isotope compositions span the entire range observed for NCCs and beyond (Table 3.4, Fig. 3.7).

It would hence be expected that mixing between NC achondrites and CI dust produces quite varied bulk isotope compositions. For example, the O isotope composition of the BE can be reproduced by accretion of between ~20 and 90% CI material, depending on which NC achondrite group is the second endmember. For $^{50}$Ti anomalies, the required CI mass fraction ranges from ~3 to 50%. Nonetheless, the inner Solar System bodies that completed their

accretion later are isotopically relatively homogeneous (Table 3.4, Fig. 3.7). Both NCCs, which formed after $^{26}$Al had substantially decayed, and the terrestrial planets, which likely accreted during and after the formation of chondrite parent bodies, display substantially less variable nucleosynthetic isotope compositions than iron and achondrite meteorites. In detail, Earth, the Moon, and possibly even Theia are indistinguishable from ECs for most isotope systems, while Mars is often intermediate between OCs and ECs (Dauphas et al., 2023, Dauphas, 2017, Canup et al., 2000). Importantly, this pattern is apparent for isotopes of elements with different geochemical affinities and that were formed by different nucleosynthetic processes.

Therefore, in order to achieve the similar compositions observed for the terrestrial planets by mixing of CI dust with isotopically diverse material equivalent to NC achondrites, either different proportions of CI dust would have to be added, consistently resulting in similar bulk compositions, or the NC material would have to be at least partially homogenized prior to or during accretion, with similar proportions of CI dust being added to each body. The first scenario requires coincidental circumstances, such that, in spite of potentially incorporating distinct NC-achondrite materials and variable amounts of CI-dust, the final bulk isotope compositions of the terrestrial planets are similar to each other and to NCCs, but without accreting the latter. In turn, the second scenario requires a separate mechanism to homogenize the NC-achondrite-like component.

Such a mechanism for homogenization of material accreted by terrestrial planets is addressed by the oligarchic growth scenario, which dictates that planetary embryos grow by accreting planetesimals from various heliocentric distances, decreasing the initial isotopic variability over time (Wetherill, 1994, Canup and Agnor, 2000, O'Neill and Palme, 2008). Based on O isotopes, it has been suggested that variations in the nucleosynthetic isotope compositions of smaller Solar System bodies are the result of statistical fluctuations, with the overall composition ultimately averaging out to those of larger bodies (Ozima et al., 2007). Notably, Run 4 of our modelling is in accord with unsampled precursor bodies that had diverse compositions, as these mix progressively to generate mean NCC-like nucleosynthetic isotope compositions. Furthermore, chondrules, which are the dominant component of all NCC groups (>40% for R chondrites, and 60-80% for OCs and ECs, Krot et al., 2014) have been hypothesized to form from collisions between growing planetary embryos (Johnson et al., 2015). If such a scenario is indeed possible, it would imply that both terrestrial planets and NC chondrules sampled the same increasingly homogenous materials, in the form of planetary embryos, which is fully compatible with their similar nucleosynthetic isotope compositions.

Another advantage of oligarchic growth is that it allows for substantial volatile depletion during accretion. As this hypothesis requires a large number of smaller planetesimals to coexist and later coalesce into embryos, it creates ample opportunity for evaporative loss during planetary growth. Hin et al. (2017) showed that collisions alone produce enough energy to induce the formation of magma oceans on planetesimals and cause subsequent vapour loss of up to 36% of mass in bodies smaller than $0.1M_{\oplus}$. This mechanism for volatile loss is preferred since the heavy mass-dependent Si, Mg, and Fe isotope compositions of the BSE are difficult to reconcile with either partial condensation from the solar nebula or with isotope fractionation during metal-silicate partitioning (Hin et al., 2017, Pringle et al., 2014). Their study also modelled isotope fractionation and elemental loss in such a scenario and was able to reproduce Earth's Mg, Si, and Fe isotope compositions and concentrations.

Furthermore, the decay of extinct radionuclides can also provide sufficient energy to melt early formed planetesimals that were large enough (>4 km), leading to the formation of magma oceans and subsequent evaporation of volatiles (Dauphas and Chaussidon, 2011). By comparing the velocities of molecules for an ideal gas under magma ocean conditions with the respective escape velocities, one can estimate the radii required for a planetesimal to retain its volatiles during degassing (Newcombe et al., 2023). Assuming a density of 2 to 4 g $cm^{-3}$, which is within the range for asteroids (Carry, 2012), the minimum radius required to retain gaseous Zn is about 550 to 780 km. For heavier moderately volatile elements, such a $Cd_{(g)}$ or $Te_{(g)}$, the threshold radii are similar at about 400 to 600 km. Thus, until planetesimals achieve radii exceeding several hundreds of km, they can be extensively devolatilized by magma ocean degassing, either as a consequence of collisions or radioactive decay. This is compatible with the modelling results of this study, which suggest that Earth accreted almost 70% of its mass from volatile-poor differentiated bodies. Once the planetesimals reached the critical size that prevented further volatile loss, late addition of chondritic material may have provided most of the volatile inventory.

Hence, while pebble accretion cannot be discarded until envelope processing is constrained, the accretion of multiple small, differentiated, volatile-depleted planetesimals, followed by the addition of chondritic material once the planetesimals have reached the critical size required to retain volatiles is fully consistent with Earth's elemental, nucleosynthetic, and Si and Mg mass-dependent isotope compositions.

### 3.5.5. Implications for the formation of habitable planets

The average Zn concentrations of the materials that provided valid results in the Run 4 models were also calculated, yielding 46 μg $g^{-1}$ for the BE, 178 μg $g^{-1}$ for CCs, 53 μg $g^{-1}$ for OCs, 148 μg $g^{-1}$ for ECs, and 9 μg $g^{-1}$ for the unsampled materials. This is consequential for the formation of habitable planets, since it implies that despite providing most of the Earth's mass (~60%), the unsampled differentiated materials only contributed ~12% of Earth's Zn inventory, thus rendering chondritic material a fundamental source of Zn, and likely other volatiles.

The limited Zn contribution from differentiated planetesimals, which likely extends to other volatiles, is in line both with geochemical evidence from achondrites (Newcombe et al., 2016) and astrophysical modelling (Lichtenberg et al., 2019), which suggest that water is efficiently lost from early formed, differentiated planetesimals, likely due to the presence of $^{26}$Al. Contrary to earlier assumptions, it is improbable that the $^{26}$Al present into the early Solar System was derived exclusively from a single supernova explosion (Young, 2014). This conclusion is important because it relaxes the constraint that newly formed planetary systems can only incorporate live $^{26}$Al if they are formed a few million years after a stellar explosion, due to the short half-life of $^{26}$Al (0.7 Ma). Instead, pre-supernova mass loss from giant stars may contribute as much as 50% of the galactic $^{26}$Al inventory. Such processes can continually replenish the interstellar medium over millions of years (Reiter, 2020) to generate appreciable levels of $^{26}$Al, particularly in the high-mass star forming regions where most planetary systems are formed.

Differentiation was ubiquitous among the first planetesimals to form in the Solar System due to the high abundance of $^{26}$Al (Dauphas and Chaussidon, 2011), and it was likely accompanied by substantial volatile loss (Hin et al., 2017). In contrast, chondrules formed later (1-4 Ma), and the parent bodies of chondritic meteorites likely incorporated less $^{26}$Al, preventing them from differentiating and losing appreciable amounts volatiles. Consequently, the late accretion of undifferentiated materials onto bodies that were large enough to retain volatiles during accretion (hundreds of km), may be required to achieve the volatile budget of terrestrial planets. Furthermore, since similar levels of $^{26}$Al are likely to be present in other nascent planetary systems, planetesimals formed outside of our Solar System are also expected to undergo differentiation accompanied by volatile loss. Thus, late accretion of undifferentiated material, which can more efficiently retain its volatile content due to limited melting and

degassing, may also be required to supply enough volatiles for the emergence of life in terrestrial exoplanets.

## 3.6 Conclusions

The nucleosynthetic Zn isotope compositions of NC achondrites and iron meteorites are in agreement with previous findings, with all groups displaying enrichments in $^{64}$Zn and depletions in $^{68}$Zn and $^{70}$Zn. Overall, the Zn isotope anomalies show considerable correlations with the anomalies of the other Fe-peak elements. Furthermore, despite substantially expanding on previous datasets by encompassing a much more comprehensive variety of materials than previous Zn isotope studies, the new results confirm early estimates that almost half of Earth's Zn inventory is derived from the carbonaceous reservoir.

Mixing models suggest that while Earth's nucleosynthetic isotope composition can be reproduced by combinations of different chondritic materials, addition of differentiated planetesimals is likely required to account for Earth's mass-dependent isotope compositions and elemental abundances. Nonetheless, models including known achondritic materials cannot simultaneously reproduce Earth's elemental abundances, nucleosynthetic and mass-dependent isotope compositions. All these characteristics can be achieved, however, if about 60% of Earth's accreting material corresponds to unsampled highly volatile-depleted differentiated planetesimals, with a mean nucleosynthetic isotope composition akin to a 55/45 mix of OCs and ECs. In this scenario, the remaining ~40% of Earth's mass is provided chondritic material, including CCs and NCCs. Importantly, the differentiated material contributes about ~12% of Earth's Zn budget, while the chondritic material supplied ~88%, likely accompanied by critical amounts of other volatiles.

The new and published analytical results, which were incorporated in comprehensive accretion models, are fully consistent with traditional accretion scenarios, which posit that planetary embryos grow primarily by the accretion of planetesimals. This scenario is preferred, as it can explain both how Earth reached its final nucleosynthetic isotope composition and why the accreting material records further substantial volatile loss. The present findings may also be accommodated by pebble accretion if the composition of the pebble material was much more diverse than proposed by other studies, but further investigations are required to constrain possible volatile loss during envelope processing.

Altogether, it appears that terrestrial planets accreted large amounts of early-formed planetesimals that had experienced large-spread melting and differentiation, due to the decay of short-lived radionuclides and highly energetic collisions. These processes lead to efficient volatile loss through degassing, and this material therefore provided only very limited contributions to the volatile inventories of planetary embryos. In contrast, chondritic planetesimals did not undergo a differentiation process, most likely because they formed only after substantial decay of extinct radionuclides. Consequently, they largely preserved their volatile budgets, which were later inherited by the terrestrial planets.

The presence of significant amounts of short-lived radionuclides such as $^{26}$Al in the interstellar medium is now thought to be commonplace in high-mass star forming regions, where most planetary systems are formed. Hence, the formation, preservation and subsequent incorporation of undifferentiated chondritic material may play a deciding role in establishing the volatile content of terrestrial planets, not only in our Solar System, but also in exoplanetary settings.

## 3.7 References


AKRAM, W., SCHÖNBÄCHLER, M., BISTERZO, S. & GALLINO, R. 2015. Zirconium isotope evidence for the heterogeneous distribution of s-process materials in the Solar System. *Geochimica et Cosmochimica Acta,* 165**,** 484-500.

ALBARÈDE, F. 2009. Volatile accretion history of the terrestrial planets and dynamic implications. *Nature,* 461**,** 1227-1233.

ALBARÈDE, F., BALLHAUS, C., BLICHERT-TOFT, J., LEE, C.-T., MARTY, B., MOYNIER, F. & YIN, Q.-Z. 2013. Asteroidal impacts and the origin of terrestrial and lunar volatiles. *Icarus,* 222**,** 44–52.

ALEXANDER, C. M. O. D. 2005. Re-examining the role of chondrules in producing the elemental fractionations in chondrites. *Meteoritics & Planetary Science,* 40**,** 943-965.

ARMYTAGE, R. M. G., GEORG, R. B., SAVAGE, P. S., WILLIAMS, H. M. & HALLIDAY, A. N. 2011. Silicon isotopes in meteorites and planetary core formation. *Geochimica et Cosmochimica Acta,* 75**,** 3662-3676.

ASHCROFT, H. O. & WOOD, B. J. 2015. An experimental study of partial melting and fractional crystallization on the HED parent body. *Meteoritics & Planetary Science,* 50**,** 1912-1924.

BRAUKMÜLLER, N., WOMBACHER, F., FUNK, C. & MUNKER, C. 2019. Earth's volatile element depletion pattern inherited from a carbonaceous chondrite-like source. *Nature Geoscience,* 12**,** 564-568.

BRAUKMÜLLER, N., WOMBACHER, F., HEZEL, D. C., ESCOUBE, R. & MUNKER, C. 2018. The chemical composition of carbonaceous chondrites: Implications for volatile element depletion, complementarity and alteration. *Geochimica et Cosmochimica Acta,* 239**,** 17-48.

BUDDE, G., BURKHARDT, C. & KLEINE, T. 2019. Molybdenum isotopic evidence for the late accretion of outer Solar System material to Earth. *Nature Astronomy,* 3**,** 736-741.

BURKHARDT, C., BORG, L. E., BRENNECKA, G. A., SHOLLENBERGER, Q. R., DAUPHAS, N. & KLEINE, T. 2016. A nucleosynthetic origin for the Earth's anomalous $^{142}$Nd composition. *Nature,* 537**,** 394-398.

BURKHARDT, C., DAUPHAS, N., TANG, H., FISCHER-GÖDDE, M., QIN, L., CHEN, J. H., ROUT, S. S., PACK, A., HECK, P. R. & PAPANASTASSIOU, D. A. 2017. In search of the Earth-forming reservoir: Mineralogical, chemical, and isotopic characterizations of the ungrouped achondrite NWA 5363/NWA 5400 and selected chondrites. *Meteoritics & Planetary Science,* 52**,** 807-826.

BURKHARDT, C., SPITZER, F., MORBIDELLI, A., BUDDE, G., RENDER, J. H., KRUIJER, T. S. & KLEINE, T. 2021. Terrestrial planet formation from lost inner Solar System material. *Science Advances,* 7**,** eabj7601.

CANUP, R. M. & AGNOR, C. B. 2000. Accretion of the Terrestrial Planets and the Earth-Moon System. In: *Origin of the Earth and Moon.* University of Arizona Press.

CARRY, B. 2012. Density of asteroids. *Planetary and Space Science,* 73**,** 98-118.

CLAYTON, D. 2003. Isotopes in the Cosmos: Hydrogen to Gallium. Cambridge University Press, Cambridge.

DAUPHAS, N. 2017. The isotopic nature of the Earth's accreting material through time. *Nature,* 541**,** 521-524.

DAUPHAS, N. & CHAUSSIDON, M. 2011. A Perspective from Extinct Radionuclides on a Young Stellar Object: The Sun and Its Accretion Disk. *Annual Review of Earth and Planetary Sciences,* 39**,** 351-386.

DAUPHAS, N., CHEN, J. H., ZHANG, J., PAPANASTASSIOU, D. A., DAVIS, A. M. & TRAVAGLIO, C. 2014. Calcium-48 isotopic anomalies in bulk chondrites and achondrites: Evidence for a uniform isotopic reservoir in the inner protoplanetary disk. *Earth Planetary Sciences Letters,* 407**,** 96-108.

DAUPHAS, N., HOPP, T. & NESVORNÝ, D. 2023. Bayesian inference on the isotopic building blocks of Mars and Earth. *Icarus***,** 115805.

DAUPHAS, N., MARTY, B. & REISBERG, L. 2002. Molybdenum evidence for inherited planetary scale isotope heterogeneity of the protosolar nebula. *Astrophysycal Journal,* 565**,** 640-644.

DREIBUS, G., KRUSE, H., SPETTEL, B. & WAENKE, H. 1977. The bulk composition of the Moon and the eucrite parent body. *Lunar and Planetary Science Conference Proceedings,* 1**,** 211-227.
FISCHER-GÖDDE, M. & KLEINE, T. 2017. Ruthenium isotopic evidence for an inner Solar System origin of the late veneer. *Nature,* 541**,** 525-527.
FITOUSSI, C. & BOURDON, B. 2012. Silicon Isotope Evidence Against an Enstatite Chondrite Earth. *Science,* 335**,** 1477-1480.
FITOUSSI, C., BOURDON, B. & WANG, X. Y. 2016. The building blocks of Earth and Mars: A close genetic link. *Earth and Planetary Science Letters,* 434**,** 151-160.
FROSSARD, P., GUO, Z., SPENCER, M., BOYET, M. & BOUVIER, A. 2021. Evidence from achondrites for a temporal change in Nd nucleosynthetic anomalies within the first 1.5 million years of the inner Solar System formation. *Earth and Planetary Science Letters,* 566**,** 116968.
HALLIDAY, A. N. 2004. Mixing, volatile loss and compositional change during impact-driven accretion of the Earth. *Nature,* 427**,** 505-509.
HIN, R. C., COATH, C. D., CARTER, P. J., NIMMO, F., LAI, Y.-J., POGGE VON STRANDMANN, P. A. E., WILLBOLD, M., LEINHARDT, Z. M., WALTER, M. J. & ELLIOTT, T. 2017. Magnesium isotope evidence that accretional vapour loss shapes planetary compositions. *Nature,* 549**,** 511-515.
JOHANSEN, A., RONNET, T., BIZZARRO, M., SCHILLER, M., LAMBRECHTS, M., NORDLUND, Å. & LAMMER, H. 2021. A pebble accretion model for the formation of the terrestrial planets in the Solar System. *Science Advances,* 7**,** eabc0444.
JOHNSON, B. C., MINTON, D. A., MELOSH, H. J. & ZUBER, M. T. 2015. Impact jetting as the origin of chondrules. *Nature,* 517**,** 339-341.
JUREWICZ, A. J., MITTLEFEHLDT, D. W. & JONES, J. H. 1991. Partial Melting of the Aliende (CV3) Meteorite: Implications for Origins of Basaltic Meteorites. *Science,* 252**,** 695-8.
KALLEMEYN, G. W., RUBIN, A. E., WANG, D. & WASSON, J. T. 1989. Ordinary chondrites: Bulk compositions, classification, lithophile-element fractionations and composition-petrographic type relationships. *Geochimica et Cosmochimica Acta,* 53**,** 2747-2767.
KALLEMEYN, G. W. & WASSON, J. T. 1986. Composition of enstatite (EH3, EH4,5 and EL6) chondrites: Implications regarding their formation. *Geochimica et Cosmochimica Acta,* 50**,** 2153-2164.
KLEINE, T., TOUBOUL, M., BOURDON, B., NIMMO, F., MEZGER, K., PALME, H., JACOBSEN, S. B., YIN, Q.-Z. & HALLIDAY, A. N. 2009. Hf–W chronology of the accretion and early evolution of asteroids and terrestrial planets. *Geochimica et Cosmochimica Acta,* 73**,** 5150-5188.
KROT, A. N., KEIL, K., SCOTT, E. R. D., GOODRICH, C. A. & WEISBERG, M. K. 2014. 1.1 - Classification of Meteorites and Their Genetic Relationships. *In:* HOLLAND, H. D. & TUREKIAN, K. K. (eds.) *Treatise on Geochemistry (Second Edition).* Oxford: Elsevier.
LEVISON, H. F., KRETKE, K. A., WALSH, K. J. & BOTTKE, W. F. 2015. Growing the terrestrial planets from the gradual accumulation of submeter-sized objects. *Proceedings of the National Academy of Sciences,* 112**,** 14180-14185.
LIEBSKE, C. & KHAN, A. 2019. On the principal building blocks of Mars and Earth. *Icarus,* 322**,** 121-134.
LODDERS, K. 2000. An Oxygen Isotope Mixing Model for the Accretion and Composition of Rocky Planets. *Space Science Reviews,* 92**,** 341-354.
LODDERS, K. 2003. Solar System abundances and condensation temperatures of the elements. *The Astrophysycal Journal,* 591**,** 1220-1247.
MAHAN, B., MOYNIER, F., SIEBERT, J., GUEGUEN, B., AGRANIER, A., PRINGLE, E. A., BOLLARD, J., CONNELLY, J. N. & BIZZARRO, M. 2018a. Volatile element evolution of chondrules through time. *Proceedings of the National Academy of Sciences,* 115**,** 8547-8552.
MAHAN, B., SIEBERT, J., BLANCHARD, I., BORENSZTAJN, S., BADRO, J. & MOYNIER, F. 2018b. Constraining compositional proxies for Earth's accretion and core formation through high pressure and high temperature Zn and S metal-silicate partitioning. *Geochimica Et Cosmochimica Acta,* 235**,** 21-40.

MAHAN, B., SIEBERT, J., PRINGLE, E. A. & MOYNIER, F. 2017. Elemental partitioning and isotopic fractionation of Zn between metal and silicate and geochemical estimation of the S content of the Earth's core. *Geochimica et Cosmochimica Acta,* 196**,** 252-270.

MANN, U., FROST, D. J., RUBIE, D. C., BECKER, H. & AUDÉTAT, A. 2012. Partitioning of Ru, Rh, Pd, Re, Ir and Pt between liquid metal and silicate at high pressures and high temperatures - Implications for the origin of highly siderophile element concentrations in the Earth's mantle. *Geochimica et Cosmochimica Acta,* 84**,** 593-613.

MARTINS, R., CHAUSSIDON, M., DENG, Z., PIGNATALE, F. & MOYNIER, F. 2021. A condensation origin for the mass-dependent silicon isotopic variations in Allende components: implications for complementarity. *Earth and Planetary Science Letters,* 554**,** 116678.

MARTY, B. 2012. The origins and concentrations of water, carbon, nitrogen and noble gases on Earth. *Earth and Planetary Science Letters,* 313-314**,** 56-66.

MCDONOUGH, W. F. 2005. Compositional model for the Earth's core. *In:* DAVIS, A. M. (eds.) *Meteorites, Comets, and Planets.* Amsterdam: Elsevier.

MCDONOUGH, W. F. 2014. 3.16 - Compositional Model for the Earth's Core. *In:* HOLLAND, H. D. & TUREKIAN, K. K. (eds.) *Treatise on Geochemistry (Second Edition).* Oxford: Elsevier.

MCDONOUGH, W. F. & SUN, S. S. 1995. The composition of the Earth. *Chemical Geology,* 120**,**.

MORBIDELLI, A., CHAMBERS, J., LUNINE, J. I., PETIT, J. M., ROBERT, F., VALSECCHI, G. B. & CYR, K. E. 2000. Source regions and timescales for the delivery of water to the Earth. *Meteoritics & Planetary Science,* 35**,** 1309-1320.

MORGAN, J. W. & ANDERS, E. 1980. Chemical composition of Earth, Venus, and Mercury. *Proceedings of the National Academy of Sciences USA,* 77**,** 6973-6977.

MORGAN, J. W., HIGUCHI, H., TAKAHASHI, H. & HERTOGEN, J. 1978. A "chondritic" eucrite parent body: inference from trace elements. *Geochimica et Cosmochimica Acta,* 42**,** 27-38.

MOYNIER, F., DAY, J. M. D., OKUI, W., YOKOYAMA, T., BOUVIER, A., WALKER, R. J. & PODOSEK, F. A. 2012. Planetary-scale strontium isotopic heterogeneity and the age of volatile depletion of early solar system materials. *The Astrophysical Journal,* 758**,** 45.

NEWCOMBE, M. E., NIELSEN, S. G., PETERSON, L. D., WANG, J., ALEXANDER, C. M. O. D., SARAFIAN, A. R., SHIMIZU, K., NITTLER, L. R. & IRVING, A. J. 2023. Degassing of early-formed planetesimals restricted water delivery to Earth. *Nature,* 615**,** 854-857.

NIE, N. X., WANG, D., TORRANO, Z. A., CARLSON, R. W., O'D. ALEXANDER, C. M. & SHAHAR, A. 2023. Meteorites have inherited nucleosynthetic anomalies of potassium-40 produced in supernovae. *Science,* 379**,** 372-376.

O'NEILL, H. S. C. 1991. The origin of the Moon and the early history of the Earth – A chemical model. Part 2: The Earth. *Geochimica et Cosmochimica Acta,* 55**,** 1159-1172.

O'NEILL, H. S. C. & PALME, H. 2008. Collisional erosion and the non-chondritic composition of the terrestrial planets. *Philosophical Transactions of the Royal Society A: Mathematical, Physical and Engineering Sciences,* 366**,** 4205-4238.

ONYETT, I. J., SCHILLER, M., MAKHATADZE, G. V., DENG, Z., JOHANSEN, A. & BIZZARRO, M. 2023. Silicon isotope constraints on terrestrial planet accretion. *Nature*.

OZIMA, M., PODOSEK, F. A., HIGUCHI, T., YIN, Q. Z. & YAMADA, A. 2007. On the mean oxygen isotope composition of the Solar System. *Icarus,* 186**,** 562-570.

PANIELLO, R. C., MOYNIER, F., BECK, P., BARRAT, J.-A., PODOSEK, F. A. & PICHAT, S. 2012. Zinc isotopes in HEDs: Clues to the formation of 4-Vesta, and the unique composition of Pecora Escarpment 82502. *Geochimica et Cosmochimica Acta,* 86**,** 76-87.

PEPLOWSKI, P. N., EVANS, L. G., HAUCK, S. A., MCCOY, T. J., BOYNTON, W. V., et al. 2011. Radioactive Elements on Mercury's Surface from MESSENGER: Implications for the Planet's Formation and Evolution. *Science,* 333**,** 1850-1852.

PRINGLE, E. A., MOYNIER, F., BECK, P., PANIELLO, R. & HEZEL, D. C. 2017. The origin of volatile element depletion in early Solar System material: Clues from Zn isotopes in chondrules. *Earth and Planetary Science Letters,* 468**,** 62-71.

PRINGLE, E. A., MOYNIER, F., SAVAGE, P. S., BADRO, J. & BARRAT, J.-A. 2014. Silicon isotopes in angrites and volatile loss in planetesimals. *Proceedings of the National Academy of Sciences,* 111**,** 17029-17032.

PRINGLE, E. A., SAVAGE, P. S., BADRO, J., BARRAT, J.-A. & MOYNIER, F. 2013. Redox state during core formation on asteroid 4-Vesta. *Earth and Planetary Science Letters,* 373**,** 75-82.
RENDER, J., BRENNECKA, G. A., WANG, S.-J., WASYLENKI, L. E. & KLEINE, T. 2018. A Distinct Nucleosynthetic Heritage for Early Solar System Solids Recorded by Ni Isotope Signatures. *The Astrophysical Journal,* 862**,** 26.
RINGWOOD, A. E. 1966. Chemical evolution of the terrestrial planets. *Geochimica et Cosmochimica Acta,* 30**,** 41-104.
RUDGE, J. F., KLEINE, T. & BOURDON, B. 2010. Broad bounds on Earth's accretion and core formation constrained by geochemical models. *Nature Geoscience,* 3**,** 439-443.
SAVAGE, P. S., GEORG, R. B., ARMYTAGE, R. M. G., WILLIAMS, H. M. & HALLIDAY, A. N. 2010. Silicon isotope homogeneity in the mantle. *Earth and Planetary Science Letters,* 295**,** 139-146.
SAVAGE, P. S. & MOYNIER, F. 2013. Silicon isotopic variation in enstatite meteorites: Clues to their origin and Earth-forming material. *Earth and Planetary Science Letters,* 361**,** 487-496.
SAVAGE, P. S., MOYNIER, F. & BOYET, M. 2022. Zinc isotope anomalies in primitive meteorites identify the outer Solar System as an important source of Earth's volatile inventory. *Icarus,* 386**,** 115172.
SCHILLER, M., BIZZARRO, M. & FERNANDES, V. A. 2018. Isotopic evolution of the protoplanetary disk and the building blocks of Earth and the Moon. *Nature,* 555**,** 507-510.
SIEBERT, J., CORGNE, A. & RYERSON, F. J. 2011. Systematics of metal–silicate partitioning for many siderophile elements applied to Earth's core formation. *Geochimica et Cosmochimica Acta,* 75**,** 1451-1489.
STELLER, T., BURKHARDT, C., YANG, C. & KLEINE, T. 2022. Nucleosynthetic zinc isotope anomalies reveal a dual origin of terrestrial volatiles. *Icarus,* 386**,** 115171.
TAYLOR, G. J. 2013. The bulk composition of Mars. *Geochemistry,* 73**,** 401-420.
TOUBOUL, M., PUCHTEL, I. S. & WALKER, R. J. 2015. Tungsten isotopic evidence for disproportional late accretion to the Earth and Moon. *Nature,* 520**,** 530-533.
TRINQUIER, A., BIRCK, J. L. & ALLEGRE, C. J. 2007. Widespread Cr-54 heterogeneity in the inner Solar System. *The Astrophysical Journal,* 655**,** 1179-1185.
TRINQUIER, A., ELLIOTT, T., ULFBECK, D., COATH, C., KROT, A. N. & BIZZARRO, M. 2009. Origin of nucleosynthetic isotope heterogeneity in the solar protoplanetary disk. *Science,* 324**,** 374-376.
WANAJO, S., JANKA, H.-T. & MÜLLER, B. 2013. Electron-capure supernovae as origin of $^{48}$Ca. *The Astrophysycal Journal Letters,* 767**,** L26.
WANG, H. S., LINEWEAVER, C. H. & IRELAND, T. R. 2018. The elemental abundances (with uncertainties) of the most Earth-like planet. *Icarus,* 299**,** 460-474.
WARREN, H. P., KALLEMEYN, G. W. 1990. Geochemistry of LEW87051 Angrite, and other basaltic achondrites. *Lunar and Planetary Science Conference XXI*, 1295.
WARREN, H. P., KALLEMEYN, G. W. 1995. Angrites: A Volatile-rich Variety of Asteroidal Basalt (Except for Alkalis and Gallium!). *Meteoritics*, 30 (5), 593.
WASSON, J. T. & CHOU, C.-L. 1974. Fractionation of moderately volatile elements in ordinary chondrites. *Meteoritics,* 9**,** 69-84.
WASSON, J. T., CHOU, C.-L., BILD, R. W. & BAEDECKER, P. A. 1976. Classification of and elemental fractionation among ureilites. *Geochimica et Cosmochimica Acta,* 40**,** 1449-1458.
WASSON, J. T. & KALLEMEYN, G. W. 1988. Compositions of chondrites. *Philosophical Transactions of the Royal Society A,* 325**,** 535-544.
WETHERILL, G. W. 1994. Provenance of the terrestrial planets. *Geochimica et Cosmochimica Acta,* 58**,** 4513-4520.
WOLF, R., EBIHARA, M., RICHTER, G. R. & ANDERS, E. 1983. Aubrites and diogenites: Trace element clues to their origin. *Geochimica et Cosmochimica Acta,* 47**,** 2257-2270.
WOOSLEY, S. E. 1997. Neutron-rich nucleosynthesis in carbon deflagration supernovae. *The Astrophysycal Journal,* 476**,** 801-810.
WU, C., & YU, J. Z. 2018. Evaluation of linear regression techniques for atmospheric applications: the importance of appropriate weighting. *Atmospheric Measurement Techniques*, 11, 1233–1250.

# Chapter 4

# The origin of nucleosynthetic zinc isotope heterogeneity in the Solar System

## 4.1 Introduction

With the exception of H and He, the compositions of Solar System bodies were mainly inherited from matter formed by stars. This includes the atoms forged in stellar interiors throughout their lives, as well as nuclides assembled in the explosive events associated with their deaths, all of which can produce gas and dust with distinct elemental and isotopic abundances. While this material was mostly homogeneously distributed prior to its accretion into planets and asteroids, some presolar dust grains formed by specific stellar sources were present in varying amounts throughout the Solar System, imparting their distinct isotopic signatures onto the bodies that incorporated them to different extents.

These small variations in isotope compositions suggest the presence of two separate reservoirs within the Solar System. Carbonaceous meteorites, from parent bodies that are thought to have accreted beyond the orbit of Jupiter, are generally enriched in isotopes that are produced in explosive nucleosynthesis. These include the neutron-rich isotopes of the Fe-peak elements, such as Ca, Ti, Cr, Ni, and Zn (Dauphas et al., 2014, Trinquier et al., 2009, Trinquier et al., 2007, Nanne et al., 2019, Chapter 2), which are produced in either Type Ia (SNIa), or Type II (SNII) supernovae, and the r-process isotopes of heavier elements like Mo, Ru, Sr, Zr, and Nd (Budde et al., 2019, Fischer-Gödde and Kleine, 2017, Yokoyama et al., 2015, Akram et al., 2015, Qin et al., 2011a). In contrast, non-carbonaceous (NC) meteorites and terrestrial planets, which formed in the inner Solar System, are depleted in the same isotopes relative to carbonaceous meteorites.

The cause of the heterogenous distribution of this presolar dust is debated. Traditionally, it has been attributed to physical processes such as grain size sorting or thermal processing, which would have concentrated dust from explosive nucleosynthesis in the outer Solar System (Trinquier et al., 2009, Ek et al., 2020, Yokoyama et al., 2015). Thermal processing has been linked to a temperature gradient in the protoplanetary disk induced by the formation of the protosun, which would have preferentially destroyed grains from explosive nucleosynthesis in the inner Solar System, while leaving the material in outer Solar System more intact. However, more recently, it has been suggested that the isotopic dichotomy reflects temporal or spatial changes in the composition of the infalling material from the molecular cloud as the protoplanetary disk was shaped (Nanne et al., 2019). In contrast with the previous scenario, in this case the carrier phases of the anomalous material were never fully homogenized. Both hypotheses can account for the observed complementarity between the

carbonaceous and NC reservoirs, as well as variations within each reservoir, making it difficult to favour one over the other.

A potential route to test the feasibility of the thermal processing scenario is to investigate the carrier phases of the anomalies and their thermal susceptibilities. Nucleosynthetic Ti, Cr, Sr, Zr, Mo, and Pd nucleosynthetic isotope anomalies have been previously interpreted as resulting from thermal processing (Trinquier et al., 2009, Ek et al., 2020, Yokoyama et al., 2015, Akram et al., 2015, Burkhardt and Schönbächler, 2015). However, due to their relatively high condensation temperatures (Lodders, 2003), these elements are less sensitive to thermal perturbations and evaporation. As a moderately volatile element showcasing substantially variable elemental depletion across different meteorites and planets (Wasson and Kallemeyn, 1988, Braukmüller et al., 2019, O'Neill, 1991, Taylor, 2013), Zn an ideal candidate to test potential links between thermal processing and Zn loss, and the heterogenous distribution of presolar Zn carriers.

Yet, while recent studies have characterized nucleosynthetic Zn isotope anomalies in a range of meteorites (Chapter 2, Savage et al., 2022, Steller et al., 2022), the carrier phases of these anomalies are still unknown. Thus, the aim of this study is to characterize the mass-independent Zn isotope compositions of distinct mineral phases in meteorite samples, by performing a stepwise acid leaching procedure. This method targets progressively more resistant phases with each step, such that the compositions of different minerals or mineral groups can be distinguished, and the carriers of the anomalies potentially identified.

## 4.2 Methods

### 4.2.1 Sample preparation and leaching procedure

The initial sample preparation was performed at the University of Cologne. Four carbonaceous chondrites (CC), including one CV, one CM, and two COs (Table 4.1), were crushed and subjected to a seven-step leaching procedure adapted from Rotaru et al. (1992) and Burkhardt and Schönbächler (2015). The reagents, their respective molarities, and volumes, as well as the duration, temperatures and target phases of each step are summarized in Table 4.2. A schematic view of the procedure is also shown in Figure 4.1. In the first step, the powdered samples were placed in Savillex beakers and treated with the respective reagent. After leaching was completed, the mixtures of samples and leaching agent were centrifuged for 10 to 30 minutes, and the liquid fractions were pipetted to a new beaker. Next, the undigested fractions were rinsed with dilute acids that varied depending on the step (Table 4.2),

and the rinse was transferred to the beaker containing the dissolved fraction. At this point, ~2% aliquots were separated from the dissolved fractions for elemental analysis and determination of Zn concentrations. Finally, the contents of the beakers containing the dissolved and the undigested fractions were dried down at 80°C, and the residues in the latter were the treated with the subsequent leaching reagent.

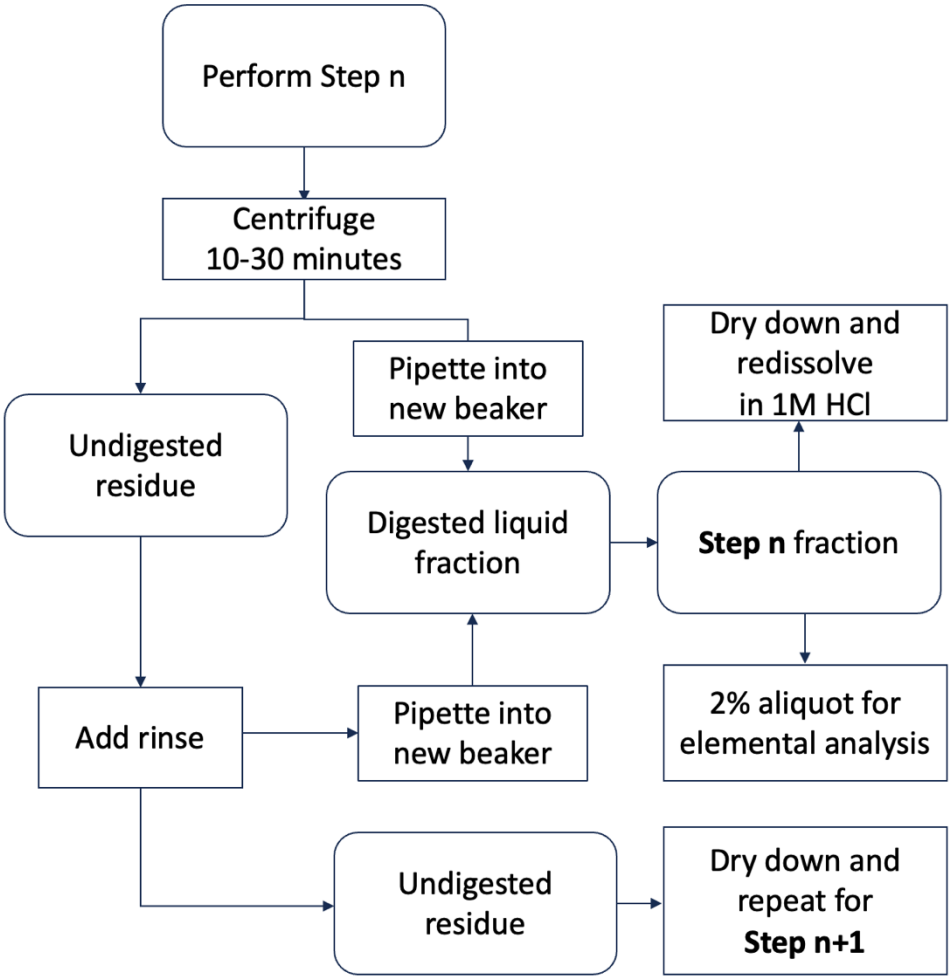



**Figure 4.1. Schematic diagram of leaching procedure.**

This process was repeated until the seventh and final step, which encompasses five stages. In the first stage, the undigested residue was treated with the same reagents as in Step 6, but now the samples were heated in a Parr bomb for three days at 180°C. After centrifuging, the supernatants were transferred to Step 7 beakers. Since there were still undigested solids remaining, likely including organics, graphite, and fluoride compounds, the residues were dried down, and refluxed in an HCl-$HNO_3$ mix at 130°C for a day. The resulting liquid fractions were transferred to the Step 7 beakers, and the residues were dried again. Next, the residues

were refluxed in a Parr bomb with 2 ml 14.5 M $HNO_3$ at 180°C for 1 day, after which the liquid fractions were also transferred to the Step 7 beakers. The remaining solids were rinsed with 1.4 M $HNO_3$, and then treated twice with 8 M HCl at 55°C and 120°C for a day each. The rinses were pipetted to the Step 7 beakers, and the residues were dried down in between each rinse. Finally, all seven digested fractions of each meteorite were dried and redissolved in 15 ml 1 M HCl ahead of the ion exchange chromatography.

**Table 4.1. Names, digested masses, and sources of the meteorite samples.**

| Sample | Classification | Mass (g) | Supplier |
|---|---|---|---|
| Allende | CV3 | 4.505 | Private Collector |
| Kainsaz | CO3.2 | 4.508 | Russian Academy of Science |
| Colony | CO3 | 4.495 | Smithsonian Institute |
| Murchison | CM2 | 4.502 | Smithsonian Institute |



**Figure 4.2. Photograph showing residues of the different leaching steps for the four meteorite samples.**

**Table 4.2. Summary of leaching procedure.** Includes reagents, molarity, volumes, temperature, and duration of each leaching step, as well as rinse procedures performed in between steps, and target mineral phases.

| Leaching Step | Reagents | Molarity | Volume (ml) | Temperature | Time (days) | Rinse | Target phases |
|---|---|---|---|---|---|---|---|
| 1 | Acetic acid | | 22 | RT | 1 | MQ | Sulphates, sulphides, carbonates, metal |
| 2 | $HNO_3$ | 4 M | 18 | RT | 5 | 15 ml 0.14M $HNO_3$ | Silicates |
| 3 | HCl | 6 M | 18 | 80ºC | 1 | 15 ml 0.1M HCl | Silicates |
| 4 | HCl - HF | 3 M – 12 M | 20 | 100ºC | 6 | 15 ml 0.1M HCl | Silicates |
| 5 | HCl - HF | 3 M – 12 M | 20 | 160°C | 2 | 15 ml 0.1M HCl | Silicates |
| 6 | $HNO_3$ - HF | 7 M – 12 M | 8 | 160°C | 1 | no rinse | Refractory phases |
| 7 | $HNO_3$ - HF | 7 M – 12 M | 8 | 180°C[a] | 3 | no rinse | Refractory phases |
| | HCl - $HNO_3$ | 6 M – 3 M | 5 | 130°C | 1 | no rinse | Organics, graphite, fluoride |
| | $HNO_3$ | 14.5 M | 2 | 180°C[a] | 1 | 5 ml 1.4M HNO3 | Organics, graphite, fluoride |
| | HCl | 8 M | 4 | 55°C | 1 | no rinse | Organics, graphite, fluoride |
| | HCl | 8 M | 5 | 120°C | 1 | no rinse | Organics, graphite, fluoride |

RT: room temperature. a: this step involved the use of Parrbombs

### 4.2.2 Ion exchange chromatography

Two initial stages of chromatography were performed at the University of Cologne as part of a Sn separation procedure described in detail by Bragagni et al. (2023). The first stage employed 200-400 mesh Bio-Rad AG-1X8 anion exchange resin in Bio-Rad columns with 2 ml resin beds (Table 4.3a). Zinc was eluted along with Sn using 1 M $HNO_3$. The Sn-Zn fractions were dried down and treated twice with 0.1 ml of a $H_2O_2$-$HNO_3$-HF mixture (5:10:1) to attack organics eluted from the resin. These solutions were again dried and redissolved in 2 ml 2 M HCl ahead of the second separation stage (Table 4.3b). This stage employed 0.8 ml of Triskem tributyl phosphate (TBP) resin and 0.4 ml of pre-filter, which were loaded into custom columns made from PE Pasteur pipettes. After loading the samples, Zn was eluted in 10 ml of 2 M HCl, which was collected in Savillex beakers and dried down.

**Table 4.3a. Stage I of ion exchange chromatography.**

| Reagent | Volume (ml) | Effect |
|---|---|---|
| AG1X8 100-200 mesh | 2 | Add resin |
| 1 M HCl | 15 | Load sample |
| 1 M HCl | 10 | Elute matrix |
| 1 M HCl | 5 | |
| 0.5 M HCl | 5 | |
| 0.5 M HCl | 5 | |
| 1 M HNO3 | 5 x 4.7 | Elute Sn and Zn |
| 10 M HCl | 2 x 7 | Collect PGE? |
| 12 M HNO3 | 2 x 7 | |

**Table 4.3b. Stage II of ion exchange chromatography.**

| Reagent | Volume (ml) | Effect |
|---|---|---|
| TBP resin/pre-filter | 0.8/0.4 | Add resin |
| 2 M HCl | 2 | Load sample |
| 2 M HCl | 1+4+2+2+1 | Collect Zn |

Further processing of the Zn cuts, using the three-stage Zn anion-exchange procedure described in detail in Chapters 2 and 3, was carried out at the MAGIC Laboratories at the Department of Earth Science & Engineering of Imperial College London. All three stages employed Teflon columns with 250 µl resin beds. Stage one employed AG-1X8 100-200 mesh resin and samples were loaded in 2 ml 3 M HCl. After the matrix elution steps, Zn was collected in 3 ml of a 0.1M HBr + 0.5 M $HNO_3$ mix (Chapter 2). The samples were then dried at 80$^{o}$C and redissolved in 2 ml 1 M HCl. Next, they were loaded onto columns containing AG-MP1

100-200 mesh resin for both stages 2 and 3. Following loading of the sample solutions and matrix elution, Zn was eluted in 7 ml 0.01 M HCl. Finally, the samples were dried and redissolved in 0.1 M $HNO_3$ ahead of the isotope analyses.

### 4.2.3 Mass spectrometry

Zinc concentrations were determined on the 2% sample solution aliquots separated prior to the ion exchange procedure. This was done using an iCAP Q inductively coupled plasma mass spectrometer (ICP-MS) in combination with a PFA nebulizer and spray chamber at the University of Cologne. The measurements were performed with external calibration to multi-element chondrite solutions using Rh as an internal standard (Braukmüller et al., 2018). The results for each leaching step are reported as mass fractions of the total Zn in the meteorite sample (in %), as characterized by the sum of the Zn determined in all steps.

The isotope measurements were performed with a Nu Instruments Nu Plasma II multiple collector (MC-) ICP-MS at the MAGIC Laboratories. A Nu Instruments DSN 100 desolvation system fitted with glass cross flow nebulizers with solution flow rates of about 120 µl $min^{-1}$ were employed for sample introduction in conjunction with a CETAC ASX-112FR autosampler. The two Faraday cup configurations that were employed for the isotope measurements, with all cups connected to $10^{11}$ Ω resistors, are summarized in Table 4.4. Analyses were carried out using the same specifications as described in Chapters 2 and 3. However, samples with low Zn contents (<3 µg) were measured for two blocks of 20 measurements per repeat, instead of the usual three blocks.

Monitoring of $^{73}Ge$ on the H10 Faraday cup during M70 block measurements (Table 4.4) revealed that Ge was consistently below the detection level. As such, no Ge corrections are needed, and the ion beam collected in Faraday cup H8 of the M64 block analyses can be attributed exclusively to $^{70}Zn$. Hence, provided that the H8 beam was sufficiently high (typically >0.4V) and stable, $\varepsilon^{70}Zn$ values collected in M64 block measurements are also reported for some samples, such as Murchison (Steps 5-7), Allende (Steps 3-5), and Kainsaz (Steps 1-5, 7).

The solutions were introduced in 0.1 M $HNO_3$, typically containing 300-450 ng $g^{-1}$ of Zn, with instrumental sensitivity ranging between 150 and 250 V/(µg $ml^{-1}$). All analyses were carried out with the sample–standard bracketing technique, in which sample runs were symmetrically bracketed by runs of the London Zn isotope reference material. Samples concentrations typically matched the standard concentrations to within 10 to 15%

**Table 4.4. Collector configurations that were used for the Zn isotope measurements, abundances of the isotopes of Zn as well as spectral interferences from isobars, $Ba^{2+}$ and the most relevant molecular ions.**

| **Faraday collector** | **L4** | **L2** | **Ax** | **H1** | **H2** | **H4** | **H6** | **H7** | **H8** | **H10** |
|---|---|---|---|---|---|---|---|---|---|---|
| **Collector configuration M64** | $^{62}Ni$ | $^{64}Zn$ | | | $^{66}Zn$ | $^{67}Zn$ | $^{68}Zn$ | $^{137}Ba^{2+}$ | $^{70}Zn$ | |
| Isotope abundance Zn | | 49.2% | | | 27.7% | 4.0% | 18.5% | | 0.6% | |
| Isotope abundance Ni | 3.6% | 0.1% | | | | | | | | |
| Isotope abundance $Ba^{2+}$ ions | | | | | 0.1% | 2.4% | 7.9% | 11.2% | | |
| Isotope abundance Ge | | | | | | | | | 20.5% | |
| **Collector configuration M70** | $^{66}Zn$ | $^{67}Zn$ | $^{68}Zn$ | $^{137}Ba^{2+}$ | | $^{70}Zn$ | | | $^{72}Ge$ | $^{73}Ge$ |
| Isotope abundance Zn | 27.7% | 4.0% | 18.5% | | | 0.6% | | | | |
| Isotope abundance Ge | | | | | | 20.5% | | | 27.5% | 7.8% |
| Isotope abundance $Ba^{2+}$ ions | 0.1% | 2.4% | 7.9% | 11.2% | | | | | | |

The isotope results are reported using the ε notation, which denotes deviations of the measured isotope ratio for a sample (sam) from the value determined for the London Zn reference standard (std) in parts per $10^4$:

$$\varepsilon^{i}Zn = \left(\frac{(\,^{i}Zn/^{67}Zn)_{sam}}{(\,^{i}Zn/^{67}Zn)_{std}} - 1\right) x\ 10^4 \qquad \text{(Eq. 3.1)}$$

where i is the isotope of interest. The $^{66}Zn/^{67}Zn$ isotope ratio was selected for internal normalization, since it is the preferred ratio in Chapters 2 and 3.

The reported uncertainty formats vary depending on the number of runs that were carried out for a given sample. If only one run was performed, the uncertainty corresponds to the 95% confidence interval of the mean (2SE) of the 40 or 60 individual measurements (cycles) performed in that run. If two runs were performed, the uncertainty corresponds to twice the standard deviation (2SD) of the two means. Finally, if more than two runs were performed, the uncertainty is equivalent to the 2SE of the mean of all repeats.

For quality control, and to ensure the results are consistent with previous studies, the US Geological Survey reference material Columbia River Basalt, BCR-2, was regularly processed and analysed along with the leachate samples. The blanks of the leaching procedure typically corresponded to less than 1% of the indigenous sample Zn, with a minimum of 0.02% and a maximum of 5.8%. This introduces a maximum uncertainty of about ±8, ±2, and ±5 ppm for $\varepsilon^{64}Zn$, $\varepsilon^{68}Zn$, and $\varepsilon^{70}Zn$, respectively, which is within the precision of the measurements. Furthermore, the ion exchange chromatography habitually yielded blanks of less than 20 ng, which typically corresponds to between 0.1 and 2% of the indigenous Zn in the processed samples. Hence, no blank corrections were performed for the isotope analysis.

## 4.3 Results

The $\varepsilon^{64}Zn$, $\varepsilon^{68}Zn$, and $\varepsilon^{70}Zn$ values of the leachates, as well as the mass fractions of Zn are shown in Table 4.5 and in Figure 4.3, with $\varepsilon^{64}Zn$ highlighted in Figure 4.4. With few exceptions, the samples showcase resolvable $^{64}Zn$ depletions, and enrichments in $^{68}Zn$ and $^{70}Zn$, a pattern that is characteristic of bulk CCs (Chapters 2 and 3). However, a few leaching steps are identical to the London Zn standard within uncertainties, while others show complementary εZn depletions and enrichments that are characteristic of NC rather than CC meteorites.

In detail, Steps 1, 2, 4, 5, and 7 for Allende all show isotope compositions that are identical to the bulk, as reported in Chapter 2 and in Table 4.6. Step 3 has slightly smaller anomalies, while Step 6 shows a resolvable depletion in $^{68}$Zn, as would be expected for an NC meteorite. Step 6 for Murchison shows similar features, with a resolvable depletion in $^{68}$Zn, while $^{64}$Zn is enriched compared to the London Zn standard. Conversely, Steps 1, 2, 3, 4 and 7 of Murchison are identical to the bulk within uncertainties. Step 5 is the only step with εZn anomalies that exceed the εZn values determined for bulk Murchison.

Colony displays very similar results for most leachates, and these overlap with the bulk value of MIL 090025, the only CO chondrite for which a measured bulk Zn composition was available, from previous work (Chapter 2). The exceptions are Step 1, which is largely unresolvable from London Zn apart from a small enrichment in $^{70}$Zn ($\varepsilon^{70}$Zn = 0.37 ± 0.13, 2sd, n=2), and Step 4, which is more anomalous than bulk COs ($\varepsilon^{64}$Zn = – 1.05 ± 0.08, 2se, n=3). Finally, most steps for Kainsaz largely overlap with and are indistinguishable from the bulk values for MIL 090025. However, some isotope ratios are unresolvable from the London Zn standard for Steps 1, 6 and 7.

A bulk nucleosynthetic Zn isotope composition was calculated for each meteorite based on the compositions of the leaching steps and their respective Zn mass fractions as follows:

$$\varepsilon^{i}Zn_{bulk} = \sum_{n=1}^{7} \varepsilon^{i}Zn_{n} \times f_{Zn}^{n} \qquad \text{(Eq. 4.1)}$$

where *i* is the isotope of interest, *n* corresponds to the leaching step and $f_{Zn}^{n}$ is the mass fraction of Zn for step *n.* The uncertainties of each estimate were calculated using the following equation:

$$2SE_{bulk}^{i} = \sqrt{\sum_{n=1}^{7} (f_{Zn}^{n} \times 2SE_{n}^{i})^{2}} \qquad \text{(Eq. 4.2)}$$

where $2SE_{n}^{i}$ is the 95% confidence interval of the mean of all repeats performed for each leaching step. For samples for which only two repeats were performed, twice the standard deviation was used instead (see Section 4.2.3).

Table 4.6 compares the estimated $\varepsilon^{i}$Zn values and respective uncertainties for the bulk meteorites with previously measured bulk values for Allende, Murchison, and MIL 090025 (Chapters 2 and 3). Apart from Murchison, all other estimates are consistent with the measured compositions of the bulk samples. The inconsistent bulk values for Murchison likely reflect

uncertainties associated with the Zn mass fraction of about 20% that was determined for Step 6 based on the elemental characterization performed by ICP-MS, which resulted in initial estimates of $\varepsilon^{64}Zn = -0.49 \pm 0.36$, $\varepsilon^{68}Zn = 0.17 \pm 0.19$, and $\varepsilon^{70}Zn = 0.45 \pm 0.23$ for the bulk. However, the actual Zn content of the sample aliquot that was processed for Zn isotope analyses was instead more consistent with a Zn fraction of <1%. If a Zn mass fraction of 1% is assumed for Step 6 and the other fractions are scaled accordingly, the estimated bulk values change to $\varepsilon^{64}Zn = -0.81 \pm 0.21$, $\varepsilon^{68}Zn = 0.37 \pm 0.20$, and $\varepsilon^{70}Zn = 0.71 \pm 0.25$, which overlap with the measured values for bulk Murchison within uncertainties ($\varepsilon^{64}Zn = -1.32 \pm 0.34$, $\varepsilon^{68}Zn = 0.53 \pm 0.09$, and $\varepsilon^{68}Zn = 1.12 \pm 0.49$, 2se). Therefore, a Zn mass fraction of 1% is assumed for the Murchison Step 6 leachate in the ensuing discussion (Table 4.6).

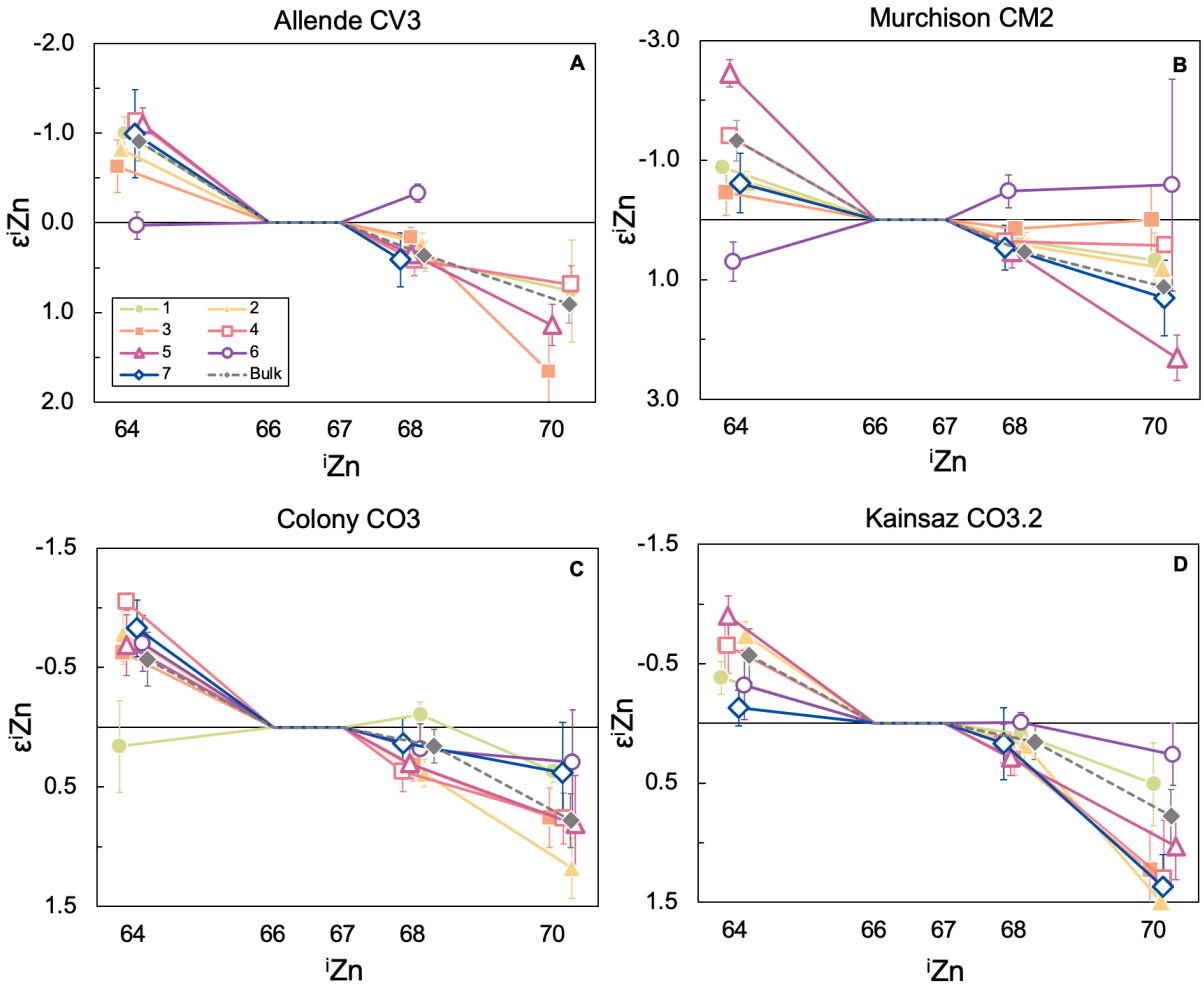



**Figure 4.3. Mass-independent Zn isotope compositions in $\varepsilon^{i}Zn$ notation.** Results of leaching steps for Allende CV3, Murchison CM2, Colony CO3, and Kainsaz CO3.2 (Table 4.5). Measured bulk compositions of Allende CV3, Murchison CM2, and MIL 0922025 CO3 (Chapters 2 and 3) are also plotted for comparison.

**Table 4.5. Mass-independent Zn isotope data (in $\varepsilon^{i}$Zn notation) and Zn mass fractions (%) of the seven leaching steps for the four meteorite samples.** n: the total number of individual analytical runs for a given sample.

| | Leaching | Data normalised to $^{66}Zn/^{67}Zn$ | | | | | | | | | | | | |
|---|---|---|---|---|---|---|---|---|---|---|---|---|---|---|
| **Sample** | **Step** | **$\varepsilon^{64}$Zn** | **2se** | **2sd** | **n** | **$\varepsilon^{68}$Zn** | **2se** | **2sd** | **n** | **$\varepsilon^{70}$Zn** | **2se** | **2sd** | **n** | **Zn fraction (%)** |
| Allende CV3 | 1 | -1.00 | 0.13 | 0.18 | 2 | 0.41 | 0.09 | 0.13 | 2 | - | - | - | - | 2.3 |
| | 2 | -0.82 | 0.28 | 0.40 | 2 | 0.24 | 0.35 | 0.49 | 2 | - | - | - | - | 5.8 |
| | 3 | -0.63 | 0.29 | 0.58 | 4 | 0.16 | 0.11 | 0.23 | 4 | 1.66 | 0.52 | 4.37 | 1 | 5.8 |
| | 4 | -1.13 | 0.22 | 0.67 | 9 | 0.42 | 0.09 | 0.34 | 14 | 1.57 | 0.57 | 1.70 | 9 | 84 |
| | 5 | -1.10 | 0.18 | 0.58 | 11 | 0.35 | 0.10 | 0.39 | 16 | 1.14 | 0.23 | 0.69 | 9 | 1.6 |
| | 6 | 0.03 | 0.10 | 0.15 | 2 | -0.33 | 0.07 | 0.10 | 2 | - | - | - | - | 0.2 |
| | 7 | -0.99 | 0.74 | 0.49 | 1 | 0.41 | 0.24 | 0.30 | 1 | - | - | - | - | 0.4 |
| Murchison CM2 | 1 | -0.88 | 0.13 | 0.25 | 4 | 0.36 | 0.11 | 0.34 | 9 | 0.67 | 0.45 | 1.01 | 5 | 66 |
| | 2 | -0.64 | 0.17 | 0.42 | 6 | 0.43 | 0.22 | 0.63 | 8 | 0.81 | 0.31 | 0.44 | 2 | 31 |
| | 3 | -0.46 | 0.38 | 0.54 | 2 | 0.15 | 0.09 | 0.21 | 5 | 0.00 | 0.59 | 1.01 | 3 | 1.1 |
| | 4 | -1.40 | 0.02 | 0.03 | 2 | 0.36 | 0.23 | 0.46 | 4 | 0.43 | 0.02 | 0.03 | 2 | 0.4 |
| | 5 | -2.45 | 0.23 | 0.46 | 4 | 0.52 | 0.14 | 0.28 | 4 | 2.31 | 0.27 | 0.38 | 2 | 0.4 |
| | 6 | 0.70 | 0.23 | 0.33 | 2 | -0.48 | 0.27 | 0.38 | 2 | -0.59 | 2.50 | 1.77 | 2 | 1 |
| | 7 | -0.62 | 0.25 | 0.31 | 1 | 0.46 | 0.18 | 0.66 | 1 | 1.31 | 0.46 | 1.88 | 1 | 0.5 |
| Colony CO3 | 1 | 0.16 | 0.38 | 0.86 | 5 | -0.10 | 0.11 | 0.28 | 7 | 0.37 | 0.09 | 0.13 | 2 | 5.4 |
| | 2 | -0.78 | 0.26 | 0.52 | 4 | 0.38 | 0.12 | 0.36 | 10 | 1.18 | 0.25 | 0.62 | 6 | 15 |
| | 3 | -0.63 | 0.07 | 0.15 | 4 | 0.32 | 0.14 | 0.39 | 8 | 0.76 | 0.00 | 0.49 | 4 | 25 |
| | 4 | -1.05 | 0.08 | 0.13 | 3 | 0.37 | 0.17 | 0.44 | 7 | 0.76 | 0.21 | 0.42 | 4 | 44 |
| | 5 | -0.69 | 0.25 | 0.76 | 9 | 0.30 | 0.12 | 0.42 | 12 | 0.81 | 0.41 | 0.82 | 3 | 6.0 |
| | 6 | -0.70 | 0.23 | 0.52 | 5 | 0.18 | 0.21 | 0.59 | 8 | 0.29 | 0.44 | 0.76 | 3 | 2.2 |
| | 7 | -0.83 | 0.24 | 0.47 | 4 | 0.13 | 0.21 | 0.55 | 7 | 0.38 | 0.42 | 0.95 | 3 | 2.3 |
| Kainsaz CO3.2 | 1 | -0.38 | 0.14 | 0.47 | 11 | 0.09 | 0.08 | 0.28 | 11 | 0.51 | 0.35 | 0.86 | 6 | 2.5 |
| | 2 | -0.74 | 0.11 | 0.30 | 10 | 0.18 | 0.17 | 0.66 | 15 | 1.49 | 0.24 | 0.75 | 10 | 4.9 |
| | 3 | -0.66 | 0.23 | 0.76 | 11 | 0.29 | 0.15 | 0.51 | 11 | 1.23 | 0.33 | 0.81 | 6 | 5.2 |
| | 4 | -0.65 | 0.23 | 0.80 | 12 | 0.17 | 0.16 | 0.56 | 12 | 1.30 | 0.49 | 1.09 | 5 | 79 |
| | 5 | -0.90 | 0.17 | 0.58 | 12 | 0.29 | 0.15 | 0.60 | 16 | 1.03 | 0.28 | 0.95 | 12 | 6.1 |
| | 6 | -0.32 | 0.29 | 0.50 | 3 | -0.01 | 0.08 | 0.18 | 5 | 0.26 | 0.18 | 0.26 | 2 | 1.4 |
| | 7 | -0.13 | 0.10 | 0.15 | 2 | 0.17 | 0.30 | 0.67 | 5 | 1.37 | 0.27 | 0.55 | 4 | 0.8 |

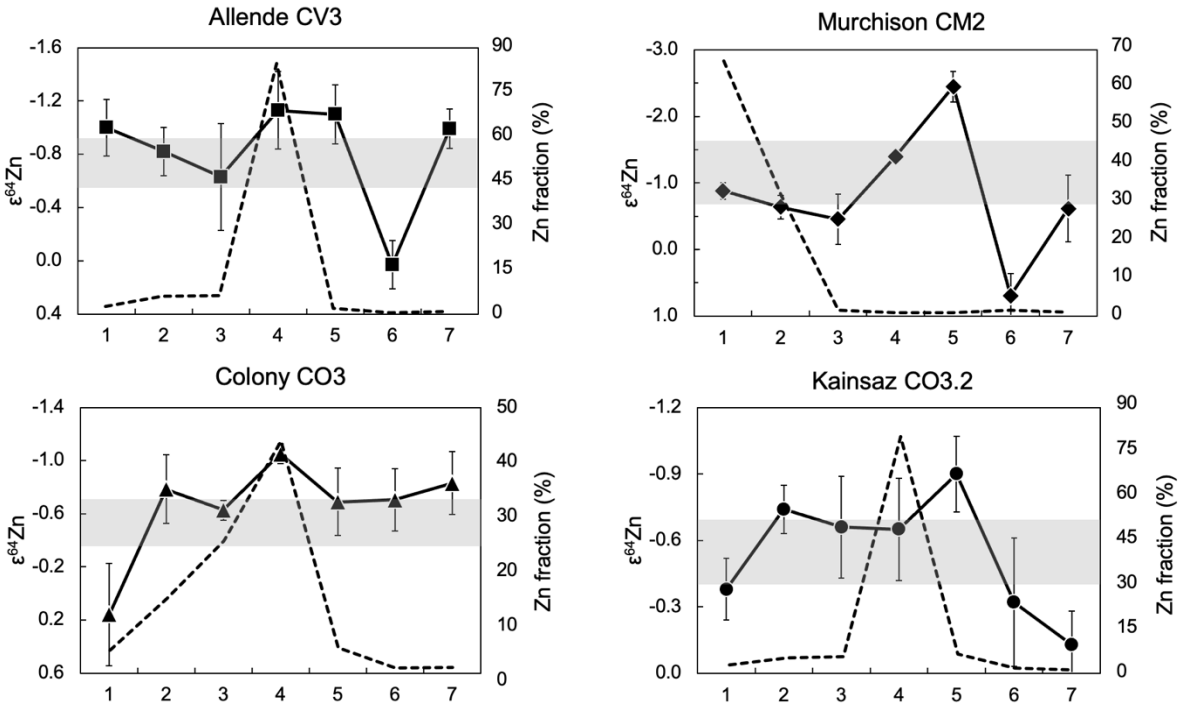



**Figure 4.4. $\varepsilon^{64}$Zn results and Zn fraction (%).** Results of leaching steps for Allende CV3, Murchison CM2, Colony CO3, and Kainsaz CO3.2 (Table 4.5). Grey band corresponds to measured mean and uncertainty for Allende CV3, Murchison CM2, and MIL 0922025 CO3 (Chapters 2 and 3, Table 4.6) for comparison.

**Table 4.6. Estimated and measured bulk compositions of meteorites.**

| **Sample** | | Allende CV3 | | Murchison CM2 | | Colony CO3 | | Kainsaz CO3.2 | |
|---|---|---|---|---|---|---|---|---|---|
| $\varepsilon^{64/67}$Zn | Calculated | -1.04 | ± 0.39 | -0.80 | ± 0.21 | -0.80 | ± 0.12 | -0.65 | ± 0.66 |
| | Measured | -0.91 | ± 0.21 | -1.32 | ± 0.34 | -0.57 | ± 0.22 | -0.57 | ± 0.22 |
| $\varepsilon^{68/67}$Zn | Calculated | 0.36 | ± 0.21 | 0.37 | ± 0.20 | 0.32 | ± 0.23 | 0.18 | ± 0.47 |
| | Measured | 0.36 | ± 0.15 | 0.53 | ± 0.09 | 0.16 | ± 0.14 | 0.16 | ± 0.14 |
| $\varepsilon^{70/67}$Zn | Calculated | - | - | 0.71 | ± 0.25 | 0.79 | ± 0.25 | 1.26 | ± 0.91 |
| | Measured | 0.91 | ± 0.60 | 1.12 | ± 0.49 | 0.78 | ± 0.25 | 0.78 | ± 0.25 |

Estimates are based on the nucleosynthetic Zn isotope compositions and Zn mass fractions of each leaching step. The measured values determined for bulk samples are from Chapters 2 and 3. No bulk samples of Colony and Kainsaz were analysed, so the composition of MIL 090025 CO3 is shown for comparison.

## 4.4 Discussion

### 4.4.1 Carrier phases of isotopically anomalous Zn

While most leaching steps that display resolvable anomalies from the London Zn standard have CC-like compositions, some of the leachates showcase complementary, NC-like compositions. To distinguish between the two types of anomalies, henceforth, the term 'anomalous Zn' will refer to CC-like isotope compositions, which corresponds to $^{64}$Zn depletions, and $^{68}$Zn and $^{70}$Zn enrichments.

All leaching steps contain some anomalous Zn for at least one of the meteorites. From the step that attacks more labile phases (Step 1), such as sulphates, sulphides, carbonates, and metal, to the ones that attack silicates (Steps 2-5), and refractory minerals (Steps 6-7), all of them presently host anomalous Zn to some extent in at least one of the meteorites. The anomalous Zn is likely derived from material produced in a specific type of nucleosynthetic source (Chapters 2 and 3), but this source is unlikely to have produced such a variety of presolar grains. Furthermore, the extent to which each step features anomalies varies between the meteorites, with some steps showcasing anomalies for some meteorites, while being largely indistinguishable from terrestrial Zn in others (i.e., $\varepsilon^{64}Zn_{Colony(6)} = -0.70 \pm 0.23$, n=5, 2se , and $\varepsilon^{64}Zn_{Allende(6)} = 0.03 \pm 0.15$, n=2, 2sd).

Hence, the ubiquitous presence of anomalous Zn in all steps is unlikely to be an original feature. Instead, the anomalous Zn is probably no longer hosted solely in its original carrier phase, but rather, it was redistributed into one or several secondary phases. This may result from processes in the solar nebula that can isotopically homogenize the compositions of distinct phases, such as the evaporation and recondensation associated with the formation of Ca-Al-rich inclusions (CAIs), or melting and recrystallization, as observed in chondrule formation events. Some degree of homogenization may also be a consequence of thermal processing and destruction of presolar grains within the parent bodies of the meteorites (Burkhardt and Schönbächler, 2015).

However, the resolvable differences between some leachate steps suggest that the different mineral phases were not fully homogenized, and, as such, some inferences can be made about the original host(s) of the anomalous Zn. For example, Step 6 is consistently one of the least anomalous for all samples, except for Colony. In detail, this step shows small but resolvable $^{64}$Zn enrichment in Murchison, $^{68}$Zn depletions for Allende and Murchison, and it is almost identical to the London Zn standard for Kainsaz ($\varepsilon^{68}Zn_{Kainsaz(6)} = -0.32 \pm 0.29$, 2se,

n=3). Some ratios for Step 7 leachates are also indistinguishable from the standard for Kainsaz and Colony. Step 1 is identical to the bulk compositions of all meteorites except Colony, where it is indistinguishable from the London Zn standard.

In contrast, Step 5 displays a larger $^{64}$Zn depletion than the bulk for Murchison ($\varepsilon^{64}Zn_{Murchison(5)} = -2.45 \pm 0.23$, 2sd, n=2), as does Step 4 for Colony ($\varepsilon^{64}Zn_{Colony(4)} = -1.05 \pm 0.08$, 2se, n=3). These two steps also showcase some of the largest $^{64}$Zn depletions for Allende and Kainsaz. Hence, it is likely that the anomalies were originally concentrated in the phases that are digested in Steps 4 and 5, rather than those of Steps 1, 6, and 7. This implies that the host of the anomalous Zn was neither a refractory, nor one of the more labile phases attacked in Step 1 (metal, oxides, sulphides, sulphates). Instead, the anomalous Zn was probably initially hosted in presolar silicates, which were attacked in Steps 2 through 5, with 4 and 5 likely targeting most of the anomalous grains since they often showcase the largest anomalies.

The conclusion that the anomalous Zn is hosted in presolar silicates is in line with the findings of a previous leaching experiment performed on Orgueil (Trinquier et al., 2009). This revealed that isotopically anomalous Ti is also hosted in presolar silicates, as most of it was released in a leaching step that employed 3 M HCl–14 M HF for 4 days at 100ºC, and which is hence similar to Step 5 of this study. Titanium and Zn isotope anomalies in bulk meteorites furthermore exhibit substantial correlation (Chapter 3, Fig 3.3, $r^2 = 0.79$). This observation is compatible with modelled anomalies that were obtained using predicted yields of Type Ia supernovae (SNIa; Woosley, 1997) and electron capture core collapse supernovae (ECSN; Wanajo et al., 2013), suggesting that they likely derive from the same nucleosynthetic source. As such, it would not be unexpected for the isotopically anomalous Zn and Ti to be hosted in the same or similar presolar carriers derived from the same source.

Notably, the magnitude of Zn isotope anomalies in CCs are smaller than expected for their given $^{50}$Ti enrichments (Chapters 2 and 3). However, this decoupling is possibly due to the variable abundance of CAIs in CCs. These refractory components were the first solids to condense from the solar nebula at very high temperatures, such that Zn condensation onto these phases would have been limited. In contrast, CAIs host substantial amounts of Ti and showcase very significant $^{50}$Ti enrichments (Torrano et al., 2019). The effect of CAIs on the bulk nucleosynthetic Ti isotope composition of meteorites can be tested by modelling a mixture between a CI-like component with CAIs, employing the following equation:

$$\varepsilon^{50}Ti_{mix} = \frac{\varepsilon^{50}Ti_{CAI} \times [Ti]_{CAI} \times f_{CAI} + \varepsilon^{50}Ti_{CI} \times [Ti]_{CI} \times f_{CI}}{[Ti]_{CAI} \times f_{CAI} + [Ti]_{CI} \times f_{CI}} \quad \text{(Eq. 4.3)}$$

Here $[Ti]$ is the Ti concentration (in weight percent, wt%) and $f$ is the mass fraction of each component, and $f_{CAI} + f_{CI} = 1$. Compositions of mixtures with $f_{CAI}$ ranging from 0 to 20% were modelled using a 1,000 trial Monte Carlo simulation. The $\varepsilon^{50}$Ti values of each component were randomly generated in a normal distribution within the uncertainty of the mean values of the two components, $\varepsilon^{50}Ti_{CAI} = 9.36 \pm 1.47$ (2sd; Torrano et al., 2019) and $\varepsilon^{50}Ti_{CI} = 1.89 \pm 0.15$ (2se; Burkhardt et al., 2021). The Ti concentrations were fixed to 0.04 wt% and 0.10wt% for the CAI and CI components, respectively, which are within the observed ranges (Wasson and Kallemeyn, 1988, Braukmüller et al., 2018, Torrano et al., 2019).

Assuming these parameters, the $\varepsilon^{50}$Ti values of CM, CV, and COs were successfully reproduced for their CAI abundances, which are 5, 10 and 13%, respectively (Fig. 4.5). Notably, the Ti concentrations of CAIs can vary significantly, such that either higher or lower concentrations than were assumed for the modelling can yield different results. However, the presented model suggests that the $\varepsilon^{50}$Ti values of the bulk meteorites can, at least in part, be influenced by CAI abundances. Hence, the different magnitudes of the Ti and Zn isotope anomalies in CCs can possibly be explained if both the anomalous Zn and Ti are hosted in presolar silicates that were thermally processed in the CAI forming regions, and, while Ti recondensed, Zn was mostly lost.

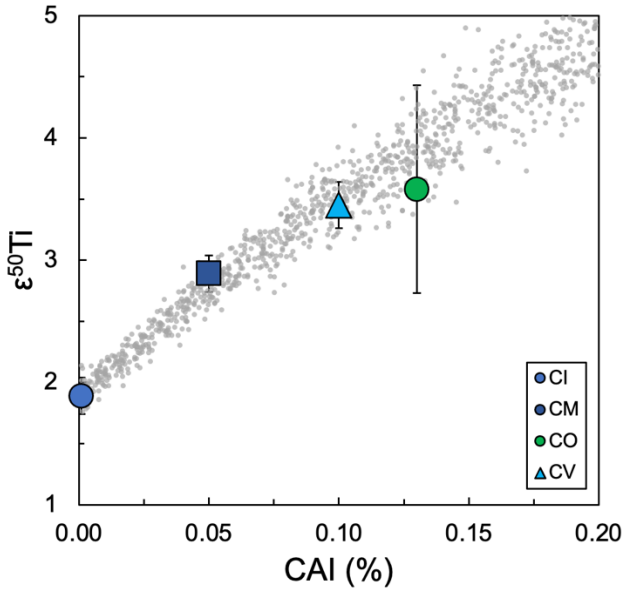



**Figure 4.5. Results of model calculations that simulate mixing between two endmembers with nucleosynthetic Ti isotope compositions akin to CAIs and CI chondrites.** Measured compositions of CM, CV, and CO meteorites (shown in blue and green data points, compiled by Burkhardt et al., 2021) can be reproduced by addition of about 5, 10, and 13% of CAIs to CI-like material, consistent with the estimated CAI content of these meteorite groups.

Presolar silicates are the most common type of presolar grain, comprising up to ~200 μg $g^{-1}$ in mass for most primitive CC meteorites (Floss and Haenecour, 2016). More specifically, most of these grains are either forsterite or enstatite. Furthermore, observations of dust clouds forming around AGB stars suggest that, while they are composed primarily of amorphous material, about 10% is present in crystalline forms, with enstatite being 3-4x more abundant than forsterite for most stellar sources. This mineralogy is also consistent with thermodynamic models of condensation under nebular conditions, which suggest that forsterite and enstatite are among the first silicates to form, and the first into which Zn condenses, at 726 K (Lodders, 2003). As such, most of the Zn, whether anomalous or not, was likely originally hosted in the same or similar silicate phases – presolar or otherwise. Indeed, apart from Murchison, most of the Zn in the other meteorites was released in leaching steps that attack silicates: 97%, 90%, and 95% for Allende, Colony, and Kainsaz, respectively (Table 4.5).

An exception to this is Murchison, for which most of the Zn was released in Steps 1 (66%), and 2 (31%), suggesting that Zn is hosted primarily in non-silicates. These two steps also display identical isotope compositions within uncertainties (i.e., $\varepsilon^{64}Zn_{Murchison(1)} = -0.88 \pm 0.13$, n=4, and $\varepsilon^{64}Zn_{Murchison(2)} = -0.64 \pm 0.17$, n=6, 2se). Murchison is the only petrological type 2 sample in this study, which means that it experienced aqueous alteration, as evidenced by the extensive amounts of phyllosilicates present in many CM2s (King et al., 2017). Since Zn is highly mobile in aqueous fluids, the leachates of Steps 1 and 2 were likely dominated by the digestion of aqueous alteration products, and not of original phases. Similarly, Step 1 in Allende displays bulk-like anomalies, which may result from the extensive metasomatism that took place on the Allende parent body (Huss et al., 2006).

In contrast, the Step 1 leachates of both COs display relatively small Zn isotope anomalies, with some ratios being unresolvable from the London Zn standard (i.e., $\varepsilon^{64}Zn_{Colony(1)} = 0.16 \pm 0.38$ (2se), n=5; $\varepsilon^{68}Zn_{Kainsaz(1)} = 0.08 \pm 0.08$ (2se) n=11) and clearly distinct from some of the other steps that display resolvable anomalies (Fig. 4.2). Colony and Kainsaz show no signs of aqueous alteration, with Kainsaz containing no phyllosilicates (Huss et al., 2006). As such, unlike for Allende and Murchison, it is likely that the Step 1 leachates of both COs primarily targeted original minerals, rather than products of aqueous alteration.

Some of the leachates produced in Steps 6 and 7 also contain anomalous Zn, with certain ratios being identical to the bulk compositions for some meteorites, such as Step 7 for Allende and

Murchison, and Steps 6 and 7 for Colony. These steps target more refractory phases (Rotaru et al., 1992), which can include both presolar grains such as SiC, spinels, diamonds, and graphite (Lodders and Amari, 2005), as well as phases that condensed from the nebular gas, including minerals that were incorporated by CAIs and amoeboid olivine aggregates (AOAs). Due to their high condensation temperatures, it is unlikely that such phases incorporated substantial amounts of Zn during crystallization, either near the stellar sources where presolar grains condensed, or in the high-temperature environments in which CAIs formed. Indeed, the measured Zn mass fractions for these two steps combined range from 0.6% for Allende to 4.4% for Colony.

As such, the refractory phases potentially include Zn that was implanted by supernovae shockwaves in the interstellar medium (ISM) in the case of presolar grains (King et al., 2012), as well as any Zn exchanged with other phases within the parent bodies as a result of thermal processing. Burkhardt and Schönbächler (2015) showed that the nucleosynthetic W isotope compositions of CC leachates for different meteorites are progressively more homogeneous for parent bodies that record higher levels of thermal alteration. This is particularly evident for the step (#5) that attacks refractory phases, which is very distinct from the bulk composition for Orgueil, which experienced little thermal alteration ($\varepsilon^{183}W_{O5} = -40.52 \pm 1.79$ compared to $\varepsilon^{183}W_{O_bulk} = -0.23 \pm 0.84$ for the bulk). The difference is much less prominent for Murchison ($\varepsilon^{183}W_{M5} = -19.17 \pm 0.86$ compared to $\varepsilon^{183}W_{M_bulk} = -0.30 \pm 0.60$), and completely absent for Allende, which records significant thermal metamorphism ($\varepsilon^{183}W_{A5} = -1.77 \pm 2.00$ compared to $\varepsilon^{183}W_{A_bulk} = -0.12 \pm 0.56$).

Hence, it is likely that the Zn isotope compositions of the phases attacked by the different leaching steps of this study were variably homogenised within the parent bodies, such that their current Zn isotope compositions are more similar to the bulk than they were initially. If the correlation that was observed between W isotope anomalies and thermal metamorphism is also assumed to be relevant for Zn isotopes, Murchison likely preserves the most pristine compositions, with Step 5 displaying the largest excess in anomalous Zn ($\varepsilon^{64}Zn_{Murchison(5)} = -2.61 \pm 0.29$, 2sd, n=2), and Step 6 featuring the largest depletion ($\varepsilon^{64}Zn_{Murchison(6)} = 0.70 \pm 0.33$, n=2, 2sd). However, even more extreme compositions are probably recorded by less thermally altered meteorites, such as CIs.

### 4.4.2 Thermal processing

Presolar silicates are very susceptible to thermal metamorphism and aqueous alteration, and hence, their variable abundances in chondrites largely reflect secondary processing within the parent body (Floss and Haenecour, 2016). However, the correlations between the abundances of more resistant presolar grains and the chemical fractionations recorded by bulk meteorite compositions have been interpreted as resulting from thermal processing in a nebular setting (Huss et al., 2003). In line with this, it has been suggested that the observed variations in explosive nucleosynthesis components throughout the Solar System could result from preferential destruction of some phases caused by radiation emitted by the protosun.

Accordingly, since $^{46}$Ti and $^{50}$Ti originate from different nucleosynthetic sources, Trinquier et al. (2009) inferred that the correlated variations observed for these isotopes in meteorites are due to by thermal processing and are not a consequence of the coincidental inhomogeneous distribution of the respective carrier phases in the early Solar System. Yokoyama et al. (2015) suggested that the $^{84}$Sr and $^{54}$Cr anomalies in the Solar System result from thermal processing and sublimation of $^{84}$Sr and $^{54}$Cr-enriched phases, and while NCs formed from the depleted residue, CAI compositions record a mixture between unprocessed CI-like material and the enriched gas. Furthermore, the absence of W isotope anomalies and Mo isotope compositions in bulk meteorites have been attributed to thermal processing and preferential loss of the more thermally susceptible Mo, while W remained unaltered (Burkhardt et al., 2012). In accord with this interpretation, Ek et al. (2020) suggested that preferential loss of presolar silicates through thermal processing is a viable mechanism to explain why Pd shows more limited variations in nucleosynthetic isotope compositions than more refractory elements, and to justify why more volatile elements such as Cd and Te lack such anomalies altogether.

As for Pd, the anomalous Zn was likely originally hosted in presolar silicates. However, the present leaching results additionally suggest that over 90% of all Zn was also present in silicate phases (Table 4.5 and Fig. 4.4). As the leachate steps that concentrate the anomalous Zn also released most of the total Zn (Steps 4 and 5), the carriers of the anomalous and the non-anomalous Zn are likely similar – if not identical. The resemblance between the carrier phases of the anomalous Zn and the remaining Zn, which must extend to their thermal susceptibilities, hence poses a challenge for separating the Zn host phases by physical processes. Instead, preferential destruction and loss of presolar silicates would most likely induce loss of both isotopically

anomalous and non-anomalous silicate phases in comparable proportions, ultimately leading to no changes in bulk isotope compositions.

Based on the results of the previous Orgueil leaching experiment (Trinquier et al., 2009), a similar outcome is also likely for Ti. While the isotopically more anomalous leaching steps encompassed about 40% of the Ti inventory, all silicate-leaching steps accounted for 99.5% of the total Ti, with less than 0.5% of Ti released from carbonates, sulphates, sulphides, metal, and refractory components. Furthermore, for both Zn and Ti, the isotopically more anomalous steps (Steps 4 and 6 for Zn, 3d-f and 4 for Ti) correspond to the most resistant silicates. Hence, if the phases that were attacked by different silicate-leaching steps could be separated by thermal processing, this would most likely result in preferential loss of the least resistant, and therefore less-anomalous phases, producing an enrichment in anomalous Zn and Ti in the inner Solar System, which is contrary to the observations.

Notably, while some refractory leaching steps have compositions identical to the bulk meteorites (i.e., $\varepsilon^{64}Zn_{Colony(6)} = -0.70 \pm 0.23$, n=5, 2se), others are indistinguishable from the London Zn standard or even showcase NC-like signatures (i.e., $\varepsilon^{64}Zn_{Murchison(6)} = 0.70 \pm 0.33$, n=2, 2sd). As discussed in the previous section, this may suggest that the refractory phases were also subjected to different extents of thermal homogenization with the carriers of the anomalous Zn. The composition of the least thermally altered sample, Murchison, therefore probably most closely resembles the original composition of the NC-like refractory component. However, more extreme depletions in anomalous Zn may have been originally present, prior to parent body processing. Hence, preferential loss of Zn from silicate phases by thermal processing could, in principle, shift bulk compositions towards more NC-like values.

Nonetheless, the fraction of Zn present in refractory components (<5%) is much lower than that hosted in silicates (>90%). Hence, in order to achieve bulk NC-like Zn isotope compositions starting from CI-like material through thermal processing, two scenarios are conceivable: (1) Either most Zn from silicates was lost, such that the bulk Zn isotope composition is then dominated by the refractory Zn component; or (2) Alternatively, the refractory component is substantially more depleted in anomalous Zn compared to what was observed even for Step 6 of Murchison. In this case, even limited loss of Zn from silicates can significantly impact the bulk Zn isotope composition. To test these scenarios, mixing models between a hypothetical NC-like refractory Zn

component and an average CC-like silicate Zn component were explored, employing the following mass balance:

$$\varepsilon^{64}Zn_{bulk} = \varepsilon^{64}Zn_{ref} \times f_{ref_final} + \varepsilon^{64}Zn_{sil} \times f_{sil_final} \qquad \text{(Eq. 4.4)}$$

Here $f_{ref_final}$ and $f_{sil_final}$ refer to the final mass fractions of Zn in each component, after Zn loss from the silicate material, and $f_{ref_final} + f_{sil_final} = 1$. Three Monte Carlo simulations were performed, each for 1,000 trials, with the refractory component being assigned a different composition for each run. As the Step 6 leachate for Murchison showcases the largest observed depletions in isotopically anomalous Zn relative to the bulk composition, $\varepsilon^{64}Zn_{ref}$ for the refractory component of Run 1 was assigned randomly generated values in a normal distribution within twice the standard deviation of the mean result obtained for this leaching step ($\varepsilon^{64}Zn_{ref} = 0.70 \pm 0.33$, n=2, 2sd). For the two remaining runs, the refractory component was assigned more extreme values, corresponding to $\varepsilon^{64}Zn_{ref} = 2.0$ and 5.0, for Runs 2 and 3, respectively. The Zn isotope compositions of the silicate components were generated with a normal distribution, varying within twice the standard deviation of the mean εZn values determined for the silicate-leaching steps (Steps 2-5) of the four analysed chondrites ($\varepsilon^{64}Zn_{sil} = -0.92 \pm 0.39$, 2sd).

Random values between 0.1 and 5% were assigned for the initial Zn mass fraction in the refractory component, $f_{ref_initial}$, which covers the range of Zn mass fractions for the refractory component of the meteorites in this study (0.6 to 4.4%). The initial Zn mass fraction for the silicate component is the complementary fraction, with $f_{sil_initial} = 1 - f_{ref_initial}$. The final fraction of Zn present in the refractory component, $f_{ref_final}$, was assigned values between 0 and 100%. Hence, the final Zn mass fraction for the silicate component can be calculated as $f_{sil_final} = 1 - f_{ref_final}$. Finally, the mass fraction of Zn lost from the silicate component by the modelled thermal processing was determined via:

$$f_{sil_lost} = 1 - \frac{f_{sil_final}}{f_{sil_initial}} \qquad \text{(Eq. 4.5)}$$

This process was then repeated using $\varepsilon^{68}Zn$ values ($\varepsilon^{68}Zn_{sil}$ = 0.31 ± 0.10; $\varepsilon^{68}Zn_{ref_1} = \varepsilon^{68}Zn_{Murchison(6)}$ = – 0.48 ± 0.38; $\varepsilon^{68}Zn_{ref_2}$ = –1.0; $\varepsilon^{68}Zn_{ref_3}$ = –2.0), to ensure that the outcome is consistent regardless of the isotope ratio employed.

The results of the simulations are plotted in Figure 4.6, which also includes mean data for the NC enstatite, ordinary and, Rumuruti chondrites (EC, OC, and RC) as well as CCs (CI, CM, CO, CV) for comparison (Chapter 3; Table A4.1, Appendix). The fraction of Zn lost from these chondrites was estimated based on mean Zn concentrations for each group, normalized to Al concentrations and to CIs, and assuming an initial CI-like Zn abundance (Table A4.1, Appendix). Since the EC3-4s have much higher Zn concentrations than EC5-6s, these petrological types are shown separately. The OC, RC, and CC groups show significantly less variability in Zn concentrations (Table A4.1, Appendix), so the mean value determined from all available petrological grades was assumed to be representative of the bulk composition.

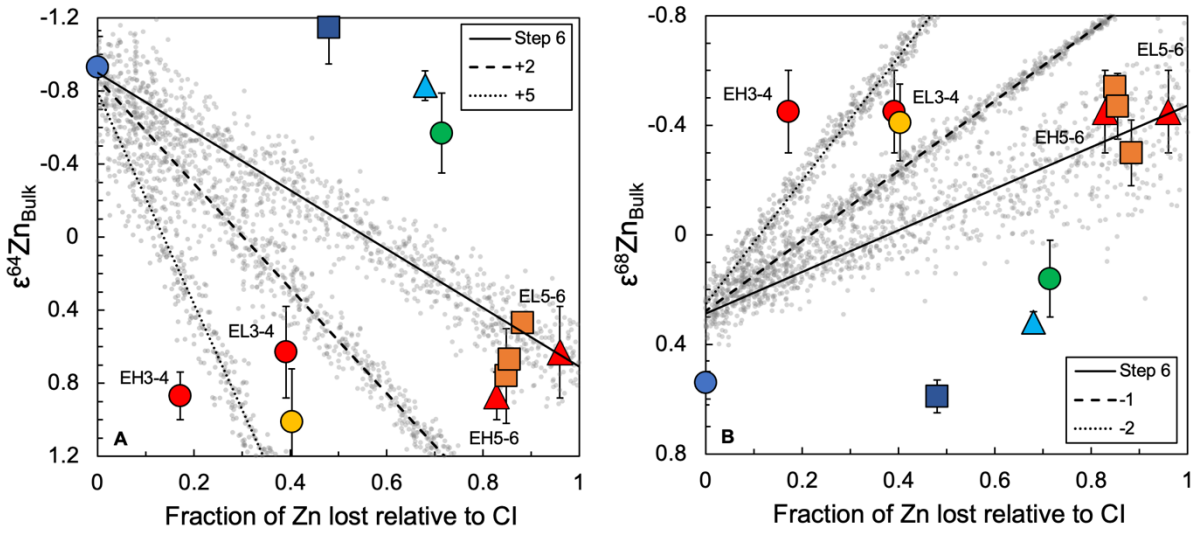



**Figure 4.6. Variable nucleosynthetic Zn isotope compositions and bulk Zn content of chondritic meteorites.** (A) Plot of bulk $\varepsilon^{64}Zn$ values versus fraction of Zn lost produced by a Monte Carlo simulation of thermal processing and preferential loss of Zn from presolar silicates (individual results are shown as grey dots and lines correspond to linear trends). The models assume a CI-like starting Zn isotope composition and concentration, and three different $\varepsilon^{64}Zn$ values for the refractory component: 0.70 ± 0.33 (Murchison Step 6), 2.0, and 5.0. Mean measured isotope compositions (Chapter 3) and concentrations (Table A4.1, Appendix) of all available chondrite groups are also shown for comparison. (B) Same as (A) but using $\varepsilon^{68}Zn$ values instead of $\varepsilon^{64}Zn$.

As expected, apart from CIs, all other CCs fall off any of the mixing trends (Fig. 4.6). This reflects that they have different Zn concentrations but similar $\varepsilon^{64}$Zn values. As such, the variable Zn depletion of CCs is incompatible with preferential Zn loss from any particular phase, and as a consequence, the variable Zn loss had no impact on the nucleosynthetic Zn isotope compositions. In contrast, the OC and EC5-6 compositions overlap with the Run 1 results, which applied the composition of the Step 6 Murchison leachate for the refractory component, combined with assumed Zn losses of approximately 80 to nearly 100% relative to CIs. Hence, some NC-like Zn isotope compositions and concentrations can be reproduced by preferential loss of Zn from presolar silicates, using the aforementioned parameters.

In contrast, EL3-4s and RCs can only be reproduced by ~40% Zn loss and assuming $\varepsilon^{64}Zn_{ref}$ and $\varepsilon^{68}Zn_{ref}$ values between 2.0 and 5.0 and between –1.0 and –2.0, respectively, for the refractory component. Furthermore, since EH3-4s show very limited Zn loss compared to CIs (<20%), their Zn isotope compositions can only be explained by thermal processing by calling for a much more extreme refractory component composition, with $\varepsilon^{64}Zn_{ref} > 5.0$ and $\varepsilon^{68}Zn_{ref} < –2.0$. While it is possible that the initial composition of the refractory component was more extreme than demonstrated by present values, an $\varepsilon^{64}Zn_{ref} > 5.0$ and $\varepsilon^{68}Zn_{ref} < –2.0$ requires a depletion in anomalous Zn that exceeds that of the most depleted CC leachate (Step 6 of Murchison) by at least a factor of x5. As there is no evidence to suggest such an extreme composition was initially present in any of the CCs analysed in this study, this scenario may require that the refractory components present in CCs and NCs were different. This, in turn, implies pre-existing isotopic heterogeneity within the Solar System, which can directly explain the observed anomalies, rendering thermal processing unnecessary.

The present Zn concentrations of the meteorites may, however, not reflect the Zn abundances of the precursor materials, as they have been subjected to secondary alteration within the parent bodies. This is especially true for ECs, which display a very substantial range of concentrations for Zn and other volatile elements (Moynier et al., 2011, Palk et al., 2018). Hence, it is possible that the Zn concentration of the bulk EC parent bodies was intermediate between EC3-4s and EC5-6s. If, for example, OC-like Zn concentrations are assumed for the EC parent bodies, then they would also be compatible with the Run 1 conditions of the model. However, this would require the EC precursor materials to have lost 80-90% of their Zn relative to CIs prior to

or during parent body accretion, followed by substantial mobilization of Zn within the parent body, further depleting EC5-6s and substantially enriching EC3-4s.

In line with this, the Te isotope systematics of ECs have been interpreted as resulting from considerable mobilization and recondensation of Te and other volatiles within the EC parent bodies (Hellmann et al., 2021). Further studies of mass-dependent Zn isotope fractionation in ECs may help elucidate if similar characteristics are also observed for Zn. If such a scenario is reasonable, at least part of the volatile depletion in the inner Solar System can be linked to the same nebular process that induced the nucleosynthetic Zn isotope anomalies. Hence, constraining the original Zn concentrations of NC, and in particular, the EC, parent bodies, as well as characterizing the refractory component of less thermally altered meteorites, such as CIs, is essential to test the feasibility of the thermal processing scenario.

### 4.4.3 Incomplete homogenization

Alternatively, the variable nucleosynthetic isotope compositions of bulk meteorites could also be achieved if the carrier phases of the anomalies were never fully homogenised at the Solar System scale. A possible scenario invokes progressive depletion in explosive nucleosynthesis components in the infalling molecular cloud material that fed the protoplanetary disk (Nanne et al., 2019). The initial material, enriched in presolar grains from explosive nucleosynthesis, would have been sampled by CAIs immediately after collapse of the molecular cloud and formation of the protosun. As the disk expanded, CAIs moved outwards by viscous drag, and the area in the vicinity of the protosun would have been replenished by infalling molecular cloud material that was increasingly depleted in explosive nucleosynthesis isotopes. This can account for the NC composition closer to the sun being depleted in material from explosive nucleosynthesis and CC composition in the outer Solar System that are intermediate between CAIs and NCs.

These changes in nucleosynthetic isotope compositions could also be linked to incomplete homogenization of material that was added to the molecular cloud or the protoplanetary disk on separate occasions. Addition of material on different timeframes is corroborated by the presence the short-lived radionuclide $^{26}$Al, which provided some of the heat that induced melting and differentiation in early planetesimals. The short half-life suggest that these nuclides were added relatively late, likely as result from a delayed injection of freshly produced matter. While, in principle, $^{26}$Al could have been evenly allocated throughout the Solar System, the homogeneous

the distribution of this nuclide has been debated for many years (Ireland, 1990, Park et al., 2017), with recently confirmed mismatches between Pb-Pb and Al-Mg ages for achondrites being interpreted as resulting from uneven spatial distribution of $^{26}$Al (Krestianinov et al., 2023). If so, it is conceivable that the nucleosynthetic isotope composition of the molecular cloud may have changed over time, and that these changes are reflected in different Solar System materials.

The idea of pre-existing Solar System-scale isotopic heterogeneity was previously rejected on the basis that highly refractory elements, such as Os (Yokoyama et al., 2010), showcase no resolvable anomalies, and because such a scenario would require coincidental distribution of material from different nucleosynthetic sources (Trinquier et al., 2009, Akram et al., 2015), including isotopes produced in SNIa, SNII, and r-process nuclides. However, while the CC versus NC dichotomy has been demonstrated for all elements that are known to display nucleosynthetic isotope anomalies (except for Si, see Onyett et al., 2023), correlations in the distribution of anomalous material derived from different nucleosynthetic sources are sometimes inconsistent.

For instance, Ca and Ti isotope anomalies, which are thought to be derived from the same nucleosynthetic source (SNIa or ECSN; Dauphas et al., 2014), display an excellent positive correlation for both CCs and NCs (Fig 4.7). These isotope systems furthermore display good correlations with Cr isotope anomalies, which may be derived from a different type of SNII (Qin et al., 2011b). However, while in NCs these correlations are positive, negative correlations are seen for CCs. In contrast, Zr isotope anomalies, which are produced in low mass AGB stars (Akram et al., 2015), showcase positive correlations with Ca and Ti isotopes for CCs, but negative correlations for NCs.

Some discrepancies are also present even among s-process anomalies. Zirconium, Nd, and Mo isotope are all produced primarily by s and r-process nucleosynthesis (Akram et al., 2015, Burkhardt et al., 2016, Dauphas et al., 2002), and whilst the elements have similar condensation temperatures (Lodders, 2003), the isotopic correlations are different (Fig 4.7). For example, no correlations are present between $\varepsilon^{95}$Mo and $\varepsilon^{96}$Zr. In principle, this could reflect that Mo are Zr are moderately siderophile and lithophile, respectively, such that the elements may be hosted in different phases, which could decouple the anomalies. Lithophile Nd, however, displays isotopic correlations with Mo. More specifically, Mo and Nd isotope anomalies have a positive correlation for CCs, but the opposite trend is seen for NCs. Conversely, Nd and Zr isotope anomalies show a weak positive correlation for both CCs and NCs. Hence, there are noticeable differences in the

correlations of different anomalies, not only for ones derived from different nucleosynthetic sites, but potentially even for ones produced by the same nucleosynthetic processes.

Amongst chondrites, ECs, which are isotopically most similar to Earth, are particularly detached from these correlations. In particular, they display the largest depletions in r-process isotopes amongst all sampled Solar System materials whilst nucleosynthetic isotope compositions of Fe-peak elements are typically intermediate between CCs and other NC groups. For instance, $^{50}$Ti enrichments increase in the order NC-achondrites<OCs<ECs≈aubrites<CCs (Trinquier et al., 2009), while for $^{95}$Mo, the general trend is EC≈aubrites<OCs≤NC-achondrites<CCs (Budde et al., 2019). And, unlike for refractory elements, for some of which the ECs exhibit isotope compositions indistinguishable from Earth, these meteorites display depletions in $^{68}$Zn and $^{70}$Zn that are akin to OCs but which exceed those determined for Earth (Chapters 2 and 3).

Consequently, if the molecular cloud was completely homogenized prior to accretion, this would require a subsequent process or combination of processes that can produce (1) an overall enrichment of isotopes generated by explosive nucleosynthesis in CCs compared to NCs; (2) opposing trends between isotope anomalies of different stellar origins in the CC and NC reservoirs; and (3) decoupled anomalies for elements with similar condensation temperatures that stem from the same nucleosynthetic processes. To achieve this, different phases would have to be preferentially destroyed in the inner and the outer Solar System, while similar phases must experience different extents of destruction. Clearly, this is difficult to reconcile with a single physical mechanism such as thermal processing.

Some of the correlations between different anomalies may, however, be linked to variable abundances of chondrite components. As for Ti isotopes, isotopic variation in Cr and Zr amongst CCs have been attributed to variable incorporation of CAIs (Qin et al., 2011b, Akram et al., 2015). Recently, Yap et al. (2023) were able to reproduce the nucleosynthetic isotope compositions and elemental abundances of Ca, Ti, Cr, and Fe for a range of CCs by mixing an OC-like component with CI-dust and CAIs. Furthermore, Hellmann et al. (2023) showed that the nucleosynthetic Ti, and Cr, and the mass-dependent Te isotope variations observed for CCs can be reproduced by mixing between matrix, chondrules, and refractory inclusions. Two component mixing has also been traditionally invoked to explain the variable volatile element depletion of Solar System materials (Larimer and Anders, 1967). Additionally, mixing between isotopically distinct metal,

sulphide and silicate phases has also been proposed to explain correlated mass-dependent Zn isotope compositions and Zn concentrations of CCs (Pringle et al., 2017).

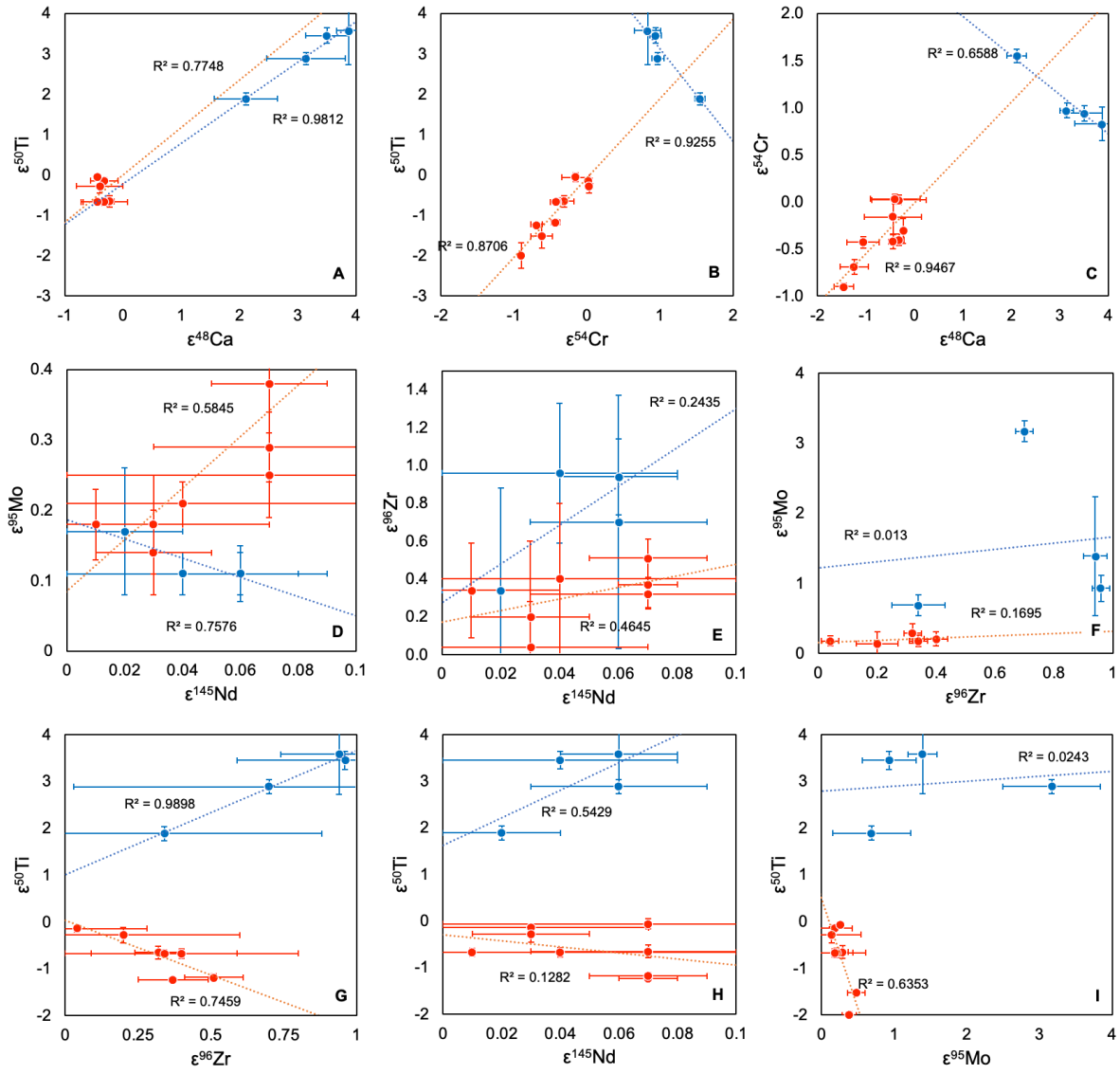



**Figure 4.7. Plots showing correlated variations between different nucleosynthetic isotope anomalies.** Compiled $\varepsilon^{50}$Ti, $\varepsilon^{48}$Ca, $\varepsilon^{54}$Cr, $\varepsilon^{95}$Mo, $\varepsilon^{96}$Zr, and $\varepsilon^{145}$Nd values for CC (blue) and NC (red) meteorites are available in Table A4.2 (Appendix).

Hence, it appears that much of the correlated isotopic variations seen in CCs can be explained by mixing between isotopically and elementally distinct components. It will be of interest to investigate whether variations of other chondrite components can also account for any isotopic trends, particularly for NCs, since they contain virtually no CAIs. Potential correlations between anomalies and variations in metal-sulphide content are especially unexplored. But, if such

correlated variations could be attributed to variable mixing between isotopically distinct components coupled with spatial or temporal depletion of the infalling material in the products of explosive nucleosynthesis, this would relax constraints on the incomplete homogenization hypothesis and eliminate the need for thermal processing.

## 4.5 Conclusions

Progressive acid-leaching of carbonaceous chondrites revealed that all leaching steps display evidence for the presence of isotopically anomalous Zn, characterized by a depletion of $^{64}$Zn and enrichments in $^{68}$Zn and $^{70}$Zn relative to a terrestrial standard, in at least one of the meteorites. This implies variable partial isotopic homogenization between different mineral phases, such that the anomalous Zn is no longer hosted solely in its original carrier. The compositions of the different leachate fractions were most commonly identical to those of the bulk meteorites, with the largest isotope anomalies present in silicate-attacking steps. In contrast, the leachates that preferentially digested more labile phases (metal, sulphides, sulphates, carbonates) and those that attacked refractory minerals showcased indistinguishable values to the terrestrial standard for some meteorites, while others even displayed small depletions in isotopically anomalous Zn, as seen for NC chondrites, suggesting that these phases were not the original hosts of the anomalies. Thus, the isotopically anomalous Zn was most likely initially hosted in presolar silicates derived from either SNIa or ECSN.

The leachate steps that carried the largest mass fractions of isotopically anomalous Zn also contained most of the total Zn inventory, with silicate-attacking steps yielding more than 90% of the total Zn budget for three of the four meteorites. The single exception is Murchison, where most of the Zn is likely hosted in aqueous alteration products. As such, the presolar carriers of the Zn isotope anomalies are similar or possibly identical to the mineral phases that host the bulk of the CC Zn inventory. This similarity renders it unlikely that the carrier phases of the isotopically anomalous Zn can be separated from the silicates that predominantly host the Zn budgets of CCs by physical mechanisms, such as thermal processing. Alternatively, if the refractory components initially had NC-like Zn isotope compositions, selective and substantial loss of isotopically anomalous (and total) Zn (>90%) from the silicates could produce the nucleosynthetic Zn isotope anomalies observed in NCs. However, the original Zn contents of OCs and particularly ECs prior

to parent body processing are poorly constrained, making it difficult to assess whether such extensive Zn loss can be accommodated.

Finally, it may be difficult to account for the correlated isotope anomalies that are observed for many elements through the action of a single physical process, such as thermal processing, on an initially homogeneous molecular cloud. A more straightforward explanation for the observed variations in nucleosynthetic isotope composition may hence be offered by the pre-existing heterogeneous distribution of the isotopic carrier phases within the molecular cloud, due to progressive depletion of the infalling material in nuclides produced by explosive nucleosynthesis, combined with variable mixing of isotopically distinct components.

## 4.6 References


AKRAM, W., SCHÖNBÄCHLER, M., BISTERZO, S. & GALLINO, R. 2015. Zirconium isotope evidence for the heterogeneous distribution of s-process materials in the Solar System. *Geochimica et Cosmochimica Acta,* 165**,** 484-500.

BRAGAGNI, A., WOMBACHER, F., KIRCHENBAUR, M., BRAUKMÜLLER, N. & MÜNKER, C. 2023. Mass-independent Sn isotope fractionation and radiogenic $^{115}$Sn in chondrites and terrestrial rocks. *Geochimica et Cosmochimica Acta,* 344**,** 40-58.

BRAUKMÜLLER, N., WOMBACHER, F., FUNK, C. & MUNKER, C. 2019. Earth's volatile element depletion pattern inherited from a carbonaceous chondrite-like source. *Nature Geoscience,* 12**,** 564-568.

BRAUKMÜLLER, N., WOMBACHER, F., HEZEL, D. C., ESCOUBE, R. & MUNKER, C. 2018. The chemical composition of carbonaceous chondrites: Implications for volatile element depletion, complementarity and alteration. *Geochimica et Cosmochimica Acta,* 239**,** 17-48.

BUDDE, G., BURKHARDT, C. & KLEINE, T. 2019. Molybdenum isotopic evidence for the late accretion of outer Solar System material to Earth. *Nature Astronomy,* 3**,** 736-741.

BURKHARDT, C., BORG, L. E., BRENNECKA, G. A., SHOLLENBERGER, Q. R., DAUPHAS, N. & KLEINE, T. 2016. A nucleosynthetic origin for the Earth's anomalous $^{142}$Nd composition. *Nature,* 537**,** 394-398.

BURKHARDT, C., KLEINE, T., DAUPHAS, N. & WIELER, R. 2012. Origin of isotopic heterogeneity in the solar nebula by thermal processing and mixing of nebular dust. *Earth and Planetary Science Letters,* 357-358**,** 298-307.

BURKHARDT, C. & SCHÖNBÄCHLER, M. 2015. Intrinsic W nucleosynthetic isotope variations in carbonaceous chondrites: Implications for W nucleosynthesis and nebular vs. parent body processing of presolar materials. *Geochimica et Cosmochimica Acta,* 165**,** 361-375.

BURKHARDT, C., SPITZER, F., MORBIDELLI, A., BUDDE, G., RENDER, J. H., KRUIJER, T. S. & KLEINE, T. 2021. Terrestrial planet formation from lost inner Solar System material. *Science Advances,* 7**,** eabj7601.

DAUPHAS, N., CHEN, J. H., ZHANG, J., PAPANASTASSIOU, D. A., DAVIS, A. M. & TRAVAGLIO, C. 2014. Calcium-48 isotopic anomalies in bulk chondrites and achondrites: Evidence for a uniform isotopic reservoir in the inner protoplanetary disk. *Earth Planetary Science Letters,* 407**,** 96-108.

DAUPHAS, N., MARTY, B. & REISBERG, L. 2002. Molybdenum evidence for inherited planetary scale isotope heterogeneity of the protosolar nebula. *Astrophysical Journal,* 565**,** 640-644.

EK, M., HUNT, A. C., LUGARO, M. & SCHÖNBÄCHLER, M. 2020. The origin of s-process isotope heterogeneity in the solar protoplanetary disk. *Nature Astronomy,* 4**,** 273-281.

FISCHER-GÖDDE, M. & KLEINE, T. 2017. Ruthenium isotopic evidence for an inner Solar System origin of the late veneer. *Nature,* 541**,** 525-527.

FLOSS, C. & HAENECOUR, P. 2016. Presolar silicate grains: Abundances, isotopic and elemental compositions, and the effects of secondary processing. *Geochemical Journal,* 50**,** 3-25.

HELLMANN, J. L., HOPP, T., BURKHARDT, C., BECKER, H., FISCHER-GÖDDE, M. & KLEINE, T. 2021. Tellurium isotope cosmochemistry: Implications for volatile fractionation in chondrite parent bodies and origin of the late veneer. *Geochimica et Cosmochimica Acta,* 309**,** 313-328.

HUSS, G. R., MESHIK, A. P., SMITH, J. B. & HOHENBERG, C. M. 2003. Presolar diamond, silicon carbide, and graphite in carbonaceous chondrites: Implications for thermal processing in the solar nebula. *Geochimica et Cosmochimica Acta,* 67**,** 4823-4848.

HUSS, G. R., RUBIN, A. E. & GROSSMAN, J. N. 2006. Thermal Metamorphism in Chondrites. *In:* LAURETTA, D. S. & MCSWEEN, H. Y. (eds.) *Meteorites and the Early Solar System II.*

IRELAND, T. R. 1990. Presolar isotopic and chemical signatures in hibonite-bearing refractory inclusions from the Murchison carbonaceous chondrite. *Geochimica et Cosmochimica Acta,* 54**,** 3219-3237.

KING, A. J., HENKEL, T., ROST, D. & LYON, I. C. 2012. Trace element depth profiles in presolar silicon carbide grains. *Meteoritics & Planetary Science,* 47**,** 1624-1643.

KING, A. J., SCHOFIELD, P. F. & RUSSELL, S. S. 2017. Type 1 aqueous alteration in CM carbonaceous chondrites: Implications for the evolution of water-rich asteroids. *Meteoritics & Planetary Science,* 52**,** 1197-1215.

KRESTIANINOV, E., AMELIN, Y., YIN, Q.-Z., CARY, P., HUYSKENS, M. H., MILLER, A., DEY, S., HIBIYA, Y., TANG, H., YOUNG, E. D., PACK, A. & DI ROCCO, T. 2023. Igneous meteorites suggest Aluminium-26 heterogeneity in the early Solar Nebula. *Nature Communications,* 14**,** 4940.

LARIMER, J. W. & ANDERS, E. 1967. Chemical fractionations in meteorites – II. Abundance patterns and their interpretation. *Geochimica et Cosmochimica Acta,* 31**,** 1239-1270.

LODDERS, K. 2003. Solar System abundances and condensation temperatures of the elements. *Astrophysical Journal,* 591**,** 1220-1247.

LODDERS, K. & AMARI, S. 2005. Presolar grains from meteorites: Remnants from the early times of the Solar System. *Geochemistry,* 65**,** 93-166.

MARTINS, R., KUTHNING, S., COLES, B. J., KREISSIG, K. & REHKÄMPER, M. 2023. Nucleosynthetic isotope anomalies of zinc in meteorites constrain the origin of Earth's volatiles. *Science,* 379**,** 369-372.

MOYNIER, F., PANIELLO, R. C., GOUNELLE, M., ALBARÈDE, F., BECK, P., PODOSEK, F. & ZANDA, B. 2011. Nature of volatile depletion and genetic relationships in enstatite chondrites and aubrites inferred from Zn isotopes. *Geochimica et Cosmochimica Acta,* 75**,** 297-307.

NANNE, J. A. M., NIMMO, F., CUZZI, J. N. & KLEINE, T. 2019. Origin of the non-carbonaceous–carbonaceous meteorite dichotomy. *Earth and Planetary Science Letters,* 511**,** 44-54.

O'NEILL, H. S. C. 1991. The origin of the Moon and the early history of the Earth – A chemical model. Part 2: The Earth. *Geochimica et Cosmochimica Acta,* 55**,** 1159-1172.

ONYETT, I. J., SCHILLER, M., MAKHATADZE, G. V., DENG, Z., JOHANSEN, A. & BIZZARRO, M. 2023. Silicon isotope constraints on terrestrial planet accretion. *Nature*.

PALK, C., ANDREASEN, R., REHKÄMPER, M., STUNT, A., KREISSIG, K., COLES, B., SCHÖNBÄCHLER, M. & SMITH, C. 2018. Variable Tl, Pb, and Cd concentrations and isotope compositions of enstatite and ordinary chondrites—Evidence for volatile element mobilization and decay of extinct 205Pb. *Meteoritics & Planetary Science,* 53**,** 167-186.

PARK, C., NAGASHIMA, K., KROT, A. N., HUSS, G. R., DAVIS, A. M. & BIZZARRO, M. 2017. Calcium-aluminum-rich inclusions with fractionation and unidentified nuclear effects (FUN CAIs): II. Heterogeneities of magnesium isotopes and 26Al in the early Solar System inferred from in situ high-precision magnesium-isotope measurements. *Geochimica et Cosmochimica Acta,* 201**,** 6-24.

PRINGLE, E. A., MOYNIER, F., BECK, P., PANIELLO, R. & HEZEL, D. C. 2017. The origin of volatile element depletion in early Solar System material: Clues from Zn isotopes in chondrules. *Earth and Planetary Science Letters,* 468**,** 62-71.

QIN, L., CARLSON, R. W. & ALEXANDER, C. M. O. D. 2011a. Correlated nucleosynthetic isotopic variability in Cr, Sr, Ba, Sm, Nd and Hf in Murchison and QUE 97008. *Geochimica et Cosmochimica Acta,* 75**,** 7806-7828.

QIN, L., NITTLER, L. R., ALEXANDER, C. M. O. D., WANG, J., STADERMANN, F. J. & CARLSON, R. W. 2011b. Extreme 54Cr-rich nano-oxides in the CI chondrite Orgueil – Implication for a late supernova injection into the Solar System. *Geochimica et Cosmochimica Acta,* 75**,** 629-644.

ROTARU, M., BIRCK, J. L. & ALLÈGRE, C. J. 1992. Clues to early Solar System history from chromium isotopes in carbonaceous chondrites. *Nature,* 358**,** 465-470.

SAVAGE, P. S., MOYNIER, F. & BOYET, M. 2022. Zinc isotope anomalies in primitive meteorites identify the outer Solar System as an important source of Earth's volatile inventory. *Icarus,* 386**,** 115172.

STELLER, T., BURKHARDT, C., YANG, C. & KLEINE, T. 2022. Nucleosynthetic zinc isotope anomalies reveal a dual origin of terrestrial volatiles. *Icarus,* 386**,** 115171.

TAYLOR, G. J. 2013. The bulk composition of Mars. *Geochemistry,* 73**,** 401-420.

TORRANO, Z. A., BRENNECKA, G. A., WILLIAMS, C. D., ROMANIELLO, S. J., RAI, V. K., HINES, R. R. & WADHWA, M. 2019. Titanium isotope signatures of calcium-aluminum-rich inclusions

from CV and CK chondrites: Implications for early Solar System reservoirs and mixing. *Geochimica et Cosmochimica Acta,* 263**,** 13-30.

TRINQUIER, A., BIRCK, J. L. & ALLEGRE, C. J. 2007. Widespread Cr-54 heterogeneity in the inner Solar System. *Astrophysical Journal,* 655**,** 1179-1185.

TRINQUIER, A., ELLIOTT, T., ULFBECK, D., COATH, C., KROT, A. N. & BIZZARRO, M. 2009. Origin of nucleosynthetic isotope heterogeneity in the solar protoplanetary disk. *Science,* 324**,** 374-376.

WANAJO, S., JANKA, H.-T. & MÜLLER, B. 2013. Electron-capure supernovae as origin of $^{48}$Ca. *Astrophysical Journal Letters,* 767**,** L26.

WASSON, J. T. & KALLEMEYN, G. W. 1988. Compositions of chondrites. *Philosophical Transactions of the Royal Society A,* 325**,** 535-544.

WOOSLEY, S. E. 1997. Neutron-rich nucleosynthesis in carbon deflagration supernovae. *The Astrophysical Journal,* 476**,** 801-810.

YAP, T. E. & TISSOT, F. L. H. 2023. The NC-CC dichotomy explained by significant addition of CAI-like dust to the Bulk Molecular Cloud (BMC) composition. *Icarus,* 405**,** 115680.

YOKOYAMA, T., FUKAMI, Y., OKUI, W., ITO, N. & YAMAZAKI, H. 2015. Nucleosynthetic strontium isotope anomalies in carbonaceous chondrites. *Earth and Planetary Science Letters,* 416**,** 46-55.

YOKOYAMA, T., O'D. ALEXANDER, C. M. & WALKER, R. J. 2010. Osmium isotope anomalies in chondrites: Results for acid residues and related leachates. *Earth and Planetary Science Letters,* 291**,** 48-59.

# Summary and Outlook

The present study characterized the mass-independent Zn isotope compositions of a range of bulk meteorites and showed that CC and NC meteorites display complementary anomalies relative to Earth for all five Zn isotopes. These anomalies are compatible with variable additions of modelled material from ECSN or SNIa, regardless of which isotope ratios are used for internal normalization of the Zn isotope data. Furthermore, the Zn isotope anomalies show good correlations with isotope anomalies of refractory elements that are produced in the same aforementioned nucleosynthetic sources. In contrast, the Zn isotope anomalies do not correlate with mass-dependent Zn isotope fractionation and the $^{67}$Zn anomalies in particular are incompatible with potential mass-independent isotope fractionations induced by the nuclear field shift effects. Hence, the most probable cause of the anomalies is heterogeneous distribution of presolar dust from explosive nucleosynthesis, which was more amply available in the CC forming region of the outer Solar System.

Multiple Zn isotope-based mixing models with different meteorite groups were performed to constrain the origin of Earth's Zn. Regardless of the meteorite groups considered, the Zn isotope ratios employed, or if the models assumed mean CC and NC compositions or were allowed to vary within the full range of compositions for each reservoir, the results consistently have a maximum probability when ~45% of Earth's Zn is derived from CC material. Values within the 30-60% range are possible if the most extreme endmember compositions are used but the probability decreases substantially for such scenarios. This stands in contrast to the findings of other Zn isotope studies, which suggest a 30% addition of Zn from CC material. Notably, the latter estimates are based on a less comprehensive set of meteorites, more limited data, and narrow assumptions about the potential endmembers involved.

To estimate the mass of CC material that was accreted by Earth, this study encompassed mixing simulations between a range of CC and NC materials while taking into account their variable Zn concentrations. In addition to the Zn isotope anomalies, the models also employed constraints from ten other nucleosynthetic isotope systems and the relative elemental abundances of the ten main rock-forming elements. These models suggest that it is not possible to reproduce the compositional characteristics of the Earth from sampled meteoritic materials. This can, however, be achieved if materials with EC- and OC-like nucleosynthetic isotope compositions but with elemental abundances and mass-dependent isotope compositions of differentiated planetesimals, such as the HED and angrite parent bodies, are considered. With such a scenario,

Earth's elemental and isotopic compositions can be reproduced by mixing of ~15% CCs and ~85% EC- and OC-like material, with the latter comprising both chondritic material (20%) and differentiated planetesimals (65%).

Two important conclusions can be derived from these models: (1) CCs provided just ~15% of Earth's mass, but nearly half of Earth's Zn, and (2) chondrites, between CCs and NCCs, provided just 35% of Earth's mass, but over 90% of its Zn. While these conclusions cannot be automatically extended to other volatiles, similar outcomes are more likely than not. This is because, while the extent of depletion varies between elements, chondrites enriched in Zn are also typically enriched in other volatile elements. Similarly, the mechanisms that induced substantial Zn loss in differentiated planetesimals, will also have induced loss of other volatiles to different extents, particularly of lighter molecules, such as water. Hence, assuming similar materials are available for accretion in other planetary systems, it is conceivable that a habitable planet could form without contributions from material formed beyond the frost-line, such as CCs. This would extensively limit the volatile content, but significant amounts of volatiles may also be available from undifferentiated materials formed within the habitable zone. However, substantial accretionary contributions from undifferentiated planetesimals may be an indispensable condition for planetary habitability.

Finally, leaching of CC meteorites revealed that the carrier phases that host the Zn isotope anomalies are likely presolar silicate grains. Mass balance modelling constrains the conditions at which the observed variations in nucleosynthetic Zn isotope compositions of bulk meteorites may have been achieved through thermal processing. Either the more refractory mineral phases were originally more depleted in isotopically anomalous Zn than at present or ≥ 90% of the original Zn inventory were lost from the silicate phases. While sufficiently strong depletions in isotopically anomalous Zn were not demonstrated for refractory components in the meteorites of this study, it is possible that such signatures were obscured by homogenization during thermal alteration within the parent body. The Zn concentrations of many chondritic meteorites, and in particular OCs and ECs, have been altered by parent body processing, making it difficult to assess the extent of Zn loss from the respective parent bodies. An alternative, and possibly more straightforward, explanation is that the observed Zn isotope variations between CCs and NC meteorites simply reflect temporal or spatial changes in the composition of the infalling material from the molecular cloud, coupled with mixing between isotopically distinct chondrite components.

Focusing on future research, it would be beneficial to characterize the Zn isotope compositions of other important meteorite groups, particularly CR and CK chondrites and angrites. These meteorites showcase nucleosynthetic and mass-dependent isotope, as well as elemental characteristics that are distinct from other groups that have already been analysed. Also beneficial would be more precise Zn isotope data, as this may reveal distinctions between meteorite groups that are currently identical within uncertainties. Such differences would be consequential as they may provide additional constraints for the origin of Earth's building blocks. For example, based on other isotope systems, the mean Zn isotope compositions of some NC achondrite groups are expected to be distinct from the NC chondrites, but with current precision, they overlap within uncertainty.

Additional leaching experiments of further meteorites, and especially a CI chondrite, could aid in constraining the original compositions of different phases, prior to nebular or parent-body processing. Improved estimates of the elemental abundances of different meteorite groups, particularly of NCCs and achondrites, could also prove consequential, not only for the feasibility of the thermal processing model, but also for the estimates of the contributions of these materials to Earth's inventory of these elements. Lastly, efforts should be made to identify nucleosynthetic isotope anomalies for other volatile elements as such data will be fundamental for understanding the role of different materials in establishing Earth's volatile inventory. Additional constraints from K isotopes and the isotope systems of other volatile elements yet to be identified, for example Te, would be valuable additions to the models presented in this study.

# Appendix

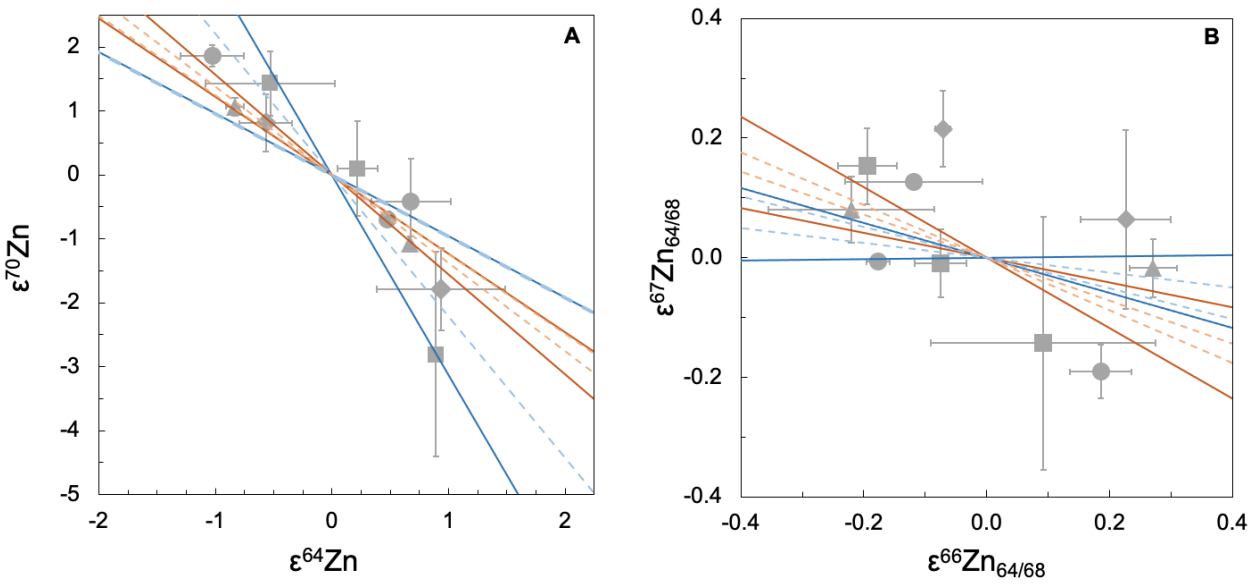



**Figure A2.1. Modelled trendlines for predicted nucleosynthetic Zn isotope anomalies.** (A) Correlation between $\varepsilon^{70}Zn$ and $\varepsilon^{64}Zn$ predicted by the addition of material from ECSN (orange lines) and SNIa (blue lines); see supplementary text for details. The full lines were used to outline the grey fields in Figure 2.6, as they encompass the results obtained for the other two variations of the respective models, shown by the dashed orange and blue lines. The meteorite data are shown in light grey for comparison. (B) same as (A), but for $\varepsilon^{67}Zn_{64/68}$ versus $\varepsilon^{66}Zn_{64/68}$.

**Table A2.1. Ti and Cr isotope data utilized in Figure 2.7**. The $\varepsilon^{50}$Ti data are from (Trinquier et al., 2009) and (Zhang et al., 2012). The $\varepsilon^{54}$Cr data are from (Qin et al., 2010).

| Sample | $\varepsilon^{50/47}$Ti | 2se | $\varepsilon^{54/52}$Cr | 2se |
|---|---|---|---|---|
| Orgueil (CI) | 1.85 | 0.03 | 1.65 | 0.07 |
| *CI mean* | 1.85 | 0.03 | 1.65 | 0.07 |
| Murchison (CM2) | 3.09 | 0.08 | 0.97 | 0.20 |
| Murray (CM2) | 2.84 | 0.05 | - | - |
| *CM mean* | 3.09 | 0.08 | 0.97 | 0.20 |
| Allende (CV3) | 4.23 | 0.77 | 0.95 | 0.10 |
| Leoville (CV3) | - | - | 0.71 | 0.15 |
| Vigarano (CV3) | - | - | 0.87 | 0.09 |
| *CV mean* | 4.20 | 0.61 | 0.87 | 0.08 |
| Kainsaz (CO3.2) | - | - | 0.87 | 0.18 |
| Lancé (CO3) | 3.46 | 0.10 | - | - |
| Ornans (CO3) | 3.37 | 0.09 | - | - |
| Isna (CO3) | 3.50 | 0.06 | - | - |
| Félix (CO3) | 4.69 | 0.12 | - | - |
| *CO mean* | 3.76 | 0.54 | - | - |
| ALHA 77295 (EH3) | - | - | 0.05 | 0.14 |
| Indarch (EH4) | -0.13 | 0.05 | 0.05 | 0.14 |
| QUE 94204 (EH7) | - | - | 0.21 | 0.08 |
| Qingzhen (EH3) | -0.12 | 0.20 | - | - |
| Sahara 97072 (EH3) | -0.15 | 0.06 | - | - |
| Adhi Kot (EH4) | -0.10 | 0.04 | - | - |
| Abee (EH4) | -0.06 | 0.04 | - | - |
| Saint-Sauveur (EH5) | -0.15 | 0.09 | - | - |
| *EH mean* | -0.12 | 0.03 | 0.03 | 0.14 |
| LAP 03601 (H4) | - | - | -0.28 | 0.11 |
| Kesen (H4) | -0.37 | 0.05 | - | - |
| Juancheng (H5) | -0.60 | 0.08 | - | - |
| St Severin (H6) | -0.74 | 0.20 | - | - |
| *H mean* | -0.58 | 0.14 | -0.28 | 0.11 |
| QUE 97008 (L3) | - | - | -0.42 | 0.14 |
| Hedjaz (L3.7) | -0.65 | 0.13 | - | - |
| Ausson (L5) | -0.64 | 0.03 | - | - |
| Isoulane-n-Amahar (L6) | -0.59 | 0.05 | - | - |
| *L mean* | -0.63 | 0.03 | -0.42 | 0.14 |
| Dar al Gani (LL3) | -0.72 | 0.16 | - | - |
| Krymka (LL3.2) | -0.66 | 0.05 | - | - |
| GRO 95552 (LL4) | - | - | -0.33 | 0.10 |
| Paragould (LL5) | -0.61 | 0.07 | - | - |
| *LL mean* | -0.66 | 0.05 | -0.33 | 0.10 |

**Table A2.2. Mean $\varepsilon^{64}Zn$, $\varepsilon^{70}Zn$, and $\varepsilon^{66/67}Zn_{64/67}$ values of endmembers used in the mass balance calculations and their respective p-values.** n is the number of meteorite groups included in each endmember. The p-values are from ANOVA tests that compared the εZn values of all meteorites (from different groups) that contribute to a given endmember.

| Endmembers | $\varepsilon^{64}Zn$ | 2se | 2sd | p-value | $\varepsilon^{70}Zn$ | 2se | 2sd | p-value | $\varepsilon^{66/67}Zn_{64/67}$ | 2se | 2sd | p-value | n |
|---|---|---|---|---|---|---|---|---|---|---|---|---|---|
| CI-CM-CO-CV | -0.81 | 0.16 | 0.43 | 0.23 | 1.20 | 0.20 | 0.53 | 0.09 | 0.27 | 0.05 | 0.01 | 0.22 | 4 |
| CI-CM | -0.86 | 0.33 | 0.56 | 0.38 | 1.47 | 0.12 | 0.20 | 0.51 | 0.28 | 0.11 | 0.19 | 0.37 | 2 |
| CO-CV | -0.77 | 0.13 | 0.26 | 0.11 | 1.01 | 0.15 | 0.31 | 0.26 | 0.25 | 0.04 | 0.08 | 0.11 | 2 |
| EC-OC-IAB | 0.75 | 0.19 | 0.64 | 0.68 | -1.39 | 0.62 | 2.04 | 0.12 | -0.24 | 0.06 | 0.21 | 0.60 | 5 |
| EC-OC | 0.76 | 0.22 | 0.67 | 0.57 | -1.61 | 0.66 | 1.97 | 0.18 | -0.25 | 0.07 | 0.22 | 0.56 | 4 |
| OC | 0.73 | 0.28 | 0.74 | 0.52 | -1.27 | 0.45 | 1.19 | 0.15 | -0.24 | 0.09 | 0.24 | 0.52 | 3 |
| EC | 0.89 | 0.06 | 0.08 | - | -2.80 | 1.60 | 2.26 | - | -0.30 | 0.01 | 0.02 | - | 1 |

**Table A2.3. Zn concentration data (in μg $g^{-1}$) for CCs, ECs, OCs and Earth reservoirs compiled from the literature and adopted in this study.**

| CC | CI | CM | CV | CO |
|---|---|---|---|---|
| Anders & Grevesse (1989) | 312 | | | |
| Wasson & Kallemeyn (1988) | 312 | 185 | 116 | 100 |
| McDonough & Sun (1995) | 310 | | | |
| Lodders (2003) | 315 | 180 | 110 | 110 |
| Palme & O'Neill (2014) | 323 | | | |
| Braukmuller et al. (2018) | 321-391 | 197 | 123 | 110 |
| **This study (adopted)** | **320** | **185** | **115** | |

| Earth | BSE | Core | BE | Core/BSE |
|---|---|---|---|---|
| McDonough & Sun (1995) | 55 ± 8 | | | |
| McDonough (2014) | 55 | (10) | 40 | 0.17 |
| Palme & O'Neill (2014) | 53.5 ± 2.7 | | | |
| Braukmuller et al. (2018) | 54.5 ± 2.5 | 50 | 52 | 0.92 |
| Wang et al. (2018) | 53.9 ± 2.5 | 29 | 46 | 0.54 |
| Mahan et al. (2018) | 56 ± 1 | 101 | 70 | 1.80 |
| **This study (adopted)** | **54** | **12-103** | **40-70** | **0.2-1.9** |

| EC | EH3,4 | EH5 | EL3 | EL5,6 |
|---|---|---|---|---|
| Wasson & Kallemeyn (1988) | 250 | | 17 | |
| Lodders (2003) | 290 | | 18 | |
| Laul et al. (1972) | 90-519 | 44-501 | | 7.5-86 |
| Kallemeyn & Wasson (1986) | 62-342 | 21-290 | | 10-23 |
| Kong et al. (1997) | 112-379 | 372 | 209-218 | 117 |

| OC | H | L | LL |
|---|---|---|---|
| Wasson & Kallemeyn (1988) | 47 | 50 | 46 |
| Lodders (2003) | 47 | 57 | 56 |
| Laul et al. (1972) | | | 44-81 |
| Luck et al. (2005) | 40-48 | 40-79 | 40-52 |
| Paniello (2018) | 17-158 | 14-109 | |

**Table A4.1. Zn and Al relative abundances for different meteorite groups adopted in this study.**

| Class | [Zn] (μg $g^{-1}$) | | [Al] (%) | |
|---|---|---|---|---|
| | Range | Adopted | Range | Adopted |
| CI | 312 - 391 | 352 | 0.80 - 0.86 | 0.83 |
| CM | 182 - 214 | 198 | 1.1 - 1.24 | 1.17 |
| CO | 100 - 119 | 110 | 1.11 - 1.43 | 1.27 |
| CV | 112 - 127 | 120 | 1.42 -1.75 | 1.585 |
| H | 41 - 55 | 48 | 1.1 - 1.2 | 1.15 |
| L | 43.5 - 63 | 54 | 1.17 - 1.26 | 1.215 |
| LL | 41 - 60.6 | 51 | 1.16 - 1.31 | 1.235 |
| EH3-4 | 290 | 290 | 0.74 - 0.87 | 0.805 |
| EH5-6 | 21-100 | 60 | 0.74 - 0.87 | 0.805 |
| EL3-4 | 213 | 213 | 1.0 - 1.14 | 1.07 |
| EL5-6 | 6 - 21 | 14 | 1.0 - 1.14 | 1.07 |
| R | 134 - 162 | 148 | 1.02 - 1.11 | 1.065 |

**Table A4.2. Compiled data of nucleosynthetic isotope compositions of different meteorite groups.**

| Group | Reservoir | $\varepsilon^{48}$Ca | 95% CI | $\varepsilon^{50}$Ti | 95% CI | $\varepsilon^{54}$Cr | 95% CI | $\varepsilon^{96}$Zr | 95% CI | $\varepsilon^{145}$Nd | 95% CI | $\varepsilon^{95}$Mo | 95% CI |
|---|---|---|---|---|---|---|---|---|---|---|---|---|---|
| CI | CC | 2.11 | 0.2 | 1.89 | 0.15 | 1.55 | 0.07 | 0.34 | 0.54 | 0.02 | 0.02 | 0.69 | 0.23 |
| CM | CC | 3.14 | 0.14 | 2.89 | 0.15 | 0.97 | 0.08 | 0.70 | 0.67 | 0.06 | 0.03 | 3.17 | 0.16 |
| CO | CC | 3.87 | 0.56 | 3.58 | 0.85 | 0.83 | 0.18 | 0.94 | 0.20 | 0.06 | 0.02 | 1.39 | 0.34 |
| CV | CC | 3.50 | 0.38 | 3.45 | 0.19 | 0.94 | 0.08 | 0.96 | 0.37 | 0.04 | 0.04 | 0.93 | 0.14 |
| H | NC | -0.23 | 0.03 | -0.65 | 0.14 | -0.31 | 0.13 | 0.32 | 0.08 | 0.07 | 0.04 | 0.29 | 0.05 |
| L | NC | -0.32 | 0.11 | -0.67 | 0.1 | -0.4 | 0.06 | 0.40 | 0.40 | 0.04 | 0.06 | 0.21 | 0.03 |
| LL | NC | -0.44 | 0.09 | -0.67 | 0.08 | -0.42 | 0.08 | 0.34 | 0.25 | 0.01 | 0.03 | 0.18 | 0.05 |
| R | NC | - | - | - | - | -0.07 | 0.03 | - | - | - | - | 0.18 | 0.05 |
| EH | NC | -0.32 | 0.56 | -0.14 | 0.07 | 0.02 | 0.05 | 0.04 | 0.24 | 0.03 | 0.04 | 0.18 | 0.07 |
| EL | NC | -0.40 | 0.51 | -0.28 | 0.17 | 0.03 | 0.05 | 0.20 | 0.40 | 0.03 | 0.02 | 0.14 | 0.06 |
| Acapulcoites | NC | - | - | -1.52 | 0.30 | -0.62 | 0.15 | - | - | - | - | 0.48 | 0.03 |
| HED | NC | -1.24 | 0.29 | -1.23 | 0.05 | -0.69 | 0.08 | 0.37 | 0.12 | 0.07 | 0.01 | - | - |
| Ureilites | NC | -1.46 | 0.20 | -2.00 | 0.32 | -0.90 | 0.04 | - | - | - | - | 0.38 | 0.04 |
| Angrites | NC | -1.06 | 0.33 | -1.18 | 0.08 | -0.43 | 0.06 | 0.51 | 0.10 | 0.07 | 0.02 | - | - |
| Aubrites | NC | -0.44 | 0.59 | -0.06 | 0.11 | -0.16 | 0.19 | - | - | 0.07 | 0.07 | 0.25 | 0.06 |